UQAC
Université du Québec
à Chicoutimi

A DISSERTATION

PRESENTED TO THE

UNIVERSITY OF QUEBEC AT CHICOUTIMI

IN PARTIAL FULFILLMENT OF THE REQUIREMENT

FOR THE DOCTOR OF PHILOSOPHY IN ENGINEERING

BY

LUKAS DION

MODELISATION OF PERFLUOROCARBON EMISSIONS BASED ON THE ALUMINA DISTRIBUTION AND LOCAL CURRENT DENSITY IN AN ALUMINIUM ELECTROLYSIS CELL

OCTOBER 2018

RÉSUMÉ

L'industrie de l'aluminium est une importante productrice de GES à l'échelle nationale tant par ses émissions de dioxyde de carbone que par ses émissions de perfluorocarbures (PFC) qui émanent lors d'un événement néfaste communément appelé effet anodique (EA). Le projet de doctorat discuté dans le présent document a été mis en place pour accroître la compréhension des mécanismes qui entraînent des émissions de PFC de façon à faciliter leur quantification tout en minimisant les émissions totales.

Globalement, les émissions de PFC pour une usine sont actuellement quantifiées en utilisant des modèles linéaires qui nécessitent des indicateurs de performance mensuels. Ces méthodologies sont toutefois imprécises pour une faible fréquence d'EA et de nouveaux modèles sont désormais nécessaires pour assurer une quantification adéquate des émissions de PFC.

Au cours du projet, plusieurs campagnes industrielles de mesure d'émissions ont été réalisées pour associer une quantité de CF_4 et de C_2F_6 spécifique à chacun des EA respectifs détecté par le système de contrôle. En se basant sur plus de mille EA individuels mesurés, de nouveaux modèles ont pu être proposés et ceux-ci ont été comparés avec les modèles déjà existants établis. Le modèle considéré comme ayant le meilleur potentiel (simple et efficace) pour une utilisation à travers l'ensemble de l'industrie considère une évolution non linéaire de la quantité de PFC émise en fonction de la durée de polarisation mesurée pendant l'EA. Une validation basée sur les performances de sept usines a permis de confirmer une meilleure précision du modèle proposée. Toutefois, l'ampérage de l'usine à un impact considérable sur le rythme d'émission des PFC. Il a donc été nécessaire d'incorporer une seconde variable dans l'équation pour un meilleur degré de précision. Ainsi, le modèle générique développé permet de quantifier individuellement les émissions de PFC issues d'EA pour toutes les technologies utilisant des anodes précuites et ayant un ampérage inférieur à 440 kilo ampères.

Le deuxième volet du projet touche les effets anodiques à bas voltage (EABV) en mettant l'emphase sur les mécanismes entraînant leur génération. À partir de mesure de composition des gaz de cuves individuelles, un premier modèle publié a été mis en place permettant de quantifier les émissions de PFC issues d'EABV. Ce modèle a une précision de ±25% pour le 2/3 des cas observés. Une analyse de sensibilité performée sur ce modèle a permis de déterminer que l'écart-type de courant anodique individuel est le paramètre ayant la meilleure corrélation avec les émissions de PFC issues d'EABV. Il a également été possible de démontrer qu'un changement dans la méthode d'échantillonnage des gaz offrirait une meilleure représentativité du comportement de la cuve, ce qui est nécessaire pour atteindre une précision plus élevée de l'algorithme de prédiction des EABV.

Un modèle mathématique transitoire a été développé permettant de simuler l'évolution de la distribution locale d'alumine et la densité du courant dans une cuve d'électrolyse pour les 20 ensembles anodiques de la cuve. Il est donc possible d'évaluer l'homogénéité de la distribution du courant et de prédire si certains scénarios d'opération sont plus à risque de générer des PFC. Des mesures industrielles ont permis de confirmer une bonne corrélation entre le simulateur et la réalité, autant au niveau de l'évolution de la concentration d'alumine que pour la prédiction d'EABV.

Enfin, les connaissances acquises au cours du projet et la proximité du partenaire industriel ont permis la mise en place d'un algorithme de contrôle des cuves qui détecte la production de PFC dans la cuve et lance automatique un traitement correctif qui agit pour éliminer cette problématique. Cette action corrective a permis une réduction de plus de 50% de la fréquence des EA ainsi qu'une réduction de près de 50% de l'instabilité des cuves étudiées sans affecter de façon négative les autres indicateurs clés de performances.

SUMMARY

The aluminium industry is an important GHG producer due to its carbon dioxide emissions but also due to the perfluorocarbons (PFC) emissions emitted during a detrimental event known as anode effect (AE). The doctoral project presented in this thesis was realised to increase the understanding of the different mechanisms leading to the generation of PFC, in order to facilitate the quantification of PFC while facilitating a reduction of the total emissions.

Globally, a smelter's PFC emissions are estimated using linear models based on monthly performance indicators. However, the precision of these methodologies is dependent on the total number of AE occurrence and new models are now necessary to assure adequate estimations of PFC emissions.

During this project, multiple measurement campaigns were performed to assign specific CF_4 and C_2F_6 amounts for each respective AE detected by the control system. Based on more than one thousand individual measurements, new models were proposed and compared to the already existing methodologies. The model considered with the best potential to be used widely across the industry, in terms of simplicity and efficiency, considers the PFC emission rate as a non-linear function of the polarised AE duration. Validation was performed based on data acquired in 7 different smelters to confirm an improved predictive efficiency. However, it also demonstrated that the line current has an important impact on the emission rate of PFC emissions. It was necessary to incorporate an additional variable into the equation to reach a higher level of precision. Finally, a generic model was developed with the ability to estimate the PFC emissions resulting from individual AE for cell technologies using prebaked anodes and line current higher than 440 kilo amperes.

The second aspect of the project is related to low voltage anode effect (LVAE) where a thorough study of the mechanism leading to their generation was performed. Based on gas composition measurements performed on individual cells, a first published model was established allowing quantification of PFC emissions resulting from LVAE. The measured accuracy of the model is ±25% for 2/3 of the studied scenarios. A sensitivity analysis was performed afterward on the model and the standard deviation among individual anode currents was found to be the variable having the best correlation with the presence of LVAE. It was also demonstrated that improvements in the gas extraction technique should lead to a better representativeness of the cell global condition, which is necessary in order to increase the predictive capability of the LVAE algorithm.

A transient mathematical model was developed to simulate the local alumina concentration and current density in an electrolysis cell for the 20 different anodic assemblies. Henceforth, it is possible to evaluate the homogeneity of the current distribution and predict if specific operation scenarios are more at risk to generate PFC

emissions. Industrial measurements confirmed that a good correlation exists between the simulator and the reality for both the evolution of the alumina distribution and the LVAE predictive capability.

Finally, the knowledge acquired during this project and the proximity of the industrial partner allowed the development of a control algorithm to detect PFC generation while automatically launching a corrective action to eliminate the threat. Usage of this preventive treatment allowed a reduction of more than 50% on the AE frequency and a reduction of almost 50% related to the cell instability without any negative impact on other key performance indicators.

REMERCIEMENTS

Au cours de mon cheminement académique, j'ai eu la chance de côtoyer un très grand nombre de personnes et je crois fortement que chacune d'entre elle m'ont influencé de façon positive. Ces quelques lignes visent à souligner les gens que je considère comme pierres angulaires de mon cheminement et sans qui, je n'aurais pas eu les mêmes succès.

En tout premier lieu, je désire remercier profondément mon directeur de recherche, **Pr. László Kiss**, non seulement pour le soutien constant que celui-ci m'a offert durant tout le projet, mais pour le partage de son enthousiasme contagieux qui a eu de nombreuses répercussions positives dans toutes les sphères de ma vie.

En second lieu, le support de mon codirecteur de recherche, **Dr. Sándor Poncsák**, a été très fortement apprécié au cours des trois dernières années. Son attitude professionnelle minutieuse a permis d'accroître considérablement la qualité de mes travaux scientifiques. Par ailleurs, je suis très reconnaissant pour ses rappels sur l'importance d'un bon équilibre entre le travail et les loisirs, de façon à demeurer en pleine forme mentalement, et ainsi performer à son plein potentiel.

Par la suite, je tiens à remercier mon superviseur en milieu pratique, **M. Charles-Luc Lagacé,** pour son soutien continu dans toutes les phases du projet, particulièrement lors de la phase initiale qui a permis de bien combiner plusieurs aspects fondamentaux avec les besoins industriels.

Il y a également plusieurs employés travaillant chez Aluminerie Alouette qui m'ont prêté main-forte à plusieurs reprises pour m'aider à réaliser mes expérimentations, assez souvent… hors du commun.

Parmi ces employés, une mention très spéciale à **Guy Ladouceur**, ainsi qu'un grand merci à toutes ces personnes formidables avec qui j'ai eu la chance de passer du temps : **Marc Gagnon, François Laflamme, Patrick Coulombe, Nadia Morais, Julie Salesse, Stephan St-Laurent, Dominic Dubé, Antoine Godefroy**, et bien d'autres que j'oublie…

Je remercie grandement le **Dr. Jerry Marks** pour son assistance technique, ainsi que pour m'avoir permis d'utiliser à plusieurs occasions un appareil de mesure de type FTIR chez Aluminerie Alouette. Sans cette contribution, il n'aurait pas été possible de réaliser un projet d'une telle ampleur.

J'en profite aussi pour remercier certains collaborateurs avec qui j'ai eu la chance de travailler sur de superbes projets. Ces collaborateurs sont **James Evans, Simon Gaboury, Jerry Marks, Pernelle Nunez, David Wong et Alexey Spirin.**

Bien entendu, la réalisation d'un tel projet en milieu industriel aurait été impossible sans le partenariat d'**Aluminerie Alouette**. Je tiens donc à mentionner que je suis

extrêmement reconnaissant de l'envergure du support que j'ai reçu, autant du côté technique que sur l'aspect financier. Le soutien financier de la part du **CRNSG** et du **FRQNT**, au moyen d'une bourse d'études BMP-Innovation est également grandement apprécié.

Par ailleurs, d'autres organisations m'ont également soutenu au moyen de bourses d'excellences, ou de bourse de soutien pour assister à des rencontres scientifiques. Je suis donc très reconnaissant auprès de la Fondation UQAC, de Rio Tinto, ainsi qu'auprès de la fondation TMS.

Enfin, je considère que l'ensemble de mes succès sont en grande partie fondés sur l'appui reçu de la part de mes parents, **Gilles Dion et Michèle Savard** qui sont une source perpétuelle d'encouragement et de motivation.

En tout dernier lieu, il m'aurait été impossible d'arriver au même point, après ces dix années d'études universitaires, sans le support de ma famille, de mes amis munchkineux, de mes deux chats, et surtout, sans le soutien de ma conjointe **Karine Leblanc**, avec qui j'ai traversé toutes les étapes importantes de ma vie.

TABLE OF CONTENT

LIST OF FIGURES

LIST OF TABLES

Table I: List of chemical compounds

Chemical formula	**Name**
Al	Aluminium
Al2O3	Aluminium oxide (Alumina)
AlF3	Aluminium Fluoride
C	Carbon
C2F6	Hexafluoroethane
CaF2	Calcium Fluoride
CF4	Tetrafluoromethane
CO	Carbon Monoxide
CO2	Carbon Dioxide
COF2	Carbonyl Fluoride
H2O	Water
HF	Hydrogen Fluoride
Na3AlF6	Cryolithe
NaF	Sodium Fluoride
SF6	Sulfur hexafluoroethane

Table II: List of abbreviations

Abbreviation	Name
(diss)	Chemical compound under dissolved form
(g)	Chemical compound under gas form
(l)	Chemical compound under liquid form
(s)	Chemical compound under solid form
ACD	Anode-cathode distance (Interpolar distance)
AE	Anode effect
AED	Anode effect duration
AEO	Anode effect Overvoltage
AETD	Anode effect treatment duration (same thing as AED)
ANN	Artificial neural network
AP40LE	Specific type of cell technology: AP40 low energy
CE	Current efficiency
CFD	Computational fluid dynamics
CFx	Family of PFC gas such as CF4, C2F6, C3F8 etc.
FTIR	Fourier-transform infrared spectrometer
GHG	Greenhouse Gases
GTC	Gas treatment center
HVAE	High voltage anode effect
Hz	Hertz
IAI	International Aluminium Institute
IPCC	Intergovernmental Panel on Climate Change
kA	Kilo ampere
LPM	Liters per minute
LVAE	Low voltage anode effect
m	Meters
MHD	Magneto-hydrodynamics
mm	Millimeters
MPV	Maximum polarisation voltage
mV	Milivolts
MVA	Multivariate analysis
PAED	Polarized anode effect duration
PFC	Perfluorocarbons
ppb	Parts per billion
ppm	Parts per million
V	Volts

Table III: List of symbols used in the different equations

Symbol	Definition	Units
	Latin symbols	
A	Area of alumina exposed to bath	m^2
A	Cross-section area of an electrical conductor	m^2
A_{bath}	Area of bath under an anode	m^2
AEM	Anode effect minutes per cells, per day	AE-Mins/cell-day
A_{ij}	Contact area between two volumes	m^2
AOE	Anode effect overvoltage	mV
BR	Bath ratio	-
C	Concentration of alumina in bath	kg/m^3
C_{CONS}	Daily carbon consumption	m/day
CE	Current efficiency	%
CE_i	Respective current efficiency	%
C_s	Concentration at saturation of alumina in bath	kg/m^3 or % wt.
D_{eq}	Equivalent diffusivity	m^2/s
DMP	Daily metal production (same as MP)	tons
E^0	Decomposition potential	Volts
EC_2F_6	Total emissions of C_2F_6	kg
ECF_4	Total emissions of CF_4	kg
F	Faraday's constant	C/mol
F	Factor used to represent the effect of bubbles under an anode	-
FC_2F_6/CF_4	Mass ratio between CF_4 and C_2F_6 emissions used to estimate C_2F_6 emissions	-
I_i	Respective amperage within an anodic assembly	A
K	Kinetic of a reaction	-
K1	Parameter used in the HVAE prediction power-law	g CF4 / tons Al / AE mins
K2	Parameter used in the HVAE prediction power-law	-
K_m	Dissolution coefficient	m/s
L	Cell length	m

L	Length between the center of two volumes	m
L	Length of an electrical conductor	m
L_C	Length of carbon on the anode	m
L_{INI}	Initial carbon height of an anode	m
L_{ROD}	Length of the aluminium rod of an anodic assembly	m
L_{TOT}	Constant length from anodic beam to the bottom of anodic assembly	m
M	Molar mass	g/mol
m_i	Respective alumina consumption	g
m_{ij}	mass transfer rate between two volumes	kg/s
MP	Metal production for 24 hours	tons
n	Specific ratio	-
N	Number of days since the anode is in the cell	days
OVC	Emission factor to estimate CF4 based on anode effect overvoltage	(kg CF_4 / tonne Al)/mV
R	Resistance	Ω
R_{bath}	Resistance of the electrolyte	Ω
SCF_4	Emission factor to estimate CF_4 emissions based on the polarized anode effect duration	(kg CF_4/tonne Al)/(AE-mins/cell-day)
T	Bath temperature	K or ˚C
w	Cell width	m
x	Dimensionless time during two simultaneous HVAE (0 = beginning and 1 = end)	-
z	Valency number of ions	-
Mathematical symbols		
ΔC	Concentration gradient between two volumes	kg/m^3
Δt	Timestep	s
Δx	Spatial distance between two volumes in the simulator	m
dm/dt	dissolution rate of the alumina	kg/s
Γ(x)	Gamma function	-
Greek symbols		
α	Variable parameter used in the beta function	-

α	Coefficient used in the calculation of the saturation point of the alumina	-
β	Variable parameter used in the beta function	-
β	Coefficient used in the calculation of the saturation point of the alumina	-
ρ	Electrical resistivity	Ω m
ρ_{bath}	Electrical resistivity of the bath	Ω m
σ	Electrical conductivity of the bath	S/cm

CHAPTER 1

INTRODUCTION

1.1 Introduction – Hall-Heroult process

Industrial aluminium production debuted in 1889, when Charles M. Hall and Paul Heroult developed, parallel to each other, a process to produce aluminium by electrolysis of the aluminium oxide using a cryolite-based solvent. This process, commonly known as the Hall-Heroult process has evolved over the century and is still widely used worldwide and considered the most practical way to obtain aluminium on an industrial scale.

Nowadays, electrolysis of the alumina is performed in large reduction cells (Figure 1-1) with a significant number of carbon anodes in parallel. An electrical current of high intensity passes through electrical conductors and these anodes to reach the cryolite-based electrolytic bath. A small concentration (typically 1 to 6%) of alumina is dissolved in the bath where the aluminium atoms will dissociate from the oxygen under the passage of a forced current through the electrolyte.

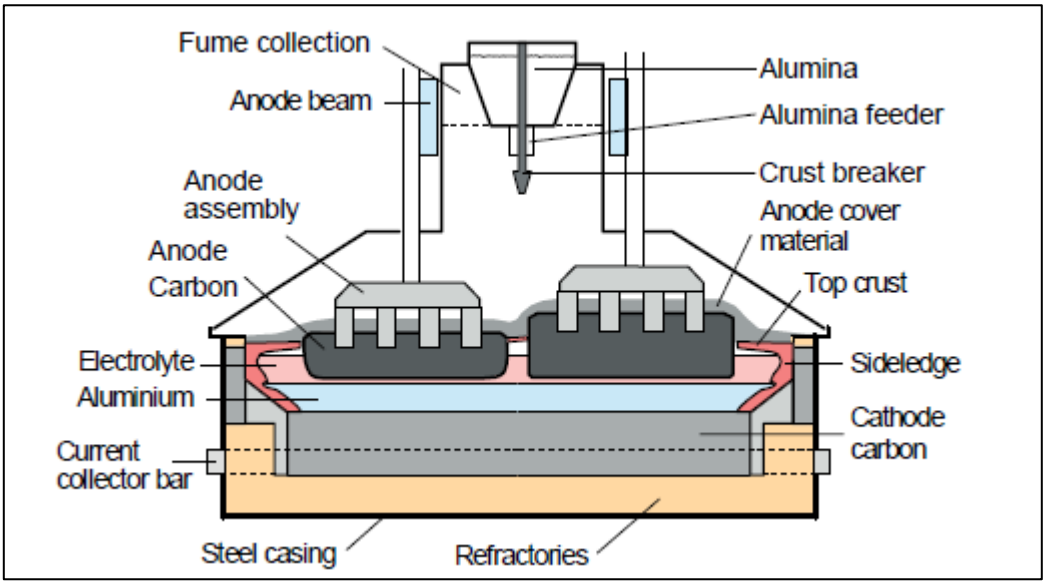

Figure 1-1: Schematic of an aluminium electrolysis cell and its main components. [1]

In most recent smelters, the alumina is routed automatically to the electrolysis cells structure, and then distributed to the bath periodically using point feeders located at specific points in the cell. The number of feeders will be dependent on the cell technology, which differs in size in order to accommodate for increasing line current. The cell technology considered in this project was operating with a total of four point feeders.

The composition of the electrolyte and the quality of the raw products (AlF_3, Al_2O_3, carbon anode, etc.) are very important to assure the consistency of the process, to maximize the production of aluminium and to reduce the occurrence of detrimental events such as anode effects. With increasing cell size and amperage, it has become a challenge to maintain homogeneity of the bath composition. For this reason, mathematical models developed to understand and predict the cell's behavior became an essential element to improve the electrolysis process.

Finally, even after more than a century of operation using this process, there is still uncertainty regarding some of the dynamics of most of the reactions occurring during aluminium electrolysis. Some extensive studies are henceforth necessary to keep improving the general understanding of this process, more importantly regarding the generation rate of some gas products which have an important effect on the environment and climate change.

1.1.1 **Generation of Greenhouse Gases**

The aluminium industry is one of the most important anthropogenic producers of greenhouse gases (GHG), particularly because it uses carbon anodes[1] which react with the

[1] Cell technologies using inert anodes do not face these challenges. However, inert anodes have not yet been deployed on a large industrial scale.

oxygen from the alumina to produce carbon dioxide. Reaction 1-1 is inherent to the production of aluminium; therefore, the carbon dioxide emissions will be directly proportional to the annual aluminium production. Based on the mass balance of the process, more than 1.2 tons of CO_2 is anticipated per tons of aluminium, with additional CO_2 expected from carbon oxidation itself.

$$2\ Al_2O_{3(diss)} + 3\ C_{(s)} \rightarrow 4\ Al_{(l)} + 3\ CO_{2(g)} \qquad (1\text{-}1)$$

Additionally, a second category of GHG is also produced by the aluminium industry: the perfluorocarbons (PFC). Tetrafluoromethane (CF_4) and hexafluoroethane (C_2F_6) are emitted during a detrimental event known as anode effect. This kind of incident occurs when the alumina concentration in the bath becomes insufficient to support the passage of the electrical current. Under such circumstances, the electrolysis bath dissociates via reactions 1-2 and 1-3, and PFC gas is produced.

$$4\ Na_3AlF_{6(l)} + 3\ C_{(s)} \rightarrow 4\ Al_{(l)} + 3\ CF_{4(g)} + 12\ NaF_{(diss)} \qquad (1\text{-}2)$$

$$2\ Na_3AlF_{6(l)} + 2\ C_{(s)} \rightarrow 2\ Al_{(l)} + C_2F_{6(g)} + 6\ NaF_{(diss)} \qquad (1\text{-}3)$$

1.1.2 Distinction between high voltage and low voltage anode effects

Anode effects may occur in the cell under different set of conditions based on the alumina feeding strategy and the size and bath volume of electrolysis cell. Within the industry, the common definition of an anode effect considers that the cell voltage needs to reach a specific threshold for a specific duration in order to be considered in anode effect. This trigger value is typically set to 8 volts, and the typical duration is 3 seconds [2]. Most recently, this type of event is referred to as **high voltage anode effect** (HVAE).

PFC emissions have also been observed in cases where the cell voltage did not reach the specific threshold of detection necessary for the cell control system to identify this event. Due to its small impact on the cell voltage, this type of emission is referred to as **low voltage anode effect** (LVAE). Even though the mechanism leading to the generation of PFC under LVAE is believed to be similar to HVAE emissions, the composition of the gas emitted appear to be mainly composed of CF_4 and only little traces of C_2F_6 have been observed under industrial LVAE conditions. This phenomenon has been explained by the alternative reaction 1-4 that necessitates a lower voltage of reaction and produces COF_2 which reacts rapidly to form CF_4 subsequently via equation 1-5.

$$2\ AlF_{3(diss)} + Al_2O_{3_{(diss)}} + 3\ C_{(s)} \rightarrow 4\ Al_{(l)} + 3\ COF_{2_{(g)}} \qquad E^0 = -1.88V \qquad (1\text{-}4)$$

$$2\ COF_{2_{(g)}} + C_{(s)} \rightarrow 2CO_{(g)} + CF_{4_{(g)}} \qquad K = 94.8 \qquad (1\text{-}5)$$

Wong et al. [3] characterized LVAE as 2 different categories:

- Non-propagating LVAE emissions: PFC emissions without impact on the cell voltage and occurring under a small number of anodes. This type of emission can last for several hours and remain undetected.
- Propagating LVAE emissions: PFC emissions having a small influence on the cell voltage, without reaching the detection threshold. This phenomenon affects a large number of anodes and can last a few minutes.

Whether or not a LVAE will propagate is dependent on the alumina distribution homogeneity in the cell. When generated, PFCs will wet the anode surface and reduce the current going through this specific anode. The current will be redirected to adjacent anodes which will increase their current density. If the alumina concentration is insufficient to handle the passage of these additional electric charges, it will eventually lead to a generation of PFC emissions under that adjacent anode. Under normal operation,

propagation of LVAE will only stop if the alumina distribution increases locally due to metal reoxydation or additional alumina feeding. If it doesn't occur, the cell will eventually reach the HVAE state.

Even though both types of LVAE emissions have been observed in the scope of this project, references to LVAE in this thesis will always refer to both categories without any specific distinction.

1.2 Goals of the thesis

This project was designed to fundamentally understand the mechanisms leading to all types of PFC emissions (HVAE and LVAE). Moreover, the acquired knowledge should lead to the development of tools that would benefit the electrolysis process in order to reduce their carbon footprint, while offering improvements in terms of metal production. Hence the goals can be resumed as:

Main objective of the thesis

Being able to identify the key factors influencing the PFC generation rate in order to quantify or predict those emissions for specific operation scenarios.

In order to achieve this main objective, the project was subdivided into three different parts. Moreover, each of the elements listed below are beneficial for the progress of science and well within the scope of a doctorate thesis:

1. Developing an improved methodology to quantify the PFC emission rate of cells during high voltage anode effect.
2. Understand the key factors leading to generation of low-voltage anode effects.

a. Determine the optimal way to predict, or detect the occurrence of LVAE in an electrolysis cell.
b. Develop a model to quantify LVAE resulting from process deviations occurring during aluminium electrolysis.

3. Developing a non-homogenous simulator to reproduce the cell behavior in terms of alumina and current distribution in order to predict PFC emissions within an electrolysis cell.

1.3 Methodologies

1.3.1 Experimental work

The project is realized in an industrial context. Thus, different kinds of measurements were necessary in order to acquire a satisfying amount of data to perform a successful analysis. The basics of these measurement techniques are presented in the following sections.

1.3.1.1 Gas Measurements

Analysis of the gas composition was performed under two different sets of conditions: individual cell gas composition monitoring and gas treatment center (GTC) gas composition monitoring. These sets of conditions are affected by the extraction point of the gas. However, in both cases the composition of the gas was determined using a Fourier-Transformed Infrared spectrometer (FTIR). FTIR spectrometry uses a calibrated infrared energy source generally emitting in a specific spectrum within the wave numbers range of 900 to 4000 cm^{-1}. Under such circumstances, the energy emitted crosses the analysis chamber filled with the unknown compound; in this case, the gas extracted from the electrolysis cells.

An essential part of the FTIR is the interferometer, which is composed of a moving mirror illustrated on Figure 1-2, creating a phase shift in the emitted signal. Henceforth, the

detected signal is known as an interferogram which is directly dependent on the position of the moving mirror at a known time step minus the energy absorbed within the sample chamber.

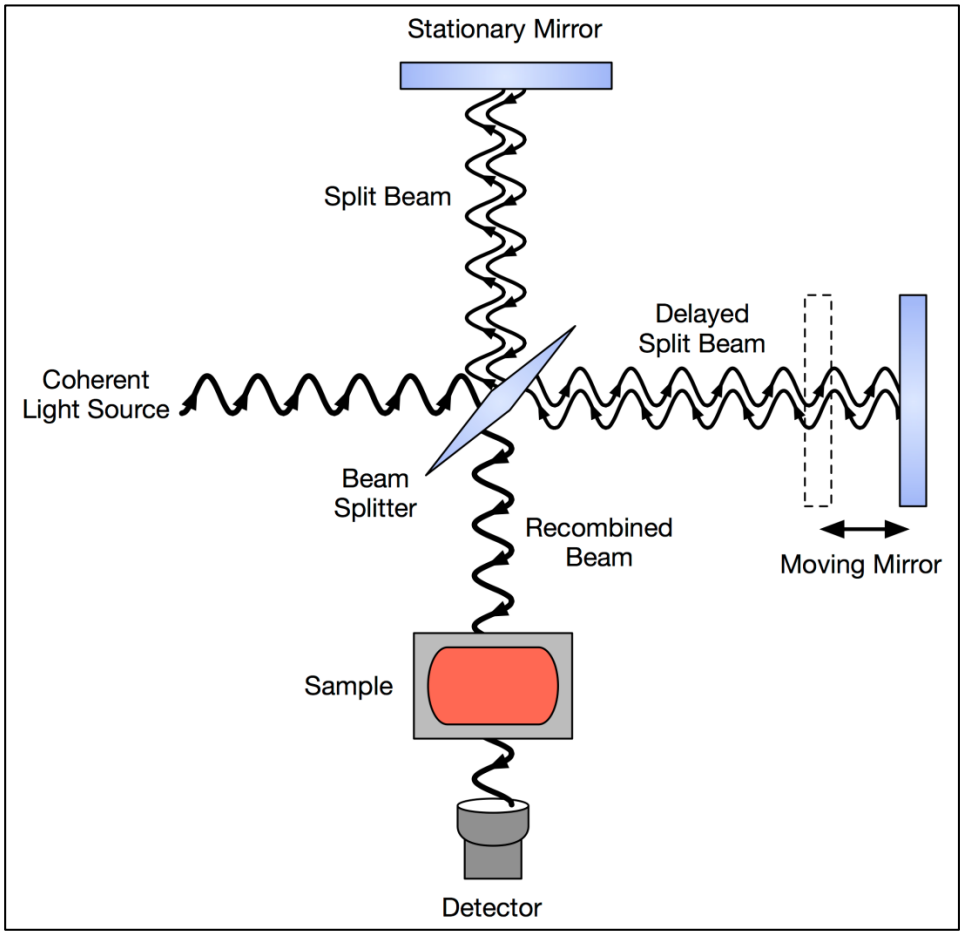

Figure 1-2 : Illustration of an FTIR spectrometer main components [4].

Using Fourier analysis, it is possible to recompose the original spectrum across the entire wave numbers range within a single analysis taking only a fraction of second. This quick response time makes FTIR analysis an ideal technique to continuously analyze the fluctuating emissions of an aluminium electrolysis cell. Moreover, the precision of the measured spectrum can be significantly increased by performing the analysis multiple times

in a row, thus reducing the effect of the noise. The analyzed IR spectrum is then compared to the databank of gas reference in order to find the best correlation gas composition as shown in Figure 1-3.

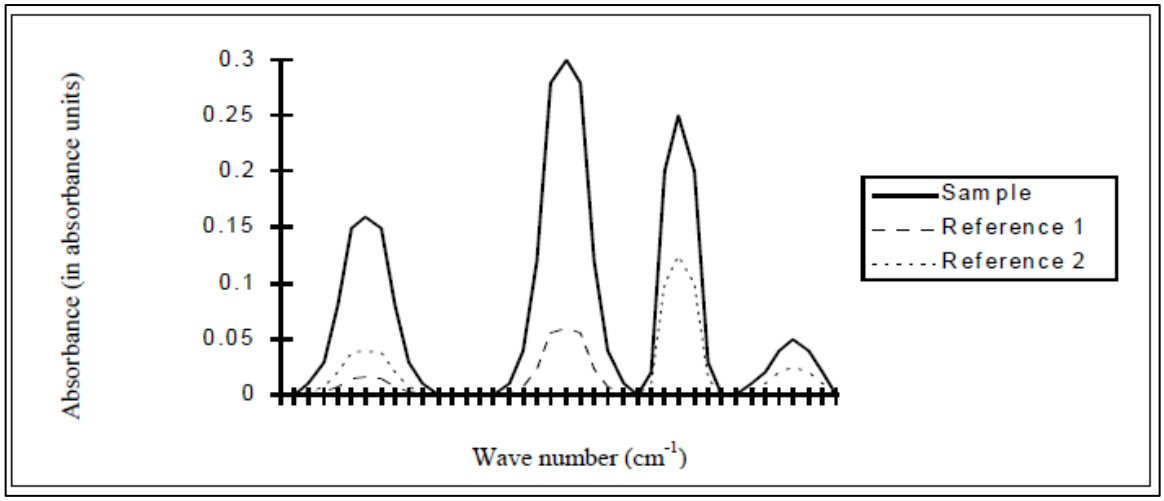

Figure 1-3 : Example of spectrum recomposition using a mixture of different gas reference. [4]

The concentration of a gas will have a non-linear influence on the IR absorbance of the compound, thus it is important to have specific reference spectra in an order of magnitude similar to the expected emissions to assure representativeness of the results and to avoid extrapolation. The effect of an increasing CF_4 concentration on the absorbance is illustrated on Figure 1-4, for the primary absorption peak. Additional details on the reference spectra for various gases studied within the scope of this project are available in Appendix A.

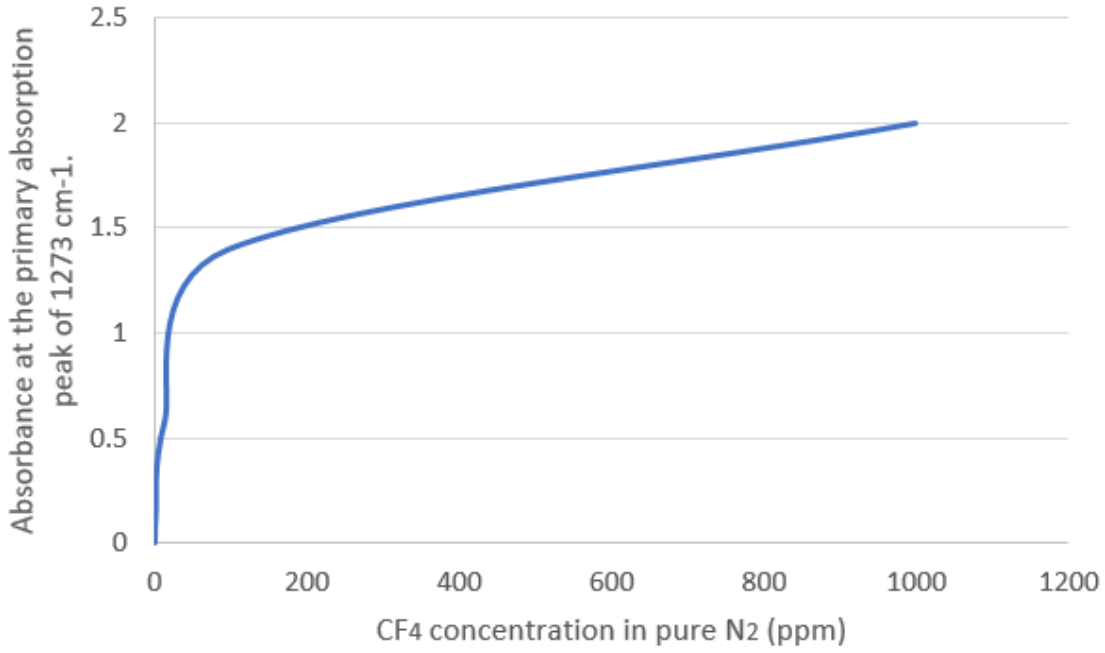

Figure 1-4 : Increase of the absorbance of CF_4 with respect to the gas concentration.

1.3.1.2 Electrolysis cell data acquisition

During normal operation of an electrolysis cells, the voltage is closely monitored continuously by the control system. Hence, no particular manipulation was necessary to acquire this information. Moreover, during HVAE conditions, the control system will automatically monitor the duration of the anode effect, and the energy released based on the evolution of the cell voltage in that time period. Finally, data on the alumina feedings of the cell were also recorded using the control system in order to determine their corresponding feeding cycles during the studied periods.

Even if this information is strongly relevant for the project, it only offers data on the global cell performance and cannot give details on the cell homogeneity. To accurately detect inhomogeneity in the alumina concentration, specific cells were selected when

performing tests on individual cells. These electrolysis cells were equipped with an on-line and continuous individual anode current monitoring system provided by Wireless Industrial Technologies [5]. This technology uses Hall effect sensors adjacent to the anode rods to measure the magnetic field, thus giving a clear indication of the anode current passing through that anode. Data was acquired with a 1 Hz frequency, which is sufficient to detect variation in the bath's alumina concentration as demonstrated in a paper by Dion et al [6].

1.4 Overview and Relationship Between the Different Chapters

As described in the previous sections, the goals of this thesis were covering three specific topics: Study of HVAE (1) and LVAE emissions (2), and development of an alumina and current distribution simulator (3). In order to demonstrate the magnitude of the work performed during this project, six chapters will be presented in this thesis covering the content of the work. This thesis is designed as a collection of articles which were all published prior to the final submission of this thesis. To avoid substantial changes to the originally published text from these articles, some additional discussions are provided in Appendix D.

In chapter 2, the quantification methods related to HVAE estimations are investigated. The inaccuracies of the actual methodologies are presented, and solutions are proposed to increase the predictive ability of PFC estimating models. On the other hand, chapter 3 investigates which type of non-linear models could be the most appropriate to be used across the entire aluminium industry.

Chapter 4 discusses the development and validation phases of the first published model with the ability to quantify PFC emissions resulting from LVAE. However, during the analysis of the results, some uncertainties related to the representativeness of the extracted gas were raised and these issues are discussed and evaluated in chapter 5.

Chapter 6 present the alumina and current distribution simulator, which indirectly connects all the themes of the thesis together. The development of the simulator, as well as the integration of a LVAE PFC estimation model are presented and discussed. In parallel, efficient ways to use this simulator to improve the industrial process are also presented.

Finally, in Chapter 7, industrial improvements resulting from the work performed in this thesis are presented, leading to a reduction of the HVAE frequency and overvoltage, as well as increased cell stability.

1.5 References

1. Asheim, H. (2017). PFC evolution in the aluminium production process. Faculty of natural sciences. Trondheim, Norwegian University of Science and Technology. Doctorate: 205 pages.

2. Tabereaux, A., (2014). Anode effects and PFC emission rates, in 8th Australasian aluminium smelting technology conference.

3. Wong, D., A.T. Tabereaux, and P. Lavoie. (2014) Anode effect phenomena during conventional AEs, low voltage propagating AEs & non-propagating AEs. in Light Metals.

4. Harris, D.C. (1999). Quantitative Chemical Analysis. Fifth Edition ed., W.H. Freeman and Company: New York.

5. Evans, J.W., A. Lutzerath, and R. Victor, (2014) On-line monitoring of anode currents; Experience at Trimet, in TMS - Light Metals. San Diego, CA. p. 739-742.

6. Dion, L., L. I. Kiss, S. Poncsak, J.W. Evans, F. Laflamme, A. Godefroy et C.-L. Lagacé. (2015) On-line Monitoring of Anode Currents to Understand and Improve the Process Control at Alouette. in Light Metals. Orlando.

CHAPTER 2

QUANTIFICATION OF PERFLUOROCARBONS EMISSIONS DURING HIGH VOLTAGE ANODE EFFECTS USING NON-LINEAR APPROACH (BASED ON DATA FROM A SINGLE SMELTER)

2.1 Summary

This chapter was previously published in *Journal of Cleaner Production*, volume 164, pages 357-366, from the year 2017. Its DOI number is 10.1016/j.jclepro.2017.06.199.

The work was performed in collaboration with Jerry Marks, Laszlo I. Kiss, Sandor Poncsak and Charles-Luc Lagacé. The model developed and presented in section 2.5.1.5 was developed by Dr. Jerry Marks. However, the writing of the article itself and the analysis were performed by the author of this thesis, with minor suggestions and comments provided by the co-authors.

2.2 Introduction

With a carbon tax being imposed more and more across the world, industries are strongly incited to deploy significant efforts to reduce their total emissions of greenhouse gases (GHG). The primary aluminium production industry is importantly affected by these new restrictions as a major producer of GHGs. For instance, the emissions of CO_2 equivalent in major smelters can reach as much as one million tonnes per year as all commercial cell technologies use carbon anodes and produce CO_2 as a by-product in the electrolysis process. Nonetheless, a significant part (generally between 5 and 10%) of CO_2 equivalent emissions are attributed to two perfluorocarbon (PFC) gases, tetrafluoromethane (CF_4) and hexafluoroethane (C_2F_6) which have global warming potential of 6630 and 11 100 times greater than CO_2 respectively (Myhre et al. 2013).

PFCs are produced when the electrolysis cells conditions reach an event called anode effect (AE). During AEs the normal electrolysis process becomes difficult due to a lack of alumina, leading to the electrolysis of the electrolytic bath. Two different sets of

conditions can eventually lead to this undesirable event. In the first and most reported case, the cell voltage will increase significantly higher than the typical cell voltage and tens to hundreds of grams of PFCs will be generated in an interval of few seconds to minutes. However, recent measurements demonstrated (Dando et al. 2015; Wong et al. 2015; Léber et al. 2013; Wong and Marks 2013) that PFC generation could also occur locally without a significant change in the overall average cell voltage leading to a low level of emission occurring over a long period, several minutes to hours. Hence, the terminology used to differentiate both sets of conditions is "high voltage anode effect" (HVAE) and "low-voltage anode effect" (LVAE), respectively.

In smelters, PFC emissions are not monitored continuously due to the cost for continuous monitoring. Instead, mathematical estimations (Marks et al. 2006) of these emissions are performed based on the good practice recommendations of the Intergovernmental Panel on Climate Change (IPCC). The most precise estimation method uses linear models quantifying the total amount of PFC emissions based on a single cell parameter which can be either "polarized anode effect duration" or "anode effect overvoltage". However, an analysis based on the rate of increase of PFCs in the atmosphere found that the amount of PFCs in the atmosphere is significantly higher than the amount of PFCs estimated by the industries known to produce PFCs (Kim et al. 2014). Part of this inconsistency can be attributed to PFC emissions resulting from LVAE which were not accounted for in the past or to an inaccurate or incomplete accounting of emissions from other industries such as semiconductor and rare metals production (Wong et al. 2015).

However, it is plausible that imprecision in the current models used to quantify HVAE can also contribute to the measured gap.

In this paper, new non-linear models are proposed to estimate the perfluorocarbon emissions resulting from high-voltage anode effects based on four different process parameters. These models were developed using data collected in the Alouette aluminium smelter and a thorough description of the processing phase of the data is included, including a novel approach to separate respective emissions from overlapping HVAE. Finally, the efficiency of these innovative models is compared to the linear models currently used in the industry to quantify PFC emissions. The results are presented and discussed as well as the positive effect that the presented models could have for the aluminium industry.

2.3 State of the art

2.3.1 Anode effect definition

During the production of aluminium, an electrical current is forced through cryolite based electrolytic bath to electrolyze the dissolved alumina following reaction 2-1. However, privation of dissolved alumina in a localized region of the bath can occur under various conditions. If it happens, transport of the electric charges is no longer supported by the standard electrolysis reaction. This will lead to an increase in the anodic overvoltage, and subsequent reactions 2-2 and 2-3 will occur in the cell, leading to the electrolysis of the electrolyte and the generation of PFCs; i.e. an AE. Once an AE occurs in the cell, the localized area where the bath is electrolyzed becomes strongly resistive to the passage of current due to the high electrical resistivity of the PFC produced and the current will be

redistributed towards other anodes in the cell. This redistribution generally provokes increased voltage elsewhere and the AE can propagate from one anode to the other until terminated, meanwhile significantly increasing the global cell voltage (Wong, Tabereaux, and Lavoie 2014).

$$2\ Al_2O_{3(diss)} + 3\ C_{(s)} \rightarrow 4\ Al_{(l)} + 3\ CO_{2(g)} \qquad E0 = \text{-}1.18V \qquad (2\text{-}1)$$

$$4\ Na_3AlF_{6(l)} + 3\ C_{(s)} \rightarrow 4\ Al_{(l)} + 3\ CF_{4(g)} + 12\ NaF_{(diss)} \qquad E0 = \text{-}2.58V \qquad (2\text{-}2)$$

$$2\ Na_3AlF_{6(l)} + 2\ C_{(s)} \rightarrow 2\ Al_{(l)} + \ C_2F_{6(g)} + 6\ NaF_{(diss)} \qquad E0 = \text{-}2.80V \qquad (2\text{-}3)$$

The main interest of this paper is focused on HVAE, thus indicating that a significant change in the cell voltage is observable and can be monitored by the cell control system. It is well established that the beginning of an HVAE is characterized by a sudden increase in voltage higher than a specified threshold and for a minimum duration. However, among the industry, there is no uniform standard regarding the voltage threshold and reports indicate that this value can fluctuate between 6 and 10 volts depending on the local smelter's practice (Marks and Bayliss 2012). Similarly, no specific duration after the threshold has been defined before the declaration of a HVAE but reports have shown that it can vary between 1 to 3 to as much as 90 seconds (Wong et al. 2015).

During an HVAE, each smelter can adopt different strategies to treat the event as rapidly as possible. As described in previous publications (Tabereaux 1994; Tarcy and Tabereaux 2011; Tabereaux 2004), these strategies involve short-circuiting the aluminium metal pad and the anodes automatically or manually. A common way to achieve this goal is by moving the anode beam up and down to create waves in the aluminium metal pad. Additionally, wooden poles can be inserted beneath the anodes to instantly generate a burst

of gas. The gas generated will create enough turbulence to short-circuit the metal pad and the anode as well as dislodge the PFC trapped underneath the anodes. Finally, additional feedings are generally applied during the HVAE to provide the necessary alumina for the electrolysis and avoid recurrence of the problem. Once the cell voltage stops fluctuating, the cell returns to normal behavior and the HVAE is considered as terminated. However, no standard condition is defined by the industry to consider if the cell conditions are back to their normal state. Moreover, there is no agreement for what length of time must pass before a following voltage excursion is considered a new anode effect or just a continuation of the first AE. These inconsistencies among the industry can lead to important differences in the reported anode effect duration or frequencies. In Alouette, the termination condition is achieved if the cell pseudo-resistance remains stable within a specific interval for at least fifteen seconds, which lead to the plateau observable on Figure 2-1. Once a high-voltage anode effect is terminated, four different parameters can be calculated based on the cell voltage for each specific HVAE as shown in Figure 2-1.

- Anode effect duration (AED): The lapse of time from the start of the anode effect up to its termination.
- Positive anode effect overvoltage (AEO): The sum of the area under the voltage curve exclusively when the values are higher than the target voltage.
- Maximum polarization voltage (MPV): The maximum voltage reached during the anode effect.
- Total anode effect polarization duration (PAED): The sum of all the seconds where the cell voltage was higher than the trigger value.

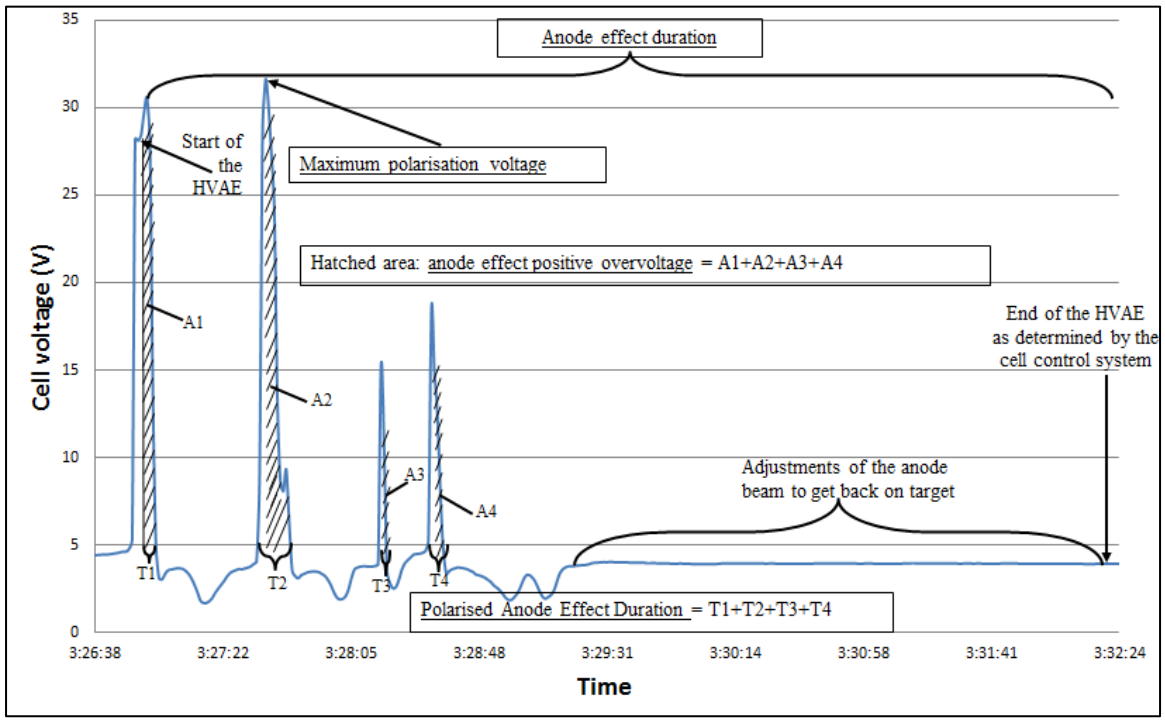

Figure 2-1: Typical behavior of the cell voltage during an anode effect.

2.3.2 **Observations from previous publications**

In the 1990s, smelters around the world showed interest in reducing their total amount of PFC emissions. Therefore, numerous researchers started investigating the respective emissions of CF_4 and C_2F_6 to try and correlate these values to some of the parameters discussed in section 2.3.1. After an exhaustive measurement campaign, Roberts and Ramsey (1994) demonstrated that there was a significant change in the emission rates of PFC mostly influenced by the frequency of HVAE and their duration. In parallel, multiple studies conducted in different locations (Tabereaux 1994; Berge et al. 1994; Marks 1998; Gosselin and Desclaux 2002) showed a linear relationship between the anode effect duration and the total amount of CF_4 generated. Moreover, a linear relationship between the anode effect overvoltage was also observed by some researchers (Bouzat, Carraz, and

Meyer 1996; Martin and Couzinie 2003; Marks et al. 2001). Some difference in the rate of emissions was observed depending on cell technologies and HVAE treatment strategies. Nonetheless, the presence of a correlation is definitive between the average anodes effect minutes per cell day and the measured average PFC emissions of an aluminium smelter. However, no publication investigated individual anode effect emissions to establish if the correlation could be improved by using non-linear relationships.

Measurements regarding C_2F_6 reveal similar behavior (Martin and Couzinie 2003; Marks et al. 2003; Marks 1998) but a few studies demonstrated that the emission rate of this gas seems to be non-linear. Tabereaux (1994) measured the gas composition from a single cell in an 180 kiloamperes (kA) prebake cell and observed that C_2F_6 emissions are only occurring during the first minutes of the HVAE. In agreement with Tabereaux, Gosselin and Desclaux (2002) found a decreasing linear correlation between the C_2F_6 / CF_4 ratio and the anode effect duration. Therefore, a non-linear estimation model could lead to more accurate results for estimating C_2F_6 emissions during HVAE.

2.3.3 **Standard Quantification Methodologies**

In order to represent adequately the PFC emissions from the aluminium industry, a standard and recognized methodology was defined based on cooperation between different government agencies and the industries. The results of this work are included in the quantification method document published by the Intergovernmental Panel on Climate Change (IPCC). This document (Marks et al. 2006) is the common standard in the primary aluminium production industry to correctly quantify GHG emissions from every step of the process.

PFC quantification methods are available with three different levels of uncertainty. The Tier 1 methodology consists of an average PFC production depending exclusively on the overall metal production of a specific smelter without concern for the frequency of HVAE, or their duration. For this reason, the uncertainty of this method can reach many hundreds of percent and is almost never used. Tier 2 methodology uses the same formula as Tier 3, but with an average emission coefficient based on the cell technology while Tier 3 uses specific smelter defined coefficients in its formula to increase the precision of the method.

For Tier 3, two different methods are suggested to quantify CF_4 based on operating parameters while only one model is suggested to quantify C_2F_6. The slope model (equation 2-4) is the methodology used in most smelters across the world to quantify CF_4 emissions (Marks 2009). It uses a specifically defined emission coefficient (S_{CF4}; [(kg CF_4/tonne Al)/(AE-Mins/cell-day)]), the total number of polarized anode effects minutes per cell-day (AEM; [AE-Mins/cell-day]) and the respective metal production (MP; [tonnes Al] to estimate the amount of CF_4 generated (E_{CF4}; [kg]) from a selected number of cells over a defined period. However, some smelters prefer to use the overvoltage method shown by equation 2-5. Instead of using the anode effect duration, the emission coefficient is determined using the overvoltage of HVAE. This coefficient (OVC; [(kg CF_4 / tonne Al)/mV]) is multiplied by the anode effect overvoltage (AOE; [mV]) and the respective metal production (MP; [tonnes Al]). Additionally, a correction based on the current efficiency (CE; [%]) is also included in this method. On the other hand, the estimated amount of C_2F_6 (E_{C2F6}; [kg]) (equation 2-6) is based exclusively on the calculation of CF_4

(E_{CF4}; [kg]) estimated previously (by either method) and a specific ratio ($F_{C2F6/CF4}$). Because these methods are based on the smelter's average performances, the respective coefficients (S_{CF4} or OVC) and the ratio ($F_{C2F6/CF4}$) must be redefined periodically using continuous measurement campaigns on site lasting multiple days to avoid major deviation.

$$E_{CF_4} = S_{CF_4} \cdot AEM \cdot MP \qquad (2\text{-}4)$$

$$E_{CF_4} = \frac{OVC \cdot AEO \cdot MP}{CE/_{100}} \qquad (2\text{-}5)$$

$$E_{C_2F_6} = E_{CF_4} \cdot F_{C_2F_6/_{CF_4}} \qquad (2\text{-}6)$$

2.4 Methodology

2.4.1 Experimental setup

Most of the data collected for this study comes from a single measurement campaign performed at Aluminerie Alouette in spring 2016. The gas output of 132 AP40LE prebake cells with point-feeder was collected and redirected to the gas treatment center (GTC). A stainless-steel sampling probe was inserted in the top part of the exhaust duct of the GTC to continuously extract the gas. During the sampling period, the line current remained constant above 380 kA. Additional data used in this paper was collected in fall 2013. At the time, the cell technology was similar, but the current was above 370 kA. However, the same protocol was used to collect and prepare the data.

Once extracted, the gas was routed to a GASMET^{TM} DX-4000 FTIR (Fourier Transformed InfraRed spectrometer) using a Peltier cooled mercury-cadmium-telluride detector (sample cell path: 9.8m, volume: 0.5L, resolution: 7.8 cm^{-1}). The sampling probe was located in the center of the GTC stack and gas was continuously fed to the analyzer at a volumetric rate of 2.5 liters per minute. The gas stream was sent sequentially through a 15-

micron filter, desiccant, activated alumina, a 5-micron filter and finally a 2-micron filter to remove dust, traces of water and hydrogen fluoride for the protection of the measuring equipment. The gas was pre-heated to 120°C before entering the FTIR and concentration measurements were performed at a rate of 10 scans per second. Average values for twenty-second periods were recorded. The background spectrum was redefined using high purity nitrogen every 24 hours.

2.4.2 **Preparation of the data**

During both sampling periods, more than 570 HVAEs were recorded by the cell control system. To efficiently develop models representing PFC emissions based on the previously discussed parameters, it was necessary to account for the respective emissions of each individual HVAE. To perform this task, each HVAE was numbered and the respective PFC emission pattern was associated to the HVAE. In most cases, it was possible to associate the correct HVAE number to the spectrum of emissions by simply using the registered starting time of the AE and by considering the traveling time of the gas through the system. However, a longer traveling time for C_2F_6 than CF_4 was observed and considered. Further investigations are necessary to understand the cause for this two minutes delay. A plausible explanation[2] for this phenomenon is related to the size of the C_2F_6 particle in comparison to CF_4. Due to molecules of bigger size and a higher density, it is hypothesized that this gas passes more slowly through the fluidised alumina bed reactors used in the GTC as well as through the different filters along the sampling line.

---

[2] Additional discussion on this phenomenon is available in appendix D, bullet #1.

Nonetheless, once correctly identified, PFC emissions were calculated using the same methodology for both CF_4 and C_2F_6. By integrating the area under the curve using a trapezoid method, we obtain a respective ppm·s value associated with each individual HVAE. Then, it is possible to multiply this value by the measured airflow from the CTG cooling tower and the gas density to obtain the total mass of PFC emitted for each respective HVAE. Additionally, to consider exclusively the PFC emissions generated by the HVAE, the constant baseline coming from noise or LVAE was retracted from the total measurements. The baseline was constant at 10 ppb for CF_4, but it had to be manually verified for C_2F_6 as it showed daily fluctuations between 1 and 9 ppb.

Moreover, C_2F_6 is produced in a smaller concentration than CF_4 during an HVAE. For this reason, it was not always possible to quantify C_2F_6 emissions when the change in concentration was insignificant in comparison to the baseline noise. To correctly assess this situation, a signal to noise ratio presented as equation 2-7 was used to determine if the signal was relevant to be used. In the case where the signal was lower than the suggested threshold (Skoog et al. 1985), the amount of C_2F_6 was considered negligible and no C_2F_6 was attributed to this specific HVAE.

$$\frac{S}{N} = \frac{mobile\ average\ over\ 5\ minutes}{standard\ deviation\ from\ a\ background\ period\ without\ HVAE} \qquad (2\text{-}7)$$

FTIR gas concentration measurements can be influenced by the analysis setting of the software depending on the concentration level of the measured gas and the available references. However, for the range of concentration measured in this investigation, the noise level is the most important source of error for the experimental measurements,

especially for C_2F_6 emissions and HVAE with very low CF_4 emissions where the signal to noise ratio can be small. By considering the maximum noise level measured at all time with the respective CF_4 and C_2F_6 emissions measured for every HVAE, it was possible to estimate that the average error for CF_4 emissions is ±5.8% while the C_2F_6 emissions estimated average error is ±8.8%.

In some cases, multiple HVAEs overlapped requiring further preparation to correctly dissociate the respective amount of emissions. To correctly differentiate the amount of PFC gas generated by overlapping HVAE, a decomposition method was used. The emission profile during an HVAE was approximated by the beta distribution described by equation 2-8. Alpha and Beta represent variable parameters that change the overall evolution of the gas distribution while "x" is a dimensionless normalized time varying between the start (0) and the end (1) of the HVAE. By using the beta distribution[3], it is possible to adequately represent the sudden rate of increase of the emissions, as well as the asymmetric and typical pattern of the emission profile issued during an HVAE.

$$f(x,\alpha,\beta) = x^{\alpha-1}(1-x)^{\beta-1} \cdot \frac{\Gamma(\alpha+\beta)}{\Gamma(\alpha)\cdot\Gamma(\beta)} \qquad (2\text{-}8)$$

By using a distinct beta distribution for each overlapping HVAE during a specific period along with an optimization tool, it is possible to change the parameters of each beta function to recompose the original measured PFC dynamics as illustrated in Figure 2-2. Once the decomposition is complete, an engineering judgment is applied to verify the adequacy of the optimization process. This intervention is to assure that the results are

[3] Additional details on the beta distribution are available under Appendix D, bullet #2.

consistent with any sudden change in the measured spectrum, as well as with the starting time of each HVAE, their respective AED and their relative importance (based on AEO). If the results are considered satisfying, the respective area under the curve for each HVAE is then multiplied by the total amount of PFC calculated by integration for the similar period.

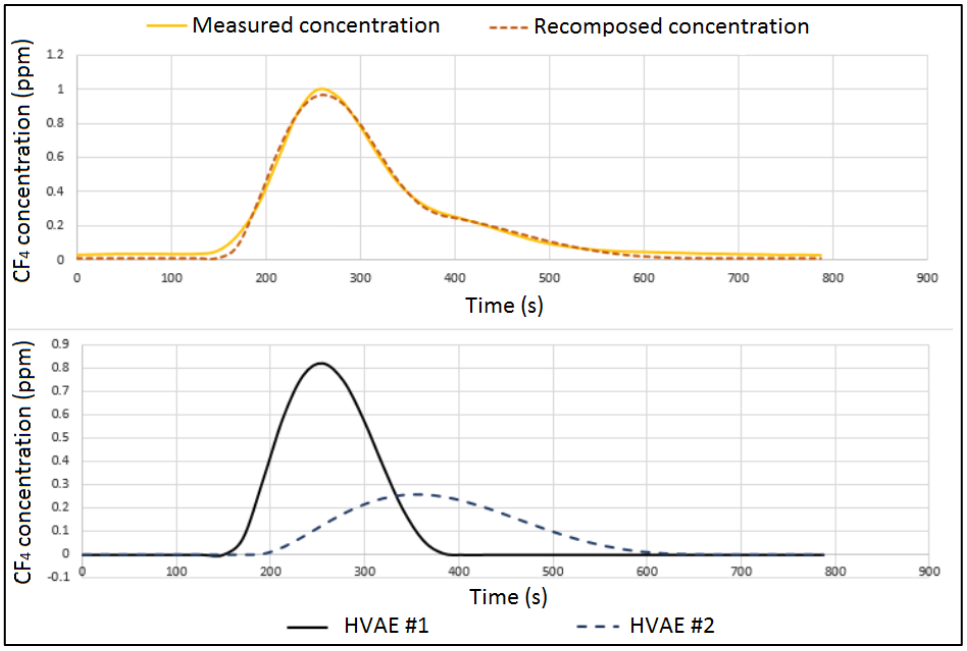

Figure 2-2: Decomposition of the CF_4 concentration for overlapping HVAE.

To evaluate the efficiency of this procedure, a validation was performed using twenty profiles collected from HVAEs without overlap. These data were divided into 10 groups and a random overlap was forced for each pair of HVAE. This overlap was determined using a random number generator and the resulting offset could vary between 0 seconds (starting simultaneously) and 90 seconds. Then, exactly the same decomposition procedure was applied for all groups to decompose the overlapping profiles and calculate the total amount of PFC emissions for each individual HVAE. A comparison between the measured values and the results from the decomposition methods were performed and

presented on Figure 2-3. The validation indicates that the calculated emissions with the decomposition procedure are representative of the measured value.

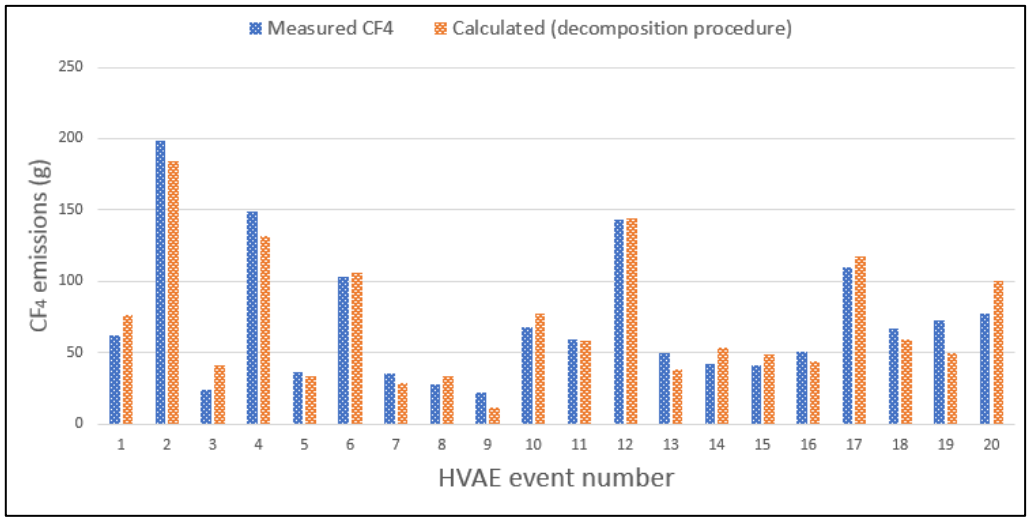

Figure 2-3: Validation of the decomposition procedure.

Finally, once respective PFC emissions were calculated for each individual HVAE, the data collected from the 2016 campaign (approximately 500 HVAEs) was randomly divided into two different groups. The data used to build the model (learning groups) is composed of 85% of the original data while the remaining 15% was kept aside for validation (Validation #1). A third group (Validation #2) is composed of the data collected in 2013 (75 HVAEs) to evaluate if the models are consistent through time.

2.5 Results and discussion (analysis on a single smelter's performances)

A total of ten different models[4] are compared to predict CF_4 or C_2F_6 emissions based on some cell parameters. These models were developed using the same set of data composed of 423 individual HVAEs. For all cases, the amount of measured PFC emissions

[4] Details on the pre-selection of the models are available in Appendix D, bullet #3.

does not consider the baseline which corresponds to noise or LVAE emissions. Additionally, the loss to the environment due to the small inefficiency of the gas collecting system was not taken into consideration.

One of the difficulties to develop predictive models results in the inconsistency of the Polarization Anode Effect Duration (PAED) or Anode Effect Overvoltage (AEO) distribution illustrated in Figure 2-4 and Figure 2-5 respectively. This difference, caused by changes in the cell control strategy, is even more important for the group from validation #2 which was collected many years apart. Therefore, changes in process parameters (feeding, current, AE killing strategy, etc.) can lead to change in the overall distribution. For this reason, an adequate model should be precise over the entire anticipated range of PAED or AEO. However, higher precision can only be achieved if enough learning data is acquired. This condition can be difficult to fulfill in the upper range of the distribution due to the rarity of such events who are highly detrimental.

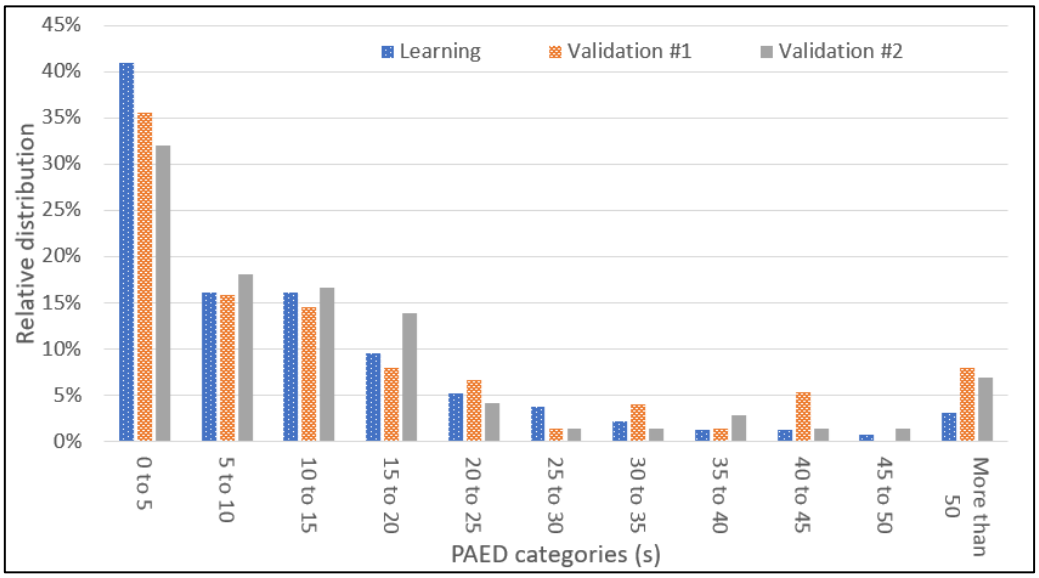

Figure 2-4: Relative distribution of the polarized anode effect duration for the data considered.

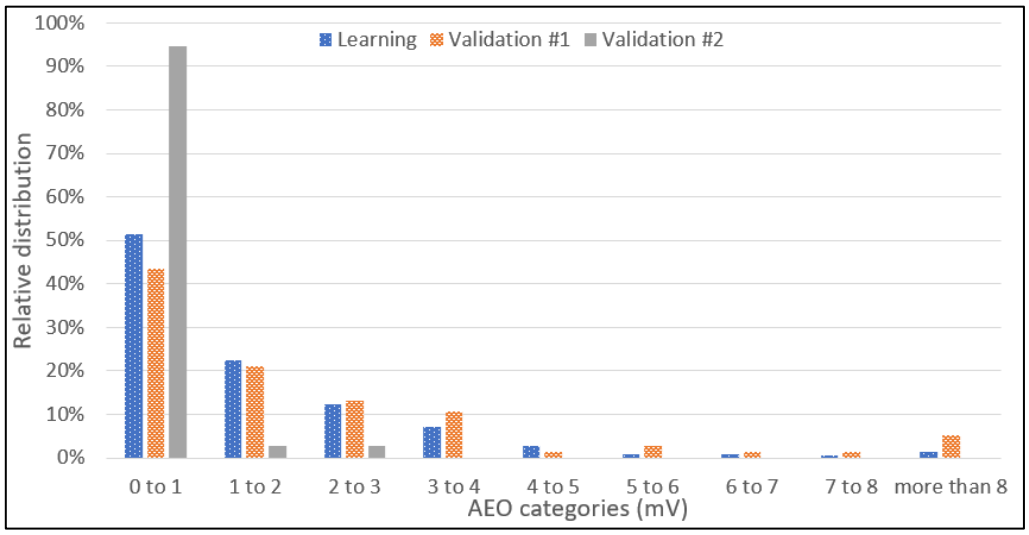

Figure 2-5: Relative distribution of the anode effect overvoltage for the data considered.

2.5.1 **Description of the different models to predict CF_4**

2.5.1.1 Linear model based on polarization anode effect duration

This model represents the standard estimation method used by most of the industry. It considers a linear relationship between the polarized anode effect duration (PAED) and the total amount of CF_4 produced during the HVAE. Using equation 2-1, it is possible to calculate the emissions coefficient S_{CF4} by summing the overall emissions of CF_4 and AE mins from the entire period, as we already know the aluminium production from the process. Henceforth we can obtain an emission coefficient corresponding to 0.139 (kg CF_4/tonne Al)/(AE-Mins/cell-day). The calculated value is really close to the Tier 2 approximation (0.143) from the IPCC protocol (Marks et al. 2006). The resulting estimation of CF_4 emissions is illustrated in Figure 2-6. We can see the inadequacy of such models to predict CF_4 emissions for very long PAED caused by the uneven distribution of emissions over the entire range of PAED.

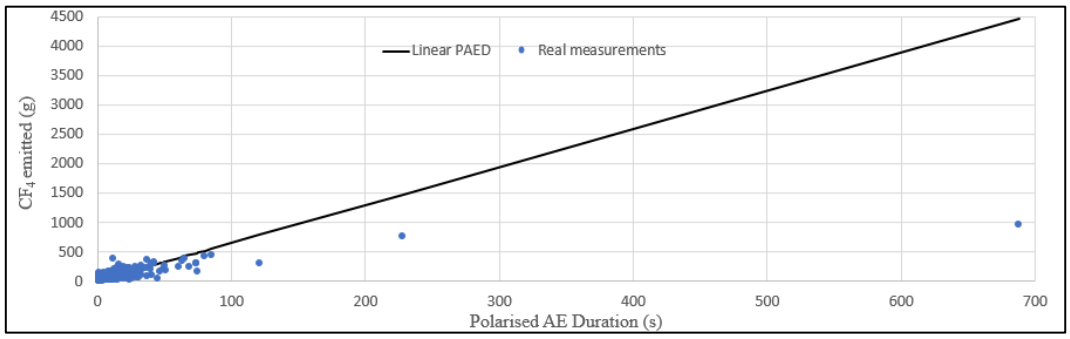

Figure 2-6: Linear PAED model in comparison to the real measured CF_4 concentration from the learning group.

2.5.1.2 Linear model based on anode effect overvoltage

This model represents the alternative way to estimate CF_4 emissions as suggested by the IPCC. Using equation 2-2, an overvoltage coefficient (OVC) was calculated using all the data from the learning group. This overvoltage coefficient is 1.62 (kg CF_4 / tonne Al)/mV). This value is higher than the Tier 2 coefficient suggested by the IPCC (1.16), however, it is representative of the most recent PFC measurements campaign performed at the smelter. The OVC model is illustrated in Figure 2-7. Similar to the PAED model, we can see that the emissions of CF_4 are overestimated once the energy developed by the anode effects reaches a certain level (>15 mV).

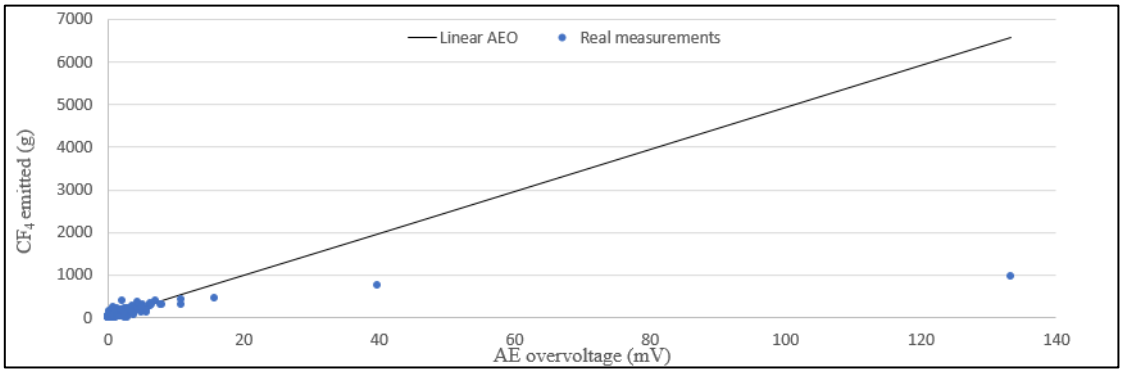

Figure 2-7: Linear AEO model in comparison to the real measured CF_4 concentration from the learning group.

2.5.1.3 Non-linear model based on polarization anode effect duration

Prior to developing the non-linear model, the data was sorted in increasing order based on the PAED. Afterwards it was divided into subsidiary groups[5] to determine the average CF_4 emissions of each respective group with similar PAEDs. Then, it was possible to determine the non-linear predictive model based on these subsidiary groups average. The model is divided into two parts for optimal correlation between data and the regression curves. When the PAED duration is shorter than 20 seconds, the model is considered as linear. After this point, a power model is considered to accurately estimate the amount of generated CF_4. It is possible to observe on Figure 2-8 that the non-linear model is more representative for the overall PAED range than the linear PAED model. Nonetheless, as the power part of this model was composed of only 18% of the available data, the accuracy of the model could benefit from additional data within this range.

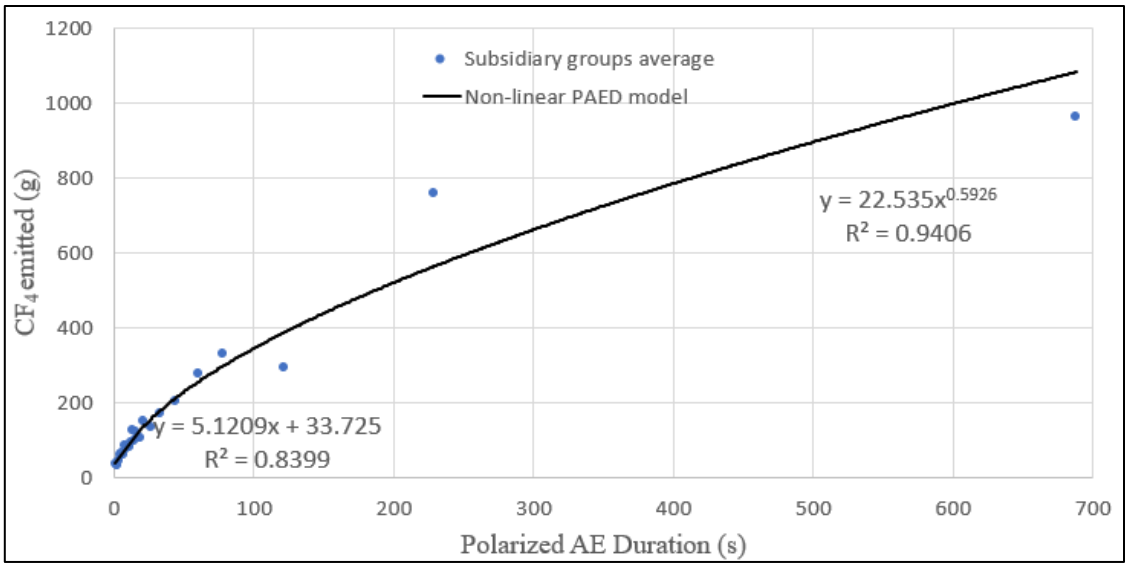

Figure 2-8: Non-linear PAED predictive model in comparison to subsidiary groups averaged CF_4 emissions.

[5] Additional details on the subsidiary groups are available in Appendix D, bullet #5.

A very interesting element resulting from this model is the presence of an intercept value. The positive intercept indicates that emissions of CF_4 are occurring before the cell control system detects an HVAE. Such an observation was anticipated for two reasons. First, as described in section 2.3.1, the identification conditions of an HVAE require the cell voltage to reach higher than a specific value for several seconds. Hence, emissions of CF_4 are occurring during this period whereas cell conditions are not yet identified as an HVAE. Secondly, it is probable that prior to triggering an HVAE, localized emissions could occur in specific areas for a long time before propagating to other anodes. If the bubble thickness of CF_4 is similar to CO_2, the corresponding volume of gas with a 5-mm layer (Thonstad 2009) would almost cover 20% of the available area under the anodes. Therefore, it is plausible that several grams of CF_4 might accumulate under some anodes prior to the actual detected HVAE and most of this gas will come out of the electrolytic cell during the HVAE treatment, which increases the total CF_4 emissions associated to a given HVAE.

2.5.1.4 Non-linear Model Based on Anode Effect Overvoltage

Like in the previous model, the original data was sorted in an increasing order based on the AEO and divided into subsidiary groups with similar AEOs. Then a non-linear AEO model was developed based on the average CF_4 emissions from each group. This model is composed of two different equations. When the AEO is under 3.5 mV, the prediction of CF_4 is considered as linear while above 3.5 mV, the behavior is considered by a power law as represented in Figure 2-9.

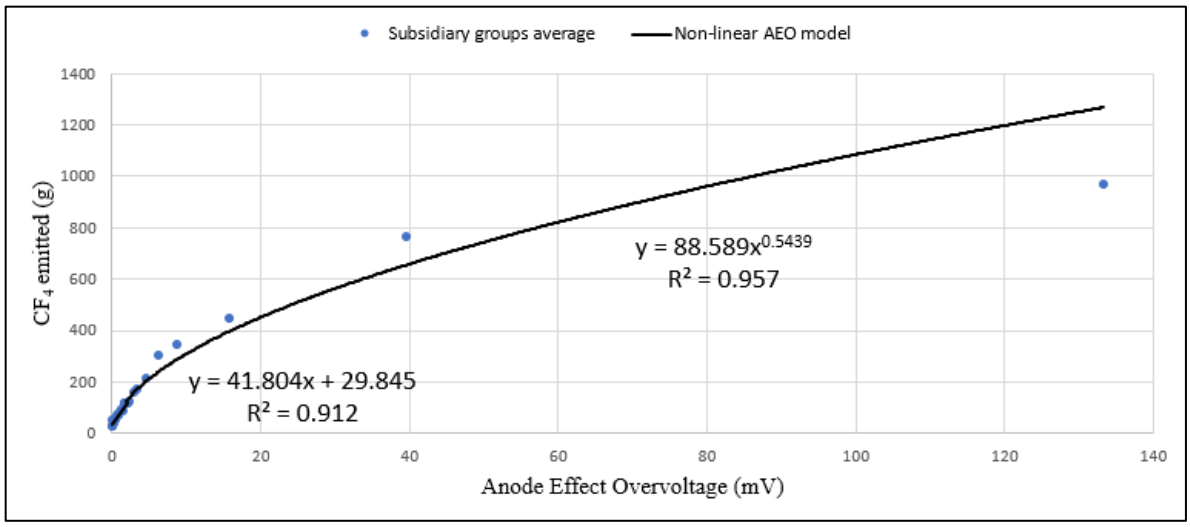

Figure 2-9: Non-linear AEO predictive model in comparison to subsidiary groups averaged CF_4 emissions.

In this case, an intercept is also present to indicate that some CF_4 is generated before the cell control system starts monitoring the HVAE. Additionally, the range of this intercept (≈30 grams) is very similar to the intercept from the previous model (≈34 grams). This indicates a good agreement between the models to represent CF_4 emissions even though the two models are based on different parameters.

2.5.1.5 Non-smelter specific and non-linear model based on polarized anode effect duration.

A co-author of this paper (Dr. Jerry Marks) is working as a consultant for the International Aluminium Institute (IAI). This organization collaborates with numerous aluminium producers to improve the understanding of PFC emissions across the industry. Using the data available in the IAI database, it was possible to extract a generic non-linear model[6] that would be representative of the PFC emissions of any aluminium smelter with similar designs and conditions. This model was developed using 34 different measurement

[6] More details on the development of this model is available in Appendix D, bullet #6.

campaigns and the CF_4 emissions of 2336 individual HVAEs were considered. The cell technology considered for this model works with prebaked anodes and point feeders. Additionally, the array of line current applied to the examined cells ranged between 82 and 560 kA.

To accurately represent the CF_4 emissions, the range of PAED had to be segmented into four different categories. In some peculiar cases, a duration of zero seconds was reported. For this model, the intercept is based on an average value for all individual HVAEs considered, normalized with respect to the cell current. Therefore, an estimated CF_4 emission corresponding to 0.576 grams per kA is considered for HVAE with a PAED equal to zero. For PAED higher than zero, three different power models were developed to take into consideration the changing rate of CF_4 generation as the PAED increases. A first model represents all PAED higher than 0 and shorter or equal to 5 seconds, the second model represents PAED higher than 5 and shorter or equal to 200 seconds while the last model represents all PAED longer than 200 seconds. The general tendency of the model is shown in Figure 2-10, compared to the learning data used in this study. The behavior of this non-smelter specific model is in good agreement with the collected data.

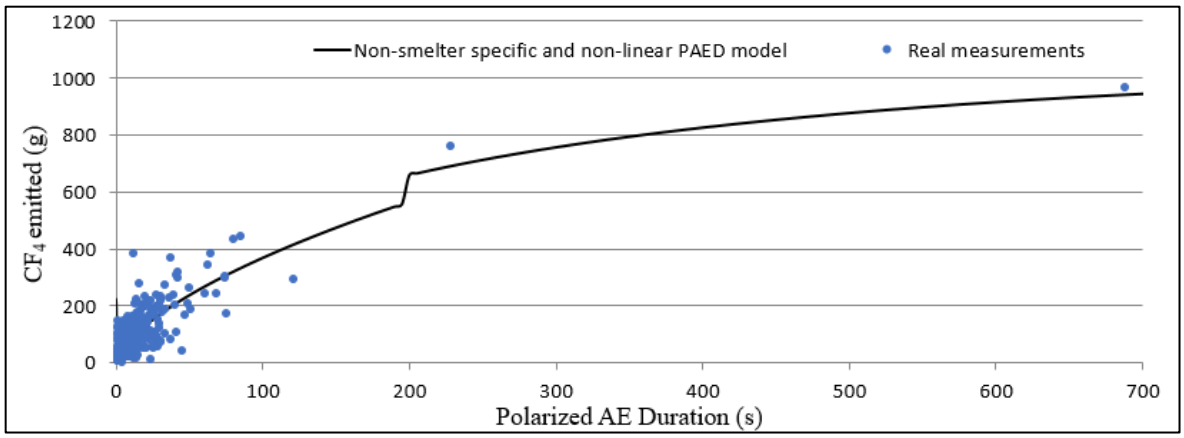

Figure 2-10: Non-smelter specific PAED non-linear model compared to real measurements from the learning group.

2.5.1.6 Model based on an artificial neural network using four input parameters

Multivariate analysis (MVA) tools are excellent to develop predictive models when numerous variables can have interrelated effects on the predicted value. For this reason, an artificial neural network[7] (ANN) was developed using STATISTICA 12®. This predictive model uses the four parameters (PAED, AEO, MPV, AED) described in section 2.3.1 as inputs to predict the CF_4 generated during an HVAE. A sensitivity analysis performed on the MVA model revealed that PAED is the most important variable to predict CF_4 emissions while maximum polarization voltage is second in importance. Their importance is approximately 2 and 1.5 times higher than that of AEO or AED, respectively.

On Figure 2-11, it is possible to observe the cross-effect of the two most important variables on the predicted emissions of CF_4. However, it is important to mention that the model was not developed using the entire range of variables as depicted by the surface in

[7] Additional details on the ANN selection is presented in Appendix D, under bullet # 4.

the figure. Therefore, in some cases (for example PAED = 600s and MPV = 6V) the surface shown is the result of an extrapolation and can be inaccurate.

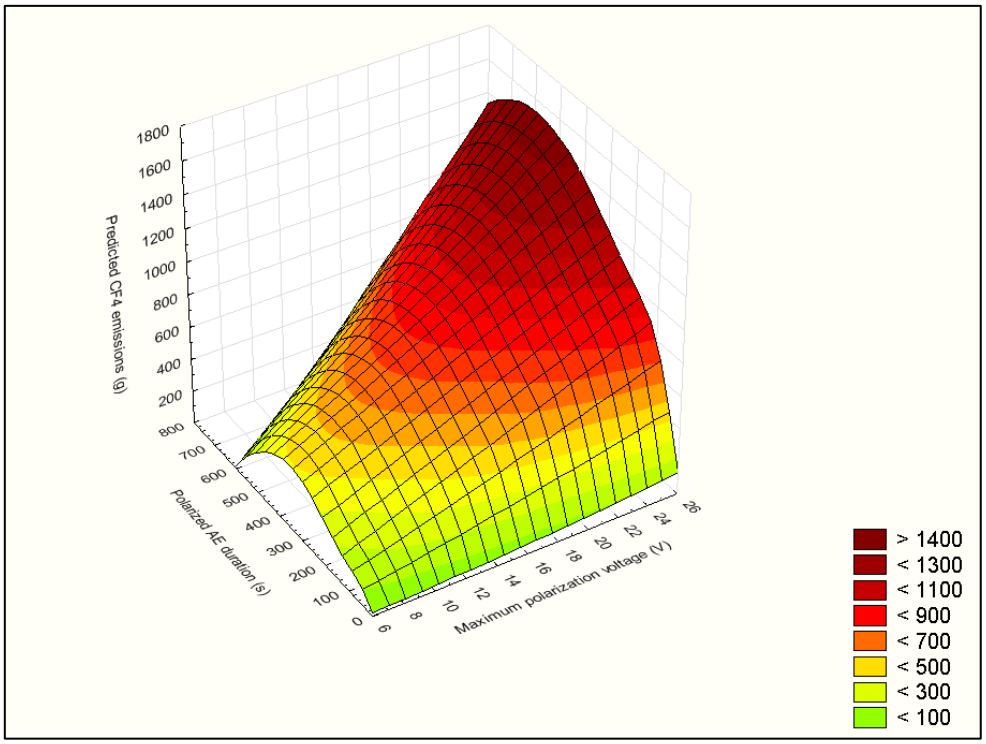

Figure 2-11: Cross-effect of PAED and MPV on the predicted emissions of CF_4 using an MVA model.

2.5.2 **Description of the different models to predict C_2F_6 emissions**

2.5.2.1 C_2F_6 to CF_4 Ratio

When using the method suggested by the IPCC, C_2F_6 emissions are estimated by multiplying the calculated CF_4 emissions by a constant ratio. However, this method is biased if the CF_4 calculations are not completely accurate. To prevent this potential error in this analysis, the C_2F_6 to CF_4 ratio was applied directly to the real CF_4 emissions measurements. Henceforth, this represents the best-case scenario with comparison to a case where an error in the estimation of the total CF_4 would be present.

To determine the ratio to use, the total amount of C_2F_6 measured for a complete set of HVAE is divided by the total amount of CF_4 generated. In this case, the calculated ratio was 0.045±0.052 kg C_2F_6 per kg CF_4. This value is lower than the suggested one by the IPCC for Tier 2 (0.121 kg C_2F_6 per kg CF_4) but is representative of the smelter's historical data. The model is represented on Figure 2-12 along with the real C_2F_6 measurements.

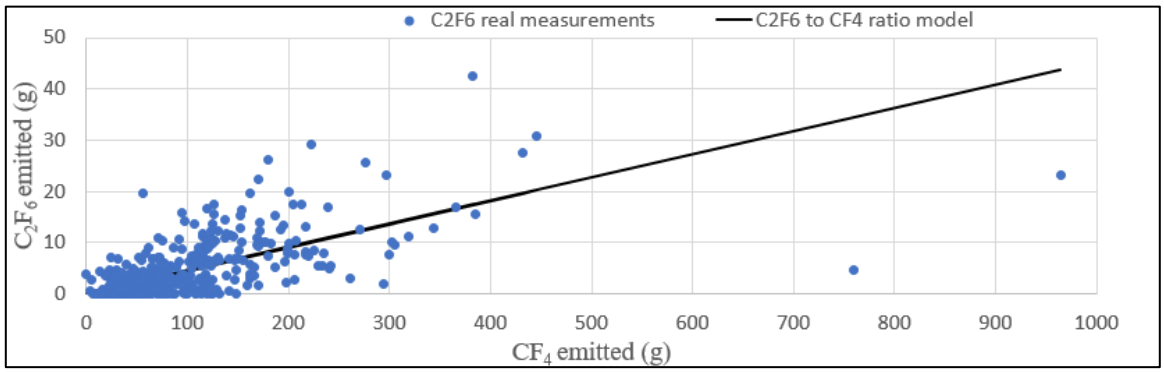

Figure 2-12: C_2F_6 to CF_4 ratio model in comparison to the real measurements.

2.5.2.2 Non-linear C_2F_6 model based on polarized anode effect duration

This model aims at calculating the specific C_2F_6 emissions based on the PAED without taking CF_4 emissions into consideration. With the similar subsidiary groups from the PAED non-linear model developed for CF_4, it was possible to develop a similar two-step model to estimate the C_2F_6 emissions as illustrated in Figure 2-13. For every PAED shorter than 20 seconds, the C_2F_6 emissions are estimated by using a linear relationship. For longer PAED, a logarithmic behavior was observed. It is important to remark that very few HVAE were recorded in the upper range of this curve. Therefore, the curve should represent the general behavior of C_2F_6 emissions, but additional data will be necessary to improve the accuracy of this predictive model.

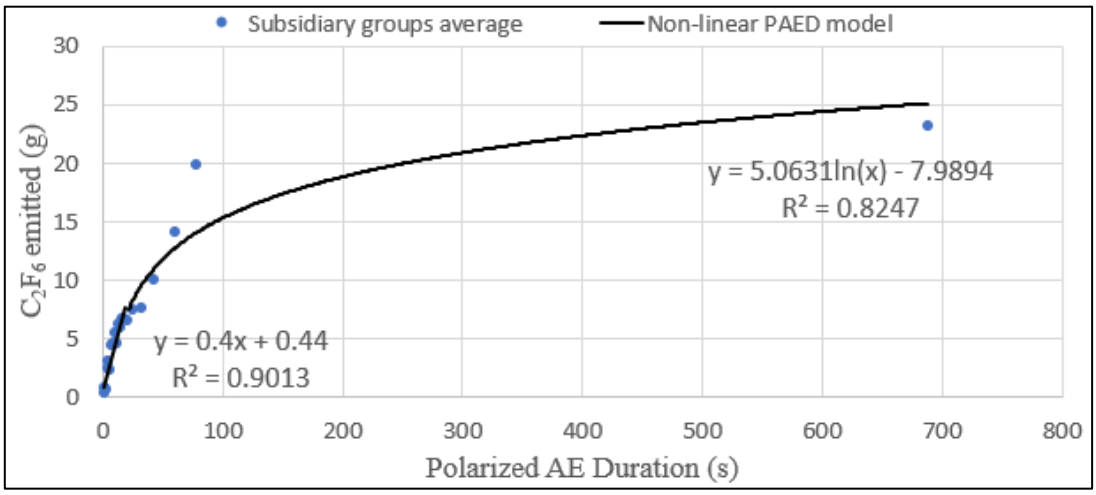

Figure 2-13: Non-linear PAED model to represent C_2F_6 emissions along with average emissions from subsidiary groups.

An intercept of 0.44 grams of C_2F_6 was observed indicating that a small amount of C_2F_6 is produced before the beginning of the HVAE monitored by the cell control system.

2.5.2.3 Linear model based on anode effect duration

A linear model was developed to predict C_2F_6 emissions exclusively based on the overall HVAE duration. This model is therefore greatly influenced by the triggering conditions for the recording of the start and end of a HVAE. Knowing that the AED is representative of the HVAE killing strategy, the positive correlation observed with this model could indicate the effect of the killing strategy on C_2F_6 emissions.

The linear model displayed in Figure 2-14 was developed by sorting the learning data increasingly with respect to AED and forming subsidiary groups. In this case, an intercept of 1.0 gram was observed indicating once again that emissions are present before the cell control system declares HVAE conditions.

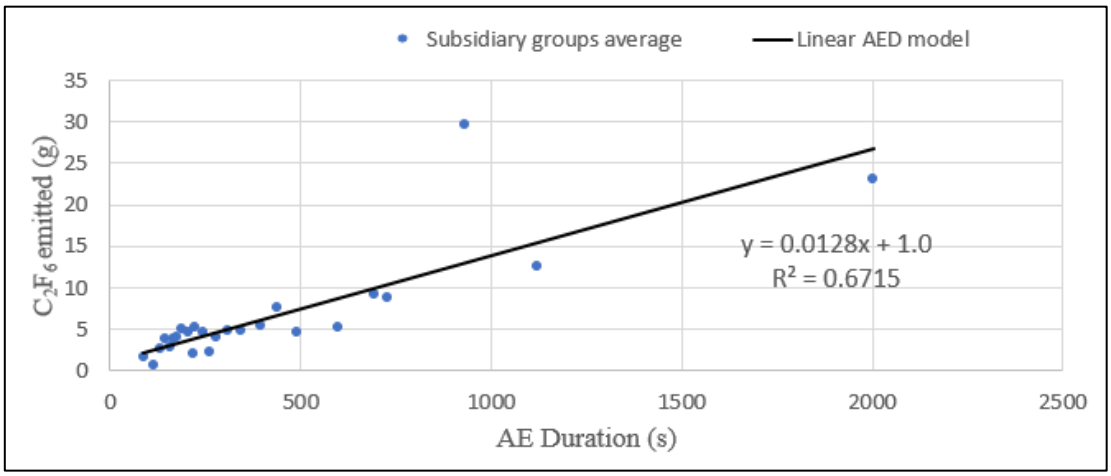

Figure 2-14: Linear AED model to estimate C_2F_6 emissions along with the average results from subsidiary groups.

2.5.2.4 C_2F_6 model based on an artificial neural network using four input parameters.

This predictive model uses the four parameters (PAED, AEO, MPV, AED) described in section 2.3.1 to predict the C_2F_6 emissions generated during an HVAE. A sensitivity analysis performed on the MVA model revealed that no variable significantly stands out as most important. However, MPV is 30% more influential and PAED is second in importance.

The cross-effect of these two dominant variables illustrated in Figure 2-15 is difficult to interpret correctly due to the hidden influence of the other two variables. However, we can see that even if the MPV remains constant, the total amount of emissions is not necessarily increasing along with the PAED. However, interpretation of this figure must be performed carefully due to the extrapolation carried out in the areas where no learning data was available.

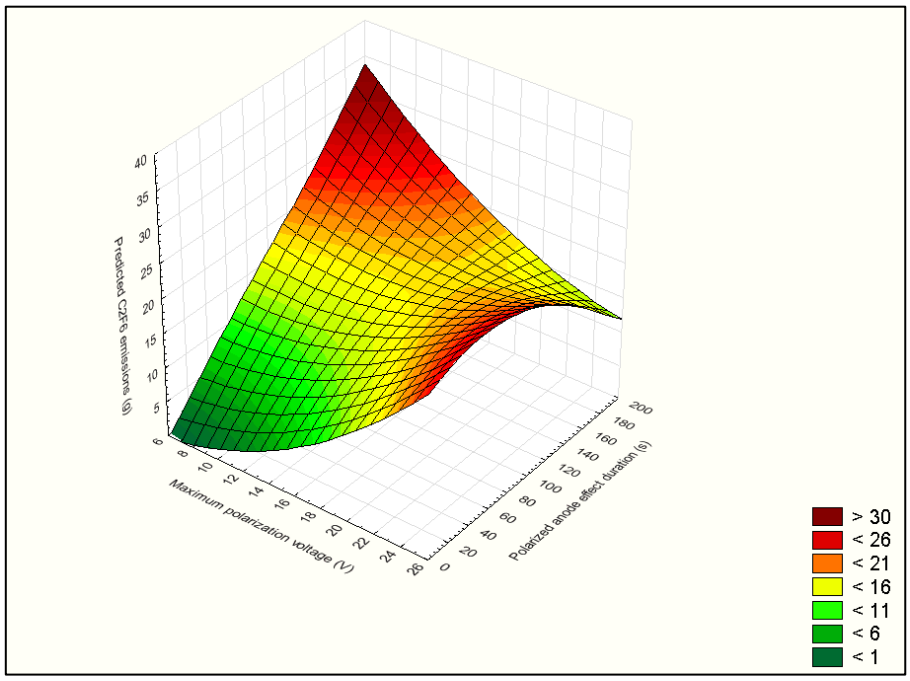

Figure 2-15: Cross-effect of PAED and MPV on the predicted emissions of C_2F_6 using an MVA model.

2.5.3 **Validation**

Validation of the models was performed by evaluating two different elements. The error percentage of each model was calculated based on the overall performance of the model to predict an entire group of HVAE. Therefore, it includes the sum of all respective emissions for the entire group and compares this value to the real measurement performed with the FTIR.

The second element investigated is the ability of each model to be accurate for individual HVAE predictions. Henceforth, the sum of the squared residues is also considered as part of the validation process. The data for each group (learning, validation #1 and validation #2) was normalized with respect to the maximum value calculated within each group.

The overall error and relative squared residues of each predictive model for the CF_4 emissions are illustrated in Figure 2-16. In the learning group, it is possible to observe a low overall error for all models. However, the new models are clearly more accurate to predict individual HVAE emissions when looking at the normalized squared residues.

Investigation through the validation group #1 indicates that the existing models (linear PAED and AOE) are both significantly overestimating the amount of CF_4 emitted with an error of 35.4 and 28.9% respectively. All other models are underestimating the amount of CF_4 emitted but closer to the real measurements with errors ranging from -20% up to -12.5%. Results from the squared residuals are clearly indicating that the individual accuracy of predictions is improved with the newer models.

Investigation with the second validation group indicates that the absolute error percentage of each model increased with this population which has a significantly different distribution regarding PAED and AEO (Figure 2-4 and Figure 2-5). However, this increase was less significant for the multivariate model which still has an error percentage below 15%. This model appears to be consistent also for individual predictions of HVAE emissions.

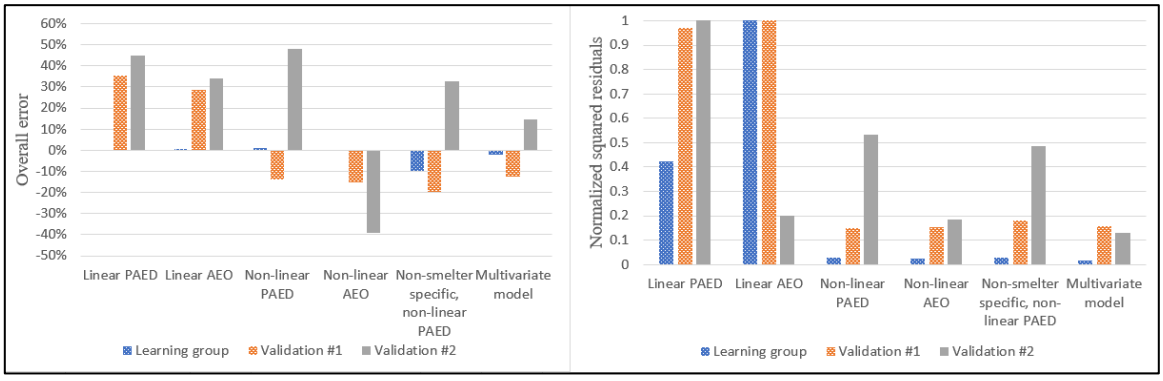

Figure 2-16: Overall errors and normalized squared residuals for predictive models regarding CF_4 emissions.

Validation of the C_2F_6 models was performed similarly to CF_4 and is displayed in Figure 2-17. Within the learning group, no significant change in the overall error was observed across the different models. However, only the multivariate model showed improvements regarding the accuracy of individual predictions. The lack of accuracy of predictive models is caused by the disparity of the C_2F_6 data and the higher level of uncertainty of individual values caused by a smaller signal to noise ratio than for CF_4.

For the validation group #1, a significant improvement can be observed with every proposed predictive model whereas the overall absolute average error remained under 8%. Individual predictions are also good with squared residuals values only 26 to 43% as high as the C_2F_6 to CF_4 ratio.

Improvements can also be observed with the validation group #2 where the absolute overall error of the new models remained almost equal or inferior to the usual method of quantification. On the other hand, the accuracy of individual predictions is less accurate than that of the C_2F_6 to CF_4 ratio.

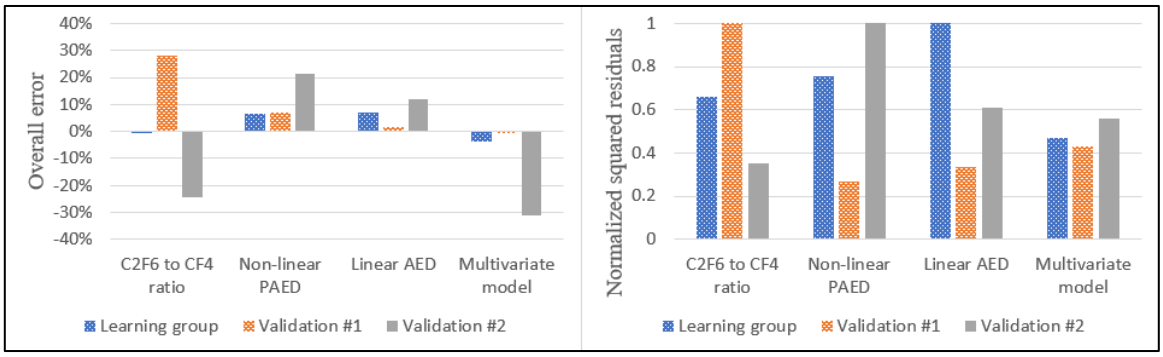

Figure 2-17: Overall errors and normalized squared residues for predictive models regarding C_2F_6 emissions

Overall the validation indicates that non-linear models are more accurate to predict CF_4 emissions resulting from HVAE. However, when using a single predictive variable, no

indicator appears to be efficient if there is a significant change in the range of variation of that respective variable, which indicates that cross-effects between some parameters are present. This affirmation is reinforced by the multivariate model which proved to be an efficient approach to predict overall CF_4 emissions through accurate individual HVAE predictions. Additionally, the behavior appears consistent within the industry as no significant improvement could be observed between the non-linear PAED model and the non-smelter specific model, using the same parameter. Finally, a comparison of the existing methods suggested by the IPCC to account for CF_4 emissions indicates that polarized anode effect duration is more accurate to represent individual anode effect emissions than anode effect overvoltage as confirmed by the relative squared residuals analysis performed. This observation is explained by the less pronounced non-linear correlation between PAED and CF_4 emissions.

Validation of the C_2F_6 models demonstrated that it is possible to directly predict the C_2F_6 emissions from an HVAE independently from the CF_4 emissions. Even though all proposed models are at least equivalent to thOSE using the C_2F_6 to CF_4 ratio, the most favorable model seems to be the linear AED model that appears to be consistent even with a change in the AED range of variation. Nonetheless, none of the proposed models showed the prediction of individual HVAE C_2F_6 emissions significantly better than the already existing methods. Finally, if we consider that the C_2F_6 to CF_4 ratio calculation is based on "best case scenario", the results could easily favor the newly proposed models if we take into consideration the error associated with the CF_4 prediction required for this method.

2.5.4 **The possible impact of the proposed models for the aluminium industry.**

The results described in the previous sections clearly indicate that the existing methods are far from their optimum to correctly estimate PFC emissions resulting from individual HVAEs. There is a high level of inaccuracy when these methods are used to estimate emissions of CF_4 and C_2F_6 from individual HVAE. Even the overall error increases rapidly if there is a change in the PAED or AEO monthly distribution, hence the necessity to recalculate the emissions coefficient at least once every 3 years and especially when operational parameters are modified. The first goal of the proposed models is to be able to adjust to a change in the variation range of the predictive variables with little impact on the overall results. We can see that this goal was achieved by the multivariate model and partially achieved with the models using one variable. For this reason, we can anticipate that an accurate model, using one or multiple variables, could precisely predict emissions without being dependent of the distribution of the predictive variables. Henceforth, the task of recalculating the emission coefficients periodically would no longer be necessary. For consistency across the industry, a non-smelter specific model could be developed as part of a collaboration between several aluminium smelters, e.g. through the IAI. The results show that the accuracy of such model would be equivalent to a smelter-specific model, but the collaboration could definitely improve the accuracy of the models in the upper range of emissions.

Using one of these models to estimate PFC emissions would facilitate the task of the process engineer and technicians when performing the GHG inventory. As a matter of fact, the authors believe that it would not be a tremendous task to implement one variable

predictive model directly into the cell control system software, knowing that most of the discussed variables are already measured by the cell control system for the most recent technologies. Hence, the proposed model could directly calculate the emissions associated with each high voltage anode effect. Such a task would not be as easy to implement for the multivariate model, but equivalent solutions are available by communicating between the cell control system and an external software. Therefore, the reporting of total PFC emissions would be automated and available daily instead of having to manually calculate the emissions every month.

Individual emissions monitoring could also change and improve the overall electrolysis process by assigning different levels of priority to the cells producing a considerable amount of PFC instead of focusing on cells where the frequency of HVAE is higher without necessarily producing more PFC. The individual amount of PFC produced would also be a significant variable to consider for improving the process by correlating the estimated PFC emissions with process parameters such as bath and metal levels, net cell heat input or alumina feeding strategies.

The development of the models revealed that triggering conditions for the detection of the beginning of a HVAE could have an impact on the estimated amount of PFC, more importantly when the HVAE has a short duration. The observed 32 grams for CF_4 and 0.72 grams for C_2F_6 for zero PAED reveals that emissions are occurring in the cell before it is declared as an HVAE. This pre-emission plausibly corresponds to the trigger period not accounted for with the usual techniques. Further investigation regarding these zero-offsets is still necessary to correctly assess their origin. Improvements to the existing models

(PAED linear and AEO linear) could be achieved by considering the trigger period when calculating the PAED and AEO of an HVAE. However, implementation of the newly proposed models could improve the situation.

Finally, as described in section 2.2, HVAEs are not the only sources of PFC emissions and in some smelters, LVAE emissions are now more important than HVAE emissions (Dando et al. 2015) when estimating the GHG inventory. Therefore, the industry might have to turn to continuous monitoring of the PFC in the future if no accurate method to estimate LVAE is developed. However, there are no indications that continuous monitoring will be required for the near future, hence the newly proposed method is still relevant to increase the precision of actual HVAE PFC emission quantification, especially in those smelters where this type of PFC emissions is still preponderant.

2.6 Conclusions

In this paper, several new models were proposed to estimate the perfluorocarbon emissions resulting from high-voltage anode effects during primary aluminium production based on four different parameters recorded during a high-voltage anode effect. These new models were developed to consider the non-linear behavior of PFC emissions with a comparison to the existing linear models. The inadequacy of the existing models to predict individual HVAE emissions of PFC was demonstrated and the new models are performing this task efficiently.

Development of the new models indicates that the non-linear behavior is strongly apparent in the upper range of emissions. Moreover, approximately 32 grams of CF_4 and

0.72 grams of C_2F_6 are generated within the trigger period of an HVAE indicating the importance of standardizing the trigger conditions to ensure similitude between smelters.

To predict CF_4 emissions, the results indicate that non-smelter specific models are equally accurate as smelter-specific models if sufficient data is provided to cover the entire range of interpolations anticipated. However, models using a single variable can be inaccurate if the distribution of this variable changes significantly from cell to cell. This problem can be resolved by using a multivariate model using all four available parameters: polarized anode effect duration, maximum polarization voltage, anode effect overvoltage and anode effect duration.

Models proposed in the present paper to predict C_2F_6 emissions offer the same accuracy as the existing methodology, but they are no longer dependent on the calculated CF_4 emissions, henceforth plausibly increasing the precision of the estimate. The linear model using anode effect duration showed the best overall results to predict overall C_2F_6 emissions even with a change in the distribution of HVAE PAED. However, with some improvements, a multivariate model could also be used efficiently to predict individual C_2F_6 emissions.

The proposed non-linear models can be accurately used for quantification of PFC emissions from individual HVAEs. Their use could facilitate GHG inventory calculations and they could also help the improvement of the reduction technology in order to reduce emissions.

2.7 Additional content not presented in the original paper

2.7.1 In-situ study[8] on the traveling time of CF_4 and C_2F_6 in the gas collection system

In section 2.4.2, it was mentioned that a delay was observed between the detection of CF_4 and the detection of the C_2F_6. It was hypothesized that the different properties of these two components (molecule sizes, density, etc.) could affect the transport of the molecules from the cells up to the gas analyser. For this reason, a test was designed using a tracer gas to try and pinpoint the root cause of this delay, i.e. to identify if this delay is caused while the gas is traveling from the cell to the analyzer or if it is indeed related to the initial generation of the gas.

2.7.1.1 Methodology

For this analysis, a tracer gas was provided by Praxair Inc. with a certified gas concentration of 50±2% CF_4 and 50±2% C_2F_6. Three different injection points were selected to introduce the gas and to measure the travel time of these two chemical components until the maximum detection peak from the FTIR. The three-selected injection points are listed below and illustrated on Figure 2-18:

1. Entry point of the filters protecting the measuring equipment
2. Entry point of the gas treatment center
3. Inside the duct of the farthest electrolysis cell away from the gas treatment center

[8] Additional discussion on this phenomenon is available in appendix D, bullet #1.

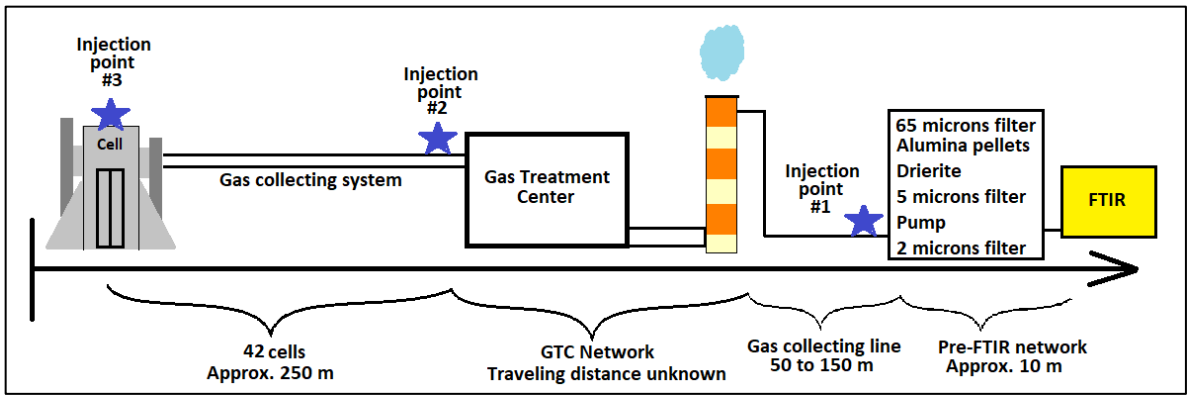

Figure 2-18: Illustration of the gas travel course with injection points (blue stars).

2.7.1.2 Results

The gas injected at the first injection point caused problems due to the high concentration of CF_4 and C_2F_6 used in this test in comparison to the spectrum reference limits of the analyzer. Additionally, a very long purge time was necessary subsequently to recover from the gas injection and clear the gas analysis chamber so only two injections were performed at this point. The results indicated that the observed delay between both gas was under one second, which is insignificant in comparison to the previously observed delay which was approximately two minutes.

Injections at the points #2 and #3 were performed 5 and 6 times respectively with a ±2s on the time of each injection. Hence it was possible to calculate the time difference between the injection and the maximum peak observed as illustrated in Figure 2-19. Additionally, it is possible to observe that in addition to the longer traveling time of the C_2F_6, the presence of C_2F_6 is observed for an extended period of time. This phenomenon was observed but not investigated in more details, nonetheless it should be related to the same mechanism that leads to an extended traveling time.

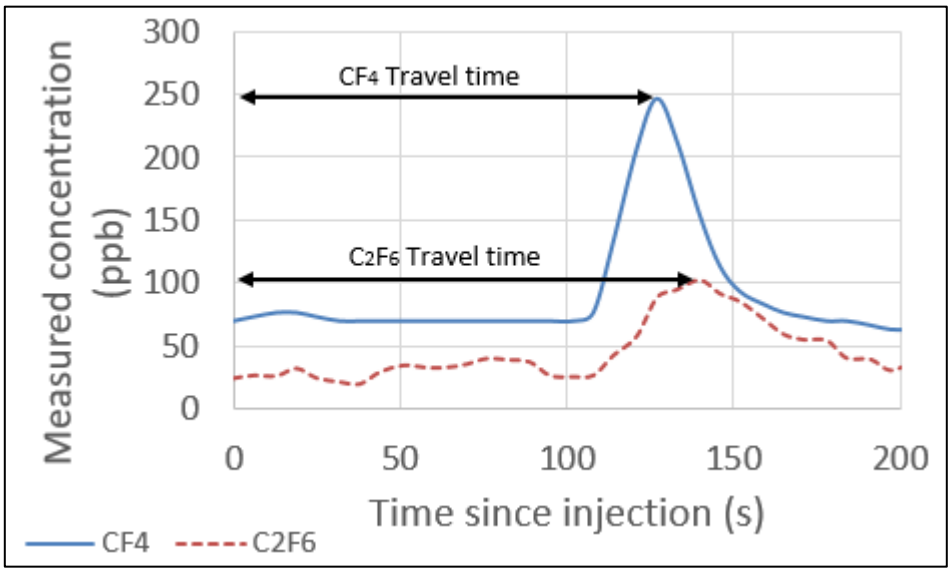

Figure 2-19: Example of calculation of the travel time for each gas.

The results of the different injections, in terms of gas types and positions are illustrated as a whisker box on Figure 2-20. A significant difference can be observed between CF_4 and C_2F_6 with regard to the total traveling time of these gases, for both injection point. The average difference of traveling time is equivalent to 31 ±14 seconds. Additionally, it was possible to observe a more important difference for injection point #2 than for injection point #3, thus indicating that the significant delay observed is related to the GTC network and the collection line of the gas. The difference observed within these experimentation (31 seconds) is still lower than what was previously stated in section 2.4.2 (2 minutes). There is no significant difference in terms of collecting lines, but the gas was collected from two different gas treatment centers. Therefore, it is plausible that different circumstances in terms of filter or bag conditions, recirculation factor, etc., affect the traveling time of the gas travelling through the GTC. Nonetheless, it is improbable that it

would explain this 90-second difference and additional investigation is recommended to correctly identify the cause of this phenomenon.

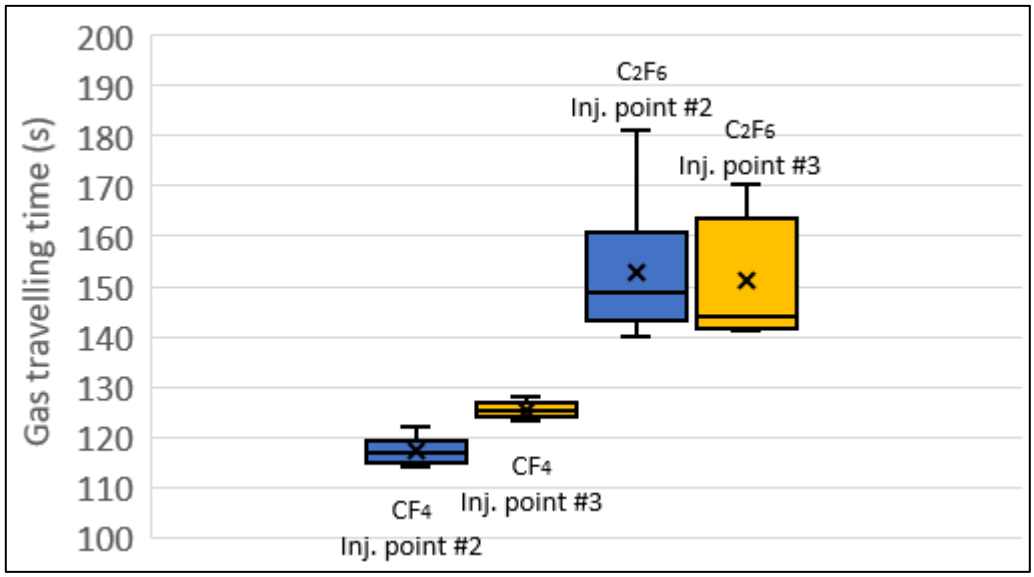

Figure 2-20: Different traveling time of the CF_4 and C_2F_6 for injection point #2 and #3.

Finally, this investigation confirms that the traveling time of CF_4 and C_2F_6 is impacted by the gas treatment center. However, the two minutes delay previously observed is unlikely explained by this single factor. Further investigations should be performed with individual cell monitoring to determine if generations of CF_4 and C_2F_6 are both generated exactly at the same time.

2.8 References

Berge, I., R. Huglen, M. Bugge, J. Lindstrom, and T. I. Roe. 1994. "Measurement and characterization of fluorocarbon emissions from alumina reduction cells." In Light Met. ed. U. Mannweiler (Warrendale: TMS), 389-92.

Bouzat, G., JC. Carraz, and M. Meyer. 1996. "Measurements of CF4 and C2F6 from prebaked pots." In *Light Met*. ed. W. Hale (Warrendale: TMS), 413-17.

Dando, N. R., N. Menegazzo, L. Espinoza-Nava, N. Westendorf, and E. Batista. 2015. "Non anode effects PFC : Measurement consideration and potential impact." In *Light Met.* ed. M. Hyland (Hoboken: Wiley), 551-55.

Gosselin, A., and P. Desclaux. 2002. "Analysis of results from a PFC measurement campaign". *CIM Bulletin,* 95: 92-95.

Kim, J., P. J. Fraser, S. Li, J. Mühle, A. L. Ganesan, P. B. Krummel, L. P. Steele, S. Park, S. K. Kim, M. K. Park, T. Arnold, C. M. Harth, P. K. Salameh, R. G. Prinn, R. F. Weiss, and K. R. Kim. 2014. "Quantifying aluminium and semiconductor industry perfluorocarbon emissions from atmospheric measurements". *Geophysical Research Letters*, 41: 4787-94.

Léber, B. P., A. T. Tabereaux, J. Marks, B. Lamb, T. Howard, R. Kantamaneni, M. Gibbs, V. Bakshi, and E. J. Dolin. 2013. "Perfluorocarbon (PFC) Generation at Primary Aluminium Smelters". in, *Essent. Read. in Light Met.*

Marks, J. 2009. "Global anode effect performance : 2010 PFC emissions reduction objective met". *Light Met*., ed. G. Bearne (Warrendale: TMS), p. 251-54.

Marks, J., R. Kantamaneni, D. Pape, and S. Rand. 2003. "Protocol for measurement of tetrafluoromethane and hexafluoroethane from primary aluminium production". In *Light Met*. ed. P. N. Crepeau (Warrendale: TMS), 221-25.

Marks, J., W. Kojo, M. F. Born, L. Green, H. Kvande, K. J. Martchek, and S. Rand. 2006. "4.4 Primary aluminium production". In *Chapter 4 : Metal industry emissions*, edited by the Intergovernemental Panel on Climate Change.

Marks, J., A. T. Tabereaux, D. Pape, V. Bakshi, and E. J. Dolin. 2001. "Factors affecting PFC emissions from commercial aluminium reduction cells". In *Light Met*. ed. J. L. Anjier (Warrendale: TMS), 295-302.

Marks, J. 1998. "PFC emissions measurements from alcoa aluminium smelters". In *Light Met*., ed. B.J. Welch (Warrendale: TMS), 287-91.

Marks, J., and C. Bayliss. 2012. "GHG measurements and inventory for aluminium production". In *Light Met*., ed. C. Suarez (Hoboken: Wiley), p. 805-08.

Martin, C., and E. Couzinie. 2003. "PFC Emissions measurement from aluminium pechiney smelters". In *Light Met.* ed. P.N. Crepeau (Warrendale: TMS), 233-38.

G.Myhre, D.Shindell, F.-M.Bréon, W.Collins, J.Fuglestvedt, J. Huang, D. Koch, J.-F. Lamarque, D. Lee, B. Mendoza, T. Nakajima, A. Robock, G. Stephens, T. Takemura, and H. Zhang, *Anthropogenic and natural radiative forcing. Climate Change 2013: The Physical Science Basis. Contribution of Working Group I to the Fifth Assessment Report of the Intergovernmental Panel on Climate Change*, ed. T.F.Stocker, D. Qin, G.-K. Plattner, M. Tignor, S.K. Allen, J. Boschung, A.Nauels, Y.Xia, V.Bex, and P.M.Midgley (Cambridge,UK and New York, NY, USA: Cambridge University Press, 2013)

Roberts, R. A., and P. J. Ramsey. 1994. "Evaluation of fluorocarbon emissions from the aluminium smelting process." In Light Met. ed. U. Mannweiler (Warrendale: TMS), 381-88.

Skoog, D. A., D. M. West, J. Holler, and T. A. Nieman. 1985. *Principles of Instrumental Analysis*.

Tabereaux, A. T. 1994. "Anode effects, PFCs, global warming, and the aluminium industry". *JOM*, 46: 30-34.

Tabereaux A.T. 2004. (Paper presented at the Eight Australasian Aluminium Smelting Technology Conference and Workshops, Yeppoon, Australia)

Tarcy, G. P., and A.T. Tabereaux. 2011. "The initiation, propagation and termination of anode effects in hall-heroult cells." In *Light Met*., ed. S. Lindsay (Hoboken:Wiley), 329-32.

Thonstad J. 2009 “Cell voltage anode effect”, *In 28th International course on process metallurgy of Aluminium: Volume 1*. Edited by the Norwegian University of Science and Technology, 285-318.

Wong, D. S., and J. Marks. 2013. "Continuous PFC emissions measured on individual 400 kA cells." In *Light Met*. ed. B. Sadler (Hoboken: Wiley), 865-70.

Wong, D. S., A. T. Tabereaux, and P. Lavoie. 2014. "Anode effect phenomena during conventional AEs, low voltage propagating AEs & non-propagating AEs." In *Light Met.* ed. J. Grandfield (Hoboken: Wiley), 529-35.

Wong, D. S., P. Fraser, P. Lavoie, and Jooil Kim. 2015. "PFC emissions from detected versus nondetected anode effects in the aluminium industry", *JOM*, 67: 342-53.

CHAPTER 3

NEW APPROACH FOR QUANTIFICATION OF PERFLUOROCARBONS RESULTING FROM HIGH VOLTAGE ANODE EFFECTS (BASED ON THE DATA FROM MULTIPLE SMELTERS)

3.1 Summary

The work presented in this chapter was published at the *2018 TMS Annual meeting & exhibition conference proceedings on Light Metals*. It was presented as part of the symposium on Perfluorocarbon generation and emissions from industrial processes and the DOI number is: 10.1007/978-3-319-72284-9_192.

The paper was written in collaboration with Simon Gaboury, Sandor Poncsak, Laszlo I. Kiss and Charles-Luc Lagacé but most of the text was written by the author of this thesis with comments and suggestions from the co-authors. However, the author acknowledges an important part of the writing to Simon Gaboury for section 0 and 3.5.5 of the paper.

3.2 Introduction

Most of the aluminium smelters worldwide estimate their annual greenhouse gas (GHG) emissions as a guide to improve their performance. There are many important direct sources of GHG emissions in the aluminium production, but most of the direct emissions are related to CO_2 production caused by the anode consumption during electrolysis [1]. However, under specific circumstances, additional reactions also occur in the electrolysis cells, leading to the generation of perfluorocarbons (PFC). PFC are composed of tetrafluoromethane (CF_4) and hexafluoroethane (C_2F_6) which have a global warming potential of 6630 and 11100 times more elevated than that of CO_2 respectively [2]. Therefore, PFC emissions can have a significant impact on the GHG inventory from a specific smelter and quantifying correctly the total amount of PFC emissions is of upmost importance.

PFCs are quantified based on the cell's average anode effect performance for a large number of electrolysis cells. However, the standard methodology used for PFC inventory is only efficient for smelters with a significant number of high voltage anode effect (HVAE) and the model's predictive capability rapidly decreases as the occurrence of this event is reduced. Because of the environmental pressure applied in the last decades on the aluminium industry, the overall anode effect performances have improved significantly [3], thus making the current estimation methodology more difficult to apply accurately.

This paper investigates the efficiency of newly proposed methodologies [4] to estimate CF_4 and C_2F_6 emissions resulting from high-voltage anode effects. These new models take into consideration that the emission rate of PFC is not linearly dependent on the polarized anode effect duration. Their efficiency was evaluated based on measurements performed in seven different smelters and they indicate that the non-linear approach is appropriate to eventually replace the actual quantification methodology. Moreover, these models were used to evaluate the monthly emissions from six different smelters over five consecutive months in order to determine whether the total GHG inventory is expected to increase or decrease with the proposed methodology.

3.3 Anode effect mechanisms and quantification of emissions

3.3.1 Generation of perfluorocarbons caused by anode effects

During the production of aluminium, an electrical current is forced through an electrolytic bath in order to dissociate the aluminium and the oxygen from the dissolved alumina by the standard electrolysis reaction (equation 3-1). This reaction permits the

passage of the electrical current, and in the rare occurrence where a lack of alumina is observed, the cell voltage will increase accordingly to maintain the flow of electric charges. Once the cell voltage reaches a certain threshold, secondary reactions (shown by equations 3-2 and 3-3 will occur in the cell to support the passage of the current.

$$2\ Al_2O_{3(diss)} + 3\ C_{(s)} \rightarrow 4\ Al_{(l)} + 3\ CO_{2(g)} \qquad E_0 = -1.18V \qquad (3\text{-}1)$$

$$4\ Na_3AlF_{6(l)} + 3\ C_{(s)} \rightarrow 4\ Al_{(l)} + 3\ CF_{4(g)} + 12\ NaF_{(diss)} \qquad E_0 = -2.58V \qquad (3\text{-}2)$$

$$2\ Na_3AlF_{6(l)} + 2\ C_{(s)} \rightarrow 2\ Al_{(l)} + \ C_2F_{6(g)} + 6\ NaF_{(diss)} \qquad E_0 = -2.80V \qquad (3\text{-}3)$$

Usually, these reactions occur first in localized regions of the cells, with minimal impact on the cell's indicators (e.g. cell voltage, or overall anode current distribution), thus classified as Low Voltage Anode Effect (LVAE). Although, if these conditions are maintained for too long, or if the alumina depletion is too important, the reactions might propagate to other regions of the cell, leading to a significant increase of the global cell voltage [5]. The cell is then considered operating under High Voltage Anode Effect (HVAE) conditions and this troublesome event is generally undesired in the standard electrolysis practices. During HVAE, the cell will become highly unstable while consuming a very important amount of energy, thus increasing the heat locally in the cell which can lead to premature ageing or even cell tap out. Simultaneously, the aluminium production is reduced significantly during this event and there is important emissions of perfluorocarbons (PFC).

3.3.2 **Standard Quantification Methodology**

Due to the important impact of the GHG on the smelter's GHG inventories, efforts have been deployed in the aluminium industry to correctly estimate the emissions resulting from HVAE. The existing methods are based on three different Tiers, which depict different level of accuracy. Tier 1 models are generic to the global process and generally based exclusively on the total mass of aluminium produced. Tier 2 models are using process parameters to estimate the total emissions, while using a generic emission factor determined using data from the industry for similar types of technologies. Tier 3 models, considered as the most accurate, use a similar approach, only with a different emission factor for each smelter based on periodic measurements taken on site.

Up to now, no existing equipment can reasonably (affordable with high durability) monitor PFC emissions for significant periods of time for an entire smelter. For this reason, PFC emissions were estimated using different methodologies suggested by the Intergovernmental Panel on Climate Change (IPCC) [6]. These approximations are based on different indicators of the smelter's performance namely: total metal production, current efficiency, anode effect frequency and duration or anode effect overvoltage. To estimate CF_4 emissions, smelters were encouraged to choose between equation 3-4 or 3-5 (below) depending on their control system or preference.

Equation 3-4 uses a specifically defined emission coefficient (S_{CF4}; [(kg CF_4/tonne Al)/(AE-Mins/cell-day)]), the total number of polarized anode effect minutes per cell-day (AEM; [AE-Mins/cell-day]) and the respective metal production (MP; [tonnes Al] to estimate the amount of CF_4 generated (E_{CF4}; [kg]) from a selected number of cells over a

defined period. However, the overvoltage model in equation 3-5 uses a specially defined overvoltage coefficient to estimate CF_4 emissions. This coefficient (OVC; [(kg CF_4 / tonne Al)/mV]) is multiplied by the anode effect overvoltage (AOE; [mV]) and the respective metal production (MP; [tonnes Al]). Additionally, a correction based on the current efficiency (CE; [%]) is also included in this model.

On the other hand, the estimated amount of C_2F_6 (E_{C2F6}; [kg]) (equation 3-6) is based exclusively on the calculation of CF_4 (E_{CF4}; [kg]) estimated previously (by either model) and a specific ratio ($F_{C2F6/CF4}$).

$$E_{CF_4} = S_{CF_4} \cdot AEM \cdot MP \qquad (3\text{-}4)$$

$$E_{CF_4} = \frac{OVC \cdot AEO \cdot MP}{CE/_{100}} \qquad (3\text{-}5)$$

$$E_{C_2F_6} = E_{CF_4} \cdot F_{C_2F_6/_{CF_4}} \qquad (3\text{-}6)$$

Those models can be efficient only when the respective coefficient (S_{CF4} or OVC) and the ratio ($F_{C2F6/CF4}$) is redefined periodically using continuous measurement campaigns on site lasting multiple days.

3.3.3 **Newly proposed quantification models**

3.3.3.1 Quantification of CF_4

The standard methodology described in the previous section can be accurate to estimate monthly emissions of a potline, if the anode effect frequency during the measurement campaign was elevated. However, the reduction technology has improved worldwide, and most smelters reached a very low anode effect frequency, thus making it difficult to define a representative emission factor within a reasonable period of in-situ measurement (approximately a week). Moreover, the previous methodology is biased for a

low number of HVAEs as it considers the PFC generation as a linear function of the polarized anode effect duration (PAED) even if this function is nonlinear. For these reasons, new quantification methodologies were proposed based on the same indicator: the polarized anode effect duration.

Previous work [4] was published on the same subject by some of the authors of this paper and it was clearly demonstrated that individual HVAE accounting could not be achieved efficiently with the standard quantification methodology. Moreover, the results from this previous study indicated no significant difference between the two existing models (polarized anode effect duration vs. anode effect overvoltage). For this reason, anode effect overvoltage was not considered in this study.

Three non-linear models are proposed in this paper to estimate CF_4 emissions resulting from HVAE:

Model A: Three range – Non-linear PAED (3R-NL-T2): This model is based on more than 2300 individual HVAE measurement resulting from more than 30 different measurement campaigns in different smelters. It was developed by Dr. Jerry Marks and previously presented by Dion et al. [4]. It is characterized as a Tier 2 methodology. A parallel paper written by Marks and Nunez [7] discusses this model in detail.

For PAED higher than zero, three different power law models were developed to take into consideration the changing rate of CF_4 generation as the PAED increases. A first model represents all PAED higher than 0 and shorter or equal to 5 s, the second model represents PAED longer than 5 and shorter or equal to 200 s while the last model represents all PAED longer than 200 s.

Model B: Two range – Non-linear PAED (2R-NL-T2): This model is based on 425 individual HVAE measurements taken at Aluminerie Alouette Inc. with cells operating above 380 kA. It was previously presented by Dion et al. [4] and it is characterized as a Tier 2 methodology.

It is divided into two ranges depending on the monitored PAED of each respective HVAE. If the PAED is shorter or equal to 20 seconds, the total amount of CF_4 emitted is considered by a linear function (equation 3-7). However, if the PAED is longer than 20 seconds, the total amount of CF_4 emitted is considered as a power-law as indicated in equation 3-8. Where $Total_{CF4}$ is the estimated amount of CF_4 [g] generated by the HVAE, PAED is the polarized anode effect duration [s] and MP is the daily metal production (tonnes) of the respective cell.

$$For\ PAED \leq 20s : Total_{CF_4} = (1.83 \cdot PAED + 12) \cdot MP \qquad (3\text{-}7)$$

$$For\ PAED > 20s : Total_{CF_4} = (8.01 \cdot PAED\text{^}0.593) \cdot MP \qquad (3\text{-}8)$$

Model C: Single range – Non-linear PAED (1R-NL-T3): A specific model[9] was developed for every smelter considered in this study based on individual HVAE measurements. It is composed of a power law estimating the emission rate of CF_4 (g/kA/s) based on the PAED. In average 95±65 HVAE were used to define the respective power-law for each smelter. However, as it is smelter-specific, it is considered a Tier 3 method. Moreover, as it was developed with the same data that will be used for the comparison of the model, it should be the "best-case scenario."

[9] Additional details on the 1R-NL-T3 model are provided in Appendix D, bullet #7.

An example of prediction of this model is illustrated in Figure 3-1.

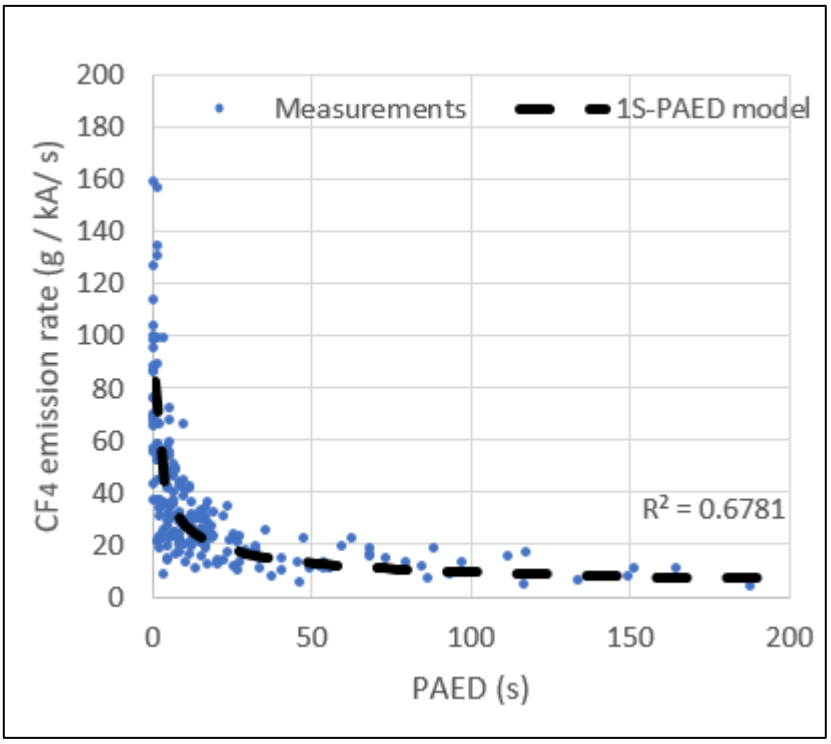

Figure 3-1: Illustration of the single range non-linear PAED model and its respective measurements.

3.3.3.2 Quantification of C_2F_6

The quantification of C_2F_6 using standard methodology is subject to the same problems as the quantification of CF_4. There is also an additional bias caused by the fact that C_2F_6 is not calculated directly. Its calculation is dependent on the preliminary estimation of CF_4. Hence any error in the estimation of individual CF_4 emission will also be present in estimation of C_2F_6. For this reason, two new models were proposed to directly estimate the C_2F_6 emissions without the need to calculate CF_4 preliminarily. Both these models are based on 425 individual HVAE measurements taken at Aluminerie Alouette

Inc. with cells operating above 380 kA. It was previously presented by Dion et al. [4] and they are characterized as Tier 2 methodologies.

Model D: Two range – Non-linear PAED (2R-PAED-T2):

It is divided into two ranges depending on the monitored PAED respective of each HVAE. If the PAED is shorter or equal to 20 seconds, the total amount of C_2F_6 emitted is considered as a linear function (equation 3-9). However, if the PAED is longer than 20 seconds, the total amount of C_2F_6 emitted is considered as a logarithmic function according to equation 3-10, where $Total_{C2F6}$ is the estimated amount of C_2F_6 [g] generated by the HVAE, PAED is the polarized anode effect duration [s] and MP is the daily metal production [tonnes] of the respective cell.

$$For\ PAED \leq 20s: Total_{C2F6} = (0.143 \cdot PAED + 0.157) \cdot MP \qquad (3\text{-}9)$$

$$For\ PAED > 20s: Total_{C2F6} = (1.8 \cdot LN(PAED) - 2.85) \cdot MP \qquad (3\text{-}10)$$

Model E: One range – Linear AE treatment duration (1R-AETD-T2)

It is a linear function depending on the anode effect treatment duration (AETD) [s] and the daily metal production of that respective cell (MP) [tonnes]. Hence, from the moment that the cell voltage reaches the designated AE voltage threshold up to the instant when the cell control system determines that the HVAE is terminated. The total amount of C_2F_6 produced is:

$$Total_{C2F6} = (0.00457 \cdot AETD + 0.357) \cdot MP \qquad (3\text{-}11)$$

3.4 Collection of data: gas measurements

This study is based on multiple measurement campaigns performed between 2013 and 2017 to obtain individual HVAE data related to CF_4 and C_2F_6 emissions. For each respective measurement campaign, the gas output of a specific section of cells was collected and redirected to its respective gas treatment center (GTC). A stainless-steel sampling probe was inserted in the upper section of the GTC, and positioned close to the center of the exhaust duct of the GTC to continuously extract the gas sample.

Once extracted, the gas was routed to a GASMET^{TM} DX-4000 FTIR (Fourier Transformed InfraRed Spectrometer) equipped with a Peltier cooled mercury-cadmium-telluride detector (sample cell path: 9.8 or 5 m, volume: 0.5 L, resolution: 7.8 cm^{-1}). The gas was continuously fed to the analyzer at a volumetric rate ranging from 1 to 5 L per minute. The gas stream was sent sequentially through a 15-micron filter, desiccant, activated alumina, a 5-micron filter and finally a 2-micron filter to remove dust, traces of water and hydrogen fluoride for the protection of the measuring equipment. The gas went through a line heated to 120 °C or 180 °C before entering the FTIR and concentration measurements were performed at a rate of 10 scans per second. Average values for every twenty-second period were recorded. The background spectrum was redefined using high purity nitrogen every 24 hours.

Result files were uploaded from the FTIR and PFC emissions were calculated using the same methodology for both CF_4 and C_2F_6. By integrating the area under the curve using a trapezoid rule, we could obtain a respective ppm·s value associated to each individual HVAE. Then, it was possible to multiply this value by the measured airflow passing

through the CTG cooling tower and the gas density to obtain the total mass of PFC emitted for each respective HVAE. A total of 664 HVAE were monitored and quantified, divided amongst seven different smelters.

3.5 Results and Discussion

3.5.1 Efficiency of the different models to estimate individual HVAE emissions.

To evaluate the efficiency of each model, individual HVAE emissions of CF_4 and C_2F_6 were estimated with every model and the overall errors and the mean squared errors were analyzed. For each smelter, the results were normalized using the prediction of the respective model showing the greatest error as reference value.

The overall error is the difference between the sum of all the estimated HVAE emissions for a specific smelter and the sum of the measured emissions for all the same HVAE. Therefore, a value close to zero indicates that the model is representative of the measurements, while a positive or negative value indicates that the model overestimates or underestimates the emissions respectively.

$$Overall\ error\ per\ smelter = \sum PFC\ estimated - \sum PFC\ measured \qquad (3\text{-}12)$$

The absolute error is composed of the sum of the squared difference between the estimated PFC emissions and the observed emissions for each HVAE from a specific smelter. Therefore, it is an indicator of the accuracy of each individual prediction.

$$Squared\ error\ per\ smelter = \sum (PFC\ estimated - PFC\ measured)^2 \qquad (3\text{-}13)$$

3.5.2 **Efficiency of CF_4 predictions**

The efficiency of the models to estimate CF_4 emissions of 7 different smelters is illustrated in Figure 3-2 by comparing the accuracy of different prediction models. The four models used for the comparison were discussed in detail previously:

- Tier 3 Standard model: Linear PAED (IPCC-L-T3)
- Tier 3 New model: One range model - Non-linear PAED (1R-NL-T3)
- Tier 2 New model: Two-range model - Non-linear PAED (2R-NL-T2)
  Tier 2 New model: Three-range model – Non-linear PAED (3R-NL-T2)

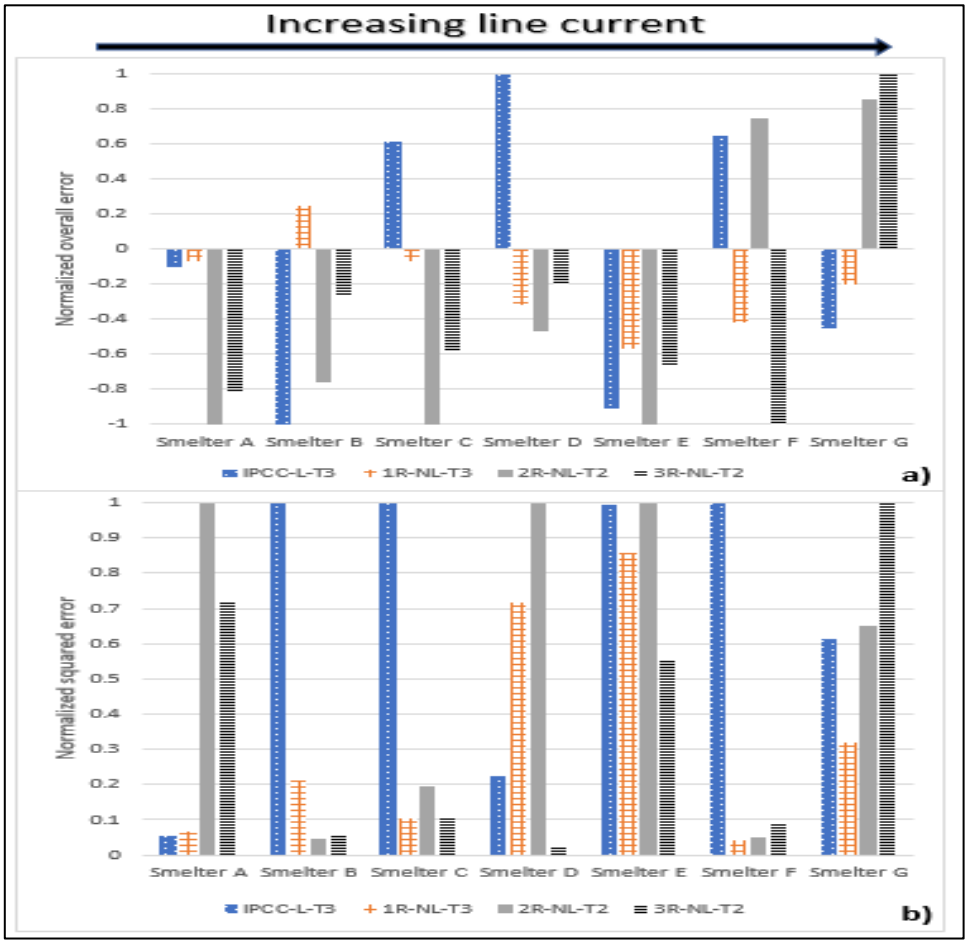

Figure 3-2: Overall error (a) and squared errors (b) of the four predictive CF_4 models for seven smelters.

When looking at Figure 3-2, we can identify that for almost every smelter, model 1R-NL is the most accurate to quantify the total amount of CF_4 emissions resulting from HVAE by demonstrating a high level of overall prediction accuracy (low overall error) and also a high level of individual prediction accuracy (low squared error). This result was anticipated because of the higher level of accuracy of the model (Tier 3) combined to the fact that the data used to calculate the error was previously used to establish the model itself.

On the contrary, the other Tier 3 methodology (IPCC-L) demonstrated a lower prediction efficiency in comparison to the other models. The only case when it gives a good estimation is for the smelter A, which had the lowest line current with no point feeder technology.

Similar results were observed for both Tier 2 methodologies (2R-NL & 3R-NL). These models appear to be more efficient in a specific range of amperage, which is directly dependent on the line current of the acquired individual anode effect measurements. Interestingly, the non-linear Tier 2 models are underestimating emissions of CF_4 for low amperage and overestimating them for higher amperage. Additionally, when comparing both Tier 2 methodologies, significantly better results were obtained with the 3S-NL-PAED, plausibly because it was designed using data from multiple smelters, with different line currents.

3.5.3 **Efficiency of C_2F_6 Predictions**

The efficiency of the models to estimate C_2F_6 emissions is illustrated on Figure 3-3. The three models used for the comparison were discussed in detail previously:

- Tier 3 Standard model: Linear PAED (IPCC-L-T3)
- Tier 2 New model: Two steps model - Logarithmic PAED (2R-PAED-T2)
- Tier 2 New model: Non-linear AETD (1R-AETD-T2)

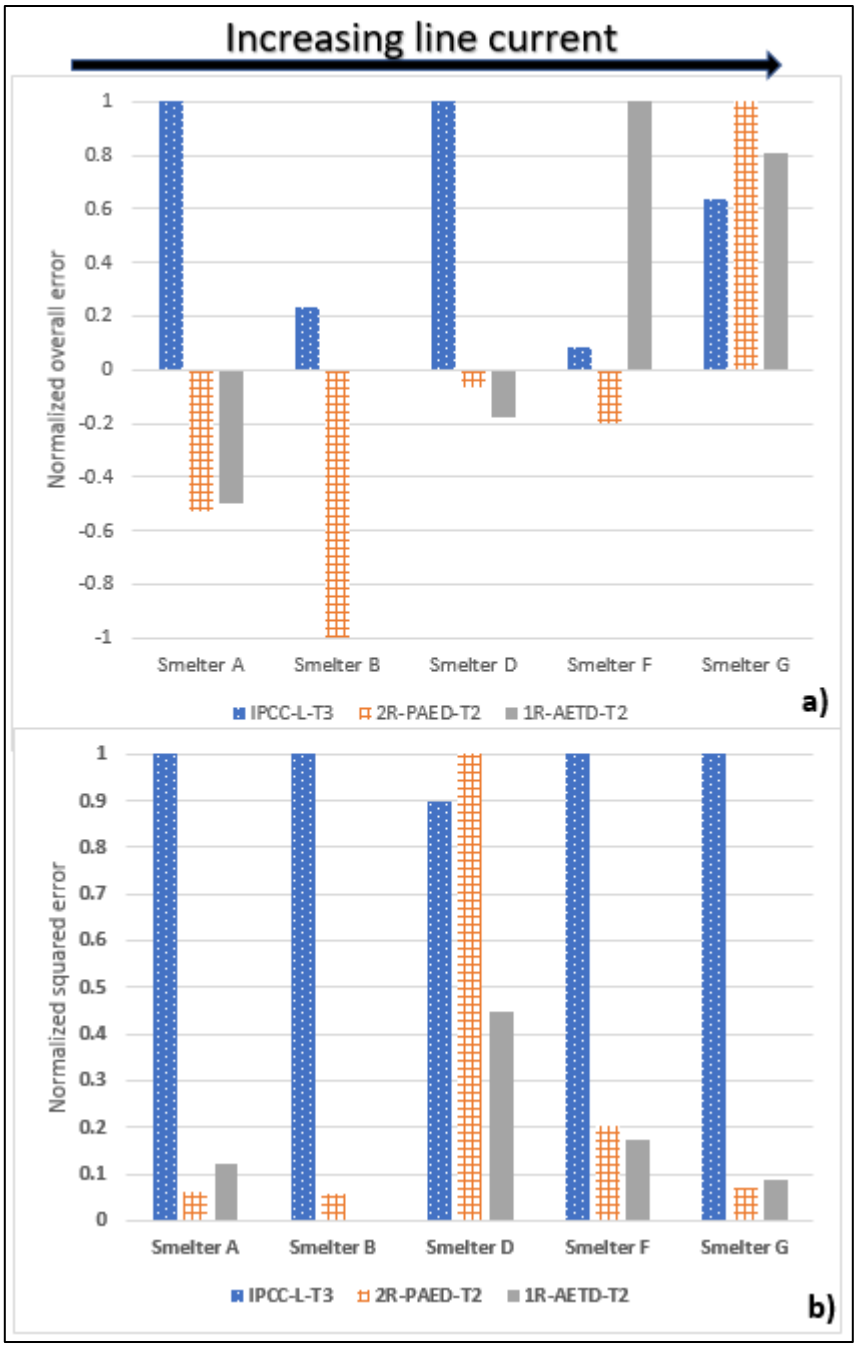

Figure 3-3: Overall error (a) and squared errors (b) of the three predictive C_2F_6 models for five smelters.

The performance of the C_2F_6 estimations models were estimated only for 5 smelters due to the impossibility of collecting accurate individual C_2F_6 measurements at the other facilities, or the impossibility of acquiring the corresponding data required for the calculation, i.e. polarized anode effect duration (PAED) or anode effect treatment duration (AETD).

The results in Figure 3-3-a) demonstrate that estimating the C_2F_6 emissions directly from individual anode effects is a viable methodology to account for this type of emissions. The accuracy of such models is even more evident in Figure 3-3-b) where all the cumulated error of the proposed methodologies is similar (± 10%) to the standard quantifying methodology, or better.

Such accuracy with every smelter is a surprise, knowing that these methodologies are considered Tier 2 and were developed exclusively based on data from a single smelter. It is highly plausible that the accuracy of the models could be increased by adding data from other smelters and developing a generic model knowing that individual C_2F_6 measurements during anode effects is more difficult to obtain due to the small concentration range observed and the high noise level.

Finally, when estimating C_2F_6 emissions, a clear influence of the line current was visible. Similar to CF_4, the results indicate that the models underestimate emissions for low cell amperage and overestimate those emissions for cells with a higher amperage. On the contrary, the tier 3 standard methodology overestimates the C_2F_6 emissions in all cases. The authors assumed in equations 3-7 to 3-11 that the total PFC emissions during individual anode effect were linearly dependent on the metal production, or line current. However, the

results demonstrate that this relationship is probably not linear. Figure 3-4 confirms such affirmation by investigating the measured amount of PFC emissions from different smelters for HVAEs with similar PAED. Such observation could be related to the fact that for a high amperage smelter, AE voltage tends to reach a much lower value in general (reducing the measured PAED), because of the inherent characteristic of these technologies (bigger cell, larger and wider anodes, higher volume of bath, etc.). Whatever the cause of this behavior, further refinements of the non-linear CF_4 and C_2F_6 predictive models can be performed by adding a component considering this effect. Thus, higher accuracy is expected from the non-linear models, especially when used with different line currents.

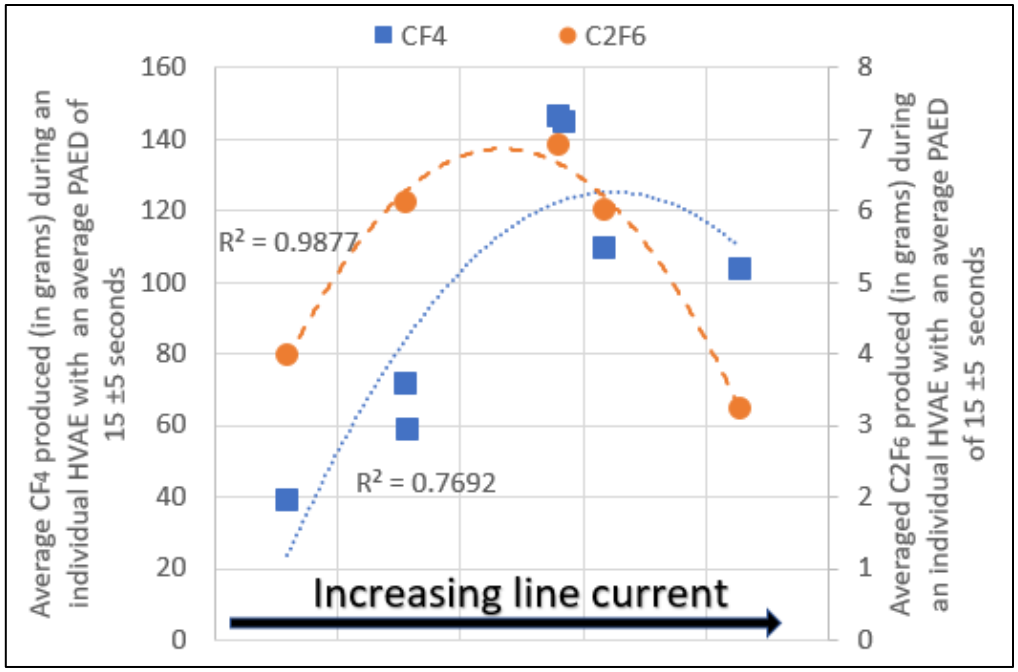

Figure 3-4: Non-linear impact of the line current on PFC emission rate for HVAE with similar PAED.

3.5.4 Comparison of the different models to account for HVAE emissions for smelters

To evaluate the time consistency of the different approaches, we calculated the PFC for the first 5 months of 2017 with specific plants record of individual HVAEs. The calculated CF_4 emissions were summed (Figure 3-5) and put in perspective for each smelter.

It can be seen that in average, both tier 3 methodologies (linear and non-linear) give very similar results, with differences lower than 2%. However, smelter by smelter, there can still be significant differences, such as in the case of smelter F. In that case, only short PAEDs were sampled during the measurement campaign, which tends to overestimate emissions factor where longer PAED are registered later in time. That said, most of the time, the tier 3 linear model seems to give accurate results.

As discussed in the previous section, the three-range model tends to overestimate GHG emissions in average, because of the discrepancies for the smelter at low and high amperage.

Similarly, the two-range model underestimates results for low amperage cells due to the absence of real measurements in the lower and upper range of amperage in the development of this model. As a result, the predictive accuracy of the model is limited to a specific range of line current. For medium range amperage smelters, the results from both tier 2 non-linear models are in good agreement with the results from the non-linear tier 3 model (±15%).

A non-linear tier 3 model could prove to be much more coherent in time, escaping the accounting problem encountered with changing PAED distributions. With a good tier 3 model, or even a good enhanced tier 2 model, it might not be necessary to validate the

emission factor regularly (such as every 3 years), unless a major change happened in the cell control technology.

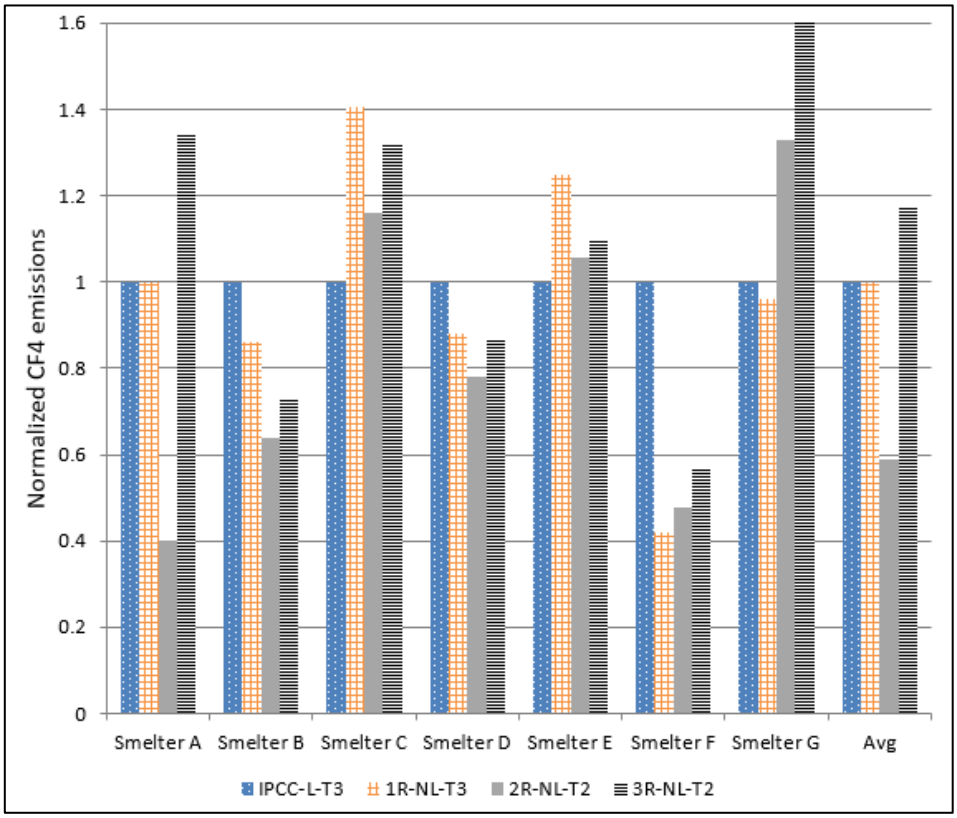

Figure 3-5 : Estimated emissions of CF_4 for 5 months of historical data for 6 different smelters and the total average.

The same process was used to quantify C_2F_6 emissions. For two of the smelters presented (A and C), it was impossible to calculate the linear model using the anode effect treatment duration, because of lack of accessible archived data. IPCC linear indirect model tends to give much higher results in general for the first 5 months of 2017 as seen in Figure 3-6. In the case of the studied smelters and in light of the previous section analysis, this would mean that a significant overestimation in C_2F_6 might be caused by the chosen IPCC model. The results from this paper regarding the proposed methodologies for estimating

C_2F_6 emissions strongly suggests that it should be considered as a possible replacement to the currently used IPCC model resulting in a direct and more precise quantification of C_2F_6 emissions.

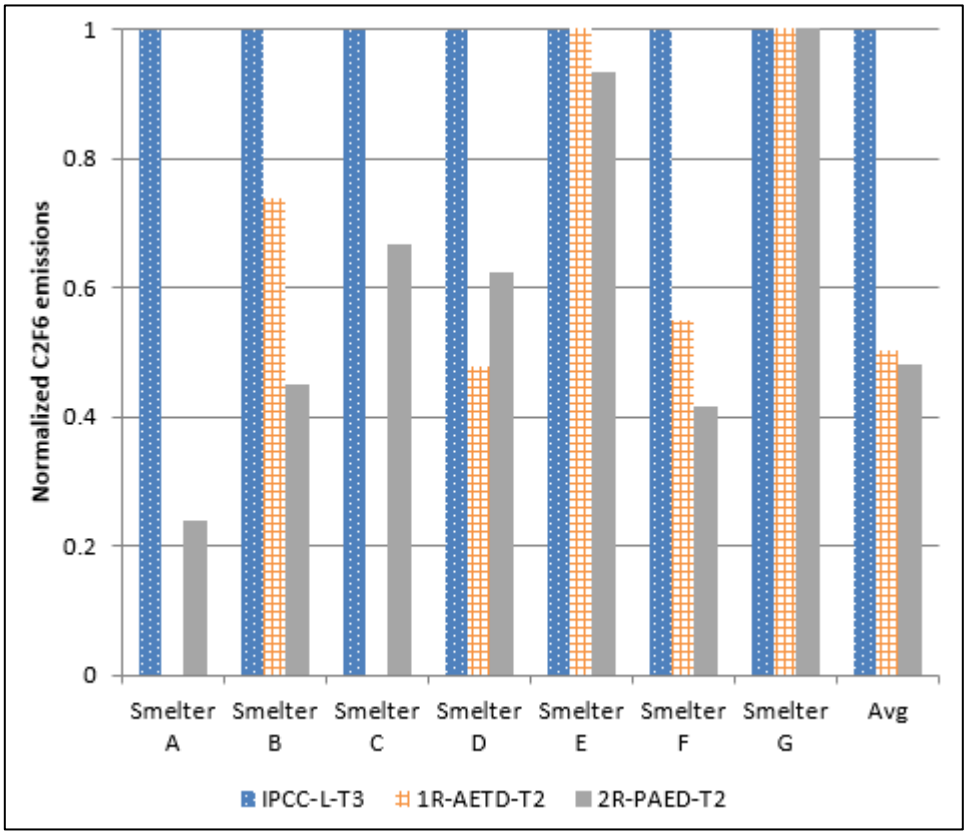

Figure 3-6 : Estimated emissions of C_2F_6 for 5 months of historical data for 6 different smelters and the total average.

3.5.5 **Simplified approach using monthly averages and non-linear models**

With the proposed non-linear models, CF_4 emissions are calculated for all individual HVAE recorded, thus implicating changes in cells control programing and archiving procedure. It would also require a change in the GHG documentation. To address this issue, a simpler non-linear approach could be proposed, in which actual monthly average data are used instead of individual HVAEs. Hence, the models are used to quantify

the CF_4 emitted using exclusively one value: the monthly PAED average. Then the result is multiplied by the total number of HVAE recorded. As shown in Figure 3-7, this approach leads to inaccurate results for most smelters, considerably overestimating the GHG emissions in comparison to the individual HVAE approach. The only exception is the highest amperage cells. For this reason, a simplified approach using monthly averages cannot be recommended without further refinements.

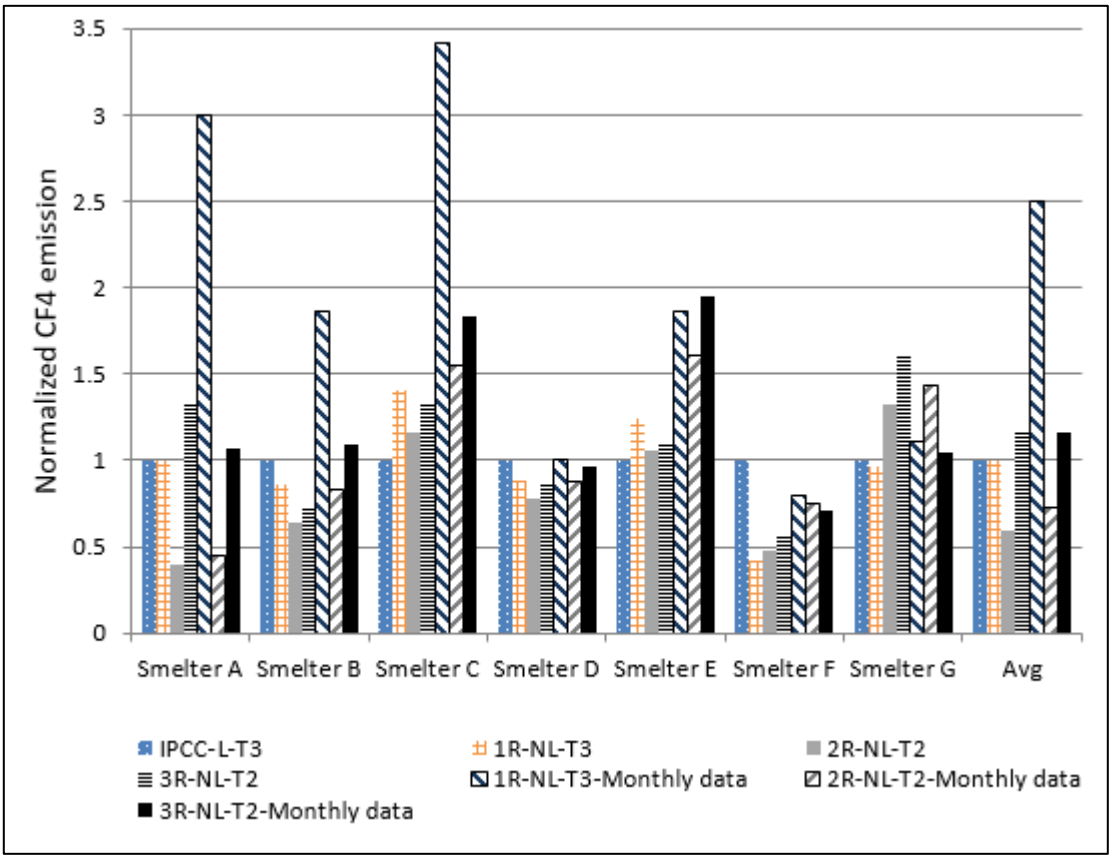

Figure 3-7 : Comparison between the proposed methodologies and simplified "monthly" methodologies.

3.5.6 **Conclusions**

In this paper, three non-linear models were presented to estimate the CF_4 emissions resulting from HVAE. The results indicate that these non-linear models have a good potential to eventually replace, or complement the usual linear methodology because of their high accuracy in estimating emissions resulting from either individual HVAE, or large groups of HVAE. The results indicate that a Tier 3 non-linear methodology (model 1R-NL-T3) is the best performing model, except for the lower amperage cells with no point feeder where the results obtained with the linear model were more accurate. However, due to the increased work required to define a specific model for each smelter, a generic model based on several measurement campaigns from different smelters could also offer satisfying results. It is, however, impossible to determine if the ideal non-linear model should be composed of one, two or three steps because the models compared in this paper were not developed using the same initial data. In any case, tier 3 non-linear models must be used with individual AE data in order to be accurate. Usage of monthly averaged data inserted into non-linear models should not be considered as it tends to largely overestimate PFC estimation, based on the case studies. While more complex to manage, non-linear models should be able to adjust to variations in the process, thus allowing a reduction of the HVAE PFC measurement frequency.

Two additional models to estimate C_2F_6 emissions were also presented. These models offer the great advantage of calculating C_2F_6 directly without prior estimation of the CF_4 emissions, in contrast to the usual IPCC methodology. Surprisingly, even with Tier 2 methodologies developed using data from a single smelter; the results indicate a significant

improvement in accuracy in comparison to the IPCC methodology. Further testing should be performed with a generic model similar to the ones proposed, but based on data from multiple smelters to improve the efficiency.

An interesting conclusion was observed for the Tier 2 non-linear models for both CF_4 and C_2F_6 estimations. For smelters with lower amperage, the models tend to underestimate the total emissions, while overestimating them for smelters with high amperage. This observation is related to the non-linear behavior of the emission rate as a function of the cell daily metal production. This is plausibly caused by the differences in cell size, causing different levels of anode effect overvoltages, thus different PFC production rates for similar PAED. Refinements should be integrated into the model for improved accuracy, especially for higher amperage cells which compose a significant, and growing fraction of the aluminium industry.

3.6 Additional content not presented in the original paper

3.6.1 Development of a non-linear PAED prediction model for quantification of CF_4 and C_2F_6 emissions for cells with different line currents.

Chapters 2 and 3 clearly demonstrated that adequate non-linear models have a significant potential to increase the accuracy of PFC estimations during HVAE. However, the predictive ability of the different PAED non-linear models is limited by the input data with which they were designed. Moreover, it was also demonstrated that for HVAE with similar PAED, the total amount of PFC emitted is different depending on the cell technology, most likely due to the size of the cell (total number of anodes), and thus directly dependent on the cell average current or daily metal production.

Due to the two independent correlations observed (PFC emission and PAED, as well as PFC emissions and daily metal production), an improved model was developed to estimate the PFC emissions released by individual high voltage anode effects based on their polarized anode effect duration for a wide variety of range of daily metal production. Based on the available data used as input, the current versions of the proposed models should not be used for cell metal production exceeding 3200 kg/day, or polarized anode effect duration longer than 800 seconds. However, additional collaboration with the aluminium industry could provide sufficient data to eventually expand these ranges.

3.6.1.1 Development of the CF_4 Model

Using the data collected for the study presented in chapter 3, a power-law representing the CF_4 emission rate with respect to PAED was established for 4 different groups of smelters where the cells daily metal production was significantly different. As illustrated in Figure 3-8 for the same PAED, the total amount of CF_4 produced, per tons of aluminium is lower for cell technologies with higher metal production. Additionally, we can observe that the respective correlation within each group is significant ($R^2 > 0.95$ in all cases).

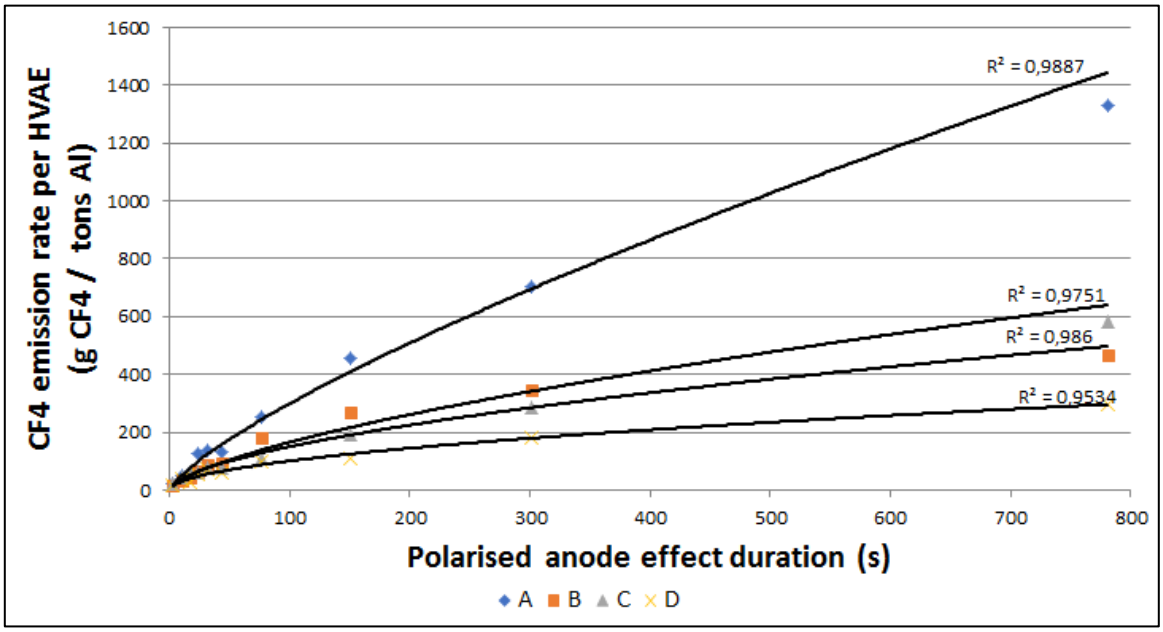

Figure 3-8: CF_4 emission rate based on PAED for groups of smelters with different daily metal production. (A < B < C< D)

The resulting power-law was similar for each group and can be described in the equation below.

$$CF_4\ emis.rate = K1 \cdot PAED^{K2} \quad (3\text{-}14)$$

Where, the CF_4 emission rate [g CF_4 / tons Al] is dependent of the PAED [AE seconds] and two constant values (K1 [g CF_4 / tons Al / AE seconds] and K2 [-]), are specific to the cell technology. By analyzing the available data, a strong correlation was observed between the different values of K2 and the respective daily metal production (DMP) but no strong correlation could be identified regarding the behavior of the K1 constant as illustrated in Figure 3-9.

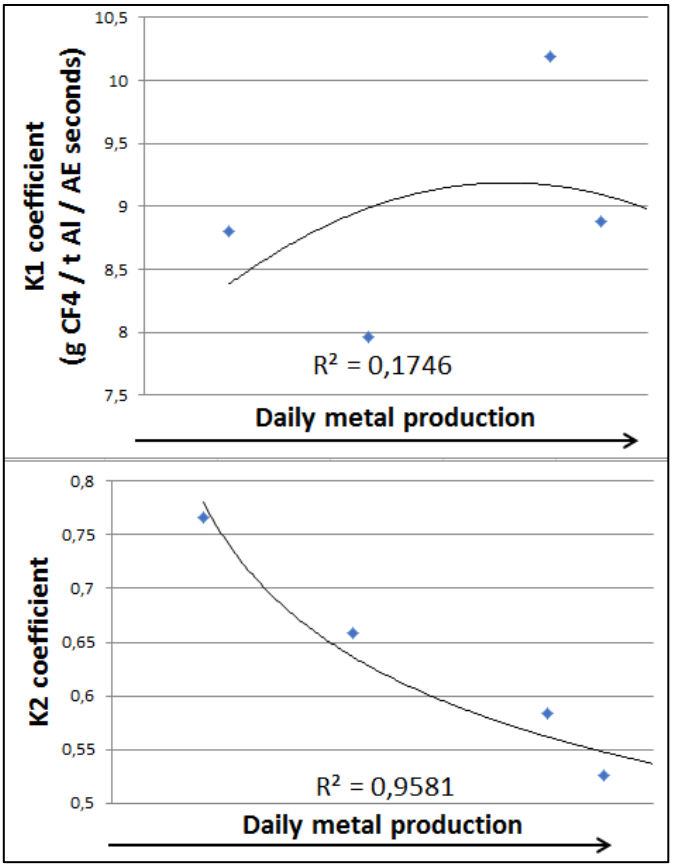

Figure 3-9: K1 and K2 behavior with respect to daily metal production to estimate CF_4 emission rate.

Refinements were applied to equation 3-14 in order to use a function to change the value of K2 based on the respective DMP. The value of K1 was considered constant, as the average value between all the points considered, hence 8.83 g CF_4 / tons Al / AE seconds. The resulting model is presented in equations 3-15 to 3-17, where the emission rate [g CF_4 / tons Al] is dependent on both the PAED [AE seconds] and the cells daily metal production [tons].

$$CF_4\ emis.rate = K1 \cdot PAED^{K2} \quad (3\text{-}15)$$

$$K1 = 8.83 \quad (3\text{-}16)$$

$$K2 = 0.7 \cdot MP^{-0.21} \quad (3\text{-}17)$$

3.6.1.2 Development of the C_2F_6 model

A similar methodology was applied to determine the C_2F_6 emission rate based on PAED and DMP. For each cell's DMP, it was possible to determine a respective power-law based on the PAED to evaluate the behavior of the K1 and K2 coefficient depending on the cell's daily metal production. However, it is important to mention that the respective correlations (PAED vs emission rate) were not as strong as the one observed for CF_4 due to less available data (R^2 ranging from 0.15 to 0.95) and a higher uncertainty associated with the measured C_2F_6 concentrations.

$$C_2F_6 emis.rate = K1 \cdot PAED^{K2} \quad (3\text{-}18)$$

$$K1 = 0.266 \cdot DMP^2 - 0.534 \cdot DMP + 0.975 \quad (3\text{-}19)$$

$$K2 = -0.0506 \cdot DMP^2 + 0.13 \cdot DMP + 0.47 \quad (3\text{-}20)$$

Nonetheless, we can observe on Figure 3-10 that a strong correlation (coefficient values vs DMP) could still be determined for both coefficients. Hence, to estimate the C_2F_6 emission rate [g C_2F_6 / tons Al] from individual HVAE, the previous equation can be used based on the respective PAED and DMP.

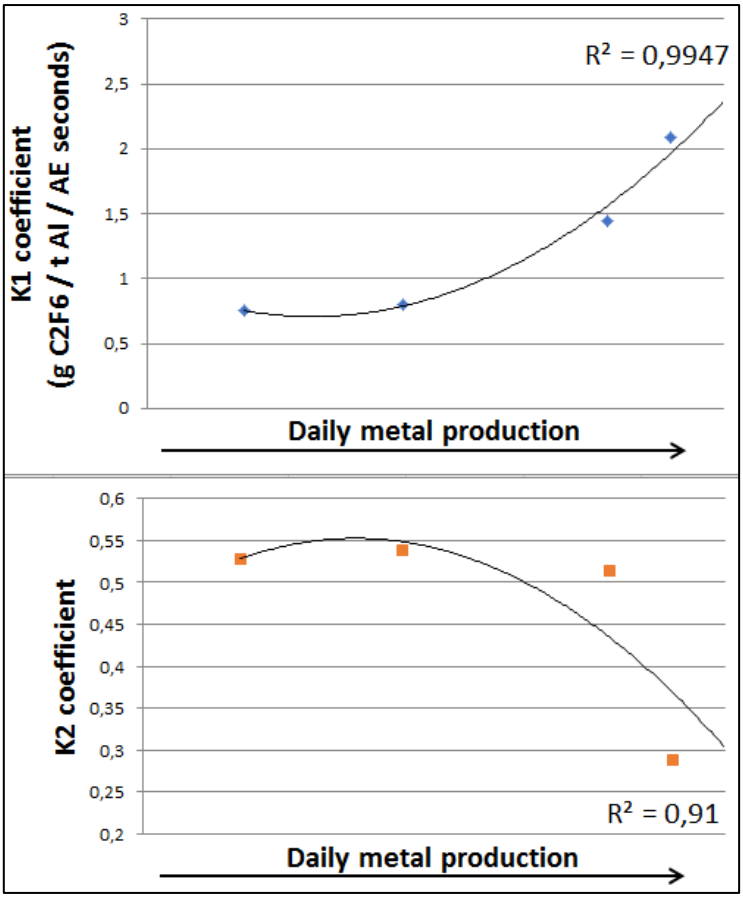

Figure 3-10: Behavior of the K1 and K2 coefficient with respect to daily metal production to estimate C_2F_6 emission rate.

3.6.1.3 Interpretation of the behavior of these models

Surface graphs of the emission rates of CF_4 and C_2F_6 calculated using these models are presented in Figure 3-11 and Figure 3-12 respectively. The results are expressed in tons of CO_2 equivalent emitted for each HVAE per tons of daily metal production, where the

global warming potential of CF_4 and C_2F_6 are estimated [2] to be 6630 and 11100 higher than CO_2.

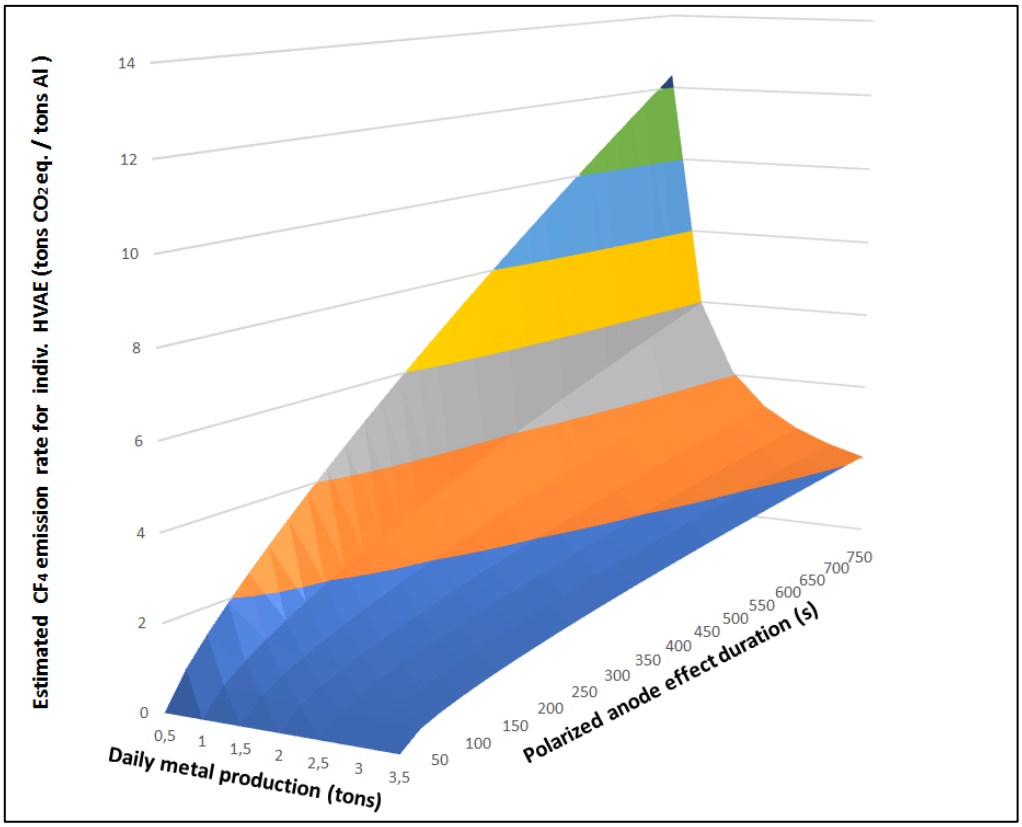

Figure 3-11: Surface graphs of the emission rate of CF_4 for different daily metal production and polarized anode effect duration.

It is possible to distinguish two different behaviors depending on the type of gas emitted. The CF_4 emission rate decreases significantly as the metal production of the cells increases. As previously discussed in chapter 3, this behavior is directly linked to the size of the cells, hence the number of anodes. Thus, when a high-voltage anode effect occurs in a cell, the maximum polarization voltage will most likely be higher for smaller cells because a more important fraction of the anode area is covered by perfluorocarbons. Additionally, the duration of those "high peaks" in voltage will likely be more important

for cells of smaller size. When looking at the emissions of C_2F_6, the effect of the cell size becomes visible for cells with a daily metal production higher than 2 tons, and significant above 3 tons /day.

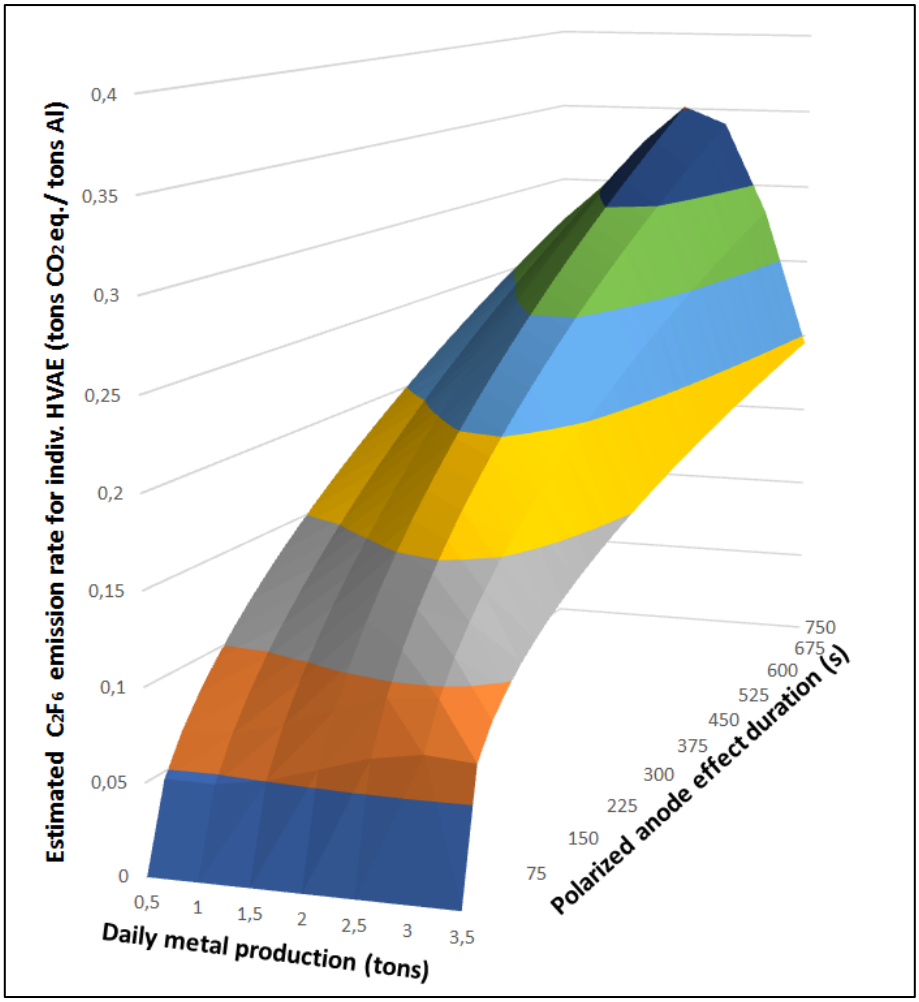

Figure 3-12: Surface graphs of the emission rate of C_2F_6 for different daily metal production and polarized anode effect duration.

The evolution of the C_2F_6 to CF_4 ratio is illustrated in Figure 3-13. It clearly demonstrates an asymptotic behavior as the PAED duration increases. This phenomenon can be explained by assuming that C_2F_6 is mostly emitted in the first minutes of an HVAE,

as previously stated by some researchers [8-9] where the cell voltage usually reaches its highest value (before the AE termination procedure starts). We can also see that for HVAEs with very low PAED, the C_2F_6/CF_4 ratio will be significant for cells of bigger size. This behavior is expected as a cell with a higher line current should produce a more important amount of C_2F_6 for an equivalent polarization voltage, which is at least dependent on the HVAE trigger value.

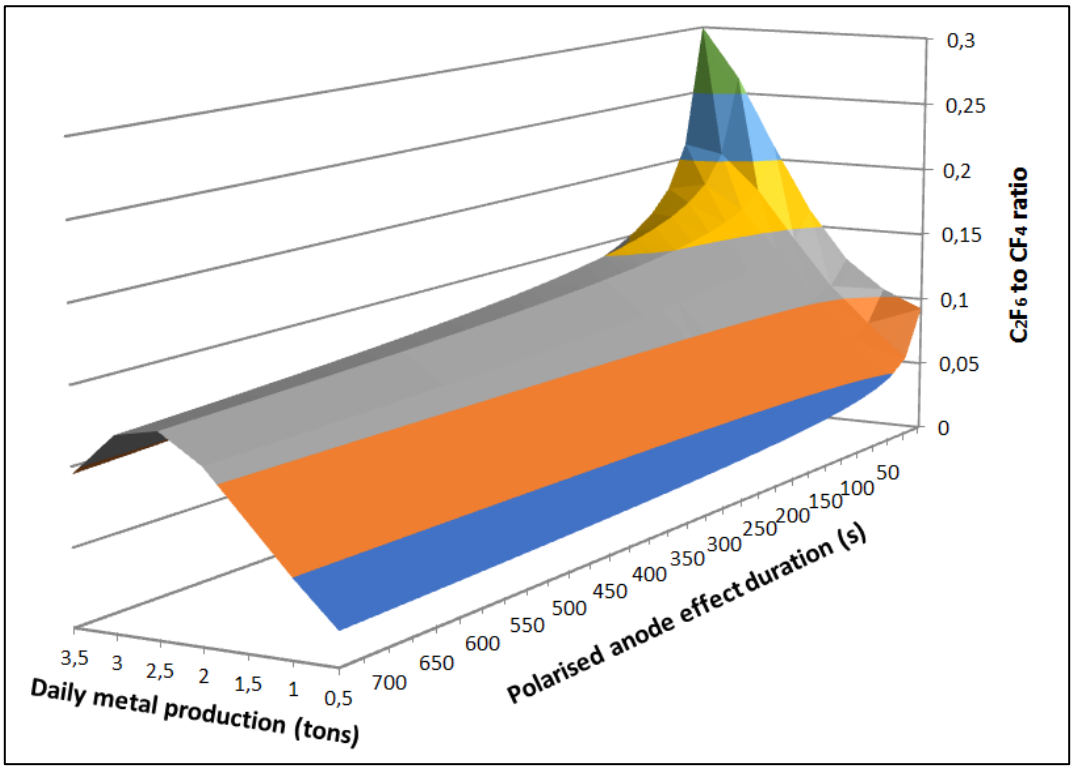

Figure 3-13: Evolution of the C_2F_6/CF_4 ratio based on the polarized anode effect duration and daily metal production for individual HVAE predictions.

3.6.2 **Performances of these generic models**

The performance of these generic models was evaluated using the same data set as previously presented in section 3.4, and normalized similarly. For clarity, the results of the proposed models are only compared to the models illustrating the best performances. The

best models presented previously[10] are the one-range non-linear PAED model (1R-NL-PAED) and the two-range non-linear PAED model (C_2F_6-NL-PAED) for CF_4 and C_2F_6 estimations, respectively.

The accuracy of CF_4 predictions resulting from this new model (PAED-DMP-MODEL) is illustrated in Figure 3-14. The results are very surprising considering that the new model proposed is generic (Tier 2) and offers individual predictions almost as good as the smelter specific model (Tier 3), while the overall error remains quite reasonable.

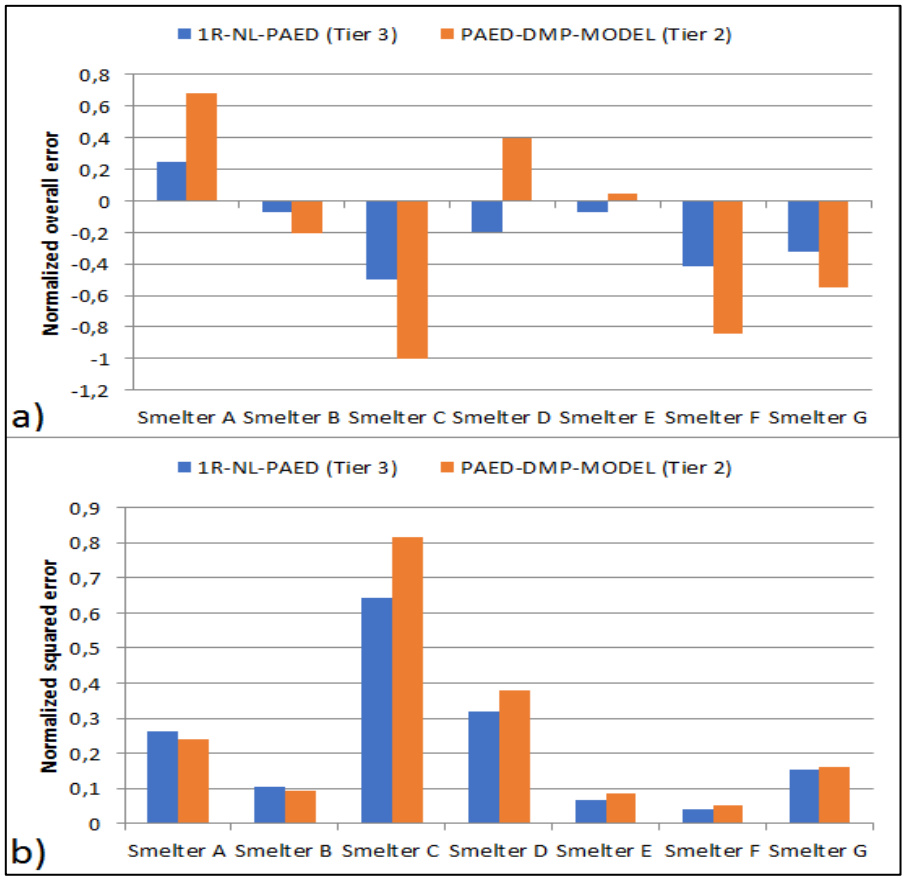

Figure 3-14: Overall error (a) and squared errors (b) of the proposed model (PAED-DMP-Model) in comparison to the best performing model previously investigated (1R-NL-PAED) for CF_4 predictions.

[10] Based on the results from Figure 3-2 and Figure 3-3.

Additionally, it is important to consider that more than 80% of the cumulative error can be attributed to a very small fraction of the population (2%) which are HVAEs with a PAED longer than 400 seconds. For this reason, additional data in the upper range of PAED should lead to quick improvement of the model.

The C_2F_6 predictions accuracy from the new model (PAED-DMP-C2F6), in comparison to a well-performing model (C2F6-NL-PAED) is illustrated in Figure 3-15. The results indicate similar results in terms of overall predictions but there is an improvement in the accuracy of individual HVAE predictions, especially for the smelters with the highest line current.

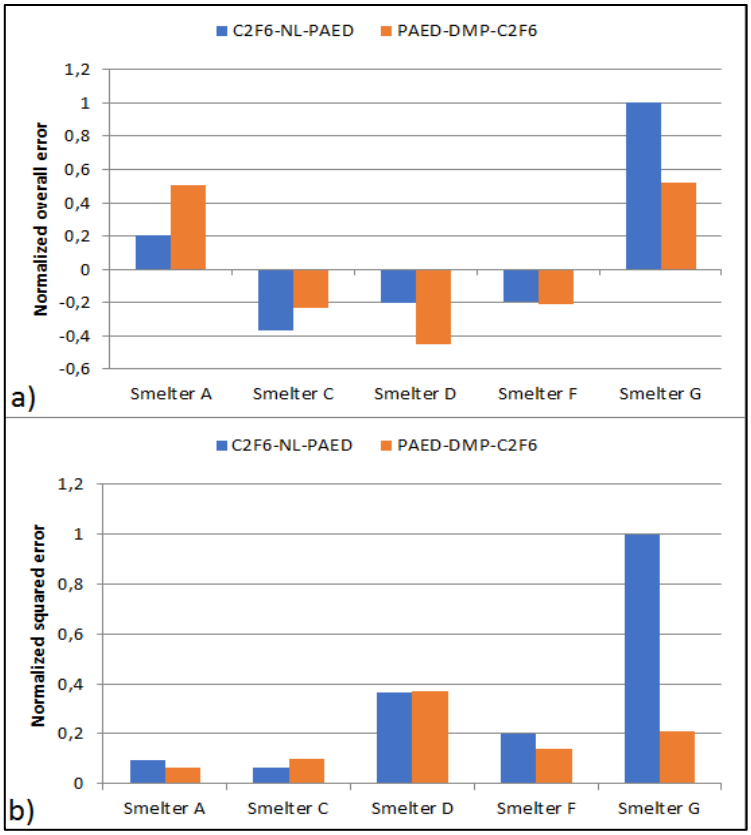

Figure 3-15: Overall error (a) and squared errors (b) of the proposed model (PAED-DMP-C_2F_6) in comparison to the best performing model previously investigated (C_2F_6-NL-PAED) for C_2F_6 predictions.

3.6.3 **Discussion of the results**

The proposed models are based on a restrictive number of smelters in comparison to the overall aluminium industry. Nonetheless, the predictive ability of these models to estimate PFC emissions resulting from individual anode effects was clearly demonstrated inside the studied group. These models could be an effective way to combine data collected from all across the industry in order to establish a generic model to predict CF_4 and C_2F_6 emissions based on a common variable, the polarized anode effect duration, while maintaining accuracy across a very wide range of line currents (cell's daily metal production). It is the author's opinion that further work should be accomplished in this direction by using data from additional smelters to improve the accuracy of the equations for the K1 and K2 coefficients.

There most significant advantage for the aluminium industry to develop a Tier 2 methodology almost as accurate as Tier 3 methods is that it does not require to setup costly on-line FTIR measurements on a regular basis. This observation is even more important for facilities with low HVAE frequency where Tier 3 measurement campaigns require very long durations (multiple weeks) in order to acquire representative data.

Finally, there is one important limitation to the proposed models that was not discussed previously. It is related to the fact that for polarized anode effect duration of zero seconds, no PFC are expected which is in opposition to the observations from section 2.5.1.3. However, this can be taken into consideration by adjusting the definition of the PAED in order to include the polarization seconds associated with the initial detection

periods (currently excluded) into the sums of the PAED seconds, thus eliminating the "zero seconds HVAEs", which are unrealistic.

3.7 References

1. Nunez, P. and S. Jones (2016), *Cradle to gate: life cycle impact of primary aluminium production.* The International Journal of Life Cycle Assessment **21**(11): 1594-1604.

2. Myhre, G., et al., *Anthropogenic and Natural Radiative Forcing.*, in *Climate Change 2013:The Physical Science Basis. Contribution of Working Group I to the Fifth Assessment Report of the Intergovernemental Panel on Climate Change*, T.F. Stocker, et al., Editors. 2013, Cambridge University press: Cambridge, United Kingdom and New-York, NY, USA.

3. International Aluminium Institute (2014), *Results of the 2013 anode effect survey*. London: 1-25.

4. Dion, L., et al. (2017), *Quantification of perfluorocarbons emissions during high voltage anode effects using non-linear approach.* Journal of Cleaner Production (164): 357-366.

5. Wong, D., A.T. Tabereaux, and P. Lavoie. (2014) *Anode effect phenomena during conventional AEs, low voltage propagating AEs & non-propagating AEs*. *Light Metals*: 529-534

6. IPCC (2006), *IPCC guidelines for national greenhouse gas inventories. Volume 3 : Industrial processes and product use*, Katima, J.H.Y., Rosland, A.: (Institute for Global Environmental Strategies (IGES): Jap*an).* 4.49-4.57.

7. Marks, J. and P. Nunez (2018). *New Algorithm for Calculating CF4 Emissions from High Voltage Anode Effects.* Light Metals.

8. Tabereaux, A. T. (1994). *Anode effects, PFCs, global warming, and the aluminium industry*. *JOM* **46**(11): 30-34.

9. Gosselin, A. and P. Desclaux (2002). *Analysis of results from a PFC measurement campaign*. *CIM Bulletin* **95**(1062): 92-95.

CHAPTER 4

PREDICTION OF LOW VOLTAGE TETRAFLUOROMETHANE EMISSIONS BASED ON THE OPERATING CONDITIONS OF AN ALUMINIUM ELECTROLYSIS CELL

4.1 Summary

The content of this chapter was written in collaboration with three co-authors and published in *Journal of Metals*, in 2016, as part of volume 68, issue #9 and pages 2472-2482. Its DOI number is 10.1007/s11837-016-2043-6.

The content presented in the article was entirely designed and written by the author of this manuscript with minor comments and suggestion provided by the co-authors: Laszlo I. Kiss, Sandor Poncsak and Charles-Luc Lagacé.

4.2 Introduction

In primary aluminium reduction, continuous efforts are made by the industry to minimize the tonnes of CO_2 equivalent produced per tonnes of aluminium. Perfluorocarbon (PFC) emissions, composed essentially of tetrafluoromethane (CF_4) and hexafluoroethane (C_2F_6) are key elements to consider in this process. The global warming potential of these two gases is 6,630 and 11,100 times greater than CO_2 respectively [1]. They are generated during an undesired event in the cell called an anode effect (AE). This event is usually associated with an important increase in the cell voltage and is easily identifiable. Hence, these 'high voltage PFC' emissions are well known in the industry and specific guidelines [2] exist to quantify the amount of gas generated during this event. For this reason, smelters have optimized their process worldwide over the years and the total amount of PFC emissions from the aluminium industry has been reduced significantly between 1990 and 2010 [3]. However, by lowering the AE frequency and duration, another source of emissions has become more apparent in recent years, characterized as 'low-voltage PFC' emissions. This particular type of emission can occur for a significant period of time with

little or no indication of misbehavior in the electrolytic cell, for instance, an increase in the cell noise or voltage. For this reason, low voltage PFC are important to take into consideration but up to now, no available method other than real-time PFC monitoring exists to account for these emissions [4]. This paper investigates the correlation between specific cell variables and the level of CF_4 emissions at the duct end of the electrolysis cell.

4.3 State of the Art

Numerous authors (see Table IV) investigated previously the occurrence of low voltage PFC. There is a general agreement in the scientific community that the basic mechanisms generating low voltage PFC are similar to the standard anode effect mechanism, which is very well documented. AE occurs due to the privation of dissolved alumina in a localized region of the bath. If it happens, transport of the electric charges is no longer supported by the standard electrolysis reaction 4-1. It will lead to an increase in the anodic overvoltage and subsequent reactions (4-2 and 4-3) will occur in the cell, leading to the electrolysis of the cryolite and the generation of PFC, therefore, an anode effect [5].

$$2\ Al_2O_{3(diss)} + 3\ C_{(s)} \rightarrow 4\ Al_{(l)} + 3\ CO_{2(g)} \qquad E^0 = \textit{-1.18V} \qquad \textit{(4-1)}$$

$$4\ Na_3AlF_{6(l)} + 3\ C_{(s)} \rightarrow 4\ Al_{(l)} + 3\ CF_{4(g)} + 12\ NaF_{(diss)} \qquad E^0 = \textit{-2.58V} \qquad \textit{(4-2)}$$

$$2\ Na_3AlF_{6(l)} + 2\ C_{(s)} \rightarrow 2\ Al_{(l)} + C_2F_{6(g)} + 6\ NaF_{(diss)} \qquad E^0 = \textit{-2.80V} \qquad \textit{(4-3)}$$

Once an AE occurs in the cell, the localized area where PFC are usually produced becomes strongly resistive to the passage of current (increase in ohmic resistance) and the current will be redistributed toward the other anodes in the cell. This redistribution generally provokes the same problem elsewhere and the AE propagates from one anode

to the other until terminated, meanwhile increasing the global cell voltage significantly. The detection limits of an AE vary from one smelter to other. However, a generally accepted value is when the cell voltage exceeds 8V [6]. For this reason, generalized AE, or high voltage anode effects (HVAE) are easily identifiable and are very well documented in the literature [6-8].

However, if the AE phenomenon occurs only locally in the cell without propagating to all the other anodes, it can lead to a continuous generation of PFC while the cell voltage still remains under the AE detection limit. This makes the detection of low voltage emissions difficult without continuous monitoring of the output gas composition. This event can either self-terminate due to alumina or current redistribution or eventually, it can lead to a HVAE. Historically, this phenomenon was called "background or non-AE PFC emissions." Lately, the International Aluminium Institute (IAI) has adopted the term "low voltage AE" (LVAE) [9]. This paper will use the latest terminology.

Some authors [10-14] refer to reactions (4-4 to 4-6) as the dominant mechanism for the generation of PFC under low voltage conditions as these reactions can occur without a significant increase in the anodic overvoltage. Furthermore, it could also explain why most of the LVAE measurements only indicate very small traces of C_2F_6 above the detection limit of the instrument. On the contrary, during HVAE, the ratio of C_2F_6 to CF_4 can change with time and cell technologies but the typical value is approximately 0.1.

$$2\ AlF_{3(diss)} + Al_2O_{3(diss)} + 3\ C_{(s)} \rightarrow 4\ Al_{(l)} + 3\ COF_{2(g)} \qquad E^0 = -1.88V \qquad (4\text{-}4)$$

$$2\ COF_{2(g)} + C_{(s)} \rightarrow 2CO_{(g)} + CF_{4(g)} \qquad K = 94.8 \qquad (4\text{-}5)$$

$$3\ COF_{2(g)} + 2C_{(s)} \rightarrow 3CO_{(g)} + C_2F_{6(g)} \qquad K = 1.2 \times 10^{-3} \qquad (4\text{-}6)$$

Past researchers have demonstrated that multiple parameters or events could be linked to the occurrence of low voltage PFC emissions. Their conclusions are summarized in **Table IV** and the most relevant points are discussed briefly afterward.

Table IV. Overview of possible correlations between cell variables or specific events in the cell with low voltage emissions of PFC

		Cell parameters											Events			
Year	Authors	Alumina concentration	Feeding strategy	Anode current density	Anodic overvoltage	Bath temperature	Bath chemistry	Superheat	Total number of anodes	Anode-cathode distance	Cell stability (noise)	Cell voltage	Anode change	Metal tapping	Overly aggressive AE treatment	Blocked feeder
2011	Li et al. [15]	**?**	**-**	**-**		**?**							**?**	**?**		
2013	Chen et al. [10]	+		+	+											
2013	Wong and Marks [16]	+		+		-	-						+			+
2013	Zarouni et al.[17]	+	+	+	+								+			
2014	Asheim et al. [5]	+														
2014	Wong et al. [7]	+		+	+				+	+						+
2015	Asheim et al.[11]	+		+	+	+										
2015	Dando et al.[18]				+						+		+	+	+	
2015	Jassim et al.[12]	+	+	+	+			+		+		+	+			
2016	Batista et al.[19]	+	+								+		+			
Sum of the positive findings		**8**	**3**	**6**	**6**	**1**	**0**	**1**	**1**	**2**	**2**	**1**	**5**	**1**	**1**	**2**

Legend:
+ indicates a correlation was observed
- indicates that no correlation was observed
? indicates that the relationship was unclear
empty cells indicate that this variable was not mentioned by the authors.

Most authors [5, 7, 10-12, 16-19] agree that alumina concentration, anode current density and anodic overvoltage have a significant impact on the onset of low voltage PFC emissions. All of these parameters are interrelated and will dictate if the localized overvoltage eventually exceeds the threshold necessary to generate PFC[11]. Similarly, LVAE related to the feeding strategy have been observed at the end of underfeeding periods. This observation confirms that low alumina concentration in the bath is more likely to generate CF_4 even during normal cell operations.

Some authors [11, 12, 15, 16] explored the influence of bath temperature, bath chemistry[12] and superheat on the PFC generation. These variables will have an influence on the maximum solubility of the alumina in the bath as well as on the kinetics of its dissolution. Hence, keeping these variables in an appropriate range will minimize the alumina concentration gradients in the electrolytic bath.

The new, high amperage cells that are becoming more prevalent in the aluminium industry are composed of a greater number of anodes with larger surface areas in order to preserve anode current density. For this reason, a local AE is less likely to propagate towards the other anodes and thus probably can last longer [7]. Moreover, as each anode are connected in parallel electrically, the effect of gas passivation under a single anode will be less significant on the global cell voltage if the total number of anodes increases.

---

[11] The threshold mentioned in this section should not be confused with the 8 volts AE detection threshold. In this case, it refers to the local conditions related to critical current density and whether or not the electrolytic bath is able to sustain normal passage of the electrical charges. The value of this overvoltage threshold will differ in the cell depending on the alumina concentration gradients and the difference in individual anode currents.

[12] Additional discussion regarding bath chemistry is available in Appendix D, bullet #8.

PFC emissions are frequently observed up to multiple hours after an anode change [12, 16-19]. This is due to the redistribution of current towards anodes that increases the current density locally. The non-uniformity of the current distribution can be amplified if the anode-cathode distance (ACD) is reduced in order to operate with lower energy consumption. In such a cell, a small imbalance in the anode setting will have a greater impact on the anode current distribution, thus increasing the risk of generating PFC.

4.4 Experimental Setup

Data used in this study were collected during two measurement campaigns of gas emissions at Aluminerie Alouette Inc. from prebaked AP40LE cells using point feeders and operating above 390 kA. They were equipped with on-line monitoring of individual anode currents using a measurement frequency of 1Hz. Cell current, voltage and pseudo-resistance were measured by the cell control system with the same frequency and all the data were recorded. Only one cell at a time was monitored therefore, there was no dilution other than the gases entering the cell through the hooding. Inspection of the hooding was frequently performed to make sure it remained in similar condition throughout the whole campaign.

During these periods, gas composition was measured with a GASMET^{TM} DX-4000 FTIR (Fourier Transformed InfraRed spectrometer) using a Peltier cooled mercury-cadmium-telluride detector (sample cell path: 9.8m, volume: 0.5L, resolution: 7.8 cm^{-1}). A stainless-steel sampling probe was located at the duct end of the electrolysis cell and gas was continuously fed to the analyzer at a volumetric rate of 2.5 liters/minute. The gas stream was sent sequentially through a 15-micron filter, desiccant,

activated alumina, a 5-micron filter and finally a 2-micron filter to remove dust, traces of water and hydrogen fluoride for the protection of the measuring equipment. The gas went through a line heated at 120°C before entering the FTIR and concentration measurements were performed at a rate of 10 scans per second. Average values for five second periods were recorded. The background spectrum was redefined using high purity nitrogen every 24 hours.

Gas composition was measured for a total of two weeks. The temporal evolution recorded was then classified into 15 scenarios. Thirteen of them were selected because the CF_4 concentration remained within the range of interest for a significantly long period. Two extra scenarios represent stable periods without LVAE. CF_4 emissions issued from HVAE were not considered in this study. Additional information on the preparation of the data was published previously [20]. After the data selecting process, 22,000 data points remained. Half of them corresponded to LVAE. This relatively high number of points was sufficient to develop the six artificial neural networks required for the predictive algorithm described below but further increase in the total number of data points could still improve its performance.

4.5 Development of the Predictive Algorithm

A predictive algorithm was developed to predict the CF_4 concentration at the duct end of an electrolysis cell using continuously measured parameters. The range of interest of the CF_4 concentration for this study is between 10 ppb and 2000 ppb. The lower limit was set according to the threshold detection of the FTIR and the upper limit was determined by

the highest CF_4 concentration that was measured under LVAE conditions. C_2F_6 was not considered as most of the data remained under the detection limit of the FTIR (20 ppb).

The strategy of the algorithm, as well as the choice of the input variables, was developed iteratively. Multiple combinations have been examined including different strategies and/or different inputs. It is important to mention that further refinement is still possible, but it would first require additional measurement campaigns.

Seventy percent of the selected data was used for the learning process to develop the artificial neural networks and the remaining thirty percent were used for validation to evaluate the accuracy of the predictions. One of the main applications of this algorithm is the sensitivity analysis that has been performed subsequently. This analysis clearly indicates the variables with the strongest influence on the emissions of LVAE as well as the expected variations over the entire range of each entry variable.

Artificial neural networks (ANN) behind the algorithm were developed using the data mining package offered with STATISTICA 12®.

4.5.1 **List of indicators**

The first selection of the potential indicators (input variables) was based on the results of the literature review indicating which parameters were most likely to correlate with the presence of low voltage CF_4 emissions. To introduce an input to the algorithm, it was necessary to have data collected with relatively high frequency (0.2 to 1 Hz) for each respective input. As alumina concentration could only be measured intermittently, it was not included as an input. After optimization, seven variables were retained as inputs for the predictive model. Most of these are related to individual current monitoring as it offers

local data on the cell behavior. More importantly, it supplies indirect information regarding the alumina distribution [21] and the influence of changing anodes. The list of the seven indicators:

- *Cell voltage (volts):* Average cell voltage computed for 5 consecutive seconds.
- *Noise (temporal stability) indicator (nanoOhms):* The difference between the maximum and the minimum pseudo-resistance measured for the cell within the last 6 seconds.
- *Maximum current driven through individual anodes (Amperes):* The highest current value that has been observed among the individual anodes.
- *Standard deviation between individual anode currents (Amperes):* For every second, the standard deviation was calculated using individual anode current measurements from the entire cell.
- *Absolute difference between upstream and downstream current averages (Amperes):* the average current value is calculated for both halves of the cell and the absolute difference between the two sides is calculated.
- *Absolute difference between tap hole and duct end side current averages (Amperes):* Same as the previous variable but the division of the cell was performed across the other axis.
- *Range of measured individual currents (Amperes):* Difference between the maximum and the minimum individual anode currents measured.

4.5.2 **Description of the algorithm strategy**

The algorithm is divided into three steps as shown in Figure 4-1. The first step is performed by an artificial neural network designed to indicate if the conditions are met for the generation of CF_4 in the electrolysis cell. The output from this ANN can either be positive or negative. A positive output indicates that CF_4 emission is expected at the duct end of the electrolysis cell under those conditions. On the contrary, a negative output indicates that the measured CF_4 concentration would be below the limit of detection. Negative outputs are considered as 0 ppb concentration. During the learning phase of the ANN, it was necessary to use weighting factors to favor the predictions of “no emissions”.

This minimizes the risk of amplifying the error caused by a wrong prediction in the following steps, which could lead to divergent predictions. Therefore, weighting factors of 2:1 were used in favor of the negative predictions.

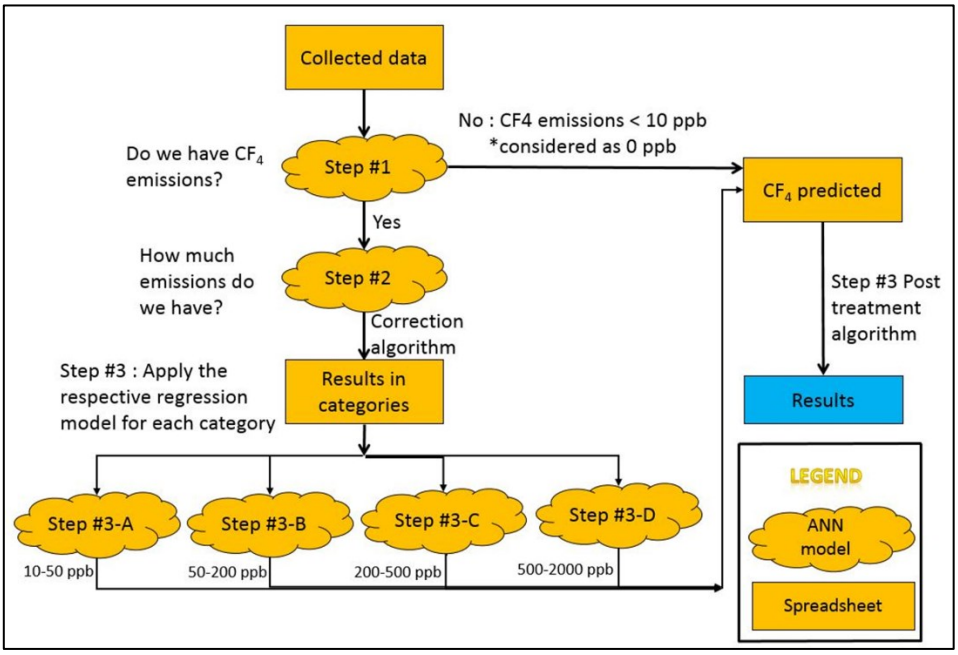

Figure 4-1: Illustration of the predictive algorithm strategy.

The second step of the algorithm is performed by another ANN that aims to classify its output in specific concentration ranges that are to be expected without assigning a quantitative value. A correction algorithm is applied after this ANN to minimize the risk of wrong classification. This correction considers the previous temporal prediction to assure consistency. The resulting output can be divided into four different categories:

A. 10 ppb to 49.99 ppb
B. 50 ppb to 199.99 ppb
C. 200 ppb to 499.99 ppb
D. 500 ppb to 2000 ppb

The last step of the algorithm assigns a quantitative CF_4 concentration to the specific entry conditions. It uses four artificial networks working in parallel depending on the respective category that was assigned in the previous steps. Once each value has been defined, a post-treatment is applied to the prediction to take into account the evolution of the CF_4 concentration over time. In this case, the post-treatment is a mobile moving average over a five-minute period.

4.6 Results and discussion

4.6.1 Validation of the algorithm

Thirty percent of the collected data was used exclusively for the validation of the model. These data were fed into the model and the results were examined after each step of the algorithm to evaluate its performance.

Figure 4-2-a) clearly indicates the ability of the model to predict the presence or the absence of CF_4 based on the input variables. The percentage of correct predictions after step #1 rises above 83%. Moreover, the effect of the weights discussed previously is clearly visible in the incorrect predictions column. Hence, when no CF_4 is present in the output gas composition, the model rarely predicts otherwise, which increase the performance in the following steps of the algorithm. Figure 4-2-b) indicates that 69% of the data is correctly classified after the second step. The results indicate that most incorrect predictions are offset only by 1 category. Further investigation revealed that the majority of incorrect classifications are due to concentrations that are near the limits of each category (i.e. 10, 50, 200 and 500 ppb). This is more important for classifications from the category A where the percentage of misclassifications exceeds the number of correct predictions. However, more

than 80% of these incorrect predictions were within the range of 10 to 15 ppb. Therefore, it might be relevant to reconsider the lower limit of prediction of the model in the future to avoid being too close to the detection limit of the FTIR. For this reason, it is unclear whether the errors came from the noise of the FTIR or if the variations within cell variables are just too small in this range of concentration to be detected above the normal variation level of each respective variable.

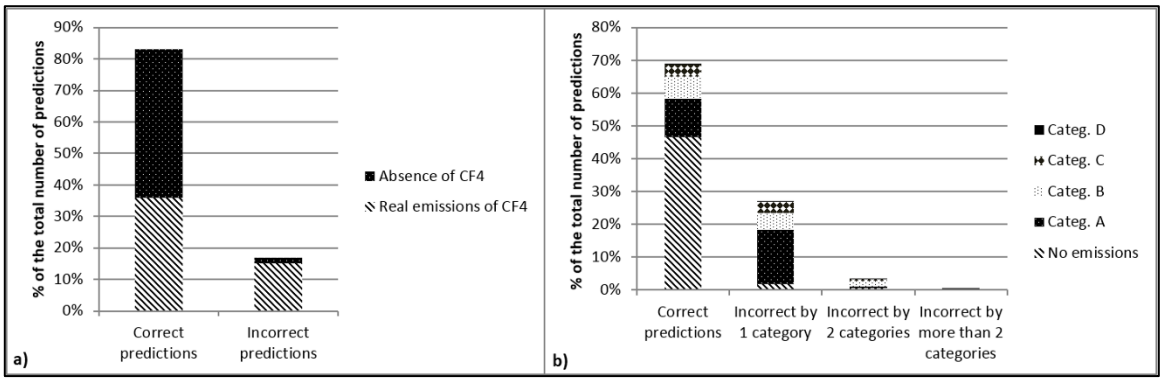

Figure 4-2: a) Percentages of correct and incorrect predictions after Step #1. b) Percentages of correct predictions along with the different offsets in incorrect predictions after Step #2.

Final validation[13] was performed by calculating the overall mass of CF_4 emitted during each specific period based on the measurements and comparing it to the overall mass obtained using the predicted values for the same periods. The mass of CF_4 was calculated using integration according to the trapezoid rule for all fifteen scenarios and by multiplying the resulting (ppb·s) by the flow rate at the duct end of the cell as well as by the CF_4 density for the corresponding temperature and pressure. Illustrative results for all scenarios are presented in Figure 4-3.

[13] Additional details on the validation are provided in Appendix D, bullet #10.

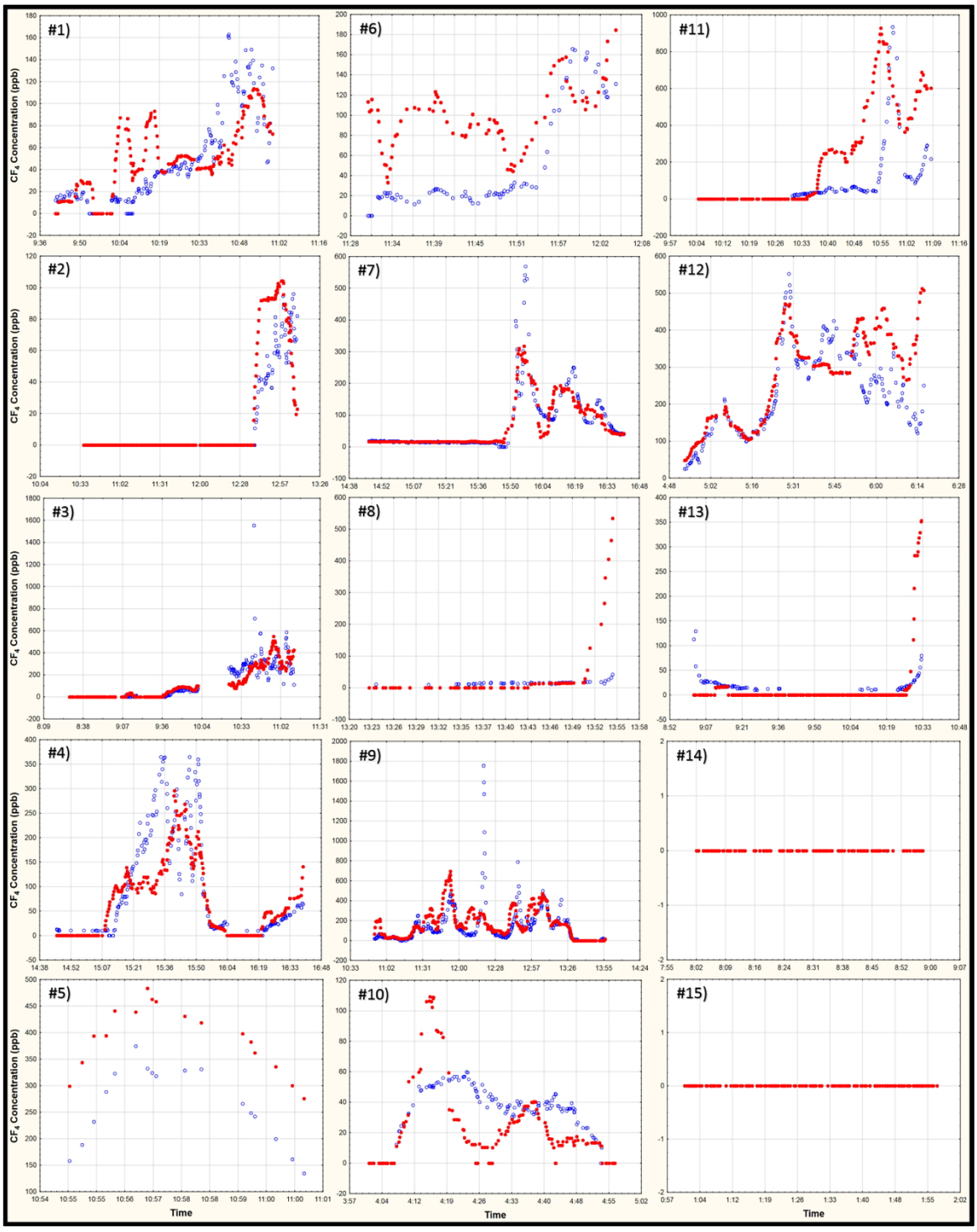

Figure 4-3: Comparison between predicted CF_4 concentrations (filled circles) and measured concentration (open circles).

In most cases, the overall behavior of the CF_4 prediction is in good accordance with the corresponding measurements, including the cases where no emissions are present (Figure 4-3-14 and Figure 4-3-15). It indicates the consistent behavior of the algorithm to quantitatively predict the concentration of CF_4 from an electrolysis cell based exclusively on some of the cell parameters. The results in Figure 4-4 are also consistent with this statement as they indicate that the model correctly predicts the total mass of CF_4 within a ±25% error margin in two thirds of the cases. If we consider that to our knowledge, no other predictive model to account for low voltage PFC emissions has been developed in the open literature, added to the fact that the average error for the entire set of data is 8%, the algorithm's performance can be considered as good. Henceforth, it is possible to proceed with a sensitivity analysis representative of the strength of influence of the inputs.

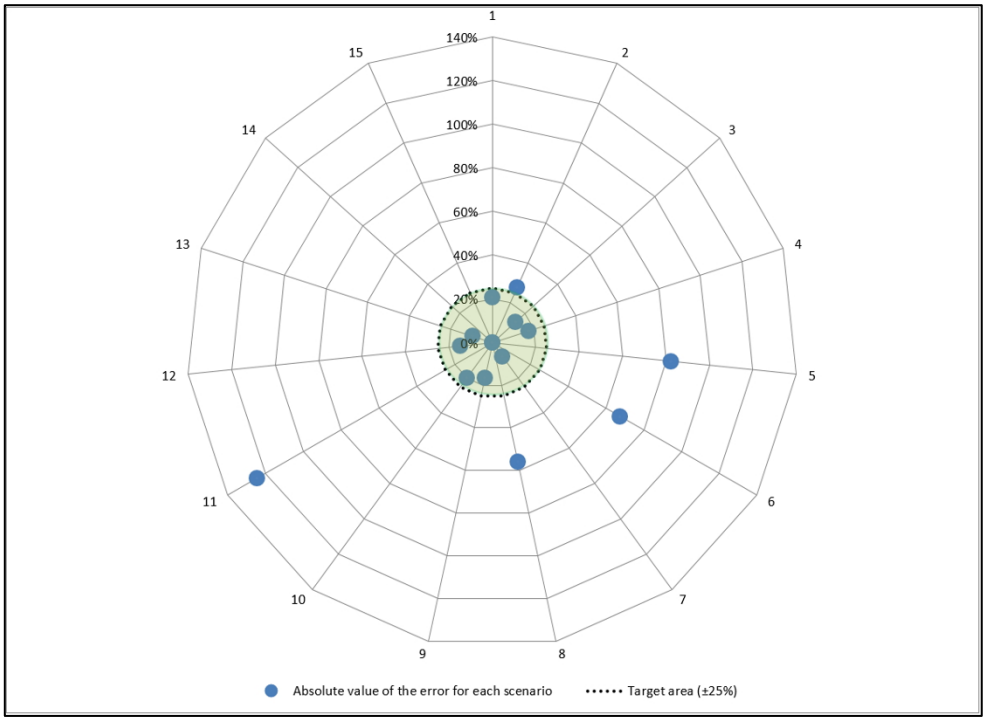

Figure 4-4: Radar chart illustrating the absolute value of the error percentages for all 15 scenarios.

4.6.2 Sensitivity analysis: individual effect of the indicators on the low voltage emissions of CF_4

A sensitivity analysis[14] was performed based on a seven-level full-factorial design [22] including all the seven indicators. Henceforth, it was possible to examine the effect of each input variable on the resulting predictions obtained with the algorithm. For the purpose of identifying the dominant input variables, most of the useful information is available after *the first step of the algorithm*. Therefore, only these results are presented, as they are more relevant.

The exploration limits of each variable were defined using their respective data distribution collected during the measurement campaign. The corresponding lower and upper limits for each variable were defined as the 1^{st} and the 99^{th} centiles in order to eliminate the atypical values. The impact of the cross-effects between the different parameters was investigated but no significant interaction was observed, hence it is not presented in this study.

An investigation regarding the probability of CF_4 emissions as a function of cell parameters was performed. For each individual variable, the total number of predicted emissions has been normalized for easier interpretation. The reference (0%) indicates the point where the variable has no influence. Hence, a positive value indicates that the presence of CF_4 is more likely. On the contrary, a negative value indicates that CF_4 emission is predicted by the model less frequently. Moreover, a threshold value has been added to each figure. This threshold is based on the actual measurements and represents the

[14] The cross-effect between the different parameters was not evaluated in this study.

transition point where the probability of occurrence of CF_4 emissions gets higher than the probability of having no emissions. Figure 4-5 illustrates the change in CF_4 emissions with respect to each input variable resulting from the sensitivity analysis. A clear correlation can be observed between a variable and the CF_4 emissions if the slope is steep and the trend is uniform along most of the range studied.

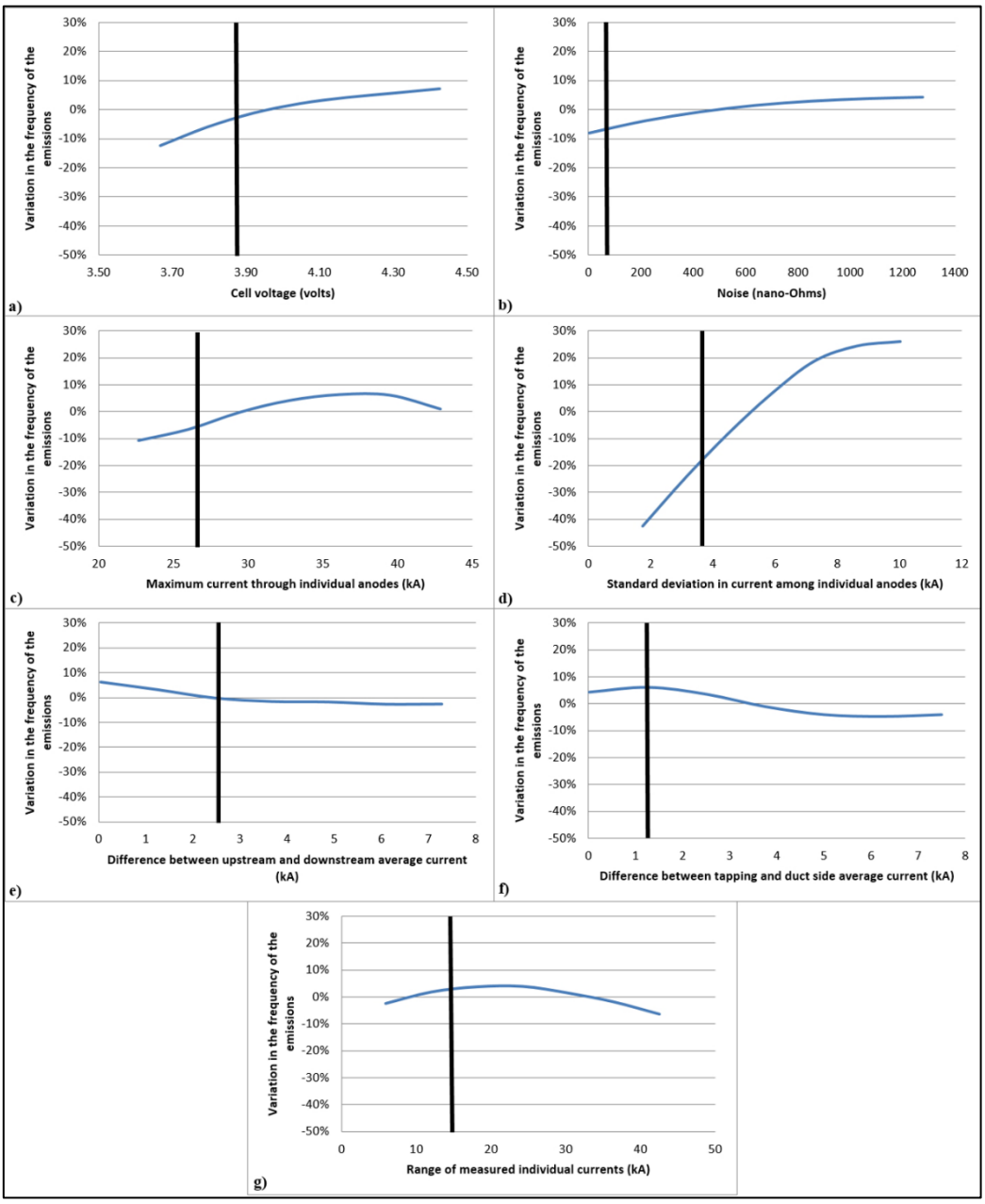

Figure 4-5: Influence level of each indicator on the frequency of predictions of CF_4 based on a full-factorial design sensitivity analysis. The vertical line represents the measured threshold value for each variable.

A positive correlation was observed between an increasing cell voltage and the occurrence of CF_4 emissions. It is important to consider that the voltage values in Figure 4-5-a are representative of a specific cell technology. However, the upper range of values

can be representative of the variation that occurs after an anode change or when higher noise is observed in the pot. Interestingly, as the cell voltage decreases below the threshold value, the slope of influence is steeper. This indicates that variations in this range have a greater effect on CF_4 emissions. It can be interpreted as a range of variation, which is more plausibly associated with an increase in overvoltage. On the contrary, very large variations in voltage are more likely associated with a change in the total resistance of the cell caused by a change of ACD.

The noise level (Figure 4-5-b) has a positive correlation with the occurrence of CF_4 emissions. However, an important variation in the stability of the cell will only generate a small increase in the probability of CF_4 emissions.

The maximum current measured among the anodes (Figure 4-5-c) appears to have a positive influence on the generation of CF_4 emissions up to 35 kA (≈1.75 times the normal level). Up to a certain point, it can be representative of the current redistribution following an anode change or when excessive gas passivates the anodes. Consequently, higher current locally consumes the alumina more rapidly that eventually leads to PFC generation in that region of the cell. Further investigations are required to see if those conditions are maintained for the same anodes or if the current jumps from one anode to the other over time. Moreover, very high currents in a single anode, maintained for a long period, can only be explained by a short-circuit generating other negative impacts for the cell. This phenomenon explains the drop in the CF_4 occurrence when the maximum current in an anode reaches more than 40 kA.

The results from Figure 4-5-d indicate a *clear and strong relationship* between the standard deviation among individual anode currents and the prediction of CF_4 emissions. These results are consistent with the literature as well as the mechanism of PFC emissions. Therefore, when a disruption of the current uniformity starts generating LVAE, the local resistivity is expected to increase under specific anodes. It will lower the current from these anodes and redistribute a part of the current toward other anodes, hence amplifying the current non-uniformity in the cell. The behavior appears to be linear up to a certain limit (7.5 kA). Afterward, there is no more significant increase of the influence of this variable on the emissions of CF_4.

Figure 4-5-e shows a negative correlation, but this effect is mainly due to a permanent offset of approximately 1.75 kA between the average individual anode currents from the upstream and downstream side under normal operations. Henceforth, it has no real correlation with LVAE.

No significant correlation can be observed on Figure 4-5-f and Figure 4-5-g between the occurrence of CF_4 emissions and those variables. However, even if these variables are not as useful in predicting the occurrence of LVAE, they are relevant in the subsequent steps of the algorithm to predict the level of these emissions when these are detected.

4.7 Conclusions

A study has been performed to determine whether certain measurable indicators permit the prediction of low voltage PFC emissions from aluminium electrolysis cells. Inspired by a literature review and a good understanding of the mechanisms, seven

indicators were selected and used to develop a predictive algorithm based on measurements carried out on selected aluminium electrolysis cells. The model is able to successfully predict the emissions of CF_4 at the duct end of an electrolysis cell using only those seven inputs. A sensitivity analysis was performed using the algorithm to understand the effect of each variable on the occurrence of low voltage CF_4 emissions.

The sensitivity analysis clearly demonstrated that inhomogeneity among individual anode currents is the best indicator to predict low voltage CF_4 emissions. Cell voltage and maximal anode current show also a significant and positive correlation with the emissions. The noise level has a positive, but not significant correlation. No other measurable cell variable was found to have a direct and significant correlation with the occurrence of low voltage PFC emissions.

The model described in this paper shows promising results as a predictive method, but further improvements are still required before it can be used as a robust quantitative tool integrated into the cell control system. Moreover, due to the variety of the reduction technologies and the limited accessibility of individual anode current monitoring across smelters worldwide, the proposed algorithm cannot be easily applied outside of the cell technology from which it was developed. However, the investigation and results described in this paper can lead to refinements that would be applicable throughout the entire aluminium industry.

Finally, the primary objective of this study was reached, namely, a new tool was developed, using certain key indicators to predict the generation of CF_4 under low voltage conditions.

4.8 References

1. Myhre, G., D. Shindell, F.-M. Bréon, W. Collins, J. Fuglestvedt, J. Huang, D. Koch, J.-F. Lamarque, D. Lee, B. Mendoza, T. Nakajima, A. Robock, G. Stephens, T. Takemura and H. Zhang, 2013: Anthropogenic and Natural Radiative Forcing. In: *Climate Change 2013: The Physical Science Basis. Contribution of Working Group I to the Fifth Assessment Report of the Intergovernmental Panel on Climate Change* [Stocker, T.F., D. Qin, G.-K. Plattner, M. Tignor, S.K. Allen, J. Boschung, A. Nauels, Y. Xia, V. Bex and P.M. Midgley (eds.)]. Cambridge University Press, Cambridge, United Kingdom and New York, NY, USA.
2. IPCC 2006, 2006 IPCC Guidelines for National Greenhouse Gas Inventories, Prepared by the National Greenhouse Gas Inventories Programme, Eggleston H.S., Buendia L., Miwa K., Ngara T. and Tanabe K. (eds). Published: IGES, Japan.
3. Fischedick M., J. Roy, A. Abdel-Aziz, A. Acquaye, J.M. Allwood, J.-P. Ceron, Y. Geng, H. Kheshgi, A. Lanza, D. Perczyk, L. Price, E. Santalla, C. Sheinbaum, and K. Tanaka, 2014: Industry. In*: Climate Change 2014: Mitigation of Climate Change. Contribution of Working Group III to the Fifth Assessment Report of the Intergovernmental Panel on Climate Change* [Edenhofer, O., R. Pichs-Madruga, Y. Sokona, E. Farahani, S. Kadner, K. Seyboth, A. Adler, I. Baum, S. Brunner, P. Eickemeier, B. Kriemann, J. Savolainen, S. Schlömer, C. von Stechow, T. Zwickel and J.C. Minx (eds.)]. Cambridge University Press, Cambridge, United Kingdom and New York, NY, USA.
4. D.S. Wong, P. Fraser, P.Lavoie, and J. Kim: *JOM*, **67**(2), 342 (2015).
5. H. Asheim, T.A. Aarhaug, A. Ferber, O.S. Kjos, and G.M. Haarberg. *Light Metals 2014,* ed. J. Grandfield. (Hoboken, NJ: Wiley, 2014), pp.535-539.
6. A. Tabereaux (Paper presented at the Eight Australasian Aluminium Smelting Technology Conference and Workshops, Yeppoon, Australia, 2004).
7. D. Wong., A. Tabereaux, and P. Lavoie, *Light Metals 2014,* ed. J. Grandfield. (Hoboken, NJ: Wiley, 2014), pp. 529-535.
8. G. Tarcy and A. Tabereaux, *Light Metals 2011*, ed. S. Lindsay (Hoboken, NJ: Wiley, 2011), pp 329-332.
9. International Aluminium Institute, *Workshop on PFC Emissions in the Aluminium Industry, (*London, UK, 2015).
10. X. Chen, W. Li, S. Qiu, Y. Zhang and C. Bayliss, *Light Metals 2013*, ed. B. Sadler. (Hoboken, NJ: Wiley, 2013), pp. 877-881.

11. H. Asheim, T.A. Aarhaug, E. Sandnes, O.S. Kjos, A. Solheim and G.M. Haarberg: *ECS Trans.*, **69**(15), 1 (2015).

12. A. Jassim, S. Ahkmetov, B.J. Welch, M. Skyllas-Kazacos, J. Bao and Y. Yao, *Light Metals 2015,* ed. M. Hyland (Hoboken, NJ: Wiley, 2015), pp. 545-550.

13. H. Asheim, T.A. Aarhaug, A. Ferber, O.S. Kjos and G.M. Haarberg, *7th Kyoto International Forum for Environment and Energy,* (Kyoto, 2014).

14. B.J. Welch (Paper presented at the 10th Australasian Aluminium Smelting Technology Conference and Workshops, Launceston, Tasmania, 2011).

15. W. Li, Q. Zhao, J. Yang, S. Qiu, X. Chen, J. Marks and C. Bayliss, *Light Metals 2011,* ed. S. Lindsay (Hoboken, NJ: Wiley, 2011), pp.309-314.

16. D. Wong and J. Marks. *Light Metals 2013,* ed. B. Sadler. (Hoboken, NJ: Wiley, 2013), pp. 865-870.

17. A.A. Zarouni, M. Reverdy, A. Zarouni and K.G. Vankatasubramaniam, *Light Metals 2013,* ed. B. Sadler. (Hoboken, NJ: Wiley, 2013), pp. 859-863.

18. N.R. Dando, N. Menegazzo, L. Espinoza-Nava, N. Westendorf and E. Batista, *Light Metals 2015,* ed. M. Hyland (Hoboken, NJ: Wiley, 2015), pp. 551-555.

19. E. Batista, N.R. Dando, N. Menegazzo and L. Espinoza-Nava, *Light Metals 2016,* ed. E. Williams (Hoboken, NJ: Wiley, 2016), pp.545-550.

20. L. Dion, L. I. Kiss, S. Poncsák and C. Lagacé. *Light Metals 2016,* ed. E. Williams (Hoboken, NJ: Wiley, 2016), pp.545-550.

21. L. Dion, L. I. Kiss, C. Lagacé, R. Victor and J. W. Evans. *Light Metals 2015,* ed. M. Hyland (Hoboken, NJ: Wiley, 2015), pp.723-728.

22. A. Saltelli, M. Ratto, T. Andres, F. Campolongo, J. Cariboni, D. Gatelli, M. Saisana and S. Tarantola: *Global Sensitivity Analysis : The Primer*, 1st ed. (Chischester, UK : John Wiley & Sons, 2008), pp.53-108.

CHAPTER 5

INFLUENCE OF HOODING CONDITIONS ON GAS COMPOSITION AT THE DUCT END OF AN ELECTROLYSIS CELL

5.1 Summary

The work discussed in this chapter was presented at the 2016 *ICSOBA* conference held in Quebec City, as part of the symposium on aluminium production, the original work of the paper is “Influence of hooding conditions on gas composition at the duct end of an electrolysis cell”.

The experimental work presented in this section was designed by the author of this thesis, as well as the analysis of the results and the writing of the paper. However, minor comments and suggestions were provided by the three additional co-authors of this paper: Laszlo I. Kiss, Sandor Poncsak and Charles-Luc Lagacé.

5.2 Introduction

During primary aluminium production, massive emissions of gas are produced as the result of numerous chemical reactions occurring in the reduction cells. For technologies using carbon anodes, carbon dioxide (CO_2) is the primary component of these emissions. Nonetheless, other gases can be present in the output flow depending on the electrolysis conditions. Some of these secondary gases include carbon monoxide (CO), sulfur dioxide (SO_2), hydrogen fluoride (HF), bath vapors ($NaAlF_4$, Na^+) and perfluorocarbons (CF_4, C_2F_6)

As most of the chemical reactions occurring during the production of these gases are well known [1], identifying the output composition of an electrolysis cell can offer relevant and instantaneous information about the cell behavior (current efficiency, net carbon consumption, etc.). For this reason, some studies [2 - 7] investigated the evolution of the

gas composition directly at the duct end of an electrolysis cell. This methodology has become particularly relevant in recent years along with studies investigating the occurrence of low voltage anode effects (LVAE). LVAE are also known as non-AE emissions or background PFCs. These emissions of CF_4 and C_2F_6 occur under conditions that are not completely understood, hence the multiple and recent studies on the subject. Analysis of the gas collected directly at the duct end of the electrolysis cell limits the dilution of the gas stream to a single cell, allowing the detection of the gas precisely when the concentration of the studied component exceeds the detection limit of the measuring instrument.

This paper investigates if gas samples collected at the duct end represents well enough the ensemble of gas mixture emitted by the electrolysis cells. Using a tracer gas, the effects of the hooding conditions and the position of the gas collection within the cell are investigated in order to understand the limitation of this methodology.

5.3 Experimental Setup

5.3.1 Cell and equipment specifications

Experiments were performed under industrial conditions on a prebaked AP40LE reduction cell, using point-feeders at Aluminerie Alouette Inc. The cell was operating above 390 kA for the entire duration of the test. A stainless-steel sampling probe was inserted at the duct end of this specific cell to sample the gas flow and route it to a Fourier-Transformed Infrared Spectrometer for analysis of the gas composition. The FTIR used was a GASMET™ DX-4000, equipped with a Peltier cooled mercury-cadmium-telluride detector (sample cell path: 9.8 m, volume: 0.5 L, resolution: 7.8 cm^{-1}). The gas was continuously directed towards the analyzer at a volumetric rate of 2 liters per minutes

(LPM). The gas stream was sent sequentially through a 15-micron filter, desiccant, activated alumina, a 5-micron filter and finally a 2-micron filter to remove dust, traces of water and hydrogen fluoride for the protection of the measuring equipment. The gas was preheated at 120 °C before entering the FTIR and concentration measurements were performed at a rate of 10 scans per second. Average values for five-second periods were recorded. The background spectrum was redefined once a day before the tests using high purity nitrogen.

Gas collection within the cell is designed to be volumetrically uniform between five different inner ducts within the cell superstructure (listed A to E on Figure 5-1). None of these gas streams is mixed until they reach the main duct at the extremity of the cell. From this point, there are approximately three feet of conduct before the stainless-steel sampling probe. Due to restriction from the surroundings, this is the only sampling point available to collect gas from a single electrolysis cell.

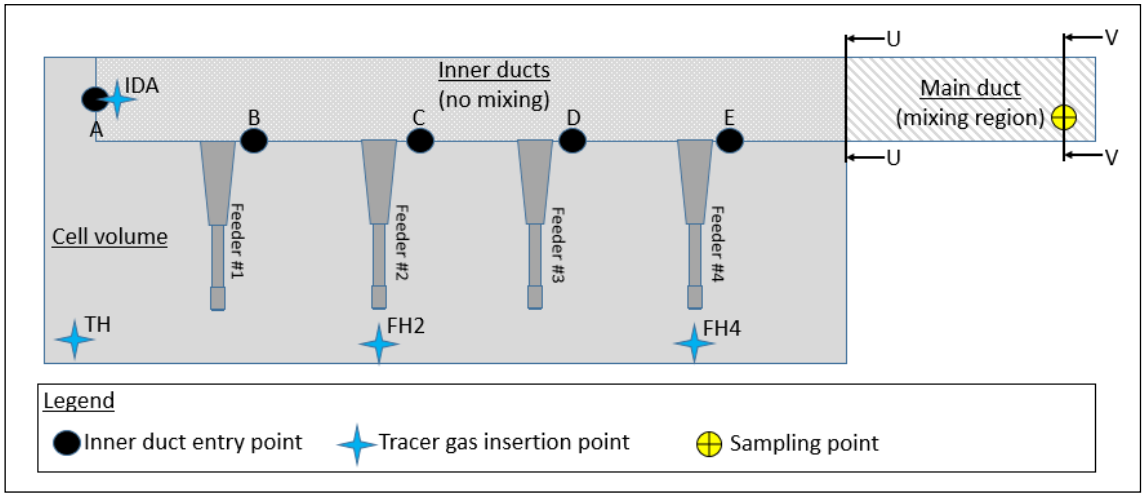

Figure 5-1: Sketch of the gas collection within the test.

5.3.2 **Test methodology**

One of the main objectives of this paper is to determine if the location of the gas generation site has an impact on the concentration measurements. Henceforth, four different locations were selected to inject the tracer gas[15]. Point 1 was selected as a reference directly inside the duct to minimize the dispersion of the gas within the inner volume of the cell as well as the changes that could be attributed to airflow going into different directions within the cell volume. The three other points were selected at different distance from the duct end of the cell considering that under ideal conditions, the gas produced by the cells usually escapes either by the tapping hole or by one of the feeder holes:

1. Directly inside the gas inner duct A (see Figure 5-1). (IDA)
2. Directly above the tapping hole. (TH)
3. Directly above feeder hole #2. (FH2)
4. Directly above feeder hole #4. (FH4)

A procedure was established during the experiments to avoid perturbations of the hooding conditions in the area next to the insertion of the tracer gas.

For each position, different hooding conditions were examined to evaluate their impact on the measured concentration of gas. Seven different scenarios were selected for this study. The scenario of reference (REF) represents ideal hooding conditions where all hoods are correctly positioned to ensure optimal sealing. Part of the other scenarios is based on two of the most frequent operations on an electrolysis cell, namely metal tapping and anode change. When metal tapping is performed, the door located on the side opposite to

[15] Release of the tracer gas was performed instantaneously by the rupture of the latex balloons

the duct end is open to allow access to the liquid aluminium via the tapping hole (TD). For an anode change, part of the hooding (about 8 %) is removed to allow access to the anode that needs to be replaced. Because we studied the effect of the position of the tracer injection in this study, we investigated three different positions where the anode change could occur; anode #11 on the tapping end (A11), anode #15 near the middle of the cell (A15) and anode #20 at the duct end of the cell (A20). Finally, two worst case scenarios were also investigated, representing a very unlikely event when 25 % of the hooding was removed from the cell. In one case (WC1), all hoods, on the half of one side of the cells were removed, leaving a significant opening next to the duct end. In the other case (WC2), one quarter of the hoods was removed uniformly across the cell. Figure 5-2 illustrates these different scenarios.

1. Perfect hooding conditions (REF)
2. Tapping door open (TD)
3. Anode change conditions at anode #11 (A11)
4. Anode change conditions at anode #15 (A15)
5. Anode change conditions at anode #20 (A20)
6. Worst case scenario #1, 25 % open next to each other (WC1)
7. Worst case scenario #2, 25 % open uniformly (WC2)

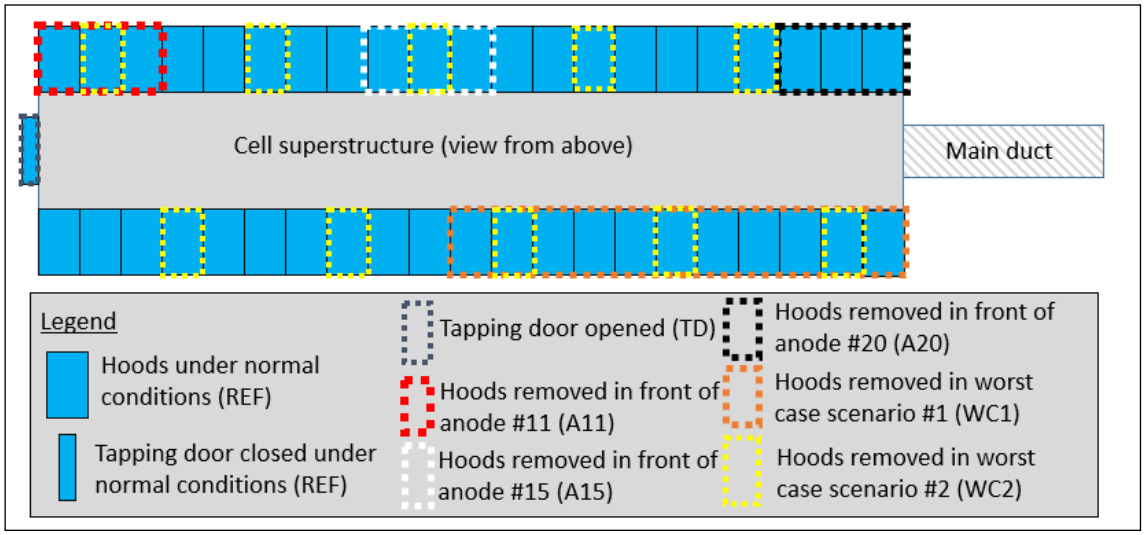

Figure 5-2: Top view of the cell showing all seven scenarios investigated.

5.3.3 **Tracer gas**

Tetrafluoromethane (CF_4) was chosen as the tracer for this study because it is the primary gas of interest related to LVAE. Another type of gas (for example sulfur hexafluoride) could have influenced the results differently due to the density of the gas, which is significantly different, i.e. 3.72 kg/m^3 and 6.17 kg/m^3 respectively.

A tank of CF_4 was obtained with a certified concentration of 1000 ppm diluted in nitrogen. A fixed quantity (8 liters) of gas was injected into the cell (Figure 5-3) using two latex balloons placed at a specific position within the cell according to the methodology presented previously. Each balloon was filled individually directly from the reference tank with a flow rate of 4 L/min (measured with a rotameter) for 1 minute.

Figure 5-3: Injection of the tracer gas during test #A11-TH.

To evaluate the repeatability of the balloon volumes, ten balloons were filled up using the same procedures. Then their content was sent through the FTIR with a specific flow rate of 2 L/min to allow calculation of the mass of CF_4 within each balloon. Individual results for each balloon tested are illustrated in Figure 5-4. It indicates that the average mass of CF_4 for each balloon was 15.4 mg ± 5.4 %. The theoretical mass of CF_4 for 4 liters of gas at 1000 ppm is 14.88 mg, indicating a good correspondence with the measurements.

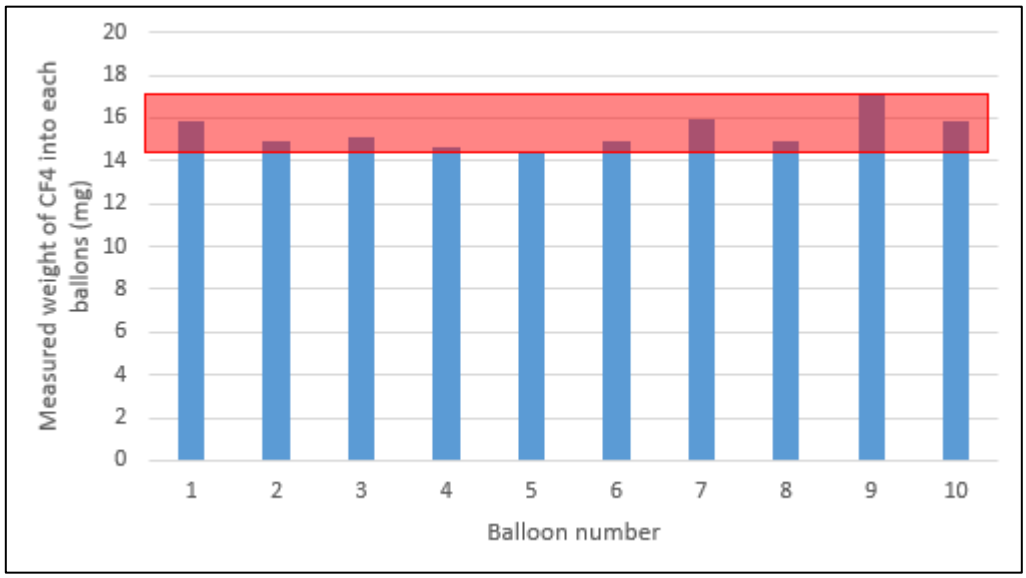

Figure 5-4: Repeatability of individual balloons fill-up.

For each combination of scenarios and positions, a minimum of three gas injections were performed to verify the repeatability of the results. Additionally, the CF_4 concentration was steadily monitored before each injection to make sure that no traces of CF_4 either from a previous test or from the cell itself were present before the test. Figure 5-5 shows a preliminary measurement sequence. It is relatively easy to notice that the baseline starts to increase after the first part of the test because of CF_4 actually produced by the cell. For this reason, this actual test was not included in the final results due to the presence of LVAE.

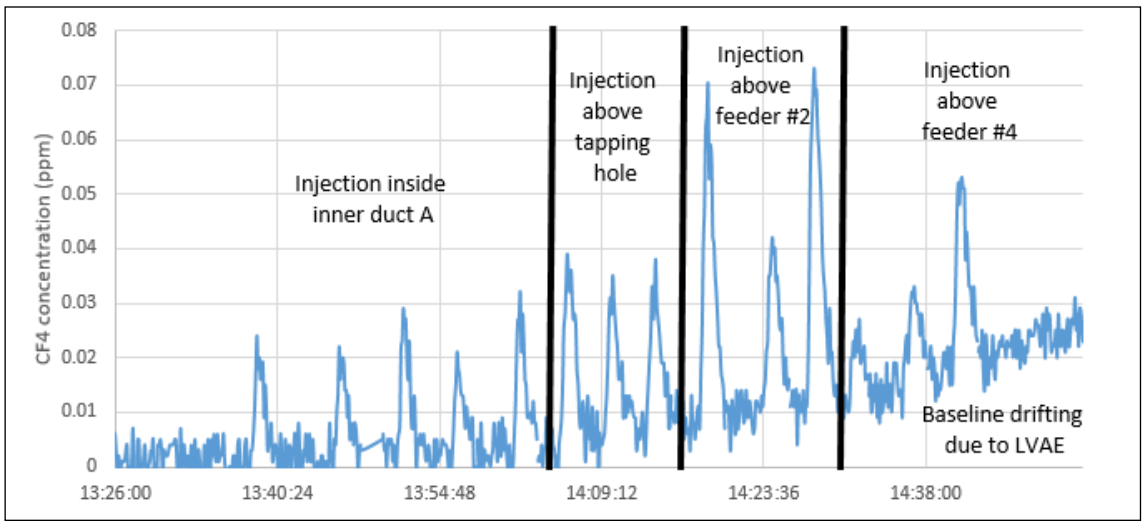

Figure 5-5: Example of a test sequence with the presence of LVAE emissions.

Dando and al. [8] mentioned that emissions of CF_4 coming from adjacent cells represent a possible error source when measuring CF_4 emissions of a given cell. For this reason, a supplementary test has been performed using tracer gas to find out if this phenomenon has a significant impact on gas emission measurements. The details of this test are described and discussed in Section 5.4.4.

5.3.4 **Additional measurements**

In addition to the continuous monitoring of the gas concentration, two other types of measurements were performed to calculate accurately the gas flow in the duct during the experimentations.

For each of the seven scenarios, the flow rate was measured within the duct of the cell using a pitot tube[16]. The measurement was performed prior to each scenario once the hooding conditions were settled as required.

The temperature of the gas was measured inside the duct from both sides before each test (under optimal hooding conditions) and each time when tracer gas was injected into the cell for a test.

With this information, it was possible to consider the influence of the temperature on the volumetric flow rate. It allows for a more accurate calculation of the mass of CF_4 that passed through the duct end of the cell using the FTIR measured concentration for each test.

5.4 Results and Discussion

5.4.1 Elements to consider to correctly interpret the results

Before presenting the experimental results, it is important to understand that various factors can have a significant influence on the detected concentration of CF_4:

The tracer gas injected in the cell should dissipate within the cell volume as more than 2000 liters of gas is passing through the duct end every second. For this reason, the residence time of the tracer gas inside the cell will affect the measured concentrations of the emissions. However, as long as the concentration remains above 10 ppb, it has little to no effect on the total mass calculation as it depends on the integration of the area under the detected evolution of the concentration curve. However, if the tracer gas is not passing

[16] Evaluation of the duct flow rate was performed using the standard practice from Aluminerie Alouette. It involves 20 different measurement points following a traverse “X pattern”.

through the duct end quickly enough, the concentration of CF_4 will fall below the limit of detection of the FTIR and it will be impossible to account correctly for this part of the tracer gas.

As mentioned previously, the gas is transported up to the duct end by five independent inner ducts. Each duct was designed with different sections to compensate for their different lengths in favor of a uniform gas collection from the various areas. Assuming that the design is correct under ideal hooding conditions, the flow rate in each duct should be similar. However, under modified hooding conditions, the concentration of CF_4 within each internal duct should be different. Figure 5-6 shows a superposition of the two sections of the duct end. Section U (rectangularly shaped) illustrates the structure of the inner ducts before the mixing of the gas. Section V (circularly shaped) is located approximately 0.92 m after section U and illustrates the point where the gas samples are extracted and where the temperature is measured. It is plausible to assume that the mixing of the gas from five different sources is not complete after such a short distance, hence it is possible that the gas collected by the probe does not represent the overall concentration of the main duct but rather a concentration influenced by the inner gas concentration coming from the nearest inner duct (A, B and D). Under perfect mixing conditions, the total flow rate going through the sampling probe should be the evenly divided between each of the five inner ducts, i.e. one fifth of the total flow is coming from each inner duct. However, this is not necessarily the case during our experiments.

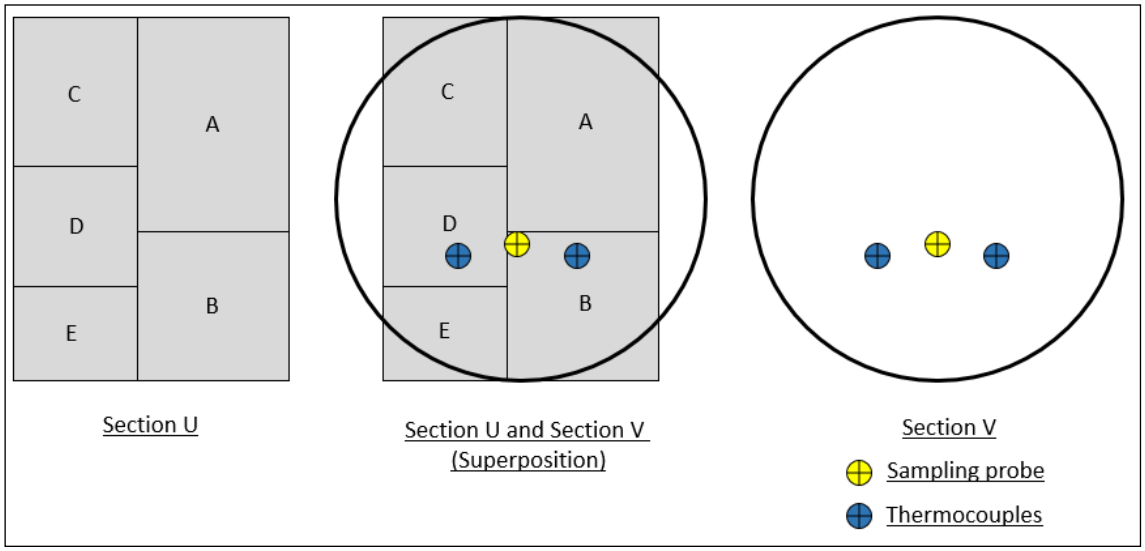

Figure 5-6: Superposition of two sections of the duct end.

In addition to the previous point, it is necessary to consider the fact that for some cases in our study, some hoods were removed to establish different conditions than what the inner ducts were designed for. Hence, it is plausible that the uniformity among those inner ducts was disrupted, allowing for different flow rates originated from different regions of the cells. Additionally, an accumulation of dust in the inner ducts during the years of operation of the cell could generate a similar effect.

5.4.2 **Influence of the Tracer Gas Injection Point**

Figure 5-7 illustrates that there are significant variations of the measured gas concentration with the different hooding scenarios and tracer injection locations. However, when examined carefully, there are several tendencies that can be clearly observed.

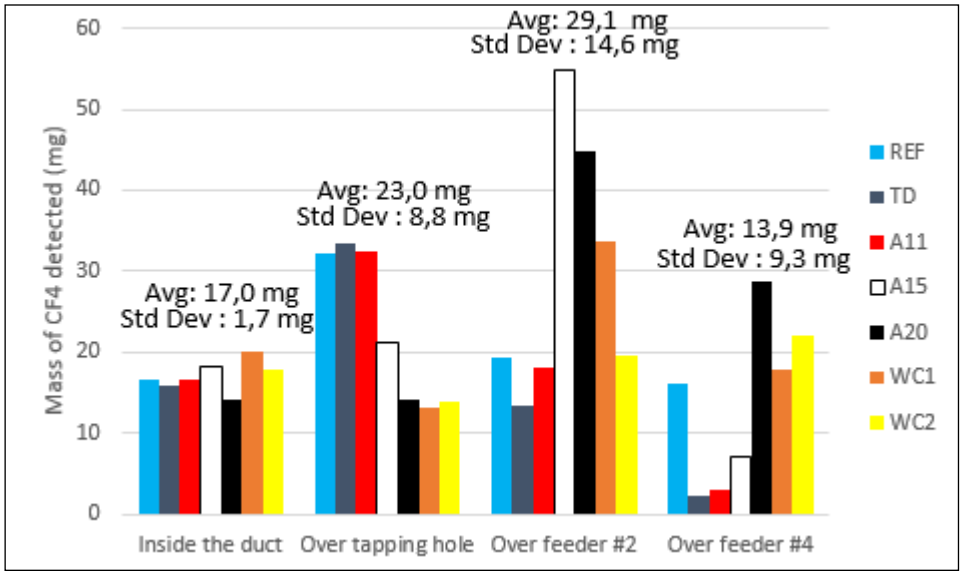

Figure 5-7: Average mass of CF_4 detected for all scenarios investigated.

The experimental results were obtained by tracer gas injections which simulates localized gas emissions during normal cell operations. Figure 5-7 demonstrates that the position of the emission will have a significant impact on the results. The impact of the hooding conditions will be investigated later in this chapter, in Section 5.4.3.

The total mass of CF_4 measured when the tracer gas was injected into the duct is relatively constant in comparison to other results (standard deviation between different perturbation cases of only 10 %). This result was expected due to the fact that the injected gas is hardly influenced by the airflow within the cell volume, limiting the possibility of the tracer to divide itself among multiple inner ducts. Hence, the effect of the hooding conditions is negligible on those results. Therefore, all of the injected gas remains inside the inner duct “A” and is transported to the region where the sampling probe collects the gas for analysis. The fact that the average mass is 17.0 mg indicates that a little more than

half of the injected mass of CF_4 is detected, therefore one can assume that approximately $1/10^{th}$ of the gas collected by the sampling probe comes from the inner duct A.

The measured average mass of CF_4 increased when the tracer gas was injected above the tapping hole. This position is in a similar distance from the sampling point as the inner duct entry point but well below it, closer to the crust. For this reason, the tracer gas can dissipate within the cell volume and the most significant part of the tracer probably goes through the inner ducts A and B. Consequently, as the tracer passes through multiple inner ducts, it is more likely to be distributed more uniformly that results in a scenario closer to the reality. However, it can be concluded that when the gas goes through a higher number of inner ducts, the effect of hooding conditions becomes more apparent and the variation of detected CF_4 mass increases accordingly.

The results obtained with the injection above feeder #2 are in good agreement with the previous statements. When the tracer gas is inserted close to the middle of the cell, multiple paths are available for the gas depending on the airflow conditions inside the inner volume of the cell. Therefore, the gas can be transported through additional inner ducts, increasing the probabilities of collecting a more accurate measurement. Hence, the measured average mass of CF_4 increased and is very close to the real mass injected (94 %). However, the variation of mass with hooding condition is even more important than that observed previously.

Once again, when the tracer gas is injected above the feeder #4, the observations correlate with the previous cases. Due to the proximity of the duct end of the cell, the tracer gas will most likely pass through a single inner duct (E). Hence, the average mass of CF_4 is

in the same order of magnitude as the first position (tracer directly injected in inner duct A). On the other hand, as it is affected by the airflow in the inner volume of the cell under the hood, the variation of the detected tracer mass will be more important.

5.4.3 **Influence of the hooding conditions**

As presented in Section 5.3.2, the different hooding conditions investigated can be classified into 4 different categories:

- Hooding conditions during tapping of metal,
- Hooding conditions during an anode change,
- Hooding conditions when an important opening is present (1/4 of the cell),
- Hooding conditions with uniformly distributed poor hooding conditions. (1 hood out of 4 removed).

The first two scenarios show a very similar impact on the detected mass. In fact, Figure 5-8 clearly demonstrates that the mass of CF_4 detected for each case is more important when there is an opening in the hooding close to the injection point. The maximums have been always reached under such circumstances; tapping doors and anode #11 for injections above the tapping hole, anode 15 for injections above feeder #2 and anode #20 for insertion above feeder #4, respectively. This behavior is caused by an increased pressure gradient in the area in the presence of an opening in the hoods, resulting in an increased airflow from the same area. This increased flow rate generates a non-uniform distribution of the airflow among the five inner ducts. Henceforth, the gas extracted with the sampling probe will more accurately represent the composition of the inner ducts closer to the opening. Furthermore, it explains why in some cases (Feeder #2 / A15 and A20), the measured mass of CF_4 is significantly higher than what was really

injected with the balloons. It also explains the opposite behavior observed for feeder #4 / TD and A11. As the injection point of the gas was really far from the favored inner duct (A), the tracer gas was less rapidly transported to the main duct, resulting in a stronger dilution. The CF_4 concentration in the gas was then very close to the lower limit of detection of the FTIR, giving a mass of CF_4 almost negligible in comparison to what was really injected into the cell.

Investigation of the worst-case scenario #1 will not be discussed in detail. The results show a similar behavior to what was previously discussed regarding scenarios A11, A15 and A20. That is to say, the mass measured increases if the tracer gas passes through multiple inner ducts. This correlation is even stronger if there is an opening in the hooding near the injection point of the gas.

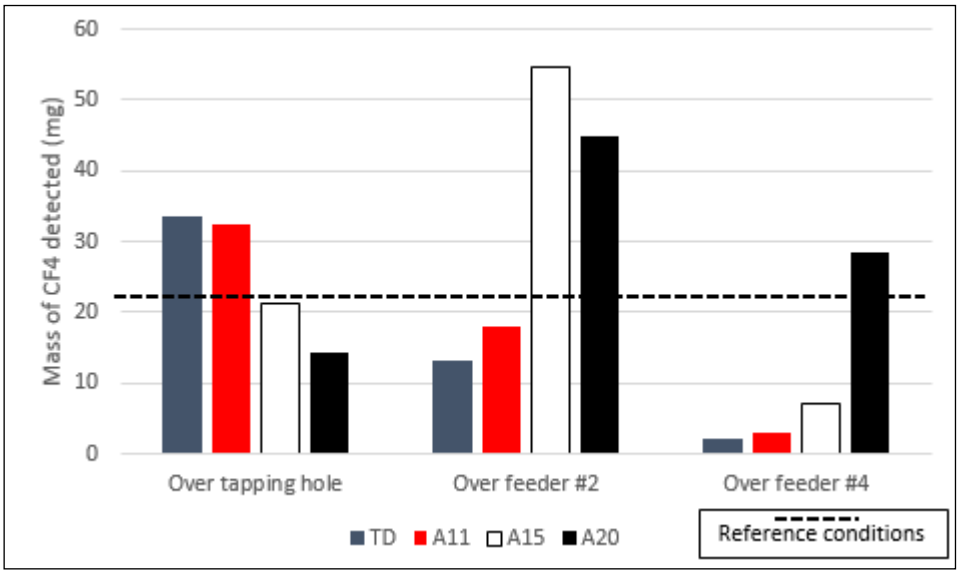

Figure 5-8: Influence of hooding conditions during routine operations. (TD = Tapping doors open / A11, A15 and A20 represent hoods opened similar to an anode change of each respective anode number / dashed line represents the reference average under perfect hooding conditions).

The last scenario to discuss represents the worst-case scenario #2 (WC2) where 25 % of the hoods are removed, uniformly across the cell. The investigation indicates that significant perturbation occurs in the airflow of the main duct under such circumstances, leading to less accurate composition measurement. This behavior is more apparent when following the concentration of carbon monoxide released by the cell (illustrated in Figure 5-9). Emissions of CO in the cells are mostly related to anode oxidation and reoxidation of the aluminium. Both phenomena will generally occur around specific anodes, which offer proper conditions for these reactions (bad anode covering, lower anode-to-cathode distance (ACD), increased liquid movement, etc.). For this reason, the concentration of CO should vary among the inner ducts. Hence, the mixing of the gas within the main duct will have a great influence on the CO concentration of the overall gas emitted. Consequently, it is possible to correlate the erratic behavior observed in Figure 5-9 with perturbations in the mixing conditions within the main duct. Thus, when multiple hoods are misplaced on the cell, increased perturbations in the gas movement will lead to inaccurate measurements of a localized phenomenon. The amplitude of the fluctuations did not change significantly but the shape is clearly different. Hence it will necessarily affect measurements that are influenced by time, which is the case in our study.

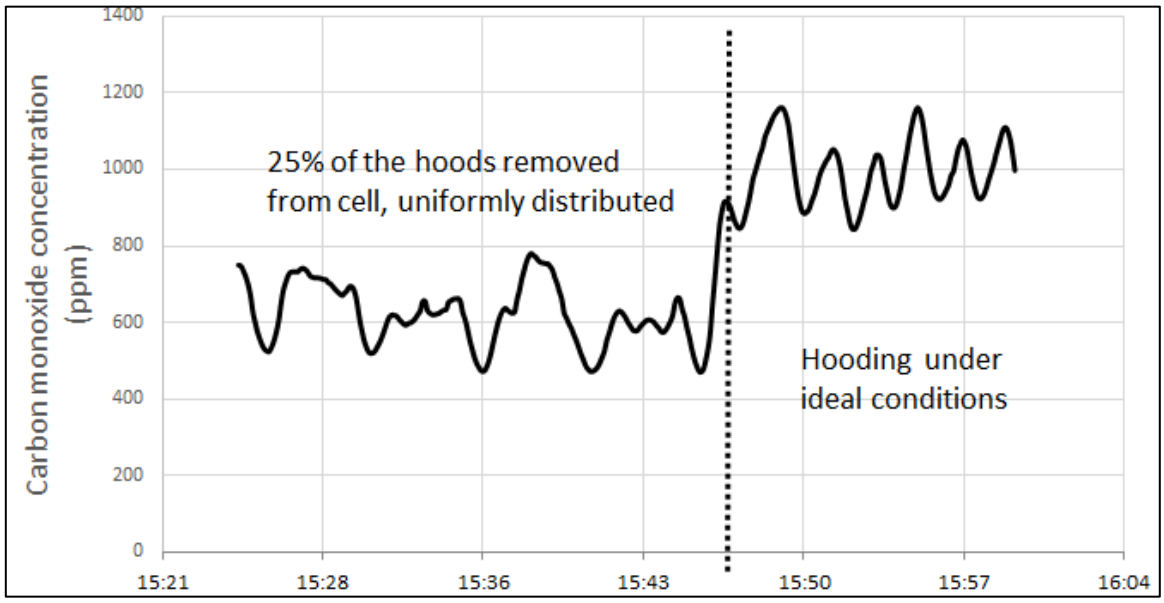

Figure 5-9: Carbon monoxide emissions under different hooding conditions.

Another phenomenon that can be observed in Figure 5-9 is a diminution of the measured concentration of the gas. Under ideal conditions, the concentration of CO coming out of the cell is close to 1000 ppm but when some hoods are misplaced, the analysis of the gas composition shows a drop of approximately 30 % in the measured average concentration of carbon monoxide. However, this observation is less likely to apply to CF_4 measurements.[17] The reason for this statement is that there is a significant difference between the densities of the two gasses at 15 °C and 1 atm. CO has a density of 1.14 kg/m^3 while the density of CF_4 is 3.72 kg/m^3 [9]. Therefore, the CF_4 is more likely to stay within the cell and follow the airflow towards the inner ducts under the effect of the pressure gradient. On the other hand, due to a smaller density then air, CO will tend to rise and leave the cell where there are no physical barriers (hoods) that restrain its movement.

[17] Precisions on the discussion regarding this phenomenon is available in Appendix D, bullet #11.

5.4.4 **Other Results of Interest**

An additional test was performed to evaluate if the conclusions published by Dando et al. [8] could apply to the cell technology used in the present study. During their work they detected PFC emissions coming from adjacent cells. It is mentioned that an excess of PFC gas was released by the cells during the start-up due to the initial long anode effect. Because CF_4 has a greater density than air, this gas would remain at pot level and could be transported to adjacent cells. However, the pot room configuration in this study is different from theirs and the hooding conditions are not necessarily similar.

In this study, sulfur hexafluoride (SF_6) was manually injected onto the cell proximity, above the hoods from an adjacent cell to reproduce the effect of the gas coming out from this adjacent cell. For both cells, the hooding conditions were kept ideal and 63.63 grams of SF_6 was used for this test, divided evenly between 7 locations (9.09 g per locations) illustrated in Figure 5-10. This represents the total mass of CF_4 that is normally produced during an above average anode effect.

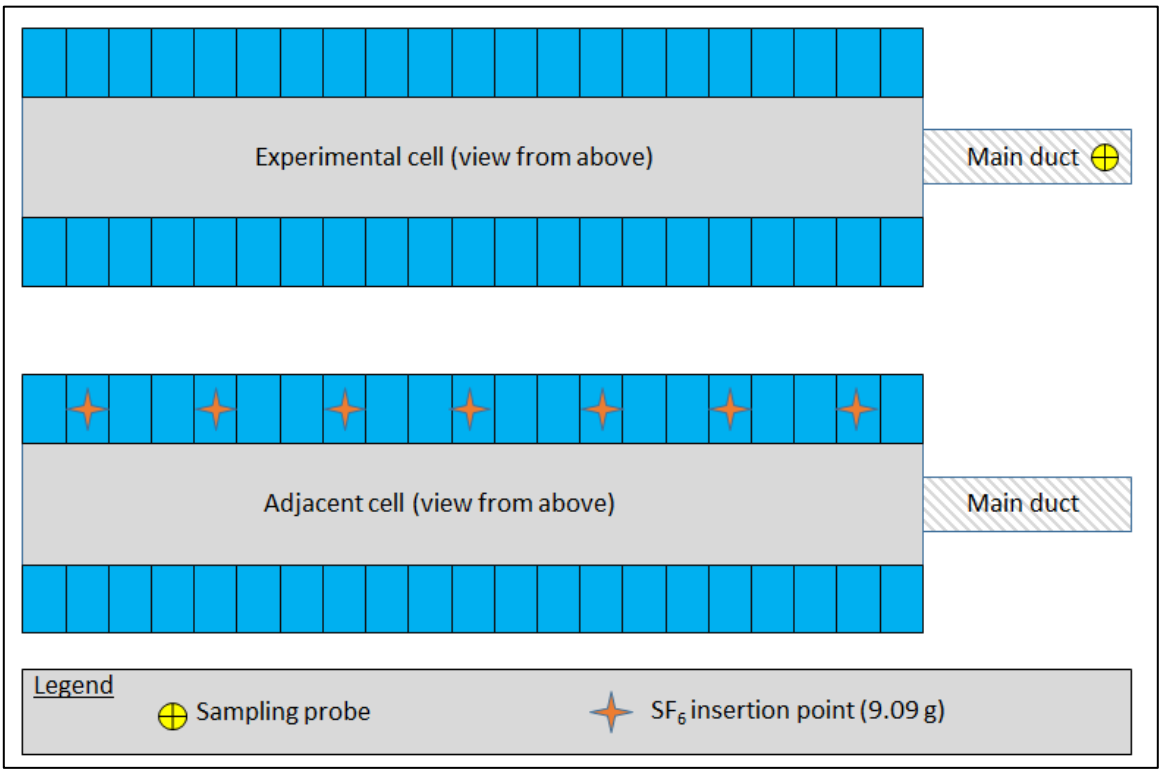

Figure 5-10: Possible contamination test coming from an adjacent cell.

The SF_6 concentration in the main duct of the experimental cell was closely monitored during the test but no traces of SF_6 higher than the noise level could be observed. This indicates that for the cell technology used in this study, the gas collection system appears strong enough to collect the gas in the cell volume as well as in an adjacent area outside its enclosure. For this reason, the collection system from the adjacent cell collected all of the SF_6 and no trace of this component was detected in the experimental cell. Hence the risk of contamination from an adjacent cell is negligible when the hooding conditions are close to ideal.

5.5 Conclusions

This paper investigated the accuracy of composition analysis performed on gas sampled directly at the duct end of an electrolysis cell. The methodology involved injecting a known tracer gas under multiple sets of conditions. The results indicate that the injection site of the tracer gas influenced significantly the detected mass of CF_4 collected in the main duct. There is a direct relation between the accuracy of the measurement and the number of inner ducts among which the tracer gas is distributed. Henceforth, it adds significant doubts regarding the accuracy of localized measurements occurring during LVAE, but the effect becomes negligible if the distribution of PFC is uniform across the entire cell volume.

Similarly, the hooding conditions affect the individual flow rate of each inner duct, changing the resulting concentration of gas collected with the sampling probe. The results clearly demonstrate that tracer gas emissions were more accurately detected when injected close to an opening in the hooding, indicating an increased airflow in that region of the cell. Additionally, very poor hooding conditions will generate significant perturbations in the airflow, leading to inaccurate results due to an inadequate mixing of the gas and extensive dilution.

Finally, this paper clearly demonstrated that measurements of the composition of gas extracted at the duct end of an electrolysis cell could be adequate for qualitative studies. However, the accuracy of such a method is influenced by too many factors and is inadequate for quantitative measurements of localized emissions. Refinements are required to investigate such phenomenon. Such refinements could include a change in the structure

of the main duct to ensure an adequate mixing of the gas coming from the five inner ducts before it is extracted and sent to an FTIR for analysis.

5.6 Additional content not presented in the original article

5.6.1 Proposition of a new sampling methodology

Based on the conclusions from Chapter 5, a new setup was designed to extract gas from the electrolysis cell in a proper way so that the measured gas composition can be representative of the entire cell's behavior. As described previously, the main problem while extracting the gas is related to the five independent inner ducts which represent different regions of the cells. The most simple solution would be to extract the gas further down the duct if appropriate mixing can be achieved. However, instead of using a single sampling probe collecting badly mixed gas, it is proposed to directly collect the gas simultaneously in each respective inner duct, using five different sampling probes.

Assuming that under ideal hooding conditions, the volumetric flow rate is equal in each inner duct, the new sampling methodology proposed to connect these 5 sampling probes to a respective rotameter in order to maintain a uniform flow rate during extraction of the gas as illustrated on Figure 5-11. In this case, a flow rate of 1 LPM was used to obtain a total flow rate of 5 LPM routed to the FTIR spectrometer. The collected gas flow went through a 5-micron Swagelok filter before reaching their respective rotameter to prevent damage that could be caused by the dust.

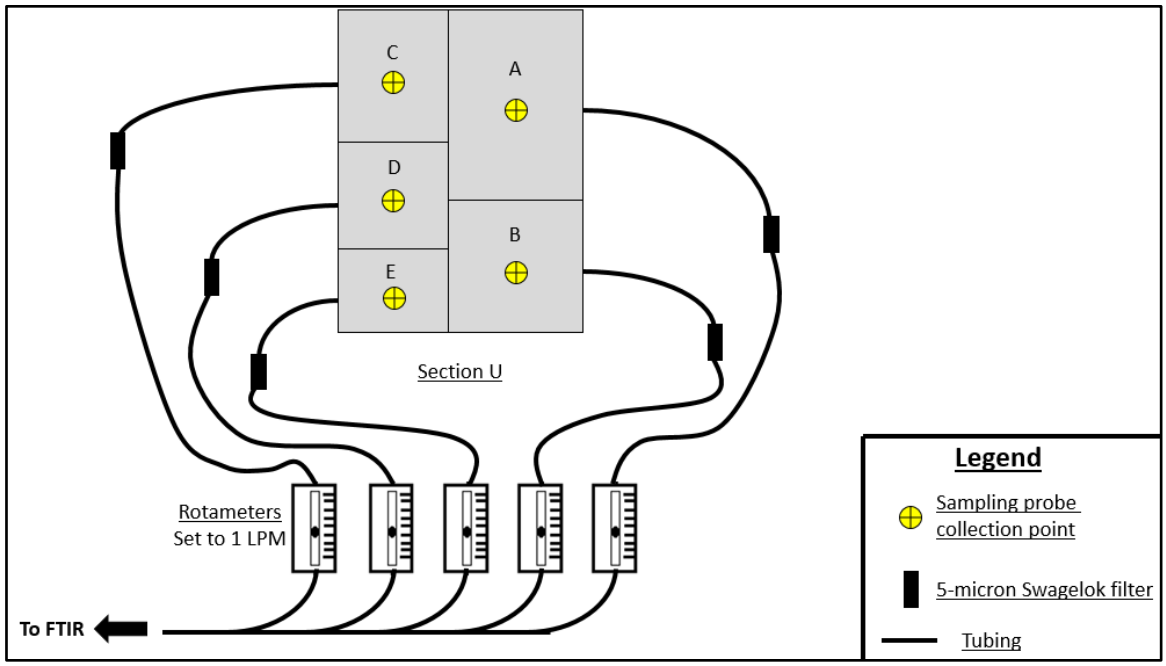

Figure 5-11: Schematic of the new gas sampling methodology with 5 sampling probes

5.6.2 **Experimental setup**

To evaluate if this new sampling methodology is representative of the overall cell behaviour, the same test as previously presented in section 5.3 was performed. A constant amount of CF_4 (30.8 mg ± 10.8%) was injected in the cell in specific positions and compared to the respective mass of CF_4 detected by FTIR measurements. The test was only performed under ideal hooding conditions, and due to time limitations at the smelter, only 3 different positions were evaluated (Inside inner duct A, over feeder #2 and over feeder #4). Part of the experimental setup is illustrated on Figure 5-12 while Figure 5-13 demonstrates the similarity of the flow rate between each individual rotameter.

Figure 5-12: New and improved gas collection methodology

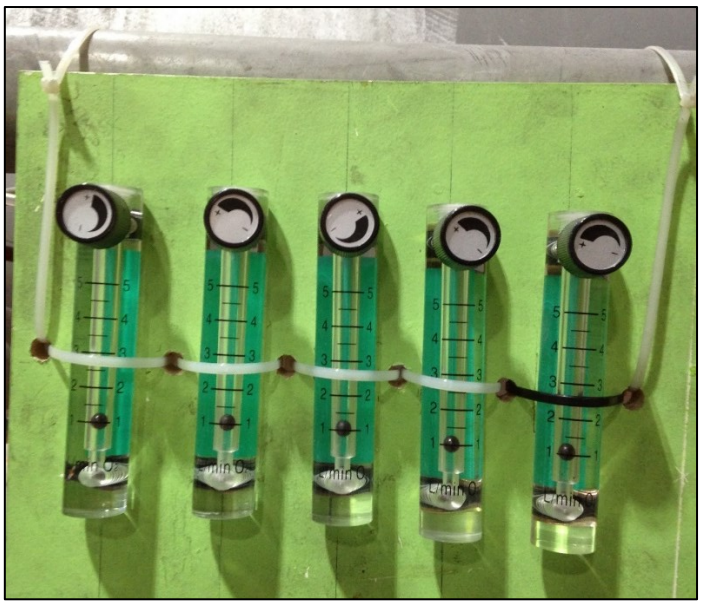

Figure 5-13: Flowmeters for the five sampling probes during testing.

5.6.3 Experimental results

The results are compared in Figure 5-14 to original measurements collected during a previous campaign using the original sampling method with a single probe.

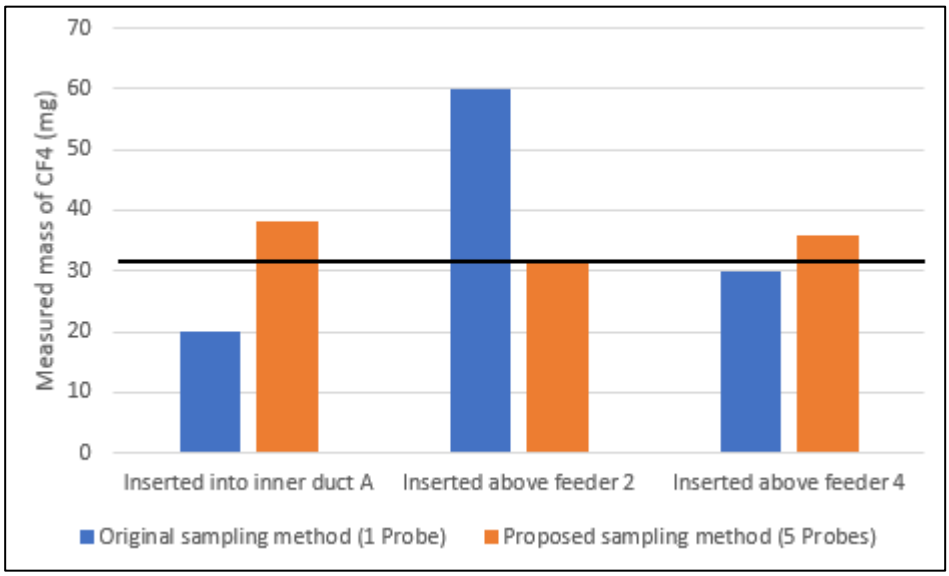

Figure 5-14: Difference in accuracy between the original and the improved sampling methods. (Horizontal lines represent the inserted mass of CF_4)

The results demonstrate that the proposed methodology can significantly improve the accuracy of on-line gas monitoring on individual cells in the cases where access to an adequate collection point is impossible (insufficient mixing). With the original methodology, the average error for all positions was 14 mg. This average error has been reduced to 4.5 mg with the newly proposed sampling method, thus demonstrating an error reduction of approximately 67%.

Additional testing is recommended to correctly evaluate the robustness of the setup and assess if the additional cost, and complexity of this setup is worth the additional gain in accuracy. It is the author's opinion that this methodology should be used when studying localized phenomenon in the cells such as low-voltage anode effects, and especially when

the precision of quantitative measurement is critical for the outcome of the study. Finally, to optimize the methodology, it is recommended to use filters with a bigger strainer size (50-60 microns) to minimize the risk of rapid obstruction that can happen due to dust accumulation. Additionally, for higher precision, the range of the selected rotameter should adequately reflect the purpose of the study (low flow rate for slow-changing phenomena and higher flow rate for quick changing phenomena) without going outside the flow rate limits of the measuring equipment.

5.7 References

1. Lukas Dion, *Bilan de matière dynamique pour une aluminerie*, M. Eng. Thesis, Département des sciences appliquées, 2014, Université du Québec à Chicoutimi, Chicoutimi, Canada. p. 116.

2. Lukas Dion, et al., Using artificial neural network to predict low voltage anode effect PFCs at the duct end of an electrolysis cell. in *Light Metals*. 2016, 545-550.

3. Lukas Dion et al., Prediction of low voltage tetrafluoromethane emissions based on the operating conditions of an aluminium electrolysis cell, *JOM,* (2016), Vol 68, Issue 9 (to be published).

4. Li Wangxing et al., On continuous PFC generation unrelated to anode effects, *Light Metals*, 2011, 309-314.

5. Xiping Chen et al., Investigation on formation mechanism of non-anode effect related PFC emissions from aluminium reduction cells, *Light Metals*, 2013, 877-881.

6. David S. Wong, and Jerry Marks, Continuous PFC emissions measured on individual 400 kA cells, *Light Metals*, 2013, 865-870.

7. Eliezer Batista et al., Sustainable reduction of anode effect and low voltage PFC emissions, in *Light Metals*, 2016, 537-540.

8. Neal R. Dando et al., Non anode effects PFC : Measurement consideration and potential impact, *Light Metals*, 2015, 551-555.

9. Air_Liquide, *Gas Encyclopedia*, 2013 [cited 2016 07-19]; Available from: http://encyclopedia.airliquide.com/Encyclopedia.asp?

CHAPTER 6

SIMULATOR OF NON-HOMOGENEOUS ALUMINA AND CURRENT DISTRIBUTION IN AN ALUMINIUM ELECTROLYSIS CELL TO PREDICT LOW VOLTAGE ANODE EFFECTS

6.1 Summary

The content of this section was published in April 2018 by the journal *Metallurgical and Materials Transactions B* in volume 49, issue #2. Its DOI number is : 10.1007/s11663-018-1174-2.

The information presented in this chapter was written by the author of this manuscript with comments and suggestions provided by the three additional co-authors: Laszlo I. Kiss, Sandor Poncsak and Charles-Luc Lagacé. The theoretical principles considered in the mathematical model presented are the results of a narrow collaboration between the PhD student, the thesis director and co-director. However, the coding was performed entirely by the student in the course of this project.

6.2 Introduction

Primary aluminium production contributes significantly to greenhouse gases (GHG) emissions due to the production of carbon dioxide (CO_2), inherent to the chemical reactions occurring in the electrolysis cells using carbon anodes. However, the aluminium industry is also known as one of the two most important anthropogenic emitters of perfluorocarbons (PFC) along with the semiconductor industry. These types of gas, namely the tetrafluoromethane (CF_4) and the hexafluoroethane (C_2F_6), are known to be produced when the cell's current distribution diverges from the normal operating range due to the lack of alumina in the electrolyte, thus leading to a harmful event called anode effect.

In the 1990s, many researchers [1-4] demonstrated that a relationship exists between the polarized anode effect duration and the amount of PFC gas generated during the occurrence of the anode effect. However, such relation is consistent with a specific type of

anode effects which perturbs strongly the cell behavior by significantly increasing the global cell voltage above the normal operation level, thus generating important amounts of heat while increasing the level of cell instability. Since the cell voltage is a well-followed indicator, such events can be easily detected by the cell control system and are classified as high voltage anode effect (HVAE). However, recent studies (early 2010s) [5-10] demonstrated that PFC emissions can also be generated locally by similar mechanisms under only a few number of anodes. Redistribution of the current might prevent propagation of this phenomenon and only a local increase in resistance is observed with no significant increase in the global cell voltage [11]. Depending on the cell technologies, the annual emissions resulting from low voltage anode effects (LVAE) can be even more important that the emission level resulting from HVAE [12].

Even though LVAE detection is very difficult currently in a fully operating smelter, some key indicators presented in the literature can be used in order to create a simulation tool which could help to improve the electrolysis process while reducing the risk of LVAE. To achieve this goal, a simulator could provide information about the evolution of non-homogeneity of the alumina distribution inside the electrolytic bath as well as information regarding non-uniform current distribution among the anodes.

In this article, the different mathematical sub-models used in the development of this simulator are presented and discussed; focusing on alumina feeding, alumina dissolution, the diffusive and convective transport within the electrolytic bath, alumina consumption by electrolysis, the cell electrical model and LVAE risk assessment. This simulator was validated by comparing the data to four specific experimental scenarios

tested at Aluminerie Alouette. Finally, possible improvements of the process resulting from using this simulator are presented and discussed.

6.3 Generation of PFC During High Voltage and Low Voltage Anode Effects

Anode effects occur in a cell when an insufficient amount of dissolved alumina is present in the bath. When this condition happens, the passage of the electrical current cannot be sustained longer by the normal electrolysis reaction (equation 6-1). Therefore, there is an increase in the anodic overvoltage, leading to the occurrence of secondary reactions within the electrolytic bath (equation 6-2 to 6-4, where E^0 is the decomposition potential).

$$2\ Al_2O_{3(diss)} + 3\ C_{(s)} \rightarrow 4\ Al_{(l)} + 3\ CO_{2(g)} \qquad E^0 = -1.18V \quad (6\text{-}1)$$

$$2\ AlF_{3(diss)} + Al_2O_{3(diss)} + 3\ C_{(s)} \rightarrow 4\ Al_{(l)} + 3\ COF_{2(g)} \qquad E^0 = -1.88V \quad (6\text{-}2)$$

$$4\ Na_3AlF_{6(l)} + 3\ C_{(s)} \rightarrow 4\ Al_{(l)} + 3\ CF_{4(g)} + 12\ NaF_{(diss)} \qquad E^0 = -2.58V \quad (6\text{-}3)$$

$$2\ Na_3AlF_{6(l)} + 2\ C_{(s)} \rightarrow 2\ Al_{(l)} + C_2F_{6(g)} + 6\ NaF_{(diss)} \qquad E^0 = -2.80V \quad (6\text{-}4)$$

As the anodic over-voltage increases, different reactions will be triggered in the cell. Reactions 6-3 and 6-4 are commonly known to be the main reactions generating PFC during HVAE because the cell voltage increases significantly (> 10 volts) and the fluoride-based bath electrolyzes itself in order to maintain the rate of passage of the current. On the other hand, reaction 6-2 is plausibly the main reaction leading to PFC generations during LVAE as the increase in anodic overvoltage is not occurring globally in the cell but rather locally under only a small number of anodes where the local conditions changed due to a

low alumina concentration. However, COF2 is thermodynamically unstable under the electrolysis bath conditions and will rapidly decompose to form CF4 or C2F6 following reactions 6-5 and 6-6, where K is the kinetic of the reactions.

$$2\,COF_{2(g)} + C_{(s)} \rightarrow 2CO_{(g)} + CF_{4(g)} \qquad K= 94.8 \qquad (6\text{-}5)$$

$$3\,COF_{2(g)} + 2C_{(s)} \rightarrow 3CO_{(g)} + C_2F_{6(g)} \qquad K= 1.2 \times 10^{-3} \qquad (6\text{-}6)$$

Several qualitative investigations were performed to determine which events or elements of the cell behavior can lead to LVAE. In agreement with the theoretical assumptions, a low alumina concentration was found to be one of the most important elements that can lead to LVAE [8, 9, 11, 13-17]. However, most of these studies also demonstrated that the current density and the anodic overvoltage were strongly related to LVAE as well [8, 9, 11, 13, 15, 16] due to the interdependence of all these elements. Coherently with these results, the onset of LVAE often appears a short while after an anode change [8, 9, 12, 16, 17] which indicates that the perturbation of the current distribution plays an important role in this phenomenon.

Only a few studies resulted in a quantitative relationship to account for the amount of PFC emitted during LVAE. Using experimental data, Chen et al. [13] demonstrated that an exponential increase of the PFC emitted can be expected when the alumina concentration in the bath is below 2% wt. and more evidently below 1.5% wt. However, as the alumina concentration is rarely measured during normal operations of an electrolysis cell, such a model can hardly be used to quantify PFC emissions resulting from LVAE. To counter this problem, the authors of this article previously developed a complex

multivariate model [18] that uses seven, monitored cell indicators to account for the level of PFC emitted during LVAE. The results of this analysis demonstrated that the dominant cell indicator that can reveal information on the presence of LVAE in the electrolysis cell is the standard deviation among all individual anode currents.

6.4 Development of the Simulator

In order to study or even predict the onset of LVAE, the electrolysis cell cannot be treated as a homogeneous entity, the spatial distribution of the intensive parameters like alumina concentration, electric potential, etc., must be analyzed to correctly assess the impact of changes in its local behavior. Complex CFD based continuum models [19-21] are regularly used to describe the temporal and spatial variations in the alumina concentration of the electrolytic bath. However, such models require a significant computing time and the details and precision exceed the level required for the LVAE study. For this reason, a new methodology is proposed that represents the electrolytic bath as a non-homogenous body with only twenty discrete volumes. Each of these volumes is considered as a lumped system representing the individual anodic assemblies (2 anodes per yoke) with their own specific alumina concentration. In parallel, the overall cell current is divided non-uniformly and distributed among these volumes according to the solution of an electrical model that permits to simulate the respective change in current distribution caused by various elements. Under industrial conditions, the twenty volumes may be different due to different ledge profile across the periphery of the cell. However, in the simulator, the total mass of the electrolyte within each distinct volume is considered to be the same.

The mathematical model is based on the balance equations of the mass of alumina and that of the electric charge with respect to the estimated current efficiency of the cell. Hence, the alumina depletion rate is coupled with the current from each zone to adequately represent the correlation between concentration and current distribution. We did not perform the thermal energy and momentum balance calculations inside our model. Obviously, the bath movement has a very important effect on the alumina distribution, so we used external literature data for imposing an estimated and simplified velocity field. Also for the sake of simplifying the calculations, we assumed a constant average temperature in the bath. Finally, the homogeneity of the predicted individual anode current distribution is also evaluated to predict LVAE emissions.

For each time step, different mathematical models are used sequentially to evaluate the transient variation in the alumina concentration, the current distribution and the risk of LVAE emissions. The seven different modules of the overall model are illustrated in Figure 6-1 and they will be thoroughly discussed in the following sections of this paper. The algorithm and the solver for the simulator and its modules were completely developed and coded by the authors using MATLAB® R2016b (student license).

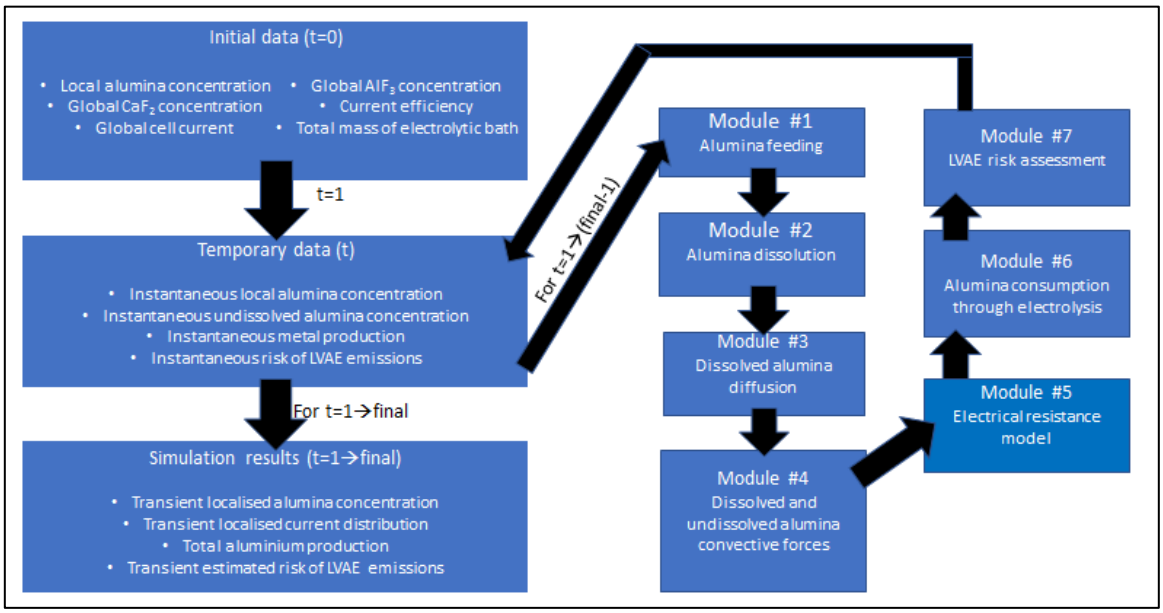

Figure 6-1: Sequential structure of the algorithms used in the simulator

6.4.1 **Input data, initial conditions**

In order to run the simulator and all its modules, initial information such as the cell amperage, the expected current efficiency, the total mass of the electrolyte in the cell and its composition (excess AlF_3 and CaF_2 concentration) are necessary. Additionally, the initial alumina distribution in the cell is required as an initial condition. This distribution is either prescribed according to the scenario that we want to study, or it is based on experimental data.

The mathematical model is based on an explicit method, advancing in time, hence data are extrapolated based on the set of data in the previous time step. As it is well known for such numerical schemes, the time step needs to be adequately chosen to assure the numerical stability of the solution. Equation 6-7 was used to evaluate the time step's maximum value in order to respect numerical stability during two-dimensional diffusion mass transfer. To assure consistency between the numerical results and the phenomenon

simulated, the time step[18] (Δt)[s] has to be smaller than the ratio between the squared distance that separates the volumes considered ($(\Delta x)^2$) [m^2] and the equivalent diffusion coefficient (D_{eq}) [m^2/s] (presented later in this paper) multiplied by a ratio (n)[-] depending on the dimension of the problem. In this case, n is equal to 4 as the study is two-dimensional.

$$\Delta t \leq \frac{(\Delta x)^2}{n \cdot D_{eq}} \qquad (6\text{-}7)$$

6.4.2 **Alumina distribution**

The respective position of each feeder according to the different anodic assemblies is presented in Figure 6-2, along with the different exchange module described in this paper.

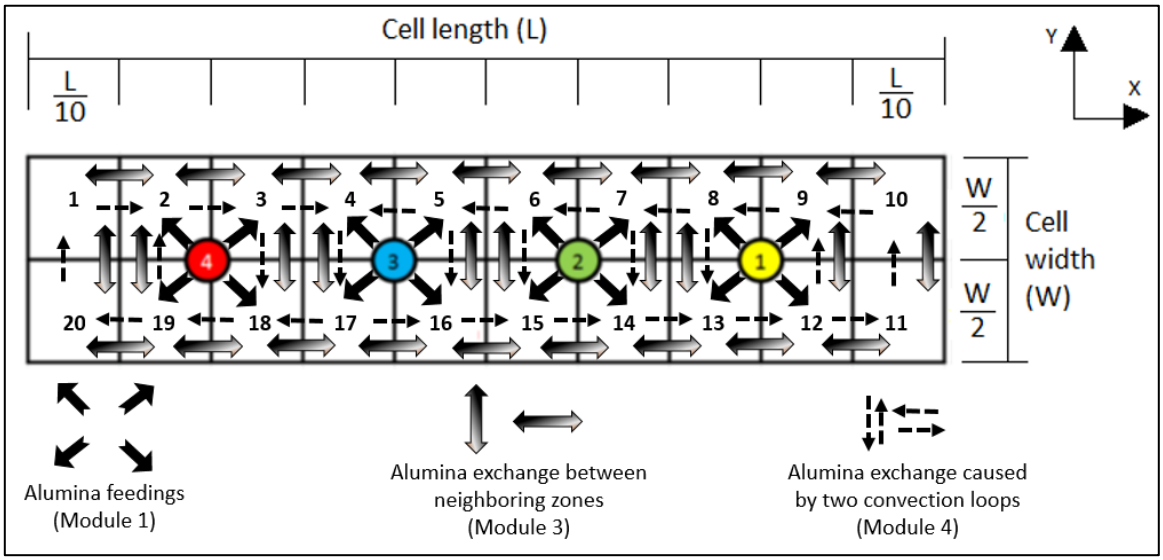

Figure 6-2: Anodic assemblies, alumina feeders' positions and alumina exchange between the different zones.

[18] The choice of a correct time step is discussed in Appendix D, bullet # 12.

6.4.2.1 Alumina feeding (Module 1)

The first module of the simulator takes into consideration any alumina addition injected by the feeders.

The feeding strategy considered is similar to the one of an operating electrolysis cell. For instance, each feeder distributes a constant amount of alumina (approximately 1 kg) with each dose following a specific sequence and a regulated time between the doses according to the desired character of feeding (overfeeding, theoretical feeding, or underfeeding). A dose of alumina is not added to the electrolytic bath as a single shot within a single time step but rather injected over several seconds to correctly represent the reality. Experiments performed by Tessier et al. [22] indicated that a longer drop time will lead to improved cell stability. However, the standard feeder's design has a relatively short drop time of 1.5 seconds [22]. Moreover, in the model, the alumina is divided uniformly into the four regions adjacent to each respective feeder. For example, if 1000 grams of alumina is added by feeder #1 over a period of 10 seconds, the amount of undissolved alumina in sections 8, 9, 12 and 13 would increase by 25 g for every second of the dosage.

The feedings are performed in a specific sequence based on the feeding strategy of an operating cell. At the beginning of the feeding sequence, there is a preliminary period without feeding, then feeder #1 will always be the first one to feed, followed by feeder #3, feeder #2, feeder #4 and it returns to feeder #1 for another cycle. The time between consecutive feedings is uniformly spaced according to the feeding period. Therefore, if the cell's feeding cycle is 60 seconds, then in every 15 seconds one of the four feeders will feed. As an example, a transition from overfeeding to underfeeding is presented in Figure

6-3. In rare cases, it is possible that the same feeder is activated twice in a row, which explains the need for the preliminary period without feeding to avoid overlapping of two doses.

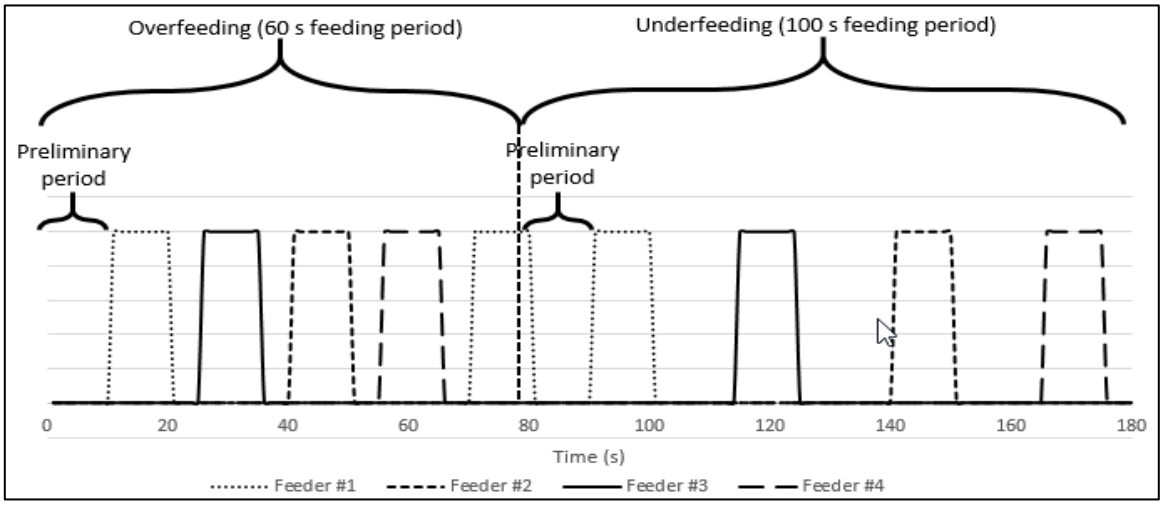

Figure 6-3: Illustration of the feeding sequence during a change in the feeding cycle.

6.4.2.2 Alumina Dissolution (Module 2)

Within each of the twenty discrete volumes, the alumina can be present in two distinct states: undissolved or dissolved. This module was developed to represent the mechanism that allows the alumina to go from undissolved state to the dissolved state accurately.

In each distinct region, the total amount of undissolved alumina is considered as a single alumina clump no matter the original provenance of the alumina (direct injection during feeding, convective currents, etc.). This clump of alumina is considered spherical[19] and the radius of the sphere is calculated based on the volume of a sphere which englobes the overall weight of alumina with its bulk density of 1 g/cm^3.

[19] The choice of a sphere geometry is discussed in Appendix D, bullet #13.

Then, the alumina dissolution rate is calculated in each region for every time step based on Equation 6-8. Where (dm/dt) [kg/s] is the dissolution rate of the alumina, (K_m) [m/s] is the dissolution coefficient, (A) [m^2] is the area of the undissolved alumina exposed to the bath, (C_s) [kg /m^3] is the saturation concentration[20] of alumina in the bath calculated using the formula (eq. 6-9) developed by Skybakmoen et al. [23], where (C_s) is in [wt. %]. This formula is based on the bath temperature (*T)* [°C] and two coefficients (α and β) which are dependent on the different additive's concentration in the bath. Finally, (C) [kg/m^3] is the bulk concentration of alumina in the region surrounding the undissolved alumina clump.

$$\frac{dm}{dt} = -K_m \cdot A \cdot [C_s - C] \qquad (6\text{-}8)$$

$$C_s = e^{[\alpha+\beta\cdot\left(\frac{1000}{T}-1\right)]} \qquad (6\text{-}9)$$

The dissolution coefficient has been defined based on results from the literature. By considering the dissolution curves published by Zhan et al. [20], Wang [24] and Welch and Kuschel [25], it was possible to approximate the dissolution coefficient (presented in Table I) from these studies for various types of alumina. In the simulator, the mean value for all these five scenarios was used[21]. However, this dissolution coefficient is only an approximation of the real conditions and increased accuracy could be obtained by determining a dissolution coefficient specific for the technology. Moreover, K_m should be re-evaluated if important changes are expected regarding the alumina properties such as the particle size distribution and shape or the raw content of alpha and gamma alumina, which

[20] Before using the C_S calculated from eq. 6-9, the value is converted in the simulator from wt % to kg/m^3 to assure consistency between units.

[21] Additional discussion of the dissolution coefficient is provided in Appendix D, bullet #14.

will affect the efficiency of the dissolution. Finally, the effect of the superheat and bath composition should also be taken into consideration when evaluating the dissolution coefficient.

Table V: Different dissolution coefficients estimated from published literature.

Study	Zhan et al. [20]	Wang [24] (Fast dissolving alumina)	Wang [24] (Slow dissolving alumina)	Welch and Kuschel [25] (Fast dissolving alumina)	Welch and Kuschel [25] (Slow dissolving alumina)	**Average Dissolution coefficient**
Approximated dissolution coefficient (K_m) [m/s]	2.95×10^{-2}	2.36×10^{-4}	1.06×10^{-4}	2.35×10^{-4}	3.75×10^{-5}	***6.02 x 10^{-3}***

6.4.2.3 Alumina transport between the different volumes.

Alumina is transported within an electrolysis cell by three different mechanisms (discussed in more details below):

- Molecular diffusion caused by different concentration gradients in the bath.
- Mixing caused by the rising bubbles generated under the anodes
- Large-scale convective loops in the bath caused by the magnetohydrodynamics (MHD) forces acting on the cell.

All these mechanisms were considered during the development phase of the simulator and specific modules were designed to represent correctly these phenomena.

6.4.2.3.1 Mass transfer between neighboring volumes (Module 3)

Diffusion across the electrolyte is a slow process in comparison to the MHD generated movement. Nonetheless, this phenomenon is important for the model accuracy as the importance of diffusion increases in opposition to a reduction of the MHD forces within

the cell. Therefore, if the simulator is used to investigate hypothetical scenarios with low or no MHD forces, consistent results with respect to theoretical considerations are still expected.

The rate of mass exchange between neighboring anodes is described quantitatively by a linear "driving force/rate of transfer" type correlation (Eq. 6-10). The driving force of the alumina transfer is the concentration gradient approximated by ($\Delta C/L$) [(kg/m^3)/m] in the equation. While ($m_{i,j}$)[kg/s] is the mass transfer rate between two adjacent volumes; the proportionality factor of "generalized conductance" takes into account the section (A_{ij})[m^2] available for the mass exchange and the so-called "equivalent diffusivity" (D_{eq}) [m^2/s]. The latter englobes several mechanisms such as the molecular diffusion and the more important turbulent mixing caused mainly by the bubbles.

$$\dot{m}_{i,j} = -D_{eq} A_{ij} \frac{(C_i - C_j)}{L} \qquad (6\text{-}10)$$

There is little information available in the literature about the molecular diffusivity of alumina in the molten electrolyte. Furthermore, we do not have any quantitative data about the equivalent turbulent diffusivity in the bath. For this reason, we estimated the value of D_{eq} from the hypothesis of having a homogenization time of 30 minutes[22]. The homogenization time is the duration needed to reach a concentration uniformly spread across all zone within ±1% after an initially uneven distribution (illustrated on Figure 6-4). With this hypothesis, the corresponding equivalent diffusion coefficient could be estimated

[22] Additional discussion about effective diffusivity is provided in Appendix D, bullet #15.

as 0.0025 m^2/s. Figure 6-5 illustrates the diffusion of the alumina with the appropriate transport coefficient. It is possible to observe that after 1800 seconds, the concentrations of all regions of the cell are between 3.96% wt. and 4.04%wt. Only half the cell is represented in the figure due to symmetry.

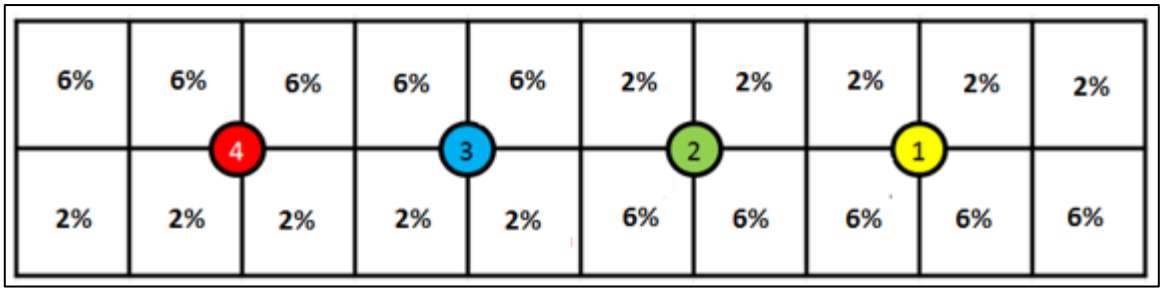

Figure 6-4: Theoretical scenario used to determine the appropriate transport coefficient.

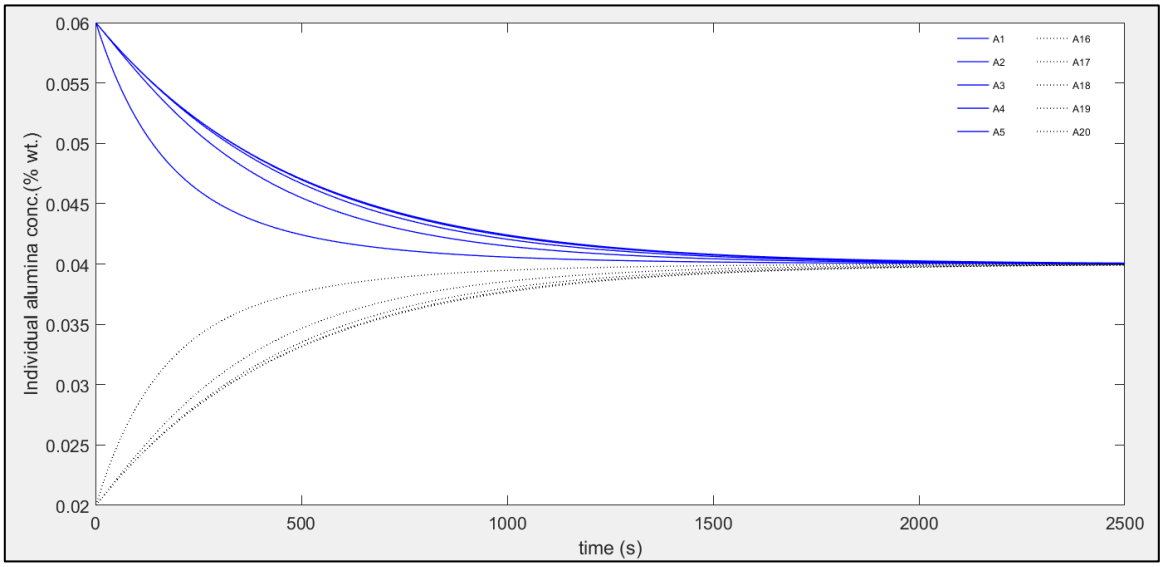

Figure 6-5: Impact of the diffusion on the alumina concentration of the different zones for a theoretical scenario with D_{eq}= 0.0025 m^2/s. 10 zones are represented by a different curve.

6.4.2.3.2 Mixing Caused by Bubbles

Bubbles are an important driving force in the mixing of the alumina [19, 26-28]. However, this phenomenon is occurring more importantly on a localized level (under the

anodes) and will be beneficial for the alumina dissolution and for local transport of the dissolved alumina. The mixing caused by the bubble is taken into consideration within the alumina dissolution module (indirect effect on the D coefficient) and the diffusion module as well (direct impact on D_{eq}). For this reason, no specific module was developed to consider the complex behavior of bubbles mixing associated with alumina transport.

6.4.2.3.3 Cell-Scale Convection Loops (Module 4)

During normal electrolysis, the high current of the cell leads to the generation of strong magnetic fields. All the cell conductors (risers, anode beam, busbars, etc.) are designed to minimize the influence of the magnetic field on the movement of the aluminium and bath but MHD generated loops are still present in the cells. These MHD forces, added to the drag force exerted between the aluminium pad and the electrolytic bath will create a movement of the bath that can affect significantly the movement of the dissolved alumina as demonstrated theoretically [19, 21, 28] and experimentally [27, 29].

In this study, the movement generated by the magneto-hydrodynamic forces is not calculated by the simulator. Instead, the pattern of the electrolytic bath flow is considered similar to the results published by Hofer [21] as part of his Ph.D. thesis. The work of Hofer was performed on a similar cell technology and similar cell amperage what we used for the simulator. As illustrated in Figure 6-6, the mass exchange between the different volumes caused by bath movement is asymmetrical as observed experimentally in a previous work by the current authors [29]. The speed of the bath across the different respective volumes

was also determined based on the Hofer's research[23] with maximum values located in the corners of the cell with a magnitude of approximately 8 cm/s.

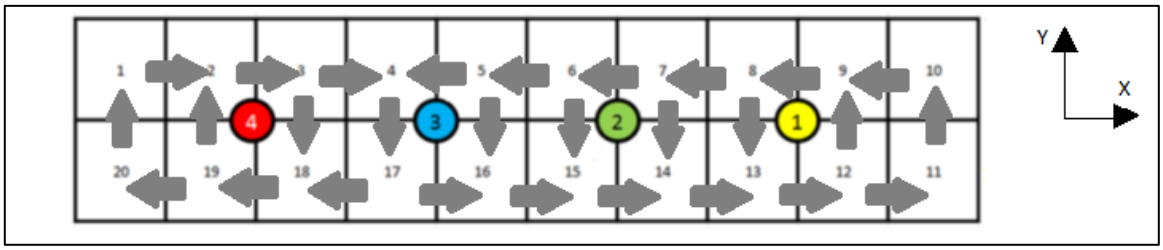

Figure 6-6: Exchange between the different volumes based on the work of Thomas Hofer [21].

Strong refinements to the simulator could be obtained by performing an MHD simulation specifically for the cell technologies considered and applying the results in a similar way to the simulator.

During the convective movement of the electrolytic bath caused by MHD dynamics, both dissolved and undissolved alumina will be carried in the electrolyte flow and eventually move from one section of the cell to an adjacent zone. It is the only mechanism considered in the model that can transport undissolved alumina to regions of the cell non-adjacent to an alumina feeder. However, a ratio can be used to limit the transport rate of the solid alumina if required. Alumina clumps are known to float on top of the electrolytic bath as a raft [30, 31]. Therefore, if the alumina clump is important, it is assumed that it will transfer less rapidly due to friction between the alumina raft and the anode cover material. No information in the literature was available to identify this ratio so this value had to be determined arbitrarily based on an engineering judgment. This value was set to 10%.

[23] Additional discussion on the exchange module is provided in Appendix D, bullet #16.

6.4.2.4 Alumina Consumption (Module 6)

During electrolysis, alumina is consumed with a specific rate determined by the respective current passing through each zone and the average current efficiency of the cell. The alumina consumption rate can be calculated for every time step using equation 6-11 based on Faraday's law of electrolysis, where (m_i) [g] is the respective amount of alumina consumed, (I_i) [A] is the amperage going through a specific section of the cell, (Δt) [s] is the time step, (M) [g/mol] is the molar mass of the alumina, (F) [$C \cdot mol^{-1}$] is the constant of Faraday, (z) [-] is the valency number of ions required for the alumina to react and (CE_i) [%] is the respective current efficiency of the section. At the current state of the simulator, the current efficiency is considered as constant for every section, but further refinements could consider localized current efficiency, more importantly for regions demonstrating a high risk of LVAE, thus a high risk of local instability.

$$m_i = \frac{I_i \cdot \Delta t \cdot M}{F \cdot z} \cdot CE_i \qquad (6\text{-}11)$$

Having calculated the individual consumption rate of the alumina for each section of the cells, the mass of produced aluminium can be calculated for each time step as an additional indicator of the cell's local performances.

Finally, a low threshold in the alumina concentration was defined arbitrarily as 0.02% wt. In the rare occurrence where the alumina concentration for specific regions gets below this threshold, the current is distributed to other regions of the cell and the alumina concentration will not decrease further to eliminate the risk of obtaining negative alumina concentration. In the unexpected occurrence where all regions of the cell would reach this

threshold, no calculation of the aluminium production would be possible until the alumina concentration increases back to value above this limit, therefore the simulator's modules 5,6 and 7 would be skipped and the cell is considered under high voltage anode effect.

6.4.3 **Electrical Current Distribution Module (Module 5)**

In the electrolysis cell, all twenty-anodic assemblies are connected parallel to each other. Therefore, the current is free to reorganize constantly to choose the path of the lowest overall resistance. This module was designed to adequately represent the entire cell conductors as well as the different resistance from the electrolysis bath in a simplified electrical model which runs for every time step.

6.4.3.1 Cell Resistance Module

The electrical network used to represent the cell's conductors was simplified to consider exclusively the principal conductors of the electrolysis cell[24]. The primary conductors considered in the resistance network are illustrated in Figure 6-7. They start at the middle busbar junction between the previous and the simulated cells and goes sequentially through the busbars, the risers, the anodic assemblies, and the electrolytic bath all the way to the aluminium metal pad. There is no need to consider any further elements such as cathodic resistance due to the possible reorganization of the current occurring in the highly conducting aluminium metal pad.

Some secondary conductors (shown in Figure 6-7) are present on a normal operating cell but no current is supposed to go through them under conditions close to the normal operation. They are, however, beneficial for the cell mechanical stability and also

[24] The impact of neglecting secondary conductors is described in Appendix D, bullet #17.

help the current equilibrium during high current instabilities such as HVAE. These secondary conductors were not considered in the model due to the significant increase in complexity that they would have required while offering very low improvements to the results.

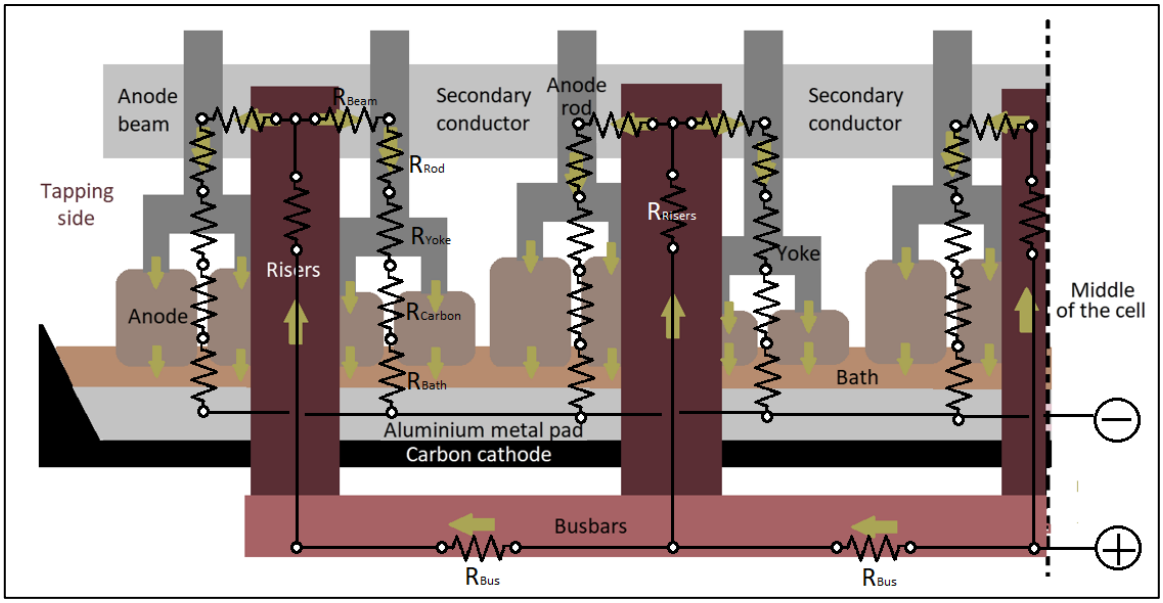

Figure 6-7: Various elements considered as part of the electrical network.

6.4.3.2 Individual resistance of the anodic assemblies

In addition to the electrical conductors, some specific elements must be considered for each individual component of the anodic assemblies. For this reason, individual resistances specific to anode position are the results of five resistances connected in series. These five resistances and any respective considerations are described in the following sections.

6.4.3.2.1 Resistance of the Anode Beam Conductor

The resistance of this element is calculated similarly to the other electrical conductors (busbars (R_{Bus}) , risers (R_{Risers}) and transversal bars) using equation 6-12. Where (R) [Ω] is the calculated resistance, (ρ) [Ω·m] is the electrical resistivity of the conductor, (L) [m] is the length of the conductor and (A) [m^2] is the area of the surface of the conductor.

$$R = \frac{\rho \cdot L}{A} \qquad (6\text{-}12)$$

6.4.3.2.2 Resistance of the anode assembly

The anode assembly is composed of three resistance elements, the anode rod, the carbon and the yoke connecting both these elements. Based on the work of other researchers [32] for the same cell technology, it was possible to define a constant resistance value for the yoke (R_{Yoke}). This resistance considers the yoke electrical network as well as the contact resistance in the anodic "clad" and the contact resistance associated with the cast-iron connections. However, further improvements to the model could consider the heat balance of the cell, which could include the effect of the temperature during the current ramp up as well as when the yoke gets closer to the electrolytic bath [32].

The anode rod (R_{Rod}) and the carbon resistance (R_{Carbon}) are also calculated as electrical conductors (equation 6-12). However, for each anodic assembly, the anode rod and the carbon length will be different depending on the anode position within the anode changing cycle. The respective length of each anode rod (L_{ROD}) [m] and carbon (L_C) [m] is calculated by considering a constant length (L_{TOT}) [m] between the anode beam and the

bottom of the anodic assembly. Then, as the initial carbon height of a new anode (L_{INI}) [m] is known, the length of carbon for each anodic assembly can be identified by subtracting the respective carbon erosion which depends on the total number of days (N) [days] since the anode was planted in the cell. The daily consumption of carbon (C_{CONS}) [m/day] is measured frequently at the smelter and the information was provided by the smelter for this study. Details of the calculation are presented in equation 6-13 and 6-14.

$$L_c = L_{INI} - N \cdot C_{CONS} \quad (6\text{-}13)$$

$$L_{ROD} = L_{TOT} - Lc \quad (6\text{-}14)$$

6.4.3.2.3 Resistance across the electrolytic bath

Three elements should be considered to adequately represent the resistance corresponding to the electrolyte: the ohmic resistance of the bath and the additional apparent resistance caused by the overvoltage and the excess resistance due to the presence of the bubbles at the bottom of the anodes. Therefore, these elements were considered in equation 6-15, where (R_{Bath})[Ω] is the resistance of the electrolyte, (ρ_{bath}) [Ω·m] is the electrical resistivity of the bath, (ACD) [m] is the interpolar distance, (A_{bath}) [m^2] is the surface area of the anode bottoms of an element and (F) [-] is a factor (F ≥ 1) used to represent the combined amplifying effect of the overvoltage and the bubbles.

$$R_{bath} = \frac{\rho_{bath} \cdot ACD}{A_{bath}} \cdot F \quad (6\text{-}15)$$

In the previous equation, two elements are dependent on the local conditions within the cell. Firstly, the resistivity of the bath is determined by equation 6-16, originally presented by Wang et al. [33], where (σ)[S/cm] is the electrical resistivity of the bath, BR [-

] is the bath ratio of the electrolyte, (T)[K] is the absolute bath temperature and (Al_2O_3, CaF_2, MgF_2, LiF, Al_4C_3) [% wt.] are the respective concentration of each component. Therefore, an uneven alumina concentration in the bath will generate different individual resistance.

$$\begin{aligned} ln\,\sigma = {} & 1.7738 + 0.3351 \cdot BR - 21.3 * 10^{-3} \cdot Al_2O_3 - 17.5 * 10^{-3} \cdot CaF_2 \\ & -32.1 * 10^{-3} \cdot MgF_2 + 27.3 * 10^{-3} \cdot LiF - 121.1 * 10^{-3} \cdot Al_4C_3 \\ & -1.5337 * 10^3 / T \end{aligned} \qquad (6\text{-}16)$$

Secondly, the minimum value of the (F) factor (under saturated bath) was determined to be 1.1212 according to Grjotheim et al.[34]. Further increase in this ratio was defined empirically based on an experimental study in Alouette's smelter[25]. The measurements carried out to develop the empirical model are illustrated in Figure 6-8. It demonstrates that the resistance increases drastically when the alumina concentration leans towards zero which is caused by the combined effect of overvoltage and a significant layer of resistive gas (PFC) under the anodes.

[25] Additional discussion on the F factor is provided in Appendix D, bullet #18.

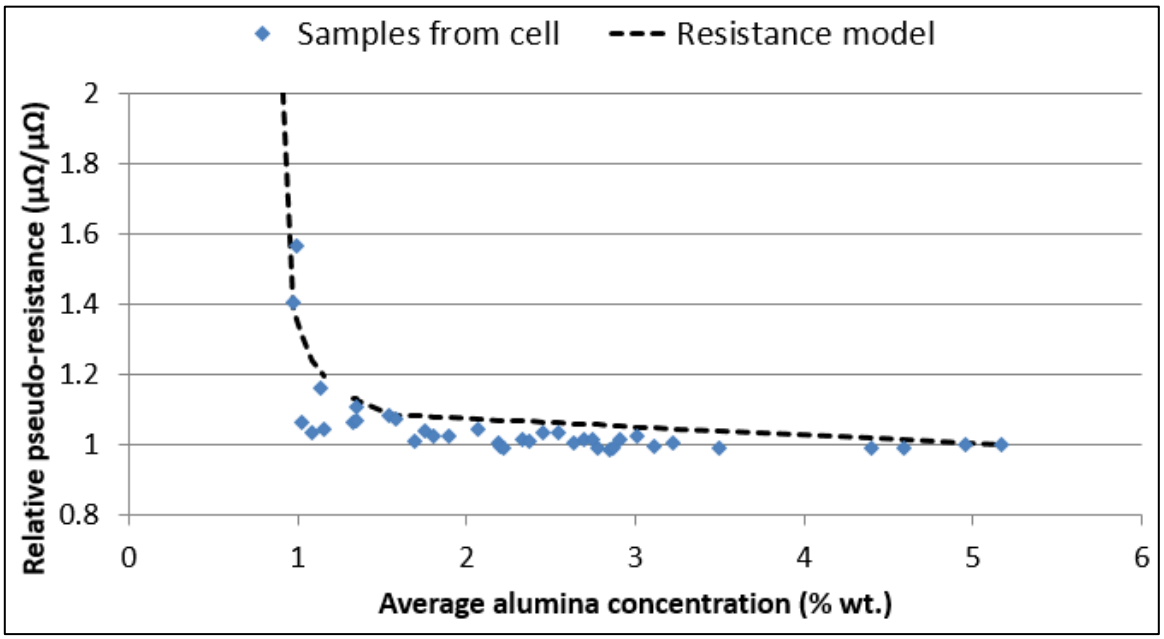

Figure 6-8: Effect of the average alumina concentration in a cell on its pseudo-resistance.

6.4.4 **Risk of low voltage anode effects (Module 7)**

Previous research by the current authors [18] demonstrated that the standard deviation among individual anode currents is the strongest indicator of LVAE. Therefore, it is easily possible to calculate the standard deviation of the individual anodic currents resulting from the simulator to predict the risk of LVAE. Experimental measurements demonstrated that the standard deviation threshold was equivalent to 3.65 kiloamperes [18].

To correctly implement this threshold in the simulator, it was necessary to determine if the resulting standard deviation from the simulator was within the same order of magnitude as the real electrolysis cell. Under normal operations, the simulation results are more than three times lower in terms of the standard deviation among individual anode currents than the real measurements for similar conditions. This difference can be attributed

to the uncertainty associated with the distance between each respective anode and the metal pad, i.e. individual anode-cathode distance (ACD). Under the industrial practice, there are small variations (few mm) attributed to the positioning of the anodes when inserted into the cell. Moreover, the aluminium metal pad is not necessarily of uniform height over the entire surface. For example, the magnetic field can shift the bath-metal interface closer, or further to some anodes depending on the positions. These considerations, combined with the different type, and level of instability can generate movement of the metal pad which will inherently change the local ACD of each anode. These elements cannot be accurately represented by the simulator due to the irregularity of these events. Consequently, by considering that the ACD is constant for each anode in the mathematical model, the small ACD variations from anode to anode in the real cells can explain the observed deviation. The effect of these variations is even more important due to the very small ACD [35] of this specific smelter. Finally, the threshold value in the mathematical model was adjusted according to this observation.

6.5 Validation of the simulator

6.5.1 Experimental setup

To validate the simulator, four different alumina feeding scenarios were generated in the cell to create alumina concentration gradients in the electrolytic bath. For all scenarios, the alumina supplied to the cell was reduced by turning off certain feeders. However, the position of the stopped feeders was changed depending on the scenarios. During these tests, individual anode currents were monitored continuously with the system provided by the aluminium smelter. Furthermore, the cell's gas composition was also

continuously monitored, while bath samples were taken periodically for analysis of the alumina concentration. The four different scenarios investigated are presented in Table VI.

Table VI: Information related to the validation scenarios investigated.

	Feeder 1	Feeder 2	Feeder 3	Feeder 4	Duration (s)
Scenario #1-A	Stopped	Stopped	Active	Active	0 to 4080
Scenario #1-B	Stopped	Stopped	Stopped	Stopped	4080 to 5700
Scenario #2	Active	Stopped	Stopped	Active	0 to 4620
Scenario #3	Active	Active	Stopped	Stopped	0 to 5400
Scenario #4-A	Stopped	Active	Active	Stopped	0 to 4020
Scenario #4-B	Active	Active	Active	Active	4020 to 4320

These scenarios were designed to deplete the overall alumina concentration in order to obtain LVAE in cells, within a reasonable amount of time (approximately 1 hour) while avoiding HVAE for as long as possible. The different locations of the feeders were chosen to assure that the model was consistent for symmetric and asymmetric scenarios. Finally, in the case of the scenarios 1 and 4, the tests had to be slightly modified to avoid disrupting the normal operations of the electrolysis process (i.e. anode change schedule).

6.5.1.1 Following the Alumina Concentration

To investigate the change in alumina concentration within the cells, samples of the electrolytic bath were extracted periodically in six different positions illustrated in Figure 6-9 using a sampling probe to obtain conical shaped samples. Prior to every test (t=0), one sample in each of the six locations was extracted to determine the initial conditions for the simulator. Then, the time lapse between each sampling was always 10 minutes or less and three samples were always taken almost simultaneously (±30 s). The three samples were extracted in order to obtain information on the concentration gradient along the longitudinal direction (x-axis) of the cell. In alternation, the 3 samples along the x-axis of the cell were

taken on opposite sides of the y-axis. Analysis of the alumina concentration was performed on site at the Alouette smelter's laboratory using the ALCAN method.

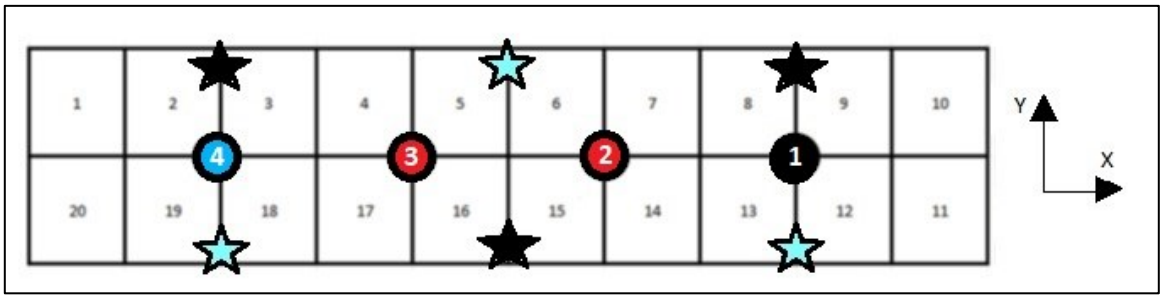

Figure 6-9: Extraction points (stars) for bath samples during the test. Stars with the same colors represent areas where the bath was sampled simultaneously.

6.5.1.2 Gas Composition Monitoring

The gas was extracted using stainless steel sampling probes directly from each of the five inner ducts that route the gas from the different parts of the cell up to the main exhaust duct in order to well represent the overall cell [36]. The flow rate of each probe was regulated to 1 LPM and the total gas flow (5 LPM) was routed to a GASMET™ DX-4000 FTIR (Fourier Transformed InfraRed) spectrometer using a Peltier cooled mercury-cadmium-telluride detector (sample cell path: 9.8 m, volume: 0.5 L, resolution: 7.8 cm^{-1}). The gas stream was sent sequentially through the desiccant, activated alumina, a 5-mm filter and finally a 2-mm filter to remove traces of water, hydrogen fluoride and dust respectively for the protection of the measuring equipment. The gas was preheated to 120 °C before entering the FTIR and concentration measurements were performed at a rate of 10 scans per second. Average values for 20 second periods were recorded. The background spectrum was redefined using high purity nitrogen prior to every test.

6.5.2 **Validation of the Cell Voltage**

A first element to be evaluated is the accuracy of the simulator to reproduce the behavior of the overall cell voltage[26], therefore, a scenario with different feeding periods was observed in the real electrolysis cell and reproduced in the simulator. As illustrated in Figure 6-10, the long-term tendencies of typical voltage variations in cell voltage provoked during different feeding periods can be adequately represented by the simulator. However, the mathematical model was not designed to represent cell events with a higher frequency such as the movement of the bubbles or cell instabilities caused by the movement of the metal pad or anode incidents (spikes). Additionally, some discrete events like the movement of the crust breaker can also perturb the cell voltage as it locally and randomly increases the gas flow out of the electrolytic bath. Despite neglecting certain events, changes in the global ACD of the cell can be represented well with the simulator. However, the actual movement of the anode beam had to be approximated in this study. More detailed results can be expected if the anode beam movements were monitored and measured precisely in terms of "distance traveled [mm]" instead of "total time of travel [s]".

[26] Even though they are not considered in the simulation, the cathode voltage drop, the decomposition potential and the voltage drop from external busbars are considered as constants to calculate the overall cell voltage.

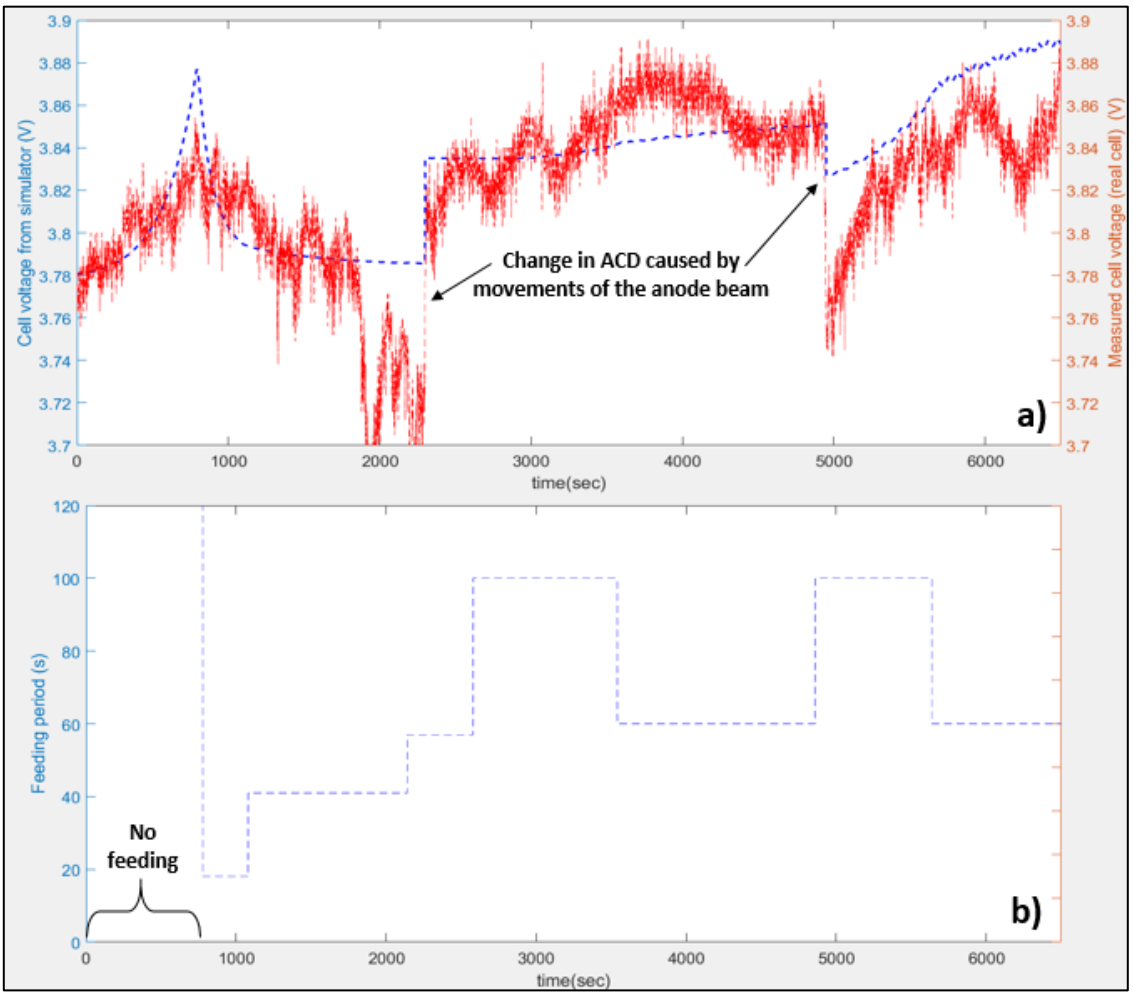

Figure 6-10: Comparison of the cell voltage between the simulator (dashed line) and real measurements (continuous line) (a) during different feeding cycles (b).

6.5.3 **Validation of the alumina distribution**

As mentioned previously, four scenarios were planned and the deviations between the simulated results and data series taken from the monitored cell were evaluated. The results of the simulation with the initial hypotheses discussed in the previous section of this paper is presented in Figure 6-11-a) to Figure 6-11-d). For each figure, the data resulting from the simulator is the average alumina concentration predicted for each element of the cell. Hence, the blue line represents the average for the duct end side, the red dashed line is

the average for the center region and the black dotted line is the average concentration on the tapping side. The results demonstrate that the general behavior is well represented by the simulator. However, there is more uniformity across the different regions of the cell in the simulator than there is in the real cell. This lack of agreement can be caused by too strong a coupling (high value of the exchange factor) between the different elementary volumes. This exchange factor is primarily dependent on the bath velocity in the cell. As a matter of fact, the average bath velocity from the simulator was estimated using the results of an external study [21]. Even if the study performed by Hofer had many similarities with the investigated cells, some differences may cause the actual bath velocity to be smaller than predicted numerically. For this reason, an optimization was performed using the data collected during the validation and as a result, a reduction of 60% was imposed on the bath velocity used in the simulator. The corrected results are presented in Figure 6-11-e) to Figure 6-11-h).

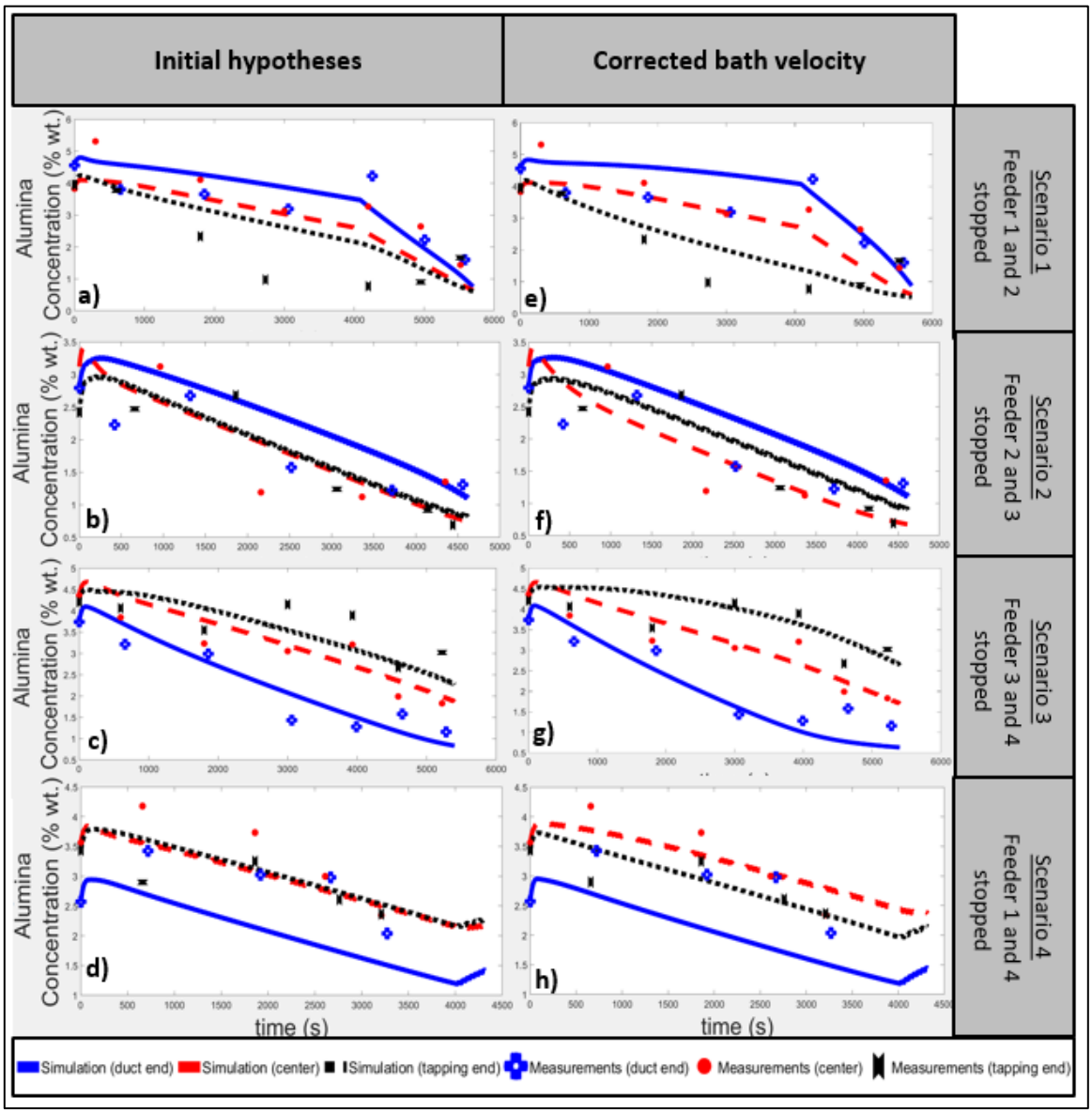

Figure 6-11: Comparison of the simulated alumina concentration history and real measurements. Figure a) to d) illustrates the results for scenario 1 to 4 respectively, with the initial hypotheses. Figure e) to h) illustrates the results for scenario 1 to 4 respectively after correction of the bath velocity.

The corrected results[27] demonstrate a better agreement with the real measurements, especially in the cases where there was an asymmetry in the alumina feeding (cases 1 and 3). Under these scenarios, the measured alumina concentration shows a higher range of

[27] Additional discussion regarding the improved results are presented in Appendix D, bullet #19.

values. Therefore, as the corrected bath velocity reduces the overall cell mixing, it describes better the cell's inhomogeneity leading to a closer agreement between the simulator and the reality. One element that the simulator cannot reproduce in its current state is the unpredictable fluctuations in the alumina additions coming from random sources such as the effect of anode cover material or the recuperation of alumina from the sludge located below in the aluminium pad. Important instabilities in the cell (e.g. during high voltage anode effect) may provoke significant reoxidation of the aluminium metal pad for short amount of time, which, in turn may generate significant alumina additions to the electrolytic bath. This phenomenon was previously observed by the authors [29] when the cell's conditions reach LVAE or HVAE. In the current study, we can observe this phenomenon at the end of scenario #3 where there is a significant increase (half a percent) in the alumina concentration at both extremities of the cell even if no additional alumina feeding was provided by the cell's feeders.

6.5.4 Validation of the standard deviation among individual anode currents and validation of PFC emissions

After optimization of the bath velocity, the efficiency of the simulator to predict LVAE was investigated using the standard deviation among the simulated individual anode currents. The evolution of this parameter for the four validation scenarios is presented in Figure 6-12, along with the standard deviation of the measured individual anode currents in the real cell. The measured concentration values of the CF_4 gas extracted at the duct end of the cell are also shown. The calculated standard deviations were normalized with respect to the average value of these respective parameters under normal behavior. Moreover, the measured standard deviation in the real cell showed an important noise level. For this

reason, the results were smoothed using a moving average of 20 seconds. Finally, the vertical arrow in each figure represents the instant where the standard deviation threshold[28] value was reached according to the simulator.

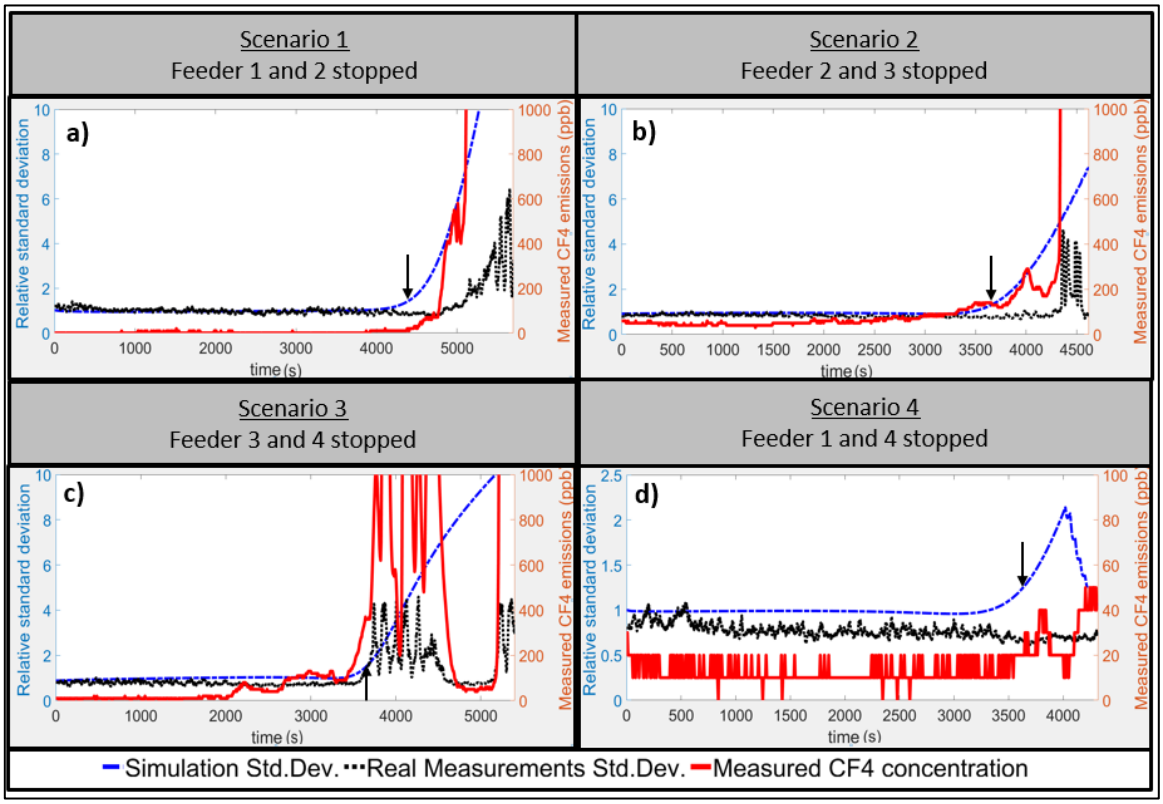

Figure 6-12: Evolution of the simulated and measured standard deviation among individual anode currents during the four different validation scenarios, a) to d) respectively, along with the measured CF_4 concentration.

The evolution of the simulated standard deviation correlates strongly with the observed PFC emissions for all the scenarios investigated, demonstrating that this indicator can be used to predict occurrence of low voltage anode effects. Interestingly, the simulator's correlation with the CF_4 emissions is stronger than the actual measured standard deviation. In all cases, the increase in the standard deviation predicted by the

[28] As described in Chapter 6.4.4, the LVAE detection threshold is a constant value based on the work originally presented in Chapter 4.

simulator is obtained earlier or at the same time as the increase in the standard deviation measured by the individual current monitoring tool. This curious behavior is mainly due to some elements discussed previously that are not considered in the simulator like cell instabilities or variations in the local value of ACD. For this reason, the real cell is less sensitive than the simulator to the variations that are caused strictly by different alumina concentrations in the cell. This observation reveals that the simulator is capable of revealing information that cannot even be observed on an operating electrolysis cell, thus making it a very effective and sensitive tool to predict low voltage anode effects.

6.6 Further Improvements and Potential of the Simulator

The simulator satisfies its original goal as to: "correctly simulate temporal and spatial variations of the alumina distribution in an electrolysis cell in order to predict low voltage anode effects". Further improvements can be achieved of the simulator to enhance its performance and provide more detailed results and useful information for improving the electrolysis process. Some of these improvements are:

- Improvement of the fidelity of the bath flow pattern and bath velocity distribution based on the specific cell technology.
- Introduction of metal pad instabilities that influence the local ACD in time.
- Current efficiency should vary in time depending on the actual state of the process, leading to higher rates of metal re-oxidation during LVAE or HVAE.
- Introducing a sink/source of alumina to represent the formation and dissipation of sludge below the metal pad.
- Incorporation of the energy balance in the mathematical model to follow the formation of hot or cold regions leading to different dissolution efficiency.

However, even in its current state, the simulator can be used efficiently to investigate and improve some elements of the electrolysis process as demonstrated in the next section.

6.6.1 **Using the simulator to improve the electrolysis cell process**

Using the alumina distribution simulator can also be beneficial to increase the understanding of some elements influencing the electrolysis process, which might lead to improvements of the cell stability and increased metal production. Investigations are presented in the next sections of this paper and the described results provide useful information as well as possible refinements on the electrolysis process.

6.6.1.1 Analysis of the Effect of the Conductors

Due to the important size of the electrolysis cell, the electrical network carrying the current is similar but not exactly the same depending on the anode positions. Therefore, the anticipated difference in current can be evaluated by the simulator. Figure 6-13 illustrates the current distribution in a cell with identical anode assemblies, i.e. with the same carbon height. Therefore, only the slight differences of the electrical resistance network prior to the anode rods will influence the current distribution. It is possible to observe a difference of 375 amperes between the anodes driving the most and less current only due to the differences in the electrical resistance network for an ACD of 25 mm. As the ACD increases to 40 mm, the difference between the different anodes diminishes due to the relatively high resistivity of the electrolyte. As expected, the figure demonstrates that when the ACD increases, the current redistributes from the region driving the most current (upstream center) to the regions that were driving the less current (downstream

extremities). Consequently, only minimal change in current can be observed in the regions of the cell where the current was already close to the theoretical average current (19.75 kA).

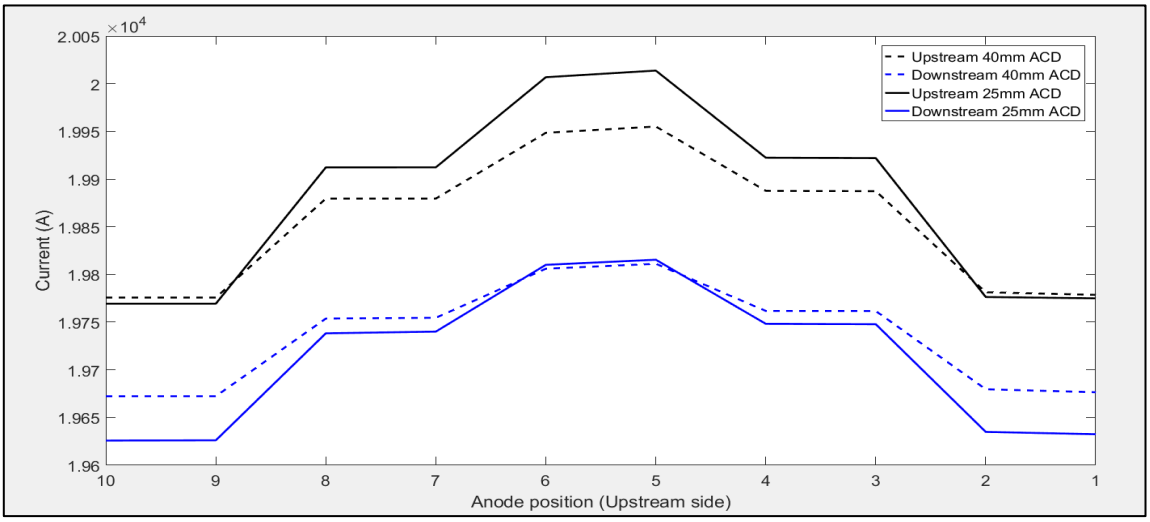

Figure 6-13: Current distribution in the cell for similar anode conditions and different ACD.

However, the case simulated in Figure 6-13 is unrealistic due to the continuous anode changes that occur in a cell, leading to different heights in carbon, hence different resistance. Figure 6-14 is more representative of the predicted current distribution during normal operations due to the different states of carbon consumption of the individual anode assemblies. In this case, a change in ACD will lead to a similar behavior but its effect is amplified. On Figure 6-13, a 15-mm change in ACD leads to a maximum change in individual current of 75 amperes. However, a similar change in ACD with different carbon height leads to a maximum change of 384 amperes. Therefore, the effect of the ACD on the local anode current can easily reach 1.3%/cm. This value appears insignificant for a small change in the global ACD. However, if the ACD is not consistent for the entire cell due to a deformed metal pad, the localized differences can be even more important.

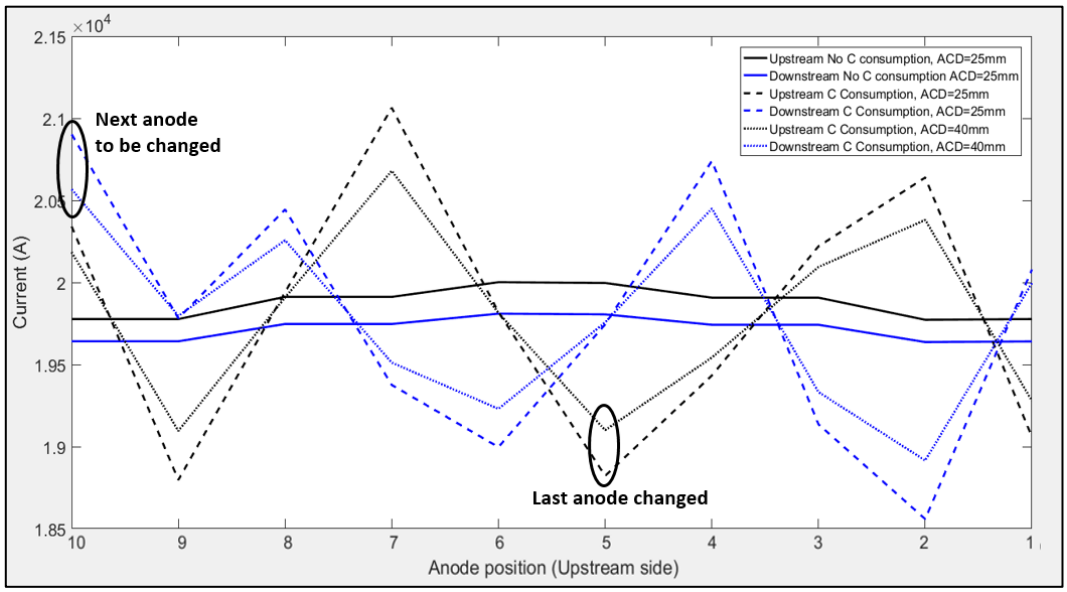

Figure 6-14: Current distribution in the cell for different anode conditions and different ACD.

On the other hand, the effect of the carbon erosion is extremely important on the individual anode current. The results demonstrate that the last anode that was changed[29] in the cell drives less current, due to a higher resistance caused by the carbon while the next anode to be changed is among the ones driving the most current. In this scenario, the overall difference between the anodes driving the most and less current is 2.9 kiloamperes (Figure 6-14). This difference represents nearly 15% of the average anode assembly current. For this reason, a study of the anode change cycle would be beneficial to evaluate if areas of the cell can be more propitious to increased cell current during specific periods, which could lead to higher risk of alumina depletion and ultimately leading to LVAE or HVAE.

[29]The study presented in this section does not consider the effect of the current pick-up (increasing temperature and frozen bath layer) but considers exclusively the resistance network of the anode assembly.

6.6.1.2 Improvement of the Feeding Strategy

In scenario illustrated in Figure 6-15, operations under normal behavior were simulated with constant feeding from each feeder with feeding periods similar to those of a real electrolysis cell. It can be observed that there is a constant irregularity in the alumina concentration of the different zones. As expected, the zones closest to the center of the cell are constantly richer in alumina than the extremities. However, the two extremities are also different from each other due to the absence of symmetry in the alumina exchange caused by the cell-scale MHD convective loops. Therefore, at the end of the underfeeding periods, the zones at the duct end of the cell tend to have a very low alumina concentration. Knowing that these zones are not as uniform as the rest of the cell, various measures can be put into place to improve the uniformity of the alumina concentration. A plausible solution to this problem could be to increase the total amount of alumina fed by the specific feeder in this region to lean toward a more uniform distribution. However, considerations, such as changing the point feeder's action pattern, should also be taken into account to assure that this additional alumina dissolves properly in order to avoid blocking the feeder and generating more problems.

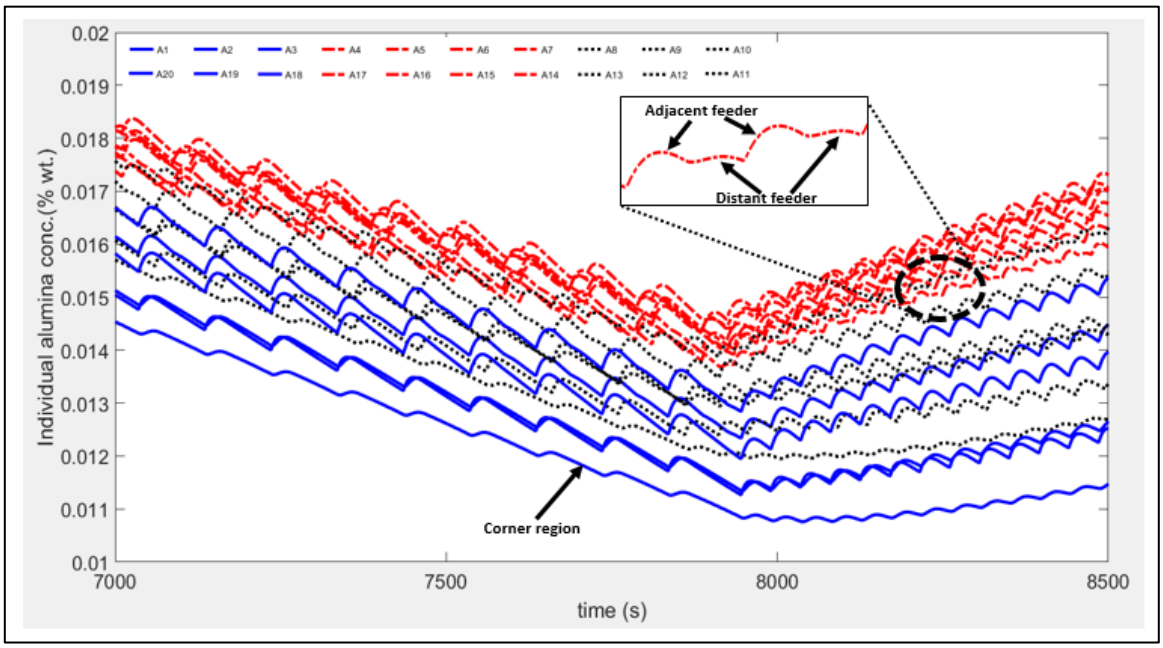

Figure 6-15: Alumina concentration of the different regions at the end during the transition from underfeeding to overfeeding.

The results also clearly demonstrate that some regions of the cell receive alumina from multiple sources. In the zoomed part of Figure 6-15, we can see that the alumina concentration of some region varies with the feeding from the adjacent feeder as well as feedings from a distant feeder. It is possible to observe this behavior due to the transfer of undissolved alumina from one region to another. The opposite behavior can also be observed in the corner regions of the cell where a smaller amount of undissolved alumina is distributed, which leads to smaller amplitude in the variation of the alumina concentrations. Consequently, these regions are more likely to be at low levels of alumina concentration.

6.6.1.3 Analysis of the Feeder Stoppage After an Anode Change

It is a common practice to stop for a significant period any feeders next to an anode that undergone a procedure such as an anode change, or anode covering. During these events, an important amount of alumina can be injected into the electrolyte by the anode

cover material, which is a mix of crushed electrolytic bath and alumina. For this reason, the feeders are generally stopped until this parasitic alumina is dissolved and consumed. However, stopping a feeder too long can have a negative impact on the cell behavior. Using the simulator, different scenarios were investigated to provide information in order to determine the ideal duration of the stoppage depending on the smelter's specific amount of alumina added during the procedure. The results of this investigation are presented in Figure 6-16.

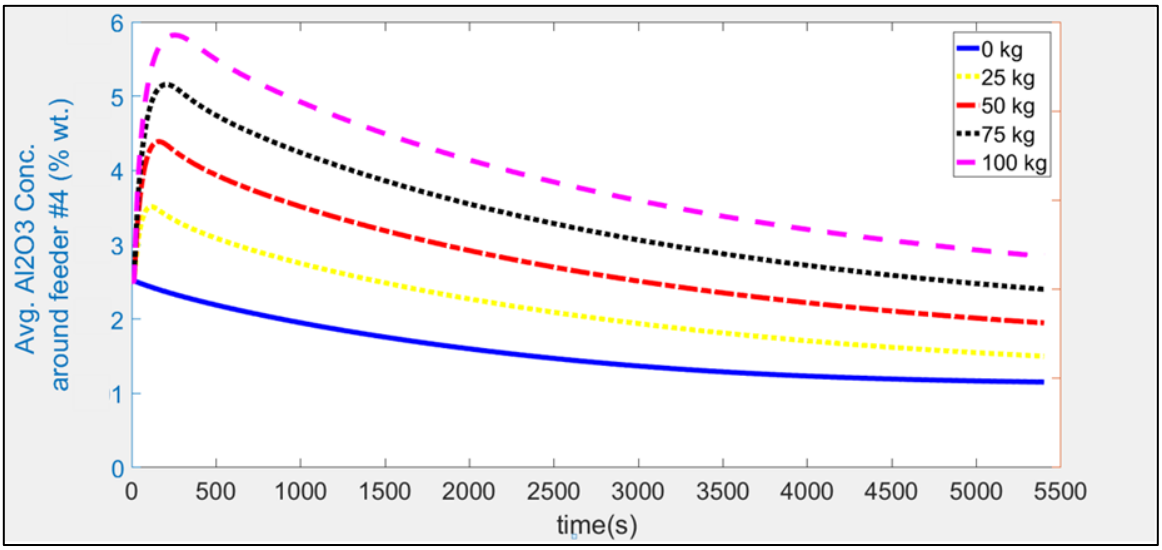

Figure 6-16: Impact of stopping a feeder after an important addition of parasite alumina.

The alumina concentrations shown in the figure represent the average alumina concentration of the four zones adjacent to the stopped alumina feeder for different stoppage times and different amounts of parasite alumina fed. While a specific feeder is stopped under these circumstances, the feeding periods of the three active feeders are shortened in order to maintain the theoretical feeding rate necessary for the cell. Finally, based on the result of the previous section, the anode changed in the simulation is anode #2,

which is located in the critical section of the cell (close to feeder 4) in order to illustrate the worst-case scenario for risks of anode effects.

The results presented in Figure 6-16 demonstrate that it is possible to determine precisely the correct duration of time that a specific feeder should be stopped if parasite alumina is anticipated, to avoid depletion of alumina, leading to anode effects or to avoid extra feeding that could lead to sludge generations. However, to use this tool correctly, a partnership with the electrolysis team (technician and engineers) is necessary to assure that the estimated parasite alumina feeding is representative of the real conditions.

Finally, the results also demonstrate that if the correct amount of alumina is provided to the cell from distant feeders, the area around the stopped feeder will eventually reach a new equilibrium concentration. In the case where no parasite alumina was provided, this new concentration is approximately 1% wt. lower than the original cell concentration. For this reason, the risks of reaching anode effect conditions while stopping a single feeder should be minimal if the average alumina concentration was close to 3 % prior to the stoppage. However, it is assumed that the other feeders perform optimally and that 100% of the dosed alumina eventually reaches the electrolysis bath, which might not always be the case, especially with an increased alumina feeding rate.

6.7 Conclusion

In this paper, a novel, non-homogenous approach was presented to simulate the alumina and current distribution within the bath of an electrolysis cell. With this information, it is possible to use the model to predict the onset of CF_4 emissions, commonly known as low voltage anode effects. This approach considers the electrolysis cell as an

assembly of twenty discrete volumes with respective alumina concentration and current density. Those discrete volumes are coupled by convective-diffusive mass transfer factors. The mathematical model is composed of seven sub-models, all detailed in this paper. Five of these are designed to assess the alumina concentration of every region, for every timestep. They are: the feeding, the dissolution, the diffusion, the mass transport (convection) and metal production sub-models. Another sub-model calculates individual anode currents based on a simplified electrical network of the cell while the remaining sub-models evaluate if LVAE emissions should be observed in the cell under the current conditions.

Multiple validations were performed to evaluate the agreement of the simulator with real measurements. The results indicate that global cell voltage variations caused by an important change in the alumina concentration, or ACD, can be adequately represented by the simulator. However, variations with higher frequencies caused by bubbles or movement of the metal pad cannot be adequately represented as they were not considered in the design of the mathematical model. Variations in the alumina concentration caused by insufficient feedings are adequately represented by the simulator for all the four scenarios investigated. An increase of the range of alumina concentration will eventually lead to an augmentation of the standard deviation among individual anode currents caused by a redistribution of the current from regions with low alumina concentration to areas with higher concentration. The results indicate that the simulated standard deviation among individual anode currents is more sensitive to variations of the alumina concentration than the measured standard deviation in a real cell. This difference in sensitivity is beneficial for the simulator's ability

to predict low voltage anode effects, which it was able to perform with great accuracy. Henceforth, the different validations performed demonstrate that the simulator can be used to represent the alumina distribution behavior reliably in an electrolysis cell for different scenarios as well as predicting LVAEs that could occur under such circumstances.

Simulations of the alumina distribution in the cell can also be used to improve the electrolysis process for multiple scenarios. Three examples were discussed in this article where the information provided by the simulator can be beneficial for the electrolysis process. The first investigation evaluated the impact of a change of ACD and the impact of different carbon height on the uniformity of individual anode current distribution. The results indicate that a difference of approximately ±15% is anticipated, with respect to the theoretical current driven by each individual anode under operational standards. The second investigation looked at the normal feeding behavior and pinpointed specific regions of the cell which are constantly operating under lower alumina concentrations. Knowing that different solutions could be used to reduce this problem, the simulator can be used to quickly identify the best scenario and then proceed with tests at the smelters hereafter. Finally, the effect of stopping a feeder for a specific amount of time was investigated in order to correctly deal with additional amounts of alumina fed to the bath during anode change or anode covering.

6.8 References

1. A.T. Tabereaux: *JOM*, 1994. 46(11): pp. 30-34.

2. B.P. Leber Jr., A.T. Tabereaux, J. Marks, B. Lamb, T. Howard, R. Kantameneni, M. Gibbs, V. Bakshi and E.J. Dolin: *Light Metals*, 1998. pp.277-285.

3. I. Berge, R. Huglen, M. Bugge, J. Lindstrom and T.I. Roe: *Light Metals*, 1994. pp.389-392.

4. J. Marks: *Light Metals,* 1998. pp. 287-291.

5. D. Wong, P. Fraser, P. Lavoie and J. Kim: *JOM*, 2015. 67(2): pp. 342-353.

6. H. Asheim, T.A. Aarhaug, A. Ferber, O.S. Kjos and G.M. Haarberg. *7th Kyoto International Forum for Environment and Energy*, 2014. Kyoto.

7. J. Thonstad., S. Rolseth, and R. Keller: *Light Metals*, 2013. pp.883-885.

8. D. Wong. and J. Marks: *Light Metals*, 2013. pp. 865-870.

9. A.A. Zarouni, M. Reverdy, A. Zarouni, K.G. Vankatasubramaniam: *Light Metals,* 2013. pp.859-863.

10. W. Li, Q. Zhang, J. Yang, S. Qiu, X. Chen, J. Marks and C. Bayliss: *Light Metals,* 2011. pp.309-314.

11. D. Wong, A.T. Tabereaux, and P. Lavoie : *Light Metals*, 2014. pp.529-535.

12. N.R. Dando, N. Menegazzo, L. Espinoza-Nava, N. Westendorf and E. Batista: *Light Metals*, 2015. pp.551-555.

13. X. Chen, W. Li, S. Qiu, Y. Zhang, and C. Bayliss: *Light Metals*, 2013. pp. 877-881.

14. H. Asheim, T.A. Aarhaug, A. Feber, O.S. Kjos and G.M. Haarberg: *Light Metals,* 2014. pp.535-539.

15. H. Asheim, T.A. Aarhaug, E. Sandnes, O.S. Kjos, A. Solheim and G.M. Haarberg: *ECS transactions*, 2015. 69(15): pp 1-12.

16. A. Jassim, S. Ahkmetov, B.J. Welch, M. Skyllas-Kazacos, J. Bao and Y. Yao: *Light Metals*, 2015. pp. 545-550.

17. E. Batista, N.R. Dando, N. Menegazzo, L. Espinoza-Nava: *Light Metals*, 2016. pp. 537-540.

18. L. Dion, L.I. Kiss, S. Poncsák and C.-L. Lagacé: *JOM*, 2016. 68(9): pp. 2472-2482.

19. Y. Feng, M. Cooksey, and P. Schwarz: *Light metals*, 2011. pp. 543-548.

20. S. Zhan, M. Li, J. Zhou, J. Yang and Y. Zhou: *Applied Thermal Engineering*, 2014. 73(1): pp. 803-816.

21. T. Hofer: *Numerical simulation and optimization of the alumina distribution in an aluminium electrolysis pot*. PhD Thesis, 2011, École polytechnique fédérale de Lausanne: Lausanne. 121 pages.

22. J.T. Tessier, G.P. Tarcy, E. Batista, X. Wang and P. Doiron: *Light Metals*, 2013. pp. 713-717.

23. E. Skybakmoen, A. Solheim, and A. Sterten: *Light metals*, 1990. pp. 317-323.

24. Xiangwen Wang: *Light Metals*, 2009. pp.383-388.

25. B.J. Welch and G.I. Kuschel: *JOM*, 2007. 59(5): pp. 50-54.

26. Y. Feng, M. Cooksey, and P. Schwarz: *Light metals*, 2007. pp. 339-344.

27. P. Lavoie. and M. Taylor: *MOLTEN16*, 2016.

28. Y. Feng, M. Cooksey, and P. Schwarz: *9th Australasian aluminium smelting conference*, 2007.

29. L. Dion, J.W. Evans, L.I. Kiss, C.-L. Lagacé and R. Victor: *Light* Metals, 2015. pp. 723-728.

30. V. Dassylva-Raymond : *Analyse et modélisation du comportement des agrégats d'alumine dans le procédé hall-héroult*, PhD Thesis in engineering. 2015, Université du Québec à Chicoutimi: Chicoutimi, Qc, Canada. 182 pages.

31.C. Kaszás, L.I. Kiss, S. Poncsák, S. Guérard and J.-F. Bilodeau: *Light Metals*, 2017. pp. 473-479.

32. S.-O. Tremblay, D. Marceau, D. Kocaefe, C.-L. Lagacé, M. Gagnon, G. Ladouceur and F. Laflamme : *Light Metals*. 2016. pp. 959-964.

33. L. Wang, A.T. Tabereaux, and N.E. Richards: *Light Metals*, 1994. pp.177-194.

34. K. Grjotheim, H. Kvande, T. Foosnaes, R. Huglen, B. Lillebuen, T. Mellerud and T. Naterstad: *Introduction to aluminium electrolysis - Understanding the Hall-Heroult process*, ed. K. Grjotheim and H. Kvande. 1993, Düsseldorf: Aluminium-Verlag. pp. 22-24.

35. P. Coursol, P. Coulombe, A. Gosselin, D. Lavoie, J.-M. Simard, J. Marks and S. Fardeau*: JOM*, 2011. 63(8): pp. 109-105.

36. L. Dion, L.I. Kiss, S. Poncsák, C.-L. Lagacé: *ICSOBA*, 2016. Quebec City.

CHAPTER 7

PREVENTIVE TREATMENT OF ANODE EFFECTS USING ON-LINE INDIVIDUAL ANODE CURRENT MONITORING

7.1 Summary

Chapter 7 was presented at the 2017 *TMS Annual Meeting & Exhibition* conference proceedings on Light Metals and was published under pages 509-517. Its DOI number is 10.1007/978-3-319-51541-0_64.

The paper itself was written by the author of the document with minor comments and suggestions provided by the six additional co-authors: James W. Evans, Laszlo I. Kiss, Sandor Poncsak, Charles-Luc Lagacé, Antoine Godefroy and François Laflamme. Acknowledgements are, however, due to Pr. Jim W. Evans for his collaboration in the designing phase of the detection algorithm (section 7.3.3) and to Antoine Godefroy and François Laflamme for their collaboration in the designing phase of the preventive AE treatment strategy (section 7.4.1).

7.2 Introduction

In the past decades, great efforts have been deployed to reduce the greenhouse gases (GHG) emitted by the primary aluminium industry. For smelters using carbon anodes, the primary source of GHG (carbon dioxide) is inherent to the production of aluminium because the carbon participates in the electrolysis reaction. However, another kind of GHG is also associated with the primary aluminium production, namely the perfluorocarbons (PFCs). CF_4 and C_2F_6 are known to have a respective global heating potential 6630 and 11 100 higher than the CO_2 [1]. PFCs are periodically produced during an event called anode effect (AE) occurring when insufficient alumina is present in the electrolytic bath. For this reason, the molten fluoride electrolyte will dissociate to support the passage of electric charges and PFCs will be generated during this reaction. The occurrence of an AE

is dependent on the electrolysis process conditions and the total number of AEs can theoretically be minimized down to zero, even if the alumina concentration is kept below saturation in order to prevent sludge formation. Hence the reason why the efforts of the industry have been able to reduce significantly the total amount of PFCs emitted between 1990 and 2010 [2].

This paper describes the most recent efforts deployed by Aluminerie Alouette to reduce significantly the AE frequency, hence the total PFCs emissions. Using on-line anode monitoring, it is possible to use an algorithm to anticipate abnormalities that are indicating upcoming anode effects. Once the information is known that an AE is imminent, it is important to react quickly and efficiently to eliminate the abnormalities in the cell without generating perturbations that can generate other problems over a long-term period. Manual tests were performed with three different preventive AE mitigation strategies to evaluate their efficiency at unblocking alumina feeders that were not distributing alumina properly.

Finally, the system has been running automatically for almost a year on two cells equipped with online anode monitoring and very good results were achieved. Key performance indicators prior and during the test are shown and described in the last section of the article.

7.3 Early detection of the anode effects

7.3.1 Limit of detection of the current technology

The production of primary aluminium requires the passage of a constant electric current through an electrolysis bath. Passage of these electric charges is made possible by the redox reaction 7-1 that occurs in the presence of alumina. However, if the alumina

concentration is not sufficient, reaction 7-1 alone cannot withstand the passage of current and other reactants will be electrolyzed by reactions 7-2 and 7-3.

$$2\ Al_2O_3 + 3C = 4\ Al + 3\ CO_2 \qquad (7\text{-}1)$$

$$4\ Na_3AlF_6 + 3\ C = 4\ Al + 3\ CF_4 + 12\ NaF \qquad (7\text{-}2)$$

$$2\ Na_3AlF_6 + 2\ C = 2\ Al + C_2F_6 + 6\ NaF \qquad (7\text{-}3)$$

When CF_4 and C_2F_6 are generated, they will most likely stay under the anodes due to the high adhesion of those gases under carbon anodes. Because these gases have an important electrical resistivity, the electrical current will be redistributed among the other anodes, increasing their respective current density. Consequently, the alumina will deplete faster in that area, eventually leading to the spreading of reaction 7-2 and 7-3 in the cell. Hence the overall mechanism that generates PFCs is auto-amplifying if no significant change is applied to the process strategy.

As the number of anodes under which PFCs are trapped increases, it will lead to an increase of the overall cell voltage as well. However, Wong et al. [3] calculated that the voltage increase is not significant if PFCs are only located under a limited number of anodes. It was calculated that when the voltage of detection of an AE is reached at 6 volts, almost half of the anodes are already in contact with PFCs. For this reason, PFCs are very hard to detect in the initial phase of its formation, that is to say when a small number of anodes are affected. The International Aluminium Institute [4] recently adopted the term Low-voltage-Anode Effects (LVAE) to describe all PFCs emissions occurring below the voltage of detection, set by each smelter (generally 6 or 8 volts). If the threshold is reached,

all PFCs generated by this cell are then considered as High-Voltage Anode Effects (HVAE) for the duration of the AE.

Knowing that the cell voltage is a bad indicator to detect LVAE or foresee upcoming HVAE, additional information is necessary to eventually detect these abnormalities. Rye et al. [5] demonstrated that a low alumina concentration can have an impact on the current distribution among the anodes. More importantly, it was shown that prior to an anode effect, several anodes will significantly change their current load, indicating that the event (AE) can be detected prior to the usual shift in cell voltage. Other studies confirmed [6, 7] that online measurements of individual anode currents is a viable solution to preventively detect anode effects.

7.3.2 **Variations of individual anode currents during LVAE.**

Figure 7-1 illustrates that the local current (left axis) drops significantly for some anodes during LVAE. In this case, as the CF_4 concentrations (right axis) rose from 0.2 ppb up to 1.5 ppm, the current from anode A16 and A17 respectively decreased by 50% and 15%. After this quick surge in emissions, CF_4 remained under A16 and A17 and thus increased the local electrical resistance. Hence the current has been redistributed according to the respective resistance of all anodes and the production of aluminium continued under these new conditions. The same phenomenon occurred two more times before the cell finally reached an HVAE six hours later. Only at that moment, the anode effect stopping procedure was started to resolve the problem. Any similar procedure launched during any of the three LVAE that occurred before the HVAE could have eliminated several hours of PFC emissions as well as the HVAE itself.

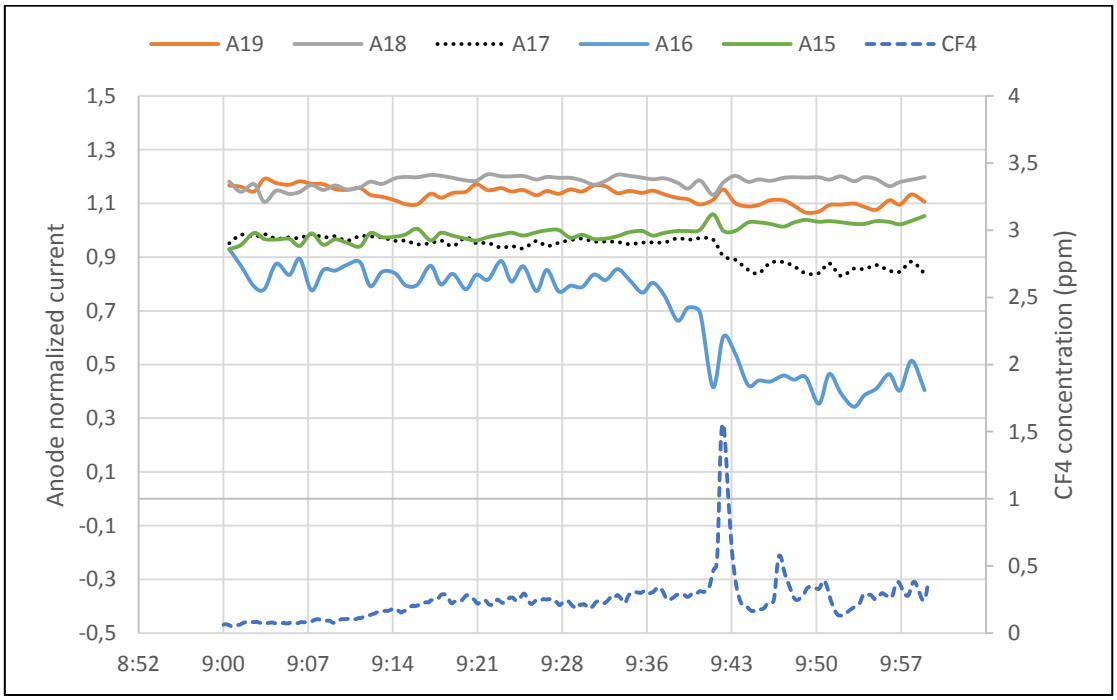

Figure 7-1 : Individual anode currents and CF_4 concentration from a single electrolysis cell during LVAE.

7.3.3 **Development of the detection algorithm**

In order to solve the problem discussed in the previous section, an algorithm was developed to detect any sudden change in individual anode currents that are related to an anode effect, with the main focus being the prevention of HVAE. Two different sets of conditions need to be reached for the cell to be considered close to an AE. The first condition is similar to the methodology published in 2015 by Dion et al. [7]. It involves the use of a short-term (1 – 5 minutes) and a long-term moving average (15 - 25 min) for each individual anode. It is possible to observe in Figure 7-2 that the current behavior[30] is significantly different in the short-term moving average (STMA) in comparison to the long-

[30] It is possible to observe a significant drift in current around 4:35. If the short-term moving average is short enough, such variations should significantly change its value in comparison to the long-term moving average.

term moving average (LTMA) used as the reference. Henceforth, once the ratio STMA/LTMA has reached a predetermined threshold for a specific number of anodes, the first condition of the algorithm becomes satisfied.

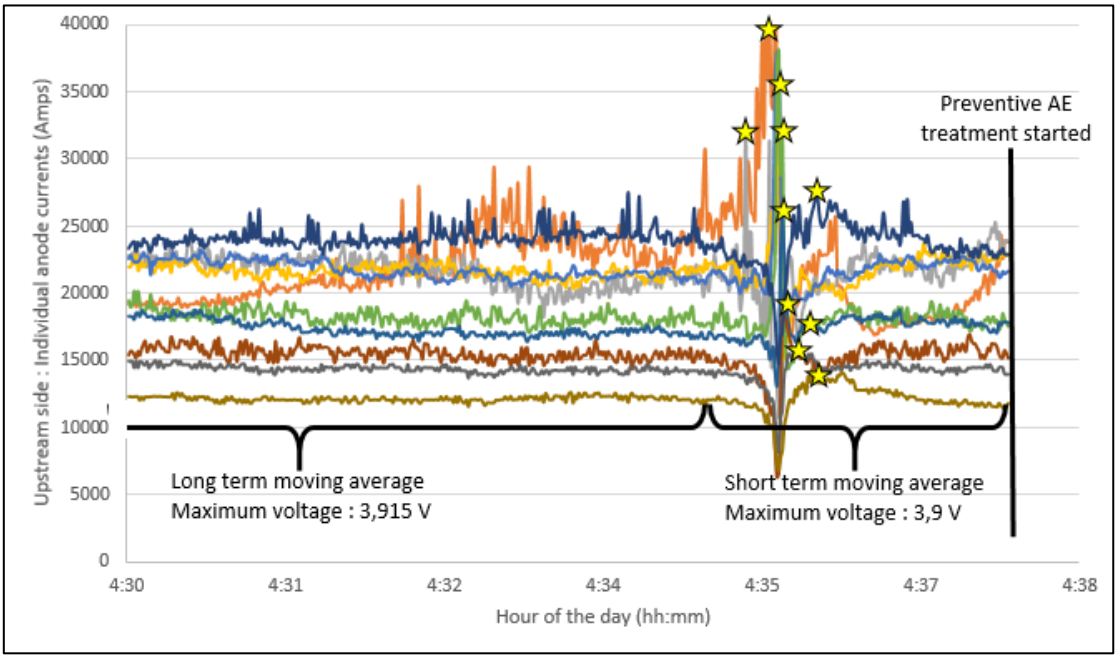

Figure 7-2 : Illustration of a cell behavior leading to preventive AE treatment. Upstream side. (Stars represent maximum current values reached for each individual anode during the short period.)

Using exclusively the first condition is sufficient to detect upcoming anode effect but it can also generate false alarms by detecting other events in the cell such as anode change, metal tapping or cell instability. To maintain the same detection sensitivity, an additional condition was established which can be attributed most likely to the generation of PFCs. This second condition investigates the maximum current value of each anode within a short period similar to the STMA. It was observed that the current value of each anode tends to reach a higher value than its reference state during an AE. This phenomenon is linked to the current redistribution that occurs when resistive gas is moving under the

anodes and can occur very quickly (less than 5 seconds). Hence it might have no significant effect on the average value of each respective anode. Figure 7-2 clearly demonstrates that 6 anodes out of 10 temporarily reached a maximum higher than the anode that is driving the most current in the LTMA period. Moreover, all the maximum values were measured within a two-minute interval.

Finally, if both conditions are satisfied for a specific cell, it is highly plausible that PFCs are generated under its anodes. Hence, if adequate actions are undertaken at this moment, the PFC emissions from this cell can be significantly reduced.

7.4 Establishment of the Preventive AE Treatment

Numerous elements have to be considered to develop a preventive AE treatment. It has to react quickly enough to eliminate any imminent AE but the treatment itself must be controlled so that it does not bother the cell significantly over a long period if numerous preventive AE treatments are launched. AE are essentially caused by an insufficient amount of alumina dissolved in the bath in a small region or in the entire cell. This lack of alumina can be caused by conditions such as low bath height or low bath temperature in the cell that makes the transport or dissolution of particles difficult in certain regions of the cell. The preventive AE treatment should be designed to assure a decent amount of alumina dissolves into the bath under a short time period to correct the situation.

In another case, an insufficient amount of alumina can be fed to the cell to compensate the necessary consumption from the electrolysis. This problem generally occurs when an alumina feeder hole is obstructed by an excessive amount of alumina. This phenomenon occurs when bad dissolution conditions are present and thus the alumina

becomes compacted by the repeated actions of the crust breaker. Under such conditions, the alumina is shaped like a mound, starting from the cathode up to the alumina feeding chute. Simulation performed by Dassylva and al. [8] showed that if the alumina is clumped, the dissolution efficiency is significantly reduced. In reality, such circumstances cause even poorer conditions than that suggested by the simulations, therefore the alumina dissolves slower than it is fed, causing an accumulation. Usually, a manual intervention is necessary to resolve the problem in such situation. However, the preventive AE treatment should be designed to unblock the majority of feeders facing this problem.

7.4.1 **Preventive AE Treatment Parameters**

To design the preventive AE treatment, the ensemble of parameters that can be controlled are divided into three different categories. For each of them, there are specific considerations to take into account when establishing the preventive AE treatment.

Alumina feeder actions: once an alarm is sent to the cell control system, commands such as ‘’stopping or changing the rate of injections’’ can be sent to the crust breakers and the alumina feeders. Knowing that a lack of alumina is probably the root cause of the problem, launching overfeeding appears as the logical step to quickly solve the problem. However, such action could easily make the cell’s conditions worse for two sets of circumstances that are likely to occur. If a feeding hole is blocked, this solution will only increase the pile of alumina above the crust. It will also increase the risk of blocking other feeders. Additionally, if a false alarm occurs, the additional alumina could increase the alumina content in the bath close to the solubility limit. Therefore, the preventive AE treatment could generate muck in the cell, which would likely increase the instability and

might cause additional false alarms, and so on. For these reasons, actions from the feeders should be defined with great care and at the same time, other ways to route alumina should be considered.

*Quenching procedure*s: movement of the anode beam has been used for years in the industry to help cure AE. Generally, quenching is composed of several up-and-down motions of the anode beam to help clear out the gas from under the anode. In addition to this positive effect, it increases the movement of the bath, in favor of the dissolution of alumina. Moreover, as the anodes are immersed into the bath, the liquid level is higher, and bath can get more easily in contact with the crust. This crust is composed of a substantial amount of alumina which then contributes to the alumina input. However, excessive movements of the anode beam can cause severe disruptions in the anode cover, exposing the anodes to increased oxidation while threatening the thermal balance of the cell. Downward movements can also compress the anode against the side ledge, causing solidified bath to stick under the anodes, increasing instability and eventually leading to anodic incidents (spikes). Finally, in the worst-case scenario when bath levels are low and when anode beam movements are badly set up (e.g. significant displacement upwards), it could lead to a rupture of the circuit (anode out of the bath); an event that must be avoided at all costs. Therefore, movements of the anode beam need to be set correctly for the treatment to assure an adequate solution.

Additional energy input: Another adjustable element is the energy input in the cell. It is possible to increase the anode-cathode distance (ACD) for several hours in order to increase the internal heat in the cell generated by Joule effect. Additional energy will play a

positive role in the dissolution of the alumina. Moreover, the additional volume of bath under the anode (higher ACD) will favor the transport of alumina to a region further away from the feeders. On the other hand, additional energy might disrupt the thermal balance of the cell. More importantly, it can melt away the side ledge and expose the sidewalls of the cell to the electrolyte. Energy inputs are not a short-term solution to prevent imminent AE and could be used as a final step to the preventive AE treatment.

7.4.2 **Efficiency of AE Treatments to Unblock Feeder Holes**

By considering the numerous elements presented in the last section, Aluminerie Alouette tested three different preventive AE treatment algorithms to evaluate their respective efficiency to unblock feeder holes. During the duration of all the 3 treatments, no alumina is fed into the cell. However, the action of the crust breaker is maintained active in order to push some alumina into the bath while movements of the beam allow for an increased contact between the electrolyte and the undissolved alumina. The main difference of the treatments resides in the quenching pattern illustrated in Figure 7-3. The goal was to test a “non-aggressive” (A) and two “aggressive” treatments (B & C) respectively. Treatment B has a high number of quenching cycles and treatment C has a larger amplitude in the movements of the anode beam. No additional energy was added to the cell after these treatments.

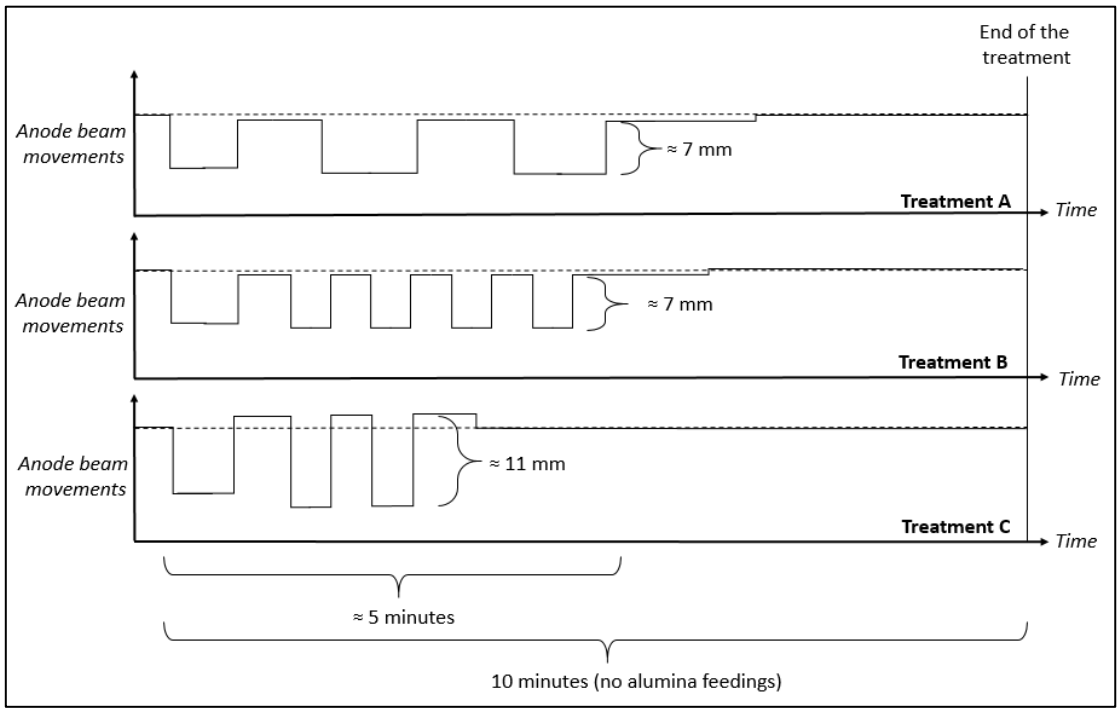

Figure 7-3 : Illustration of three different preventive anode effect treatment procedures.

During several weeks, manual tests were performed to evaluate the capability of each treatment to unblock feeder holes. When a feeder was observed in conditions similar to Figure 7-4-A), a preventive AE treatment was manually initiated on this cell to observe its effect on the feeder hole. In addition, the bath level was measured prior and after the treatment for supplementary information.

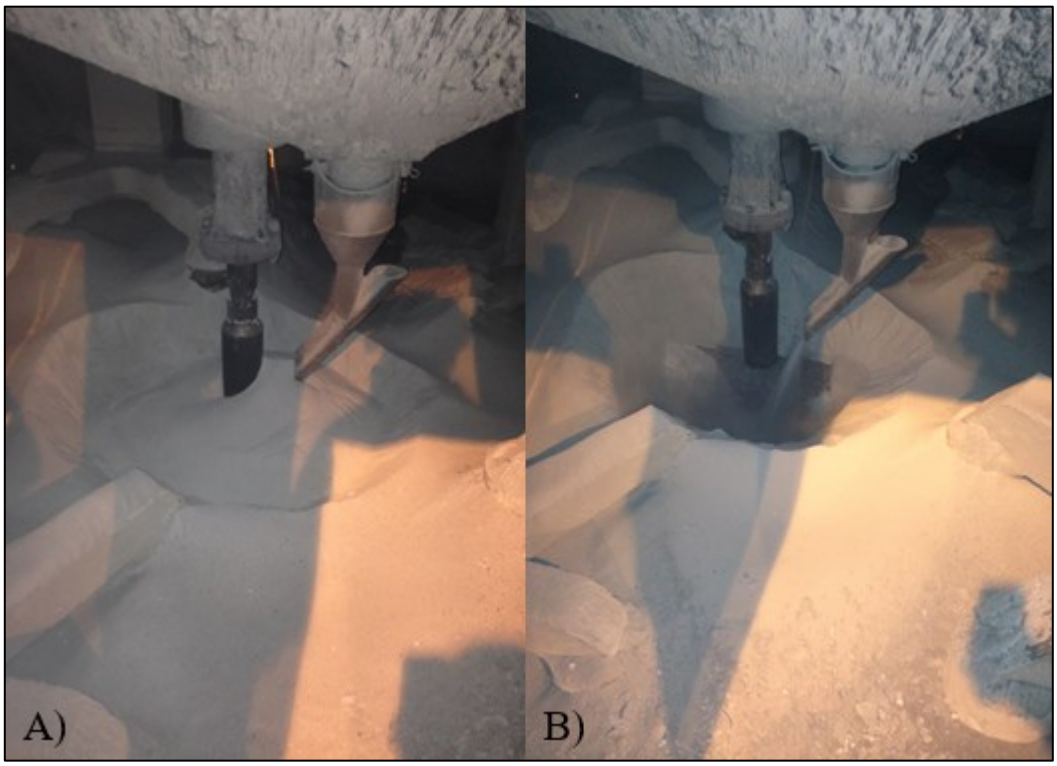

Figure 7-4 : Illustration of a feeder before and after a preventive AE treatment. A) Blocked feeder. B) Unblocked feeder after a successful treatment.

The results shown in Table VII indicate that the three preventive AE treatments were successful in unblocking feeder holes for the majority of the cases. Results from treatment B showed an important increase in the efficiency of the preventive AE treatment to unblock the holes while the results from treatment C were slightly lower than the results from treatment A. Therefore, it is possible to determine that the number of quenching cycle is the most important parameter in favor of unblocking feeder holes. Moreover, a certain amount of time is necessary to allow for the dissolution of anode cover material and alumina. The results from treatment C indicate that a larger amplitude of the anode beam movement is not as efficient as a longer quenching period.

Bath level measurements performed during the tests indicate that the bath level difference occurred after treatment B was applied to the cell. On the other hand, the average bath level difference between each group is significantly smaller than the respective standard deviation of each treatment. For this reason, the average bath level difference between each group cannot be considered as significant.

Table VII : Success rates and the difference in bath levels for the tested preventive AE treatments.

	Treatment A	Treatment B	Treatment C
Success rate (%)	68	90	60
Average Bath Level Difference (after - before) (cm)	-0.25	0.30	-0.39
Bath Level Difference Standard Deviation (cm)	0.73	1.30	0.95
Number of Feeders Tested	57	30	25

It is important to take into consideration that these tests represent the conditions subsequent to a preventive AE treatment. In some cases, it is possible that the feeding holes might be blocked again, thus the interest in temporarily adding some energy to the cell. Moreover, the preventive AE treatment will not be efficient enough if a mechanical problem is present in the cell (e.g. feeder malfunction) or if the bath level remains significantly too low. However, the preventive AE treatments are registered as an intervention in the cell control system. Hence, multiple preventive AE treatments will send an alarm to the process technicians and actions can be undertaken to address the problem. Henceforth, the preventive AE treatment allows for additional time to operate without the negative impacts of AE occurring in the cell.

7.5 Key Performance Indicators of Cells With Automatic AE Treatment

To evaluate the effectiveness correctly of the preventive AE treatment, the algorithm was connected to the cell control system on two cells to launch automatically the preventive AE treatment when required. A close follow-up of the performance indicators of the selected cells will allow for a better evaluation of the overall efficiency of such treatment during several months of operations.

To perform this analysis, two cells were implemented with automatic AE detection and preventive AE treatments. For comparison, 5 other cells were monitored as a reference. All of these 7 cells are part of the AP40LE technology, using four point-feeders and prebaked anodes. The current intensity of all these cells remained at the same level for the entire period. Finally, process parameters such as bath and metal level, temperature target, etc. were also similar for all the cells.

For comparison, four different periods were selected. Period #1 was the reference period where no actions were taken on the cell related to the preventive AE treatment. In period #2, preventive AE treatment was active for both test cells in the preliminary phase of the project. Then in period #3, optimizations were performed on the system to increase the detection efficiency. For periods #2 and #3, preventive AE treatment A was activated once an imminent AE was detected. Finally, in period #4, the same parameters remained for the detection of AE but preventive AE treatment B was active. However, one of the two test cells was excluded from period #4. For this cell, the results were not representative of the preventive AE treatment's real potential due to a significant number of mechanical

problems that occurred in this cell. The specific duration of each period is listed in Table VIII and the key performance indicators for all periods are listed in Table IX.

Table VIII : Details on the four periods selected for testing the preventive AE treatments.

Periods	Active treatment protocol	Start date	End date	Total number of days
1	None	2015/09/01	2015/12/10	101
2	Treatment A	2015/12/17	2016/03/31	106
3	Treatment A (with optimized detection)	2016/04/01	2016/06/14	75
4	Treatment B (with optimized detection)	2016/06/15	2016/08/20	66

Table IX : Comparison between the test group and reference cells over four periods.

	Period #1		Period #2		Period #3		Period #4	
	Reference cells	Test cells	Reference cells	Test cells	Reference cells	Test cells	Reference cells	Test cells
Total number of AE (AE/cell*day)	**0.89**	**0.90**	**0.68**	**0.36**	**0.49**	**0.18**	**0.68**	**0.16**
Standard Deviation	*1.51*	*1.48*	*1.17*	*0.79*	*1.02*	*0.45*	*1.11*	*0.44*
Anode effect overvoltage (mV)	**1.81**	**2.39**	**0.92**	**1.05**	**2.08**	**0.39**	**1.18**	**0.70**
Standard Deviation	*6.25*	*7.30*	*2.44*	*5.23*	*21.85*	*1.37*	*3.06*	*2.90*
Cell instability (nanoOhms)	**121**	**94**	**102**	**64**	**95**	**55**	**124**	**58**
Standard Deviation	*74*	*71*	*56*	*24*	*58*	*28*	*63*	*40*
Additional energy input (microOhms)	**0.056**	**0.046**	**0.051**	**0.034**	**0.049**	**0.032**	**0.053**	**0.030**
Standard Deviation	*0.036*	*0.028*	*0.028*	*0.024*	*0.049*	*0.018*	*0.023*	*0.018*
Daily mass of bath produced (kg/cell*day)	**50**	**29**	**52**	**42**	**94**	**130**	**48**	**60**
Standard Deviation	*292*	*224*	*334*	*209*	*290*	*260*	*297*	*230*
Number of alumina doses (doses / day)	**5692**	**5684**	**5753**	**5781**	**5628**	**5617**	**5679**	**5688**
Standard Deviation	*347*	*323*	*358*	*218*	*398*	*258*	*362*	*203*
Parasite alumina feeding indicator	**5.81**	**6.55**	**4.85**	**4.55**	**6.50**	**7.41**	**5.93**	**5.88**
Standard Deviation	*3.80*	*4.25*	*4.01*	*1.94*	*3.67*	*2.67*	*4.56*	*1.63*
Iron level in aluminium (ppm)	**650**	**475**	**506**	**516**	**678**	**582**	**800**	**720**
Standard Deviation	*182*	*106*	*123*	*72*	*139*	*162*	*123*	*263*
Number of anodic incidents (Normalized to potline average)	**165%**	**110%**	**131%**	**72%**	**81%**	**65%**	**146%**	**7%**
Standard Deviation	*329%*	*223%*	*279%*	*182%*	*234%*	*187%*	*308%*	*55%*

The principal performance indicators that were investigated are the total number of anode effects and the anode effect overvoltage. The results (illustrated on Figure 7-5) clearly indicate that a significant change occurred once the system was fully operational. The daily number of AE was similar to the reference cells in period #1 and dropped significantly in periods #3 and #4. It illustrates the effectiveness of the algorithm to detect AE as well as the efficiency of the preventive AE treatment to eliminate the threat before the event occurs. Moreover, the AE overvoltage significantly dropped alongside the total number of AE indicating that the magnitude of the anode effects that still occurred was not

worse than usual. Hence by considering that the total PFC emissions are calculated based on a linear relation between a predetermined factor and this indicator, the results confirm that fewer PFCs are produced when using this system. However, to accurately quantify the reduction, on-line gas measurements monitoring should be performed to account for the low voltage anode effects as well.

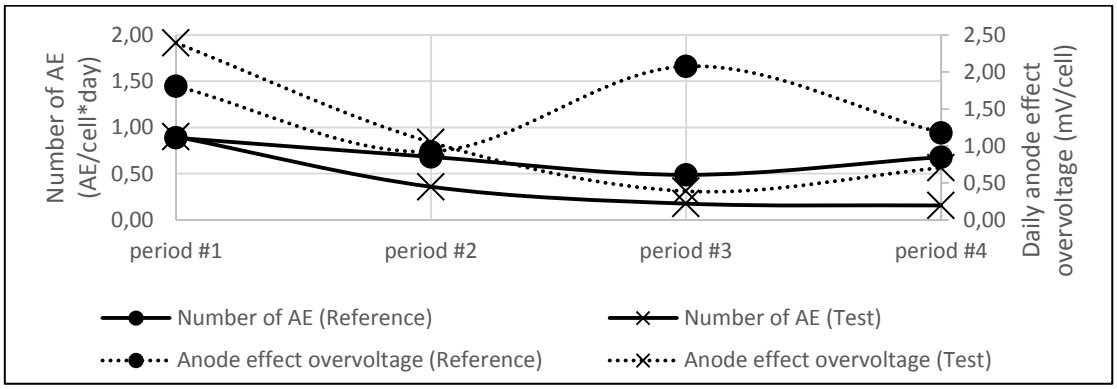

Figure 7-5 : Performance indicators related to anode effects for the four periods of testing.

A positive effect was observed on the cell stability when using preventive AE treatments. Even if the instability of the test cell were lower than that of the reference in the control period, the difference increased while the preventive AE treatment was active. More importantly, the standard deviation of this variable was reduced significantly indicating that values are less scattered and closer to the average, hence confirming the increase in cell stability. With the active preventive AE treatment, it is launched in the beginning phase of LVAE or HVAE. Therefore, the cell can recover quickly and remains stable, instead of being unstable for plausibly several hours. Additionally, when the cell is unstable, a resistance increase is introduced into the cell by the control system, consequently increasing the ACD and thus adding some extra energy to the bath. In periods #2, #3 and #4, this additional energy input was significantly reduced due to an increased stability.

The quenching effect of the procedure is designed to consume part of the anode cover. For this reason, the daily production of bath is higher with the active preventive AE treatment. However, when this treatment will be applied to multiple cells, it will be possible to adjust the crushed bath and alumina ratio from the anode cover material to account for the effect of the preventive AE treatments. A correlation can be observed between the daily mass of bath produced and the parasite alumina feeding indicators. Therefore, even if the number of alumina feedings slightly decreased for some period, it was simply replenished from another source. Overall, the alumina fed to the electrolysis cell remained similar to the reference cells, hence we can assume that the metal production was equivalent as well.

Finally, the quenching of the anode beam could lead to an increased bath exposure of the anode stubs or to an increase in the frequency of anodic incidents. However, during our tests, no undesirable difference between the reference and the test cells was observed. Therefore, it indicates that under the tested conditions, the preventive AE treatment generates no negative effect regarding these indicators. It is important to mention that some data were intentionally excluded from this analysis if the iron contamination came from an excessive exposure of the stubs that was not a result of the quenching procedure. Such exposure could be caused by a failure of the clad or if the anode detached from its stubs.

7.6 Conclusion

A successful preventive treatment procedure was presented in this paper to minimize the occurrence of anode effects. This procedure is based on an algorithm that detects the variation in the individual anode currents that indicates an anode effect is about to occur. It is effective to detect both low voltage and high voltage anode effects. This

algorithm then sends an alarm to the cell control system and a preventive AE treatment can be initiated on the cell to avoid the negative impact caused by an AE.

Three different preventive AE treatment procedures were tested to evaluate their ability to unblock feeder holes. A success rate ranging from 60 to 90% was observed. Additionally, two different preventive AE treatment procedures were tested and automatically launched on two cells for several months to assess the overall performance of these cells on a long-term basis. The results indicate that a significant decrease in the total number of AE is observed. This outcome is also observed in the anode effect overvoltage which confirms that fewer PFCs are generated from high-voltage anode effect on the cells with the preventive AE treatment active.

Moreover, a positive effect was observed regarding the cell stability and for this reason, a smaller amount of extra energy was added to the cell. However, bath production increased with the preventive AE treatment. No negative effect from the preventive AE treatment was observed regarding the total number of alumina doses, the total number of anodic incidents or regarding iron contamination.

With the positive results obtained in the initial phase of this project, Aluminerie Alouette plan on stepping up the number of cells using the proposed methodology in the near future. More cells will allow to correctly evaluate the economic gain from such procedure for a whole pot room, hence justifying a part of the investment cost necessary to implement continuous anode current monitoring across the entire smelter.

7.7 References

1. Myhre, G., et al., Anthropogenic and Natural Radiative Forcing., in Climate Change 2013:The Physical Science Basis. Contribution of Working Group I to the Fifth Assessment Report of the Intergovernemental Panel on Climate Change, T.F. Stocker, et al., Editors. 2013, Cambridge University press: Cambridge, United Kingdom and New-York, NY, USA.

2. Fischedick, M., et al., Mitigation of Climate Change. Contribution of Working Group III to the Fifth Assessment Report of the Intergovernmental Panel on Climate Change. 2014, Cambridge University press: Cambridge, United Kingdom and New-York.

3. Wong, D., A.T. Tabereaux, and P. Lavoie. Anode effect phenomena during conventional AEs, low voltage propagating AEs & non-propagating AEs. in Light Metals (2014: San Diego,USA), 529-535.

4. International Aluminium Institute, Workshop on low voltage emissions of PFC, Workshop attendees. (2015: London, UK).

5. Rye, K.Å., M. Königsson, and I. Solberg. Current redistribution among individual anode carbons in a Hall-Heroult prebake cell at low alumina concentrations. in Light metals. (1998),241-246.

6. Welch, B.J. Quantifying PFC emissions from smelter cells. in Proceedings of the 10th Australasian aluminium smelting conference. (2011: Launceston, Tasmania).

7. Dion, L., et al. On-line Monitoring of Anode Currents to Understand and Improve the Process Control at Alouette. in Light Metals. (2015: Orlando,USA), 723-728.

8. Dassylva-Raymond, V., et al. Modeling the behavior of alumina agglomerate in the Hall-Héroult process. in Light Metals. (2014: San Diego,USA), 603-608.

CHAPTER 8
CONCLUSIONS AND RECOMMENDATIONS

8.1 Conclusions

As indicated in chapter 0, three different themes were considered in this project, and specific goals were defined for the project to be considered successful.

The first goal was to suggest improvements to the existing techniques used to quantify PFC emissions generated during high voltage anode effects. Chapters 2 and 3 clearly demonstrated an increase in accuracy of more than 50% when using non-linear approaches instead of the linear models currently used in the industry to estimate PFC emissions resulting from HVAE. It was also demonstrated that the polarised anode effect duration is an adequate indicator of PFC emissions for a specific smelter. However, results demonstrated that the daily metal production has a strong influence on the PFC emission rate during HVAE. Thus, the most favorable model developed within the scope of this project is dependent on two variables: the polarized anode effect duration and the daily metal production of the cell. This model showed consistent results for seven different smelters with different line amperage going from 70 to 440 kiloamperes. The proposed model could be incorporated into the cell control system to automatically quantify PFC emissions for each individual cell, thus leading to more accurate information for the process control team.

The second goal of this thesis was to investigate the phenomenon known as low voltage anode effects. An algorithm was developed and validated using fifteen different operational scenarios lasting from several minutes to multiple hours. The obtained predictive accuracy was evaluated as ±25% for two-thirds of the scenarios investigated. As it was the first published quantitative LVAE emissions model, this model can be considered

a significant lead in the understanding of LVAE generation mechanisms. With this algorithm, the standard deviation from individual anode currents was pinpointed as the main indicator to detect LVAE in electrolysis cells, with an effect three times more important than any other indicators investigated.

Additionally, the representativeness of performing gas monitoring on individual cells was evaluated based on the available gas extraction point. The results clearly indicate that the measurements are not representative of the overall cell behavior if hoodings are not perfectly positioned. Moreover, the measuring technique is also inadequate to correctly quantify localized emissions occurring in specific regions of the cells. Cross-effects between position and hooding conditions can lead to a ±100% variation of the measured gas concentration in comparison to the expected value. This lack of representativeness can explain an important fraction of the errors observed when validating the LVAE predictive algorithm. For this reason, instead of using a single sampling probe to extract the gas, a more appropriate methodology using five sampling probes was proposed to assure representativeness. This methodology was tested and more accurate results were acquired.

With regards to the third goal of this project, a transient simulator was developed to represent the cells behavior in terms of alumina and current distribution. In this simulator, the electrolysis cell is considered as twenty different regions with their own specific properties such as alumina concentration, undissolved alumina agglomerate, and current density. A simplified electrical model considers the shift in electrical resistance caused by different conditions to re-evaluate the current distribution amongst the different anodic

assembly. Hence, based on the current distribution, LVAE may be predicted if there is significant inhomogeneity within the cell.

Validations proved that the simulator is efficient to represent drift in alumina concentration caused by different feeding strategy. Moreover, there is good agreement with the LVAE predictive ability of the simulator and measurement of the gas composition at the duct end of the electrolysis cell. The simulations demonstrated that the results are more sensitive to the standard deviation among individual anode currents in the simulator than in real cells. This variation in sensitivity is caused by various elements (metal pad instability, different local ACD, etc.) that were not incorporated in the simulator. Such phenomenon increase the normal value of this indicator in real cells, thus lowering its sensitivity to small variations. Nonetheless, the additional sensitivity from the simulator is beneficial to investigate LVAE emissions, proving that the developed tool can predict LVAE while simple indicators from the real cells are still inadequate. Simulations performed with the simulator can lead to improvements in the process by adjusting the feeding strategy during critical parts of the operations; for example, following anode changes or during the underfeeding phase of the alumina. Such improvements should lead to a reduction of LVAE and HVAE frequencies due to a better redistribution of the alumina. Additionally, the simulator can quantify the unavoidable but expected change in current distribution caused by standard procedure of the electrolysis process such as anode change, different carbon heights or ACD variations.

Additionally, a fourth goal was also achieved within the scope of this Ph.D., although unspecified in the academicals objectives of the project. Individual anode current

monitoring performed during the experimental phase allowed to identify typical patterns during the initial phase of LVAE and HVAE. Collaboration with the industrial partner has allowed the development of an on-line algorithm to identify imminent high voltage anode effect and part of the low voltage anode effect occurrences. Additionally, a quenching procedure was developed to act upon detection of imminent AE and eliminate the problem before it perturbs significantly the cells behavior. This protocol was tested on two electrolysis cells and the results demonstrated a reduction of AE frequency ($\Delta\approx$ 0.3 AE / cell*day), a reduction of the AE overvoltage ($\Delta\approx$48 mV), and an reduction of the cells instability ($\Delta\approx$40 nanoOhms) without negative impact on other key performance indicators.

To conclude, the different tasks performed during this project were sufficient to identify key indicators of PFC generations while theoretical and industrial tools were developed to predict and reduce this type of GHG emissions. Thus, fulfilling all the initial expectations and demonstrating the positive effect of a successful collaboration between the academia and an industrial partner.

8.1.1 List of Innovative Realisations Performed During this Project.

In the scope of this project, numerous concrete achievements were accomplished in favor of the general progress of science, thus fulfilling an essential requirement of a doctorate thesis.

1. Proposition of generic non-linear models to estimate CF_4 and C_2F_6 emissions during high voltage anode effects. (section 3.6.1)
2. Development of a decomposition method to respectively associate emissions from high voltage anode effect to their respective cells when emitted simultaneously. (Section 2.4.2)
3. Demonstration of a phase shift between CF_4 and C_2F_6 when gas is routed from the electrolysis cell up to the FTIR gas analyzer while passing through a gas treatment center[31]. (Section 2.7.1)
4. Development of an algorithm to predict and quantify low voltage CF_4 emissions occurring from single cells based on individual anode current monitoring and the cell voltage. (Chapter 4)
5. Standard deviation amongst individual anode current was pinpointed as the main indicator of the presence of low voltage anode effects in an electrolysis cell. (Chapter 4.6.2)
6. Evaluation of the cell's representativeness when gas extraction occurs at the duct end of an electrolysis cell and suggestion of an improved gas extraction protocol. (Chapter 5)
7. Development of a simulator to illustrate the non-homogeneous distribution of the current, and the alumina within an electrolysis cell with a novel approach using only a limited number (20) of different volumes. (Chapter 6)
8. Development of an efficient simulator to predict the occurrence of low voltage PFC emissions for different operational scenarios. (Chapter 6.5.4)
9. Industrial development and optimisation of an imminent anode effect detection algorithm based on individual anode current monitoring. (Section 7.3.3)
10. Industrial development and implantation of a preventive quenching procedure to eliminate threats of anode effects to reduce PFC emissions and increase cells stability. (Section 7.4-7.5)

---

[31] Additional investigations should be performed to correctly understand the mechanisms leading to this phenomenon.

8.2 Suggestions for Future Developments

Unfortunately, due to the limited time frame of a Ph.D. project, many of the ideas for improvements that were discussed could not be tested or implanted. Nonetheless, a summary of the most important ideas is reported in this section to suggest improvements paths for future researchers working in similar fields, or using the tools developed in the scope of this project, or similar ones.

8.2.1 **Estimation of HVAE Emissions.**

1. The K1 and K2 coefficients from equations 3-15 and 3-18 should be defined with a more important database of smelters to increase the overall precision of the models.
2. Additional data would be beneficial in the upper range of polarised anode effect duration for increased predictive accuracy.
3. The common anode effect definition standard should be standardized among the worldwide aluminium industry. A common trigger threshold should be used and the polarised anode effect duration should include the initial detection period.
4. Individual high voltage anode effect PFC quantifications should be implanted into the cells control system for automatic calculations of both CF_4 and C_2F_6.
5. The mechanism leading to generation of CF_4 and C_2F_6 should be investigated on individual cells to deepen the understanding of the mechanisms.
    a. Determine if there is a phase shift between the emission of CF_4 and C_2F_6.
    b. Determine if additional variable should be considered to increase the accuracy of a predictive model such as maximum voltage, anode effect overvoltage, or anode effect energy.

8.2.2 **Estimation of LVAE Emissions.**

1. Gas composition monitoring performed on individual cells should use an adequate technique to be representative of the overall cell emissions.
2. Multivariate analysis should be used again to strengthen the understanding of LVAE emission behaviors using data collected using an optimal extraction technique.
3. Individual anode current monitoring should be considered as a critical component of any LVAE study.

8.2.3 **Simulator of Alumina and Current Distribution.**

1. The simulator should be exploited by process technicians and engineers in order to optimize the pot lines performances.
2. Optimizations of the current existing modules from the simulator should be performed to enhance its accuracy.
    a. Consideration of the secondary conductors as part of the electrical network of the cell ***or*** evaluation of the bias caused by the approximation.
    b. Usage of a more realistic alumina clump geometry (cylindrical, multiple spheres, etc.) to simulate alumina dissolution.
    c. Perform MHD analysis to determine the specific convective loop, and bath velocity of the AP40LE cell technology and incorporate this pattern into the simulator.
    d. Perform alumina dissolution experiments to determine the dissolution coefficients specific to the technology used.
    e. Optimize the exchange mechanisms for the transport of solid alumina.
    f. Improve the F-factor equation based on localized measurements instead of using the pseudo-resistance of the cell.
3. Additional elements should be incorporated into the simulator to optimize its performance or increase its potential.
    a. Incorporation of an HVAE simulation module.
    b. Introduction of a function for the current pick-up of a newly posed anode.
    c. Introduce a function to simulate different local ACD based on permanent metal pad deformation or metal wave instability.
    d. Introduce variations of the local current efficiency based on localized properties. Hence during LVAE, some re-oxidation of the aluminium should occur in these regions.
    e. Incorporation of an exchange mechanism for undissolved alumina with the metal pad to consider a possible generation of sludge under specific conditions.
    f. Incorporation of an energy balance into the simulator.

APPENDIX A – REFERENCE SPECTRA USED DURING FTIR ANALYSIS

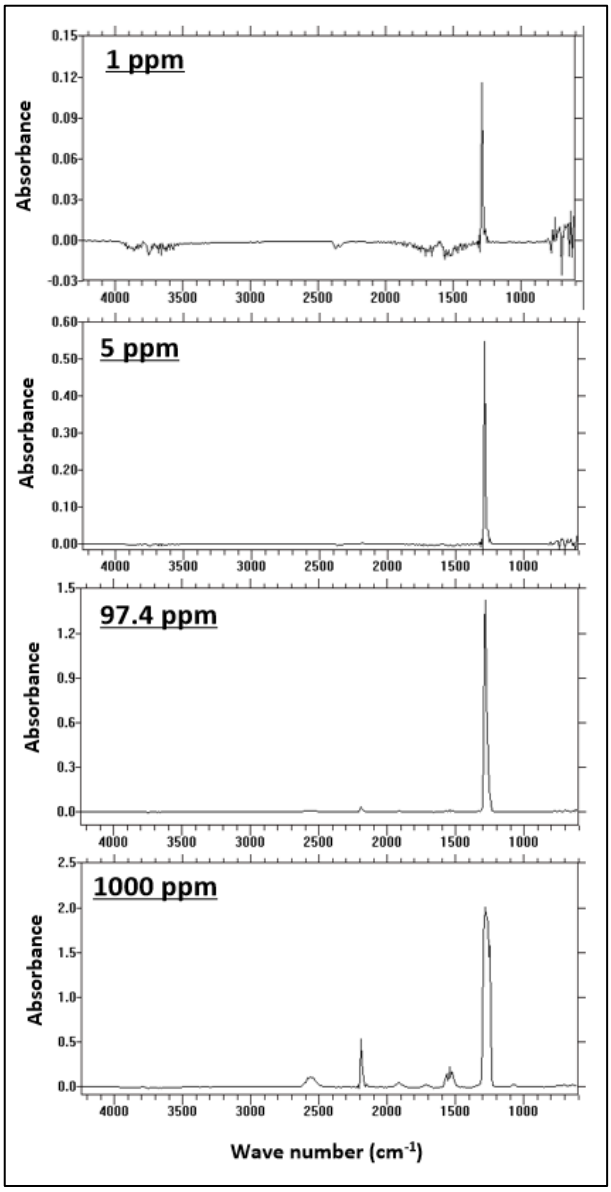

Figure A-1: CF_4 reference spectra used during FTIR analysis

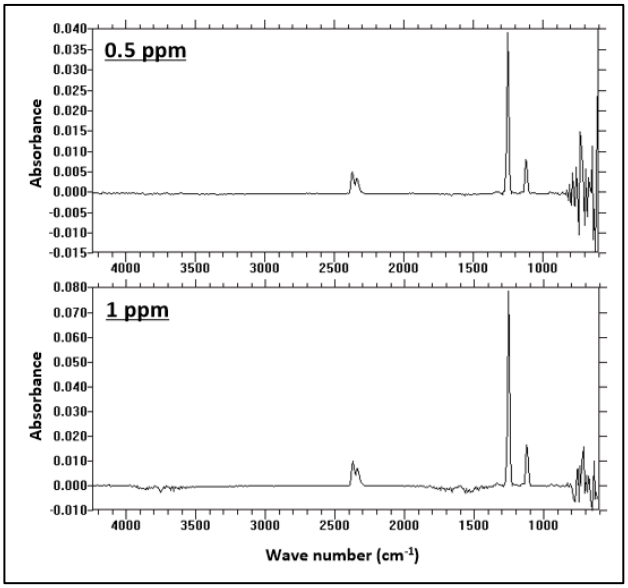

Figure A-2: C_2F_6 reference spectra used during FTIR analysis.

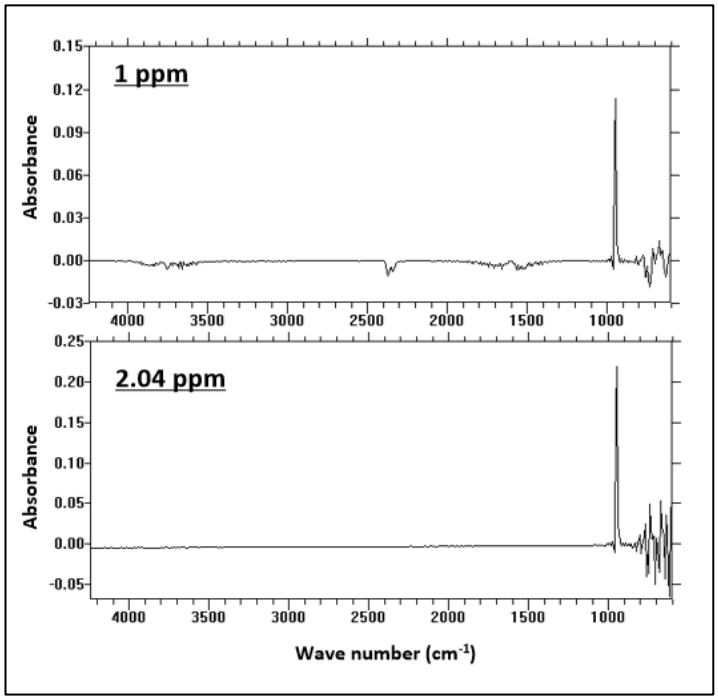

Figure A-3: SF_6 reference spectra used during FTIR analysis.

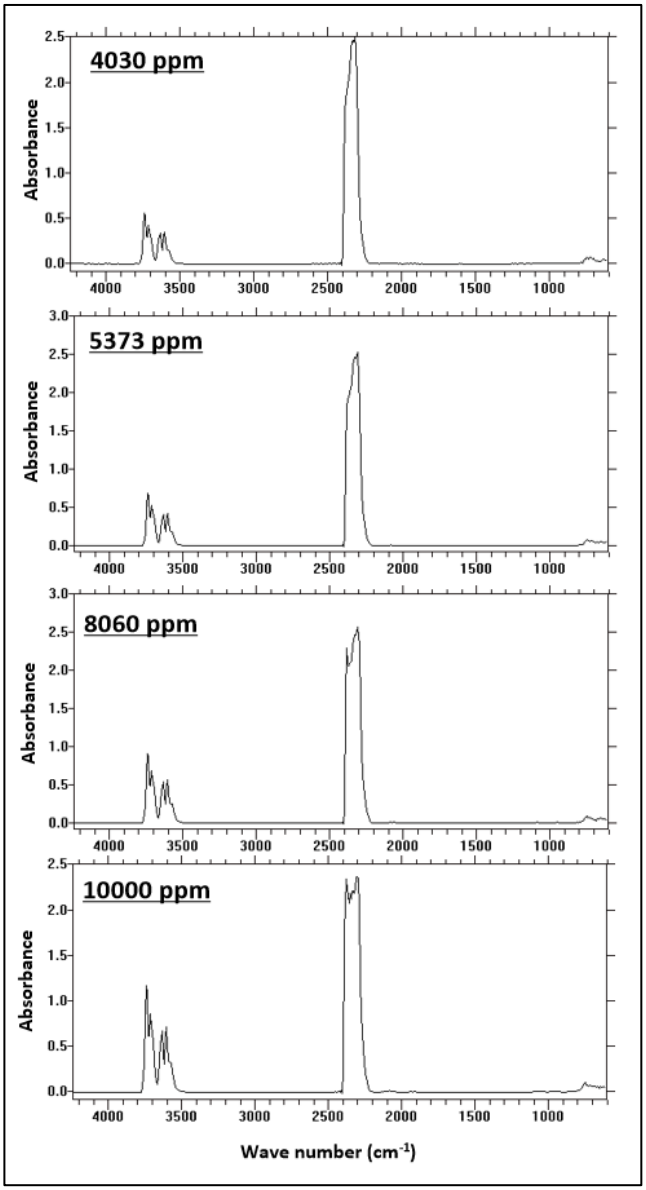

Figure A-4: CO_2 reference spectra used during FTIR analysis.

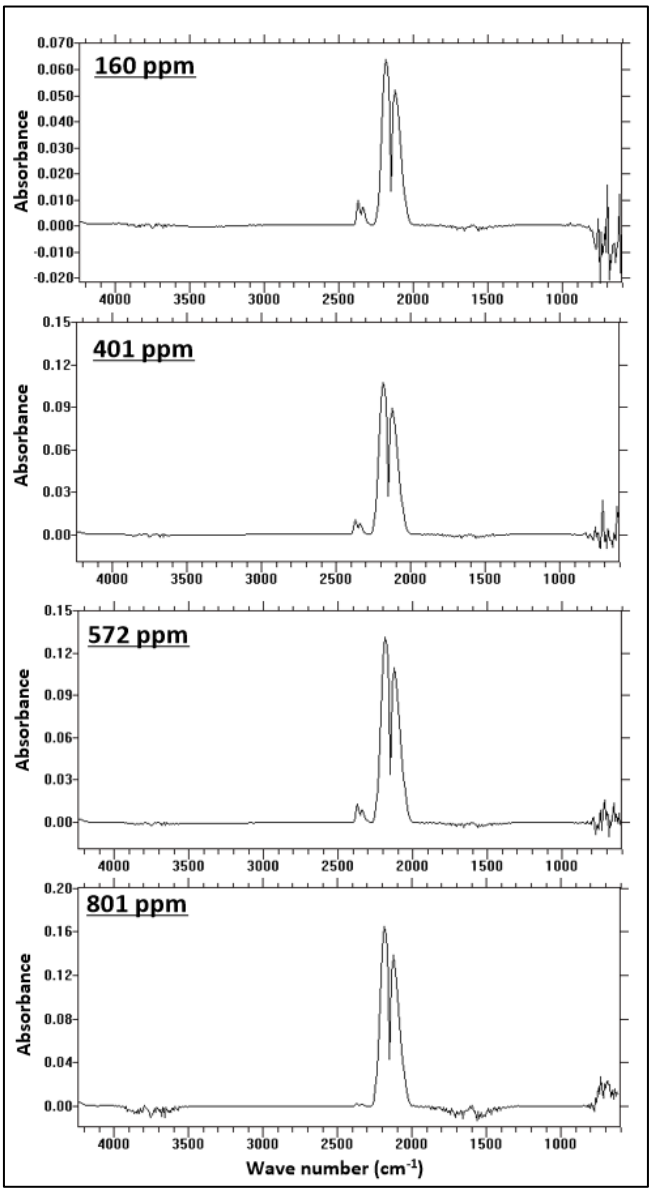

Figure A-5: CO reference spectra used during FTIR analysis.

APPENDIX B – LIST OF PUBLICATIONS

Dion, L., S. Gaboury, F. Picard, N. Morais, L. Kiss and S. Poncsak, (2018). "Universal approach to estimate perfluorocarbon emissions during individual high voltage anode effect for prebaked cell technologies." JOM, DOI # 10.1007/s11837-018-2848-6

Dion, L., P. Nunez, D. Wong, A.Spirin and S. Gaboury (2018). "Evaluation of time consistency when quantifying emissions of perfluorocarbons resulting from low voltage anode effects." Light Metals, Phoenix, AZ, USA.

Dion, L., S. Gaboury, L.I. Kiss, S. Poncsak and C.-L. Lagacé. (2018). "New approach for quantification of perfluorocarbons resulting from high voltage anode effects." Light Metals, Phoenix, AZ, USA.

Intergovernemental Panel on Climate Change (IPCC), (2017-2018). Participation as lead author in the new guidance: "2019 refinements to the 2006 IPCC guidelines for national greenhouse gas inventories".

Dion, L., L.I. Kiss, S. Poncsak and C.-L. Lagacé. (2018). "Simulator of non-homegeneous alumina and current distribution in an aluminium electrolysis cell to predict low voltage anode effects." Met.Trans. B. DOI # 10.1007/s11663-018-1174-2

Dion, L., J. Marks, L.I. Kiss, S. Poncsak and C.-L. Lagacé. . (2017). "Quantification of perfluorocarbons emissions during high voltage anode effects using non-linear approach." Journal of Cleaner Production(164): 357-366.

Dion, L., J.W. Evans, A. Godefroy, F. Laflamme, L.I. Kiss, S. Poncsak and C.-L. Lagacé.. (2017). Preventive treatments of anode effects using on-line individual anode current monitoring. Light Metals, San Diego.

International Aluminium Institute (IAI), (2015-2017). Participant : "Annual workshop on PFC emissions resulting from the aluminium industry".

Dion, L., L.I. Kiss, S. Poncsak and C.-L. Lagacé. (2016). Influence of Hooding Conditions on Gas Composition at the Duct End of an Electrolysis Cell. ICSOBA, Quebec City.

Evans, J. W., L. Dion, L.I. Kiss, S. Poncsak and C.-L. Lagacé. (2016). Recent On-Line Measurements of Individual Anode Currents at Alouette. ICSOBA, Quebec City.

Dion, L., L.I. Kiss, S. Poncsak and C.-L. Lagacé.. (2016). "Prediction of low voltage tetrafluoromethane emissions based on the operating conditions of an aluminium electrolysis cell." JOM **68**(9): 2472-2482.

Dion, L., L.I. Kiss, S. Poncsak and C.-L. Lagacé. (2016). Using artificial neural network to predict low voltage anode effect PFCs at the duct end of an electrolysis cell. Light Metals, Nashville.

Dion, L., L.I. Kiss, S. Poncsak and C.-L. Lagacé. (2016). Prediction of perfluorocarbon emissions based on the alumina distribution from an aluminium electrolysis cell. Scientific Poster. JER 2016.

Dion, L., J.W. Evans, R. Victor, L.I. Kiss, S. Poncsak and C.-L. Lagacé. (2015). On-line Monitoring of Anode Currents to Understand and Improve the Process Control at Alouette. Light Metals, Orlando.

Dion, L., L.I. Kiss, S. Poncsak and C.-L. Lagacé. (2015). Developing a predictive model for CF_4 emissions from an electrolysis cell under low voltage anode effect conditions. Scientific Poster. JER 2015.

Dion, L., L.I. Kiss, S. Poncsak and C.-L. Lagacé. (2014). Quantifying the CF_4 and C_2F_6 total emissions under dynamic conditions on an electrolysis cell. Scientific poster. JER 2014.

APPENDIX C – INPUTS AND OUTPUTS OF THE DIFFERENT MODULES OF THE ALUMINA AND CURRENT DISTRIBUTION SIMULATOR

Module 1 - Alumina feeding

Input variables:

- Positions of the feeders.
- Feeding frequency.
- Time past since previous alumina shot of each feeders.
- Mass of an alumina feeding.
- Feeder activity (On/Off).

Mechanisms considered for each volume:

- Verification of each feeder's activity. (Is a dose required?).
- Addition of undissolved alumina to the respective regions of the bath.
- Re-initialization of the previous shot time. (If feeder was used).

Output variables:

- Adjusted mass of undissolved alumina.
- Adjusted time since previous alumina shot.

Module 2 - Alumina dissolution

Input variables:

- Mass of bath respective to each volume.
- Concentration of alumina dissolved in each volume.
- Mass of undissolved alumina in each volume.
- Bath density (calculated for every time step).
- Alumina clump density (constant value).
- AlF_3 and CaF_2 concentration in bath (constant values).
- Bath temperature (constant value).
- Dissolution coefficient (constant value).

Mechanisms considered for each volume:

- Calculation of the saturated alumina concentration.
- Calculation of the available area of alumina exposed to bath.
- Calculation of the dissolution rate.
- Calculation of the new respective alumina concentration.

Output variables:

- Adjusted mass of bath respective to each volume.
- Adjusted alumina concentration respective to each volume.
- Adjusted mass of undissolved alumina.

Module 3 - Dissolved alumina diffusion

Input variables:

- Mass of bath respective to each volume.
- Concentration of alumina dissolved in each volume.
- Geometric position of each volume (constant value).
- Effective diffusivity (constant value).

Mechanisms considered for each volume:

- Calculation of the concentration difference between each pair of adjacent volume.
- Development of an exchange matrix between each pair of adjacent volume.
- Adjustment of the alumina concentrations of each respective volume.

Output variables:

- Adjusted mass of bath respective to each volume.
- Adjusted alumina concentration respective to each volume.

Module 4 - Dissolved and undissolved alumina transport

Input variables:

- Mass of bath respective to each volume.
- Concentration of alumina dissolved in each volume.
- Mass of undisolved alumina in each volume.
- Bath density (calculated for every time step).
- Area of contact between two adjacent volumes.
- Matrix for material exchange flow between volumes (flow direction and speed are considered constant).
- Fraction of undissolved alumina exchanged between volumes during each time step.

Mechanisms considered :

- Exchange of undissolved alumina between adjacent volumes.
- Exchange of bath and dissolved alumina between adjacent volumes.
- Calculation of the new respective alumina concentration.

Output variables:

- Adjusted mass of bath respective to each volume.
- Adjusted alumina concentration respective to each volume.
- Adjusted mass of undissolved alumina respective to each volume.

Module 5 - Electrical resistance model

Input variables:

- Length and cross-area of the electrical conductors
- Electrical properties of the different materials
- Cell current
- AlF_3 and CaF_2 concentration in bath (constant values)
- Bath temperature (constant value)
- Daily carbon consumption (cm per day)
- Standard sequence of anode changing
- Alumina concentration of the respective volumes
- Cathode voltage drop (constant value).
- External busbar voltage drop (constant value).
- Decomposition potential to produce aluminium (constant value).
- Last anode that was changed

Mechanisms considered :

- Calculation of the resistance of most electrical conductors.
- Calculation of the resistance of each individual anode assembly based on their respective carbon consumption.
- Calculation of the ohmic resistance of the bath for each respective volume.
- Calculation of the F value for each respective volume.
- Calculation of the electrical network resistance and calculation of the current through every anode assembly.
- Calculation of the overall cell voltage

Output variables:

- Respective current distribution within each anode assembly
- Estimated cell voltage

Module 6 – Alumina consumption

Input variables:

- Mass of bath respective to each volume.
- Respective current distribution passing through each volume.
- Concentration of alumina dissolved in each volume.

Mechanisms considered :

- Calculation of the alumina consumed in each respective volume.
- Calculation of the adjusted alumina concentrations.

Output variables:

- Adjusted alumina concentrations for each respective volume.
- Respective aluminium production for each respective volume.

Module 7 - LVAE risk assessment

Input variables:

- Respective current distribution passing through each volume.
- Threshold of detection for LVAE emissions.

Mechanisms considered :

- Calculation of the standard deviation among individual anode current.
- LVAE risk assessment.

Output variables:

- Are LVAE generated in the cell? (Yes or No).

APPENDIX D – ADDITIONAL DISCUSSIONS

1: To the author's knowledge, the demonstration of a delay between CF4 and C2F6 during the routing of the gas from aluminium electrolysis cells was not discussed in previous publications. The purpose of introducing this phenomenon as part of this study was not to identify the mechanisms that generate the delay but to identify where this delay is generated and put emphasis on the difficulties of quantifying HVAE emissions on smelters with high HVAE frequency. The explanations offered in Chapter 2 should be considered as hypotheses and additional investigations are strongly required to correctly identify the reason for this phenomenon.

2: The beta distribution "f(x,α,β)" is dependent of the beta function B(α,β) which, in turn, is strongly dependant on the gamma function "Γ": where "B(α,β)= Γ(α)· Γ(β) / Γ(α+β)". Once the definition of the gamma function is applied "Γ(x)=(x-1)!", the beta function can be reduced to "(α-1)!)·(β-1)! / (α+β-1)!".

3: Multiple models were originally investigated in this study. However, only the models showing the greatest interest were presented in Chapter 2 and the other models were not discussed because of their lower accuracy.
The CF_4 estimation models that were not considered are listed below:

- Continuous non-linear PAED model (without the linear part).
- Linear and non-linear model using AED.
- Non-linear model using the maximum polarisation voltage.
- Multivariate linear regression using 2 variables (PAED and AEO).
- Multivariate linear regression using 4 variables (PAED, AEO, AED and MPV).

- Automated neural network using 2 variables (PAED and AEO).

The C_2F_6 estimation models that were not considered are listed below:

- Non-linear model using the AEO.
- Non-linear model using the maximum polarisation voltage.
- Multivariate linear regression using 2 variables (PAED and AEO).
- Multivariate linear regression using 4 variables (PAED, AEO, AED and MPV).
- Automated neural network based on 2 variables (PAED and AEO).

4: The software STATISTICA has been used in Aluminerie Alouette to perform multivariate analysis on various occasions in the past. In the software, different algorithms are available to develop predictive models such as random forest generators, multilayer perceptron neural network, radial basis function neural network, etc. Based on the historical data of the facility, the multilayer perceptron neural network was selected as the tool with the best potential for the purpose of multivariate analysis performed during this study. In every case were an ANN was used during this project, the precision of the ANN was compared to other multivariate tools and the results were always substantially more efficient.

5: Individual HVAE measurements are subject to a more important level of imprecision than long period measurements. The quantification of CF_x emissions involves different step (measurement by the instrument, cross-identification of the HVAE attributes, quantification of overlapping HVAE, etc.) with different level of uncertainties. Therefore, by using the mean value of multiple HVAE with similar attributes (PAED, or

AEO), it eliminates part of the bias caused by the measurement technique and should improve the fitting of the proposed equations.

6: The development work of the model presented in section 2.5.1.5 was realized by Dr. Jerry Marks and was a work in progress at the time where the content of Chapter 2 was published. The equations were still under development in order to try and eliminate the fact that the predictive model was not continuous when there was a step change in PAED, i.e. around 5 and 200 seconds. Moreover, it is important to mention that the data points presented in Figure 2-10 were not the same ones originally used to develop the original equations. Finally, the detailed equations used for this model were published by Marks and Nunez in Light Metals 2018: reference #7 from Chapter 3.

7: The specific equations used in this model are not presented in Chapter 3 because they differ from smelter to smelter (being Tier 3). However, the general equation is presented below, where $Total_{CF4}$ (g) is the mass of CF_4 emitted per HVAE, PAED (s) is the polarized anode effect duration, kA (kA) is the cell current, dE/dt (g CF_4 / kA /s) is the emission rate during the HVAE, and C1 and C2 are constant specific to the smelter.

$$Total_{CF_4} = \frac{dE}{dt} \cdot PAED \cdot MP \qquad \textit{(D-1)}$$

$$\frac{dE}{dt} = \frac{C1}{PAED^{C2}} \qquad \textit{(D-2)}$$

8: The results presented in Table IV illustrate only one variable which appears to have no real effect on the LVAE occurrence: bath chemistry. The absence of a relationship with LVAE may be linked to the slow variations of bath chemistry (AlF_3, CaF_2, etc.) that

generally occurs in a cell (over a few days), while LVAE generation occurs on a shorter time frame (minutes, to hours). On the other hand, a high concentration of bath additives should be disadvantageous in terms of LVAE emissions as it reduces the alumina's capability for dissolution. Even though these details were not discussed in the literature presented in table IV, they could be relevant topics of research.

9: The distribution in terms of CF_4 concentration of the complete dataset was the main driver in the selection of the number of categories. For the development of the ANNs from step 3 (A to D), it was necessary to have data uniformly distributed over the entire range of each sub-model while maximizing the total number of data point to increase precision. Hence, by taking these factors into consideration, it was possible to select the four categories and the specific threshold (50, 200 and 500 ppb) to find a balance between uniformity and precision. The distribution of the dataset is illustrated in Figure D-1.

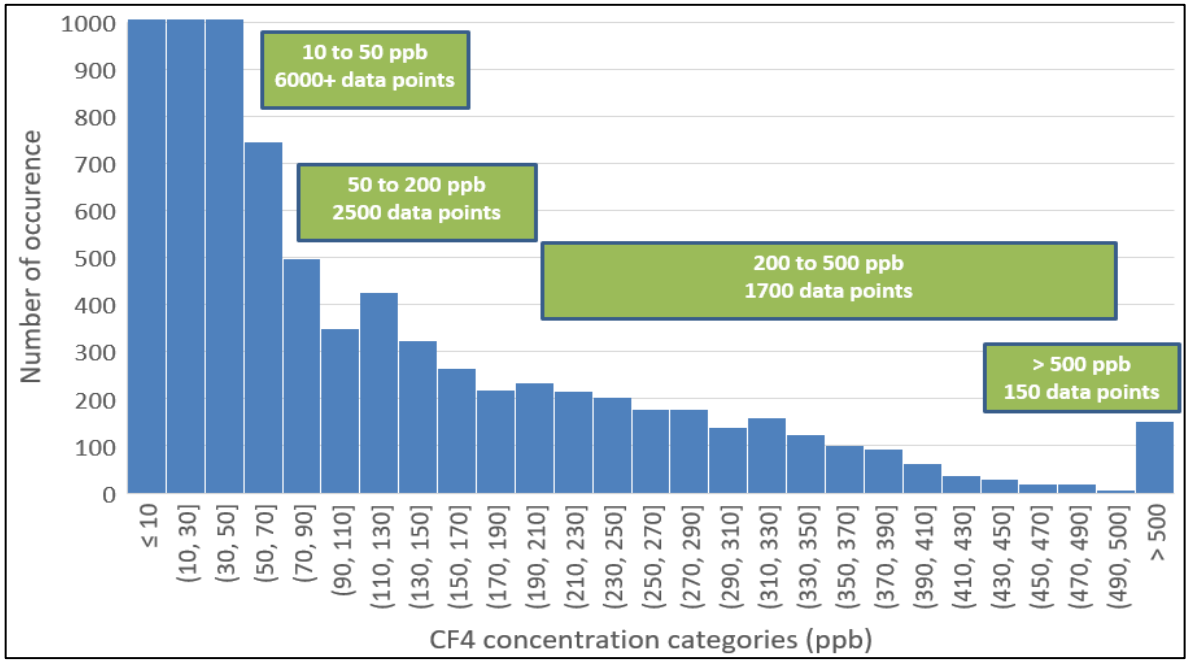

Figure D-1: CF4 concentration of the dataset used in Chapter 4.

10: For the validation, the thirteen scenarios selected were the only moments were CF_4 was observed under low voltage conditions during the test. In order to achieve such conditions, it was necessary to reduce the alumina feeding within the control system by approximately 10 to 30%. The additional two scenarios were selected arbitrarily from long periods where PFC emissions were not observed. The validation methodology aimed at evaluating the capability of the model to quantify CF_4 emissions resulting from LVAE for a period of multiple hours similarly to the actual quantification methodology from HVAE emissions which is based on a monthly average.

11: The discussions related to Figure 5-9 are only hypotheses and additional investigations are strongly required in order to provide an accurate explanation for this phenomenon. Moreover, gas flow measurements or simulation are also necessary to determine if the observed CO behaviour can apply or not to CF_4. The only conclusion that we can confirm under such conditions (25% of the hoods removed uniformly) is that it strongly change the gas flow and can add an important bias to measurements of the gas composition extracted from the exhaust duct during that time.

12: The time step used for the simulations was 0.1 second, which is way lower than the restriction described as equation 6-7 which correspond to a time step limitation of approximately 196 seconds.

An additional limitation to consider is the Courant-Friedrich-Lewy condition which applies to mass transfer under convective forces. The CFL condition under two dimensions is characterized as:

$$\Delta t \cdot \left(\frac{u_x}{\Delta x} + \frac{u_y}{\Delta y}\right) \leq 1$$

Hence, for a maximum flowrate of 0.1 m/s and the actual dimensions of the volumes, the maximum time step would be 7.9 seconds.

13: To simulate alumina dissolution, the alumina clump was considered spherical for its simplicity with the intention of optimizing the mechanisms in a next step (not included in the scope of the project). However, it is clear, that this assumption may affect the dissolution rate of the alumina. This effect becomes more important when the undissolved content of alumina increases in a specific region of the cell. At this point, additional concept such as sludge formation should also be considered for accuracy.

14: It is clear from the absence of uniformity within the literature that the alumina dissolution coefficient is dependent on multiple factors. It was decided to use an average between the different coefficients found in the literature because it was unclear which conditions were most similar to the one that we tried to simulate. Optimal results would be achieved by performing laboratory testing under controlled conditions to determine a typical K_m specific to our project. Unfortunately, such testing was not performed as part of this project.

15: The two main mechanisms considered to be included in the equivalent diffusivity equation are the convective forces and the turbulent movement generated by the bubbles. However, it is almost impossible to separate the effect of one another when determining the equivalent turbulent diffusivity. At the time where chapter 6 was sent for publication, no information was found in the literature regarding any approximative value for D_{eq}. For this reason, it was necessary to determine a set of conditions that would approximate the value of $D_{eq.}$ This set of condition (30 minutes homogenization time) was

made conjointly by the author of this manuscript and his supervisors. However, it is clear that this part of the simulator should be improved if adequate data is available.

An accurate observer may perceive that the equivalent diffusion coefficient presented in this thesis is different than the one presented in the original publication from MMTB. An error was identified in the units from the modeling code which changed the actual value of $D_{eq.}$ Hence, the value of 0.0025 m^2/s is accurate for comparison with the literature. This error had no impact on the results presented further in this chapter.

16: As mention in Chapter 6, the development of the mass exchange between the volumes is based on the thesis from Thomas Hofer. The different flow direction illustrated in Figure 6-6 was obtained from the original figure from Hofer reproduced below:

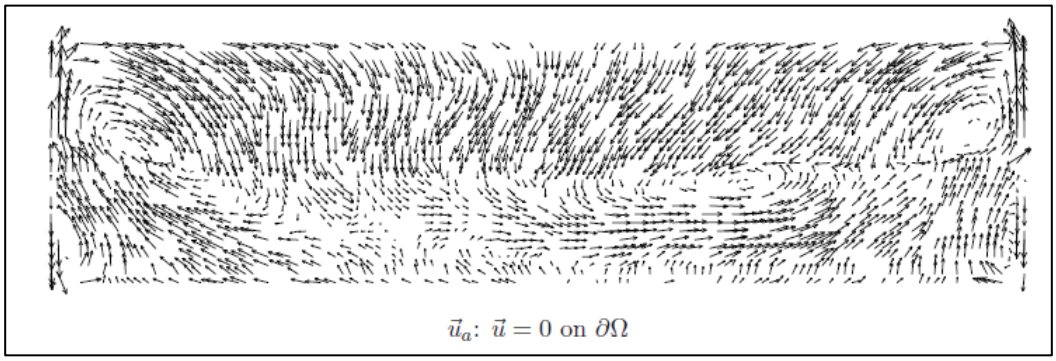

Figure D-2: Illustration of the bath flow reproduced from the thesis of Thomas Hofer, page 54.

Using the bath flow map and knowing that the maximum velocity was in the corner regions of the cell, it was possible to impose a mass exchange matrix in the simulator in order to assure that mass balance is respected for every time step, i.e. the mass exiting a specific volume is replaced by an equivalent amount coming from a combination of adjacent volumes. In addition, a specific verification is performed for every time step to verify the mass balance integrity.

17: The choice to consider exclusively the primary conductors was based on in-situ measurements performed at the smelters. Observations during normal operations demonstrated that only an insignificant fraction of the current goes through the secondary conductors, thus justifying the possibility of neglecting them to simplify the electrical network of the simulator. Nonetheless, this choice will have an impact on the simulating capability of the process. This is especially true for large deviation of the process that could occur if newly set anodes are included in the simulator or during the increase of resistivity caused by the PFC generated under the anodes during HVAE. Before using the simulator for such kind of simulations or for important process decisions, it is necessary to quantify the impact of this approximation by comparing specific scenarios using different electrical network simulation tools. This comparison was performed by investigating the redistribution of the current when an anode is removed from an electrolysis cell. It demonstrated that the approximation "without secondary conductors" had an maximum error lower than 1% of the total current in comparison to a case where such secondary conductors are considered. However, the error may be more important if the purpose is to adequately represent the current flowing through other conductors such as busbars or risers.

18: In the present study, the F factor value is only dependant on the localized alumina concentration within the bath. However, in real cells, the film of gas under the anodes will be dependant on multiple factors, such as alumina concentration, current density, loose carbon, concentration and activation over potentials, CO_2 and CO bubbles, etc. Henceforth, the impact of these elements should eventually be considered and included

to the simulator. For this purpose, the F factor was included in the simulator as a simple function, allowing for improvements to be included easily to the simulator in future steps.

19: The validations presented in Figure 6-11 were presented as functions of the time to illustrate the evolution of the concentration considering that at the origin (t=0) the values were imposed based on real measurements. Nonetheless, using fit statistics, we can see the improvement resulting from the change in bath velocity as illustrated in Figure D-3.

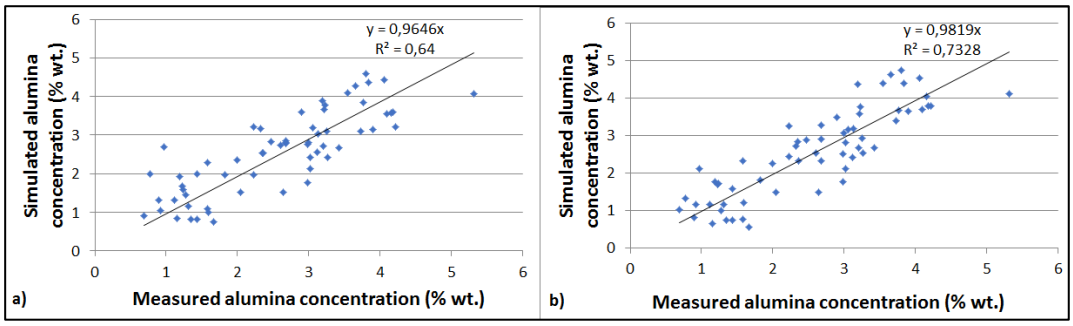

Figure D-3: Linear regression between the simulated and measured alumina concentration for a) the initial hypotheses and b) the corrected bath velocity.

As observed, on the previous figure, by correcting the bath velocity, the R-squared coefficient improved from 0.64 to 0.733 confirming that such improvements were beneficial to the simulations. Moreover, the slope of the correlation has also improved slightly, going from 0.9646 to 0.9819.